

FERROMAGNETIC JOSEPHSON JUNCTIONS CARRYING
SPIN-TRIPLET SUPERCURRENT FOR CRYOGENIC MEMORY

By

Joseph Allen Glick III

A DISSERTATION

Submitted to
Michigan State University
in partial fulfillment of the requirements
for the degree of

Physics—Doctor of Philosophy

2017

ABSTRACT

FERROMAGNETIC JOSEPHSON JUNCTIONS CARRYING SPIN-TRIPLET SUPERCURRENT FOR CRYOGENIC MEMORY

By

Joseph Allen Glick III

In this thesis we present the first experimental demonstration of phase-controllable Josephson junctions that carry long range spin-triplet supercurrent. These junctions exhibit ground-state phase shifts of either 0 or π and are of considerable interest for the development of random access memory for energy efficient superconducting computers.

We demonstrate a scheme by which spin-triplet supercurrent in the junctions is generated through the ferromagnetic proximity effect using three magnetic layers with noncolinear magnetizations. The central layer is a synthetic antiferromagnet with magnetization perpendicular to the plane, while the other two ferromagnetic layers have in-plane magnetization. First, we establish that the supercurrent in these junctions is spin-triplet in nature by observing the characteristic slow decay of the critical current versus the central layer thickness when compared to other junctions that do not have the in-plane layers and carry only spin-singlet supercurrent. The phase state of the junctions is revealed by measuring the interference between two such Josephson junctions in a Superconducting QUantum Interference Device (SQUID) loop. By switching the magnetization of one of the layers by 180° without disturbing the other two layers, we show that the phase state of the Josephson junctions can be controllably switched between 0 and π over a thousand times without error, opening possibilities for their use in superconducting memory.

We also show that there are easier ways to make a phase-controllable cryogenic memory device using spin-singlet supercurrent. We discuss how Josephson junctions containing only

two magnetic layers of appropriate thickness arranged into a spin-valve configuration exhibit controllable $0-\pi$ switching, first demonstrated by the Birge group at Michigan State University in 2016 using a similar SQUID measurement scheme. I describe the main contributions I made as a part of that effort, in particular the development of a general asymmetric SQUID fitting program that provided the unambiguous proof that the devices switched between the 0 and π phase states.

We also discuss a number of material studies that served as stepping stones toward the development and improvement of both of the previously mentioned phase-controllable memory demonstrations. We use primarily Fraunhofer physics and SQUID magnetometry to characterize the magnetic and superconducting properties of Josephson junctions containing the ferromagnets: Ni, Ni₈₁Fe₁₉, Ni₆₅Fe₁₅Co₂₀, Pd₉₇Fe₃, and multilayers of Pd/Co. We examine the relative advantages and disadvantages that each of these materials offer to the development of future superconducting memory devices and compare the strengths and weaknesses of the two phase-control memory schemes.

Copyright by
JOSEPH ALLEN GLICK III
2017

To my mother and father.

ACKNOWLEDGMENTS

I have been fortunate to work alongside many excellent people while in the Birge group at Michigan State University (MSU). I thank Norman Birge who is truly the best advisor I could have asked for, and likewise a fantastic person and friend. You are an exceptional teacher, mentor, and a great wellspring of ideas from whom I learned new things everyday. I appreciated your patience in allowing me to grow and develop as an experimental physicist, the great level of autonomy you gave me during our research pursuits, the incredible opportunities you opened up to me to collaborate with industry and academic researchers, and encouraging me to attend many academic conferences and workshops.

I thank Reza Loloee, for his inspiring dedication to students such as myself. Needless to say, you saved a great number of my sputtering runs from certain disaster. I thoroughly enjoyed working with you to fix vacuum systems and low-temperature probes, times when I learned so much from your knack for creative troubleshooting. Your insightful suggestions helped lead to the selection of some of the materials used in this work and the improvement of many of our sample fabrication processes. You were also one of the first people that helped me feel welcome at MSU, always filling the lab with laughter.

I thank William Pratt for teaching me so much about low-temperature physics and magnetic materials, and I appreciated his clear and systematic approach to physics. None of the transport measurements in this work could have been done without your masterfully designed probes and cryostats, in addition to several of your vacuum chambers for thin-film deposition. I already miss your sagely wisdom, witty stories, and impeccable craftsmanship.

I appreciate the helpful advice of Baokang Bi regarding sample fabrication, especially in electron-beam lithography, and for keeping the Keck microfabrication clean room facility at

MSU running smoothly and efficiently, despite its many users.

To all of the former graduate students of the Birge group who I worked with: Yixing Wang, Eric Gingrich, William Martinez, Mazin Khasawneh, and Bethany Niedzielski. Each of you taught me parts of the fabrication and measurement process that made my own research possible. I also benefited immensely from your own research efforts and progressed only by building off of the foundation that you had laid. It was truly rewarding to see some of our ideas become experimental realities.

I am also grateful to the current graduate students Victor Aguilar and Alex Madden. I am glad to know that you both will be instrumental in carrying our group's research forward. Victor, I want to especially thank you for your help with LabVIEW programming, which saved me untold days of measurement time in addition to working alongside me to develop our technique to pattern magnetic bit arrays.

I enjoyed working with our postdocs and visitors to our group including Nathan Satchell, Adel Gougam, and Demet Korucu as well as the many undergraduates, including Josh Willard, Sam Edwards, Anna Osella, Thomas Bertus, and Kevin Werner who helped me perform a number of experimental studies. Special thanks to Alex Cramer for his assistance in writing code to fit I-V curves that account for thermal rounding.

Together all of the Birge group members, past and present, made for a collaborative team that was both fun and intellectually stimulating.

I thank our collaborators at Northrop Grumman Corporation, especially Anna Herr, Don Miller, Ofer Naaman, Tom Ambrose, Jackson Chang and Steve Van Campen. Working with you has been an invaluable experience and your many insightful suggestions have aided in my thinking and greatly benefited this work. I've learned much from our collaborators at Arizona State University, Nate Newman and Nick Rizzo. Nick's expertise in magnetic

materials directly aided in the development of many of my samples. To our collaborators at Sandia National Laboratory, namely Nancy Missert and Paul Kotula, your amazing Scanning Transmission Electron Microscopy images of my samples were key in understanding some of the issues regarding our sample fabrication process.

I am grateful for the funding from the Intelligence Advanced Research Projects Activity (IARPA) in addition to the encouragement from Scott Holmes and Marc Manheimer. Further financial support from the MSU physics department and Northrop Grumman Corporation during my time at MSU were essential to the completion of this work.

I thank Megan Donahue, Johannes Pollanen, David Tomanek, and Scott Pratt for serving on my thesis committee and for their many helpful comments. Scott, I want to especially thank you as some of the biggest decisions I made during my time at MSU were strongly influenced by the guidance you gave me.

I thank my parents Steve and Linda, my brother Aaron, and my sisters Hannah and Emily, as well as my wife's family for the incredible love and encouragement they have always given me. You all inspired me to challenge and continually improve myself both as a person and as a scientist, all the while helping me to counterbalance the stresses of graduate school. *F.c.* Fermi and Nambu have also shown me how to take a more relaxed perspective during vexing circumstances.

Finally, I thank my wife Jen for her steadfast love, perseverance, and fortitude that have aided and replenished me everyday on this journey we took together. Besides this, she has made countless indelible scientific contributions to this work.

TABLE OF CONTENTS

LIST OF TABLES	xi
LIST OF FIGURES	xii
Chapter 1 Introduction	1
1.1 Energy Efficient Superconducting Computing	1
1.2 Chapters Overview	5
Chapter 2 Superconductivity	8
2.1 The Meissner-Ochsenfeld Effect and London Theory	9
2.2 Ginzburg–Landau Theory	11
2.3 BCS Theory	15
2.4 The Josephson Effect	18
2.5 The RCSJ Model	20
2.5.1 Overdamped Junctions	22
2.6 Flux Quantization and SQUIDS	24
2.6.1 Magnetic Flux Quantization	24
2.6.2 SQUIDS	27
Chapter 3 Ferromagnetism	33
3.1 Historical Overview	33
3.2 Magnetic Domains	35
3.3 Magnetic Anisotropy	38
3.3.1 The Stoner-Wohlfarth Model: Uniaxial Anisotropy	39
3.3.2 Types of Magnetic Anisotropy	44
Chapter 4 Interplay Between Superconductivity and Ferromagnetism . .	46
4.1 The Proximity Effect at S/N Interfaces	47
4.2 The Proximity Effect at S/F Interfaces	51
4.3 π -Phase Josephson Junctions	56
4.4 Fraunhofer Patterns in Ferromagnetic Josephson Junctions	58
4.4.1 The Josephson Effect in the Presence of Magnetic Flux	58
4.4.2 Adding a Ferromagnetic Layer	63
4.5 Generating Long-Range Spin-Triplet Correlations with Ferromagnetic Barriers	65
Chapter 5 Experimental Techniques	70
5.1 Sputtering	70
5.2 Photolithography	75
5.3 Electron-Beam Lithography	77
5.4 Ion Milling	80
5.4.1 Ion Mill and Thermal Evaporation Chamber	83

5.5	Josephson Junction Sample Fabrication	84
5.6	Measurement Probes and Low Noise rf SQUID Electronics	90
5.7	SQUID Magnetometry	92
Chapter 6	S/F/S Josephson Junctions: Materials Characterization	94
6.1	Role of π -Junctions in Cryogenic Memory	95
6.2	Sample Fabrication and Characterization	98
6.3	Critical Current Oscillations of Josephson Junctions	104
6.3.1	Junctions Containing Ni ₆₅ Fe ₁₅ Co ₂₀	104
6.3.2	Junctions Containing Permalloy	118
6.3.3	Junctions Containing Pd ₉₇ Fe ₃	122
6.3.4	Junctions Containing Ni	130
6.4	Conclusion	132
Chapter 7	Controllable Phase SQUIDs: Spin-Singlet	134
7.1	Spin-Valve Josephson Junctions and SQUIDs	135
7.2	Theory of the Asymmetric DC SQUID	142
7.3	SQUID Oscillation Data: Comparison to Theory	150
Chapter 8	Spin-Triplet Josephson Junctions Containing a PMA SAF	153
8.1	Magnetic Properties of Pd/Co Multilayers and Synthetic Anti-Ferromagnets With Perpendicular Magneto-Anisotropy	155
8.1.1	Synthetic Anti-Ferromagnets	157
8.2	Josephson Junctions	159
8.2.1	Sample Fabrication	160
8.3	Transport Measurements and Analysis	165
8.3.1	Fraunhofer Patterns	166
8.3.2	Critical Current vs Thickness	171
8.4	Conclusion	176
Chapter 9	Controllable Phase SQUIDs: Spin-Triplet	178
9.1	SQUID Sample Fabrication	179
9.2	Measurement of SQUID Oscillations	182
9.3	SQUID Oscillation Data: Comparison to Theory	191
9.4	Repeated Switching Experiment	194
9.5	SQUID Measurements Below 4.2 K in a Dilution Refrigerator	196
9.6	Conclusion	199
Chapter 10	Conclusion	202
APPENDIX	206
REFERENCES	222

LIST OF TABLES

Table 5.1: Sputtering parameters used for the various metallic targets	73
Table 5.2: Ion mill settings	81
Table 5.3: Ion mill conversion factors for various materials	82
Table 6.1: Parameters obtained from fits of the Ivanchenko-Zil'berman function to the data shown in Fig. 6.5	109
Table 6.2: Best-fit parameters from Eq. (6.5) corresponding to the data in Figs. 6.7(a) and 6.11(a)	115
Table 7.1: Best-fit parameters for the four magnetic states of the SQUID using the asymmetric SQUID theory	150
Table 7.2: Inductances and critical currents extracted from the least-squares fits . . .	151
Table 8.1: Fitting the data in Fig. 8.8 to Eq. (8.2) yields the best-fit parameters . . .	173
Table 9.1: Best-fit parameters for the P and AP states for SQUID 2A-4	192
Table 9.2: Summary of the the seven spin-triplet SQUID samples measured	194
Table 1: Best-fit parameters for the P and AP states for SQUID 2A-1	208
Table 2: Best-fit parameters for the P and AP states for SQUID 2A-2	209
Table 3: Best-fit parameters for the P and AP states for SQUID 2A-3	211
Table 4: Best-fit parameters for the P and AP states for SQUID 3A-3	214
Table 5: Best-fit parameters for the P and AP states for SQUID 4A-1	217
Table 6: Best-fit parameters for the P and AP states for SQUID 4A-2	219

LIST OF FIGURES

Figure 2.1:	The equivalent circuit for the RCSJ model of a physical Josephson junction	20
Figure 2.2:	The tilted washboard potential of the RCSJ model.	22
Figure 2.3:	The time-average voltage difference, Eq. (2.32), across the overdamped junction in the RCSJ model (solid line). For $ I \leq I_{c0}$, the voltage remains zero, but approaches Ohm's law (dashed line) when $ I \gg I_{c0}$	23
Figure 2.4:	The symmetric dc SQUID with total supercurrent I	28
Figure 2.5:	Symmetric SQUID oscillations	32
Figure 3.1:	Ferromagnetic domain structures	37
Figure 3.2:	Schematic setup for the Stoner-Wohlfarth model	38
Figure 3.3:	Magnetization reversal in the Stoner-Wohlfarth model	40
Figure 3.4:	Hysteresis loops showing the magnetization M vs. the magnetic field H applied along the easy axis of the ferromagnet	42
Figure 3.5:	Astroid diagram from the Stoner-Wohlfarth model	43
Figure 4.1:	Proximity effect near the interface of a superconductor and a normal metal	48
Figure 4.2:	Density of states at a superconductor/normal metal interface and Andreev reflection	49
Figure 4.3:	A simplified toy model of a normal metal and a ferromagnet	52
Figure 4.4:	Proximity effect near the interface of a superconductor and a ferromagnet	55
Figure 4.5:	$0-\pi$ phase oscillations in an $S/F/S$ Josephson junction	57
Figure 4.6:	Geometry for calculating the Fraunhofer pattern in a Josephson junction with rectangular cross-section of area LW	59
Figure 4.7:	Fraunhofer patterns for rectangular and circular Josephson junctions . .	62
Figure 4.8:	Fraunhofer patterns for a ferromagnetic Josephson junction	63

Figure 4.9: Schematic for the generation of long-range spin-triplet correlations using noncollinear magnetizations	65
Figure 4.10: One method for the generation of 0 and π phase junctions using long-range spin-triplet correlations	68
Figure 4.11: Schematic for the generation of long-range spin-triplet correlations using noncollinear magnetizations	69
Figure 5.1: 7-target sputtering chamber with active plasma	71
Figure 5.2: Bit arrays written with electron-beam lithography	79
Figure 5.3: The ion milling and thermal evaporation vacuum chamber	84
Figure 5.4: Ferromagnetic Josephson junction fabrication steps, part 1	86
Figure 5.5: Ferromagnetic Josephson junction fabrication steps, part 2	87
Figure 5.6: Josephson junction sample design and images	88
Figure 5.7: rf-SQUID comparator measurement circuit	92
Figure 6.1: Cryogenic phase-sensitive memory cell proposed by Northrop Grumman Corporation	97
Figure 6.2: A schematic representation of the cross-sectional structure of our $S/F/S$ Josephson junctions.	99
Figure 6.3: Cross-sections through the center of our $S/F/S$ Josephson junctions prepared with focused ion beam (FIB) milling and imaged with Scanning Transmission Electron Microscopy (STEM) to validate the fabrication process.	100
Figure 6.4: The voltage across an overdamped $S/F/S$ Josephson junction containing a 2 nm layer of NiFeCo, versus the applied current	106
Figure 6.5: The voltage across an $S/F/S$ Josephson junction versus the applied current at applied magnetic fields of 18 mT (circles) and 36 mT (diamonds), using two different measurement schemes	108
Figure 6.6: Fraunhofer patterns of Josephson junctions containing NiFeCo	110
Figure 6.7: Critical current oscillations and Fraunhofer pattern shifts in Josephson junctions containing NiFeCo	113

Figure 6.8: Switching field distribution for both the NiFeCo and NiFe based $S/F/S$ junctions	117
Figure 6.9: NiFeCo hysteresis loops of unpatterned films with d_{NiFeCo} ranging from 1-5 nm	119
Figure 6.10: Fraunhofer patterns of Josephson junctions containing NiFe	120
Figure 6.11: Critical current oscillations and Fraunhofer pattern shifts in Josephson junctions containing NiFe	121
Figure 6.12: Hysteresis loops of unpatterned films containing PdFe with thickness d_{PdFe} spanning 8-16 nm.	124
Figure 6.13: Fraunhofer patterns of Josephson junctions containing PdFe	125
Figure 6.14: Magnetic switching of PdFe Josephson junctions at small applied fields.	127
Figure 6.15: Critical current oscillations and Fraunhofer pattern shifts in Josephson junctions containing PdFe	129
Figure 6.16: Critical current oscillations in Josephson junctions containing Ni	131
Figure 7.1: Scheme to control the phase-state of a spin-valve Josephson junction	135
Figure 7.2: Spin-valve SQUID schematic and the configuration of the four magnetic states	138
Figure 7.3: Oscillations in the critical current versus the current applied to the flux-line and the in-plane set field used to control the magnetic state of the SQUID	141
Figure 7.4: Asymmetric SQUID theory, closed solutions	145
Figure 7.5: Asymmetric SQUID theory, open solutions	147
Figure 7.6: Using asymmetric SQUID theory to fit the SQUID oscillation data from the four magnetic states	152
Figure 8.1: Hysteresis loops of a Pd/Co multilayer film measured at 5K using a SQUID magnetometer	156
Figure 8.2: Hysteresis loop measurements of synthetic antiferromagnet (SAFs) films measured using a dc-SQUID magnetometer	158

Figure 8.3:	A schematic representation of the vertical cross sectional structure of our Josephson junctions (not to scale)	161
Figure 8.4:	Vertical cross sections of the junctions described in Fig. 6.2 (b) prepared using a focused ion beam (FIB) were investigated by high-resolution scanning transmission electron microscopy (STEM) and energy dispersive x-ray spectroscopy (EDX)	163
Figure 8.5:	The critical current, I_c , is plotted versus the applied in-plane field H for junctions with the structure shown in Fig. 8.3 (a) (without F' and F'') .	167
Figure 8.6:	Critical current, I_c , vs. the applied in-plane field H , for a sample with $F' = F'' = \text{Ni}$ (1.6 nm), and $n=1$, similar to Fig. 8.3 (b)	169
Figure 8.7:	I_c is plotted vs. the applied in-plane field H , for junctions with the structure shown in Fig. 8.3 (b) with $F' = \text{Py}$, $F'' = \text{Ni}$	172
Figure 8.8:	Comparison of the critical current decay in spin-triplet and spin-singlet samples and their area-resistance products	174
Figure 9.1:	Spin-triplet Josephson junction structure and SQUID loop design	180
Figure 9.2:	Flowchart describing the measurement process for probing the two main aspects of the SQUID samples	183
Figure 9.3:	A 3D plot of a complete minor magnetization loop, for SQUID 2A-4	185
Figure 9.4:	The average critical current $I_{c,\text{Avg}}$ oscillates with the current applied to the flux line I_{flux} for the P and AP states of SQUID 2A-4	187
Figure 9.5:	[A 3D plot of a complete minor magnetization loop, for SQUID 2A-1	188
Figure 9.6:	Fitting the P and AP states from SQUID 2A-4	192
Figure 9.7:	Repeated switching between the P and the AP-states.	195
Figure 9.8:	Critical current versus temperature for SQUID 2A-2 in a dilution refrigerator	197
Figure 9.9:	Critical current versus flux-line current and temperature for SQUID 2A-1 in a dilution refrigerator	198
Figure 1:	Repeated switching between the P and the AP-states from SQUID 2A-1.	207
Figure 2:	Fitting the P and AP states from SQUID 2A-1	208

Figure 3:	A 3D plot of a complete minor magnetization loop, for SQUID 2A-2 . . .	209
Figure 4:	Fitting the P and AP states from SQUID 2A-2	210
Figure 5:	A 3D plot of a complete minor magnetization loop, for SQUID 2A-3 . . .	211
Figure 6:	Repeated switching between the P and the AP-states from SQUID 2A-3.	212
Figure 7:	Fitting the P and AP states from SQUID 2A-3	213
Figure 8:	A 3D plot of a complete minor magnetization loop, for SQUID 3A-3 . . .	214
Figure 9:	Repeated switching between the P and the AP-states from SQUID 3A-3.	215
Figure 10:	Fitting the P and AP states from SQUID 3A-3	216
Figure 11:	A 3D plot of a complete minor magnetization loop, for SQUID 4A-1 . . .	217
Figure 12:	Fitting the P and AP states from SQUID 4A-1	218
Figure 13:	A 3D plot of a complete minor magnetization loop, for SQUID 4A-2 . . .	219
Figure 14:	Repeated switching between the P and the AP-states from SQUID 4A-2.	220
Figure 15:	Fitting the P and AP states from SQUID 4A-2	221

Chapter 1

Introduction

1.1 Energy Efficient Superconducting Computing

Energy use by U.S. data and computing centers is projected to increase from 72 to 176 TWh from 2009 to 2020 [1]. Reducing data center energy consumption by a factor of 10 would save the United States approximately \$15 billion per year in 2020, assuming an energy cost of 0.1 \$/kWh. The current push towards exascale computing and beyond with conventional devices will soon require untenable power consumption, increasing the appeal for energy-efficient solutions to these growing problems.

Superconducting computing has been recently targeted by the U.S. Department of Energy as a possible way to meet their energy dissipation goal for exascale high-performance computing [2].[†] While it is difficult to project, at large scales superconducting computers are thought to be orders of magnitude more energy efficient than conventional systems based on Complementary Metal Oxide Semiconductor (CMOS) technologies [1,3].

The gains in energy efficiency derive from a unique property of superconducting materials, namely that electrical current can be driven through them with zero energy loss from Joule heating. In the superconducting state, the resistance of such a material is exactly zero, provided it is below a certain critical temperature. Since the critical superconducting transition temperature T_c of most elemental superconductors (such as Niobium) is below 10 K,

[†]The Japanese government is also currently involved in an effort to develop large-scale superconducting computers.

cryogenic cooling is required, typically by immersion in liquid Helium (≈ 4.2 K). While most data centers today utilize some form of refrigeration for cooling, the energy gains of a superconducting computer would have to offset the additional costs of liquid Helium in order to be economical assuming all other factors, such as performance, were equal.[†]

Some projections have shown that if the circuits for logic and memory operations as well as the interconnects between them were made of superconductors, the gains in energy efficiency would be 10-100 times that of current CMOS technologies, after accounting for the cost of cryogenic cooling [1]. Also, researchers and industry partners alike are actively investigating digital superconducting computers and circuits (near 4.2 K) as possible intermediate systems that would interface above the cold space with quantum computers that operate in the mK temperature regime.[‡]

Efforts to harness the advantages offered by superconductors for computing have been waged since the 1950s with varying levels of success. An early example was the “cryotron” switch invented by Dudley A. Buck at the Massachusetts Institute of Technology Lincoln Laboratory, who wound a straight superconducting rod of Ta with an insulated superconducting Nb wire [4]. The current through the Ta rod could be switched on or off by driving a current through the Nb wire to generate a magnetic field that would suppress the superconducting properties of the Ta. The device was later used to develop several different types of logical circuits.

When the Josephson effect was discovered in 1962, it paved the way for superconducting devices based on Josephson junctions, *i.e.* two superconductors separated by a thin barrier

[†]High-temperature superconductors (for example with T_c higher than 77 K, the temperature of liquid nitrogen) could significantly reduce the cost of cooling, but the incompatibility of those materials with most microfabrication techniques remains a barrier to their expanded use.

[‡]Although some quantum computing architectures utilize superconducting elements, their operations are performed on quantum bits (qubits), unlike the superconducting computers we discuss here, which operate on classical bits.

material such as an insulator, normal metal, or ferromagnet. The decades that followed produced a number of technological advances towards the fabrication of more reliable Josephson junctions. In 1985, a new logic family based on Josephson junctions called Resistive Single-Flux Quantum (RSFQ) logic was proposed by Konstantin Likharev, Oleg Mukhanov, and Vasili Semenov at Moscow State University, who suggested a way to achieve fast switching on picosecond time scales [5]. The general idea is to use brief picosecond Single Flux Quantum (SFQ) voltage pulses to transmit binary information, rather than dc voltages (as in most semiconductor-based logic schemes). The SFQ pulses can be transmitted at nearly a third of the speed of light along superconducting lines [6]. Circuits derived from more recent classes of SFQ logic have been successfully demonstrated to operate at frequencies up to 770 GHz [7]. Major advances via the development of new superconducting logic families in 2011, for example Reciprocal Quantum Logic (RQL) invented at Northrop Grumman Corporation [8] and energy efficient RSFQ (eeRSFQ) by researchers at HYPRES, Inc. [9, 10], have greatly improved the energy efficiency of logical superconducting circuits.

Several groups are now actively pursuing the development of scalable computers that utilize superconducting elements in both the logic and memory portions of their circuits. In 2005 the National Security Agency’s Superconducting Technology Assessment forecasted that the limiting factor in the eventual development of a successful, fully superconducting computer would be the memory and storage, and not the processor performance [11]. This prediction rings true today, as memory development is still catching up with the impressive advances in superconducting logic.

While there are many possible approaches to building a memory device, a viable system would ideally need to be energy efficient, fast, non-volatile (retaining the memory information even while the device is turned “off”), and random-access (where the access time is not

impacted by the physical location of the requested bits within the memory bank). For example, Magneto-resistive Random-Access Memory (MRAM) has been utilized successfully since 2006 in conventional computing. In the pursuit of a memory with these characteristics for superconducting computing many researchers today, including the Birge group at Michigan State University, are studying Josephson junctions containing ferromagnetic layers [12–21]. Because superconductivity and ferromagnetism are inherently antagonistic forms of order[†] combining and simultaneously controlling those effects in a ferromagnetic Josephson junction is not a faint-hearted endeavor. Nevertheless, it is precisely the juxtaposition of these competing forms of order that opens a rich area of physics with new possibilities for superconducting memory.

For example, if we can modify the amplitude, phase, or type of supercurrent inside a ferromagnetic Josephson junction in a controllable manner, those degrees of freedom can be used to represent the logical states of a superconducting memory device. The work presented here falls under the general scheme proposed by researchers at Northrop Grumman Corporation called Josephson Magnetic Random-Access memory (JMRAM), a superconducting energy-efficient variant of MRAM that operates by controlling the phase of the supercurrent across a ferromagnetic Josephson junction [22].

In this thesis, we discuss the materials characterization, optimization, and testing that culminated in the successful experimental implementation of two types of phase-controllable superconducting memory devices using ferromagnetic Josephson junctions, both compatible with JMRAM. In the first type of device, the phase state of the junction is controlled by tuning the relative orientations of two different ferromagnetic layers in the center of the junction [18]. In the second type, a series of three ferromagnetic layers with noncolinear

[†]As we will see in Ch. 4, ferromagnetic materials destroy or strongly suppress superconductivity.

magnetizations is utilized to generate a supercurrent carried by long-range, spin-triplet electron pairs. While the physics is much different from the first type of device, the phase state of this junction is also controlled by modifying the relative magnetization direction of one of the layers [21]. An overview of the remaining chapters in this thesis is provided below.

1.2 Chapters Overview

In Ch. 2, we give a brief review of superconductivity theory, explaining some relevant aspects of Josephson junctions and Superconducting Quantum Interference Devices (SQUIDs), the latter of which is used to make low-noise voltage measurements and for phase-sensitive detection of the memory devices.

In Ch. 3, we discuss the physics of ferromagnetism and some of the necessary considerations that go into the design of controllable magnetic memory bits, including magnetic domains and different types of magnetic anisotropy.

In Ch. 4, we discuss how the interplay of superconductivity and ferromagnetism (via the proximity effect) can be advantageously used in various types of ferromagnetic Josephson junctions. We describe the schemes by which the supercurrent in junctions can be manipulated to produce spin-singlet or spin-triplet supercurrent and the methods for controlling either the amplitude of the current or the phase across the junctions.

In Ch. 5, we describe the experimental methods, procedures, and equipment used to fabricate and measure our Josephson junctions and SQUIDs. The basic principle of the various techniques used such as sputtering, photolithography, electron-beam lithography, ion milling, and SQUID magnetometry are also discussed.

In Ch. 6, we outline a scheme for using ferromagnetic junctions as a phase-sensitive

superconducting memory. As a precursor to that effort we present four separate experimental materials characterization studies of Nb-based micron-scale elliptically-shaped Josephson junctions containing the central ferromagnetic layer of either $\text{Ni}_{65}\text{Fe}_{15}\text{Co}_{20}$, Permalloy (abbreviated as Py, the alloy $\text{Ni}_{81}\text{Fe}_{19}$), $\text{Pd}_{97}\text{Fe}_3$, and Ni. We compare the results to theory and discuss the comparative advantages and disadvantages that each of these materials offer as potential components in cryogenic memory devices.

In Ch. 7, we discuss the first experimental demonstration that the phase state of a Josephson junction can be controllably switched between 0 and π , *i.e.* a phase-sensitive cryogenic one-bit memory device using spin-singlet supercurrent. The phase-sensitive detection is achieved by adding two ferromagnetic Josephson junctions with a “spin-valve” configuration into a SQUID loop. Since that was the main work of Bethany Niedzielski and Eric Gingrich, we will focus on my main contribution to that effort: the development of a general asymmetric SQUID fitting program that provided the unambiguous proof that their devices switched between the phase values of 0 and π . That program is also used to fit the data in Ch. 9. This type of spin-valve junction is currently being used as part of superconducting memory cell by our collaborators at Northrop Grumman Corporation [23].

In Ch. 8, we present measurements of a different type of Josephson junction that generates spin-triplet supercurrent through the use of three ferromagnetic layers with noncolinear magnetizations. The central layer is a synthetic antiferromagnet composed of Pd/Co multilayers on either side of a Ru spacer with magnetization perpendicular to the plane. The other two ferromagnetic layers, either Py or Ni, have in-plane magnetization. We demonstrate that the junctions carry spin-triplet supercurrent by observing the relative enhancement of the critical current in those junctions compared to other junctions without the in-plane layers that carry only spin-singlet supercurrent.

In Ch. 9, we verify experimentally one of the most salient predictions of the spin-triplet theory, namely that a Josephson junction containing three magnetic layers with noncolinear magnetizations exhibits a ground-state phase shift of either zero or π depending on the relative orientations of those magnetizations. We implement two of the same types of junctions presented in Ch. 8 into a SQUID loop to achieve the phase-sensitive detection, similar to the technique used in Ch. 7. We show that the phase can be reliably switched between the zero or π states for seven different spin-triplet SQUID devices measured, a number of which we were able to switch between the two states over a thousand times without error. This type of phase-controllable junction could also be used as a novel memory element in a superconducting computer.

In Ch. 10, we conclude by summarizing the results and discuss some remaining open questions. In light of the results obtained we discuss the future outlook for energy efficient superconducting memory.

Chapter 2

Superconductivity

It has been well over a hundred years since the discovery of superconductivity in 1911, when the Dutch physicist Heike Kamerling Onnes cooled a sample of mercury below 4.2 K and watched its electrical resistance precipitously drop from about 0.1Ω to an unmeasurably small value (or $< 10^{-5} \Omega$, as precise as they could claim at the time) [24]. The superconducting state, onset by a second-order phase-transition, was later realized to be a manifestation of quantum mechanical phenomena expressed over macroscopic scales. It has striking and magnificent physical consequences: electrical currents which can flow in a material for years in the absence of a driving field, without transferring heat or dissipating energy, the complete expulsion of magnetic flux within their interior, and an energy gap, just to name a few. And though superconductivity first appeared to be a curious anomaly, it has been found to be a rather ubiquitous phenomenon under the right conditions. A majority of the metals in the periodic table, and many of their alloys, have been discovered to exhibit superconductivity under the right conditions, for example, at a low enough temperature, high enough pressures, assuming quality growth conditions, purity, etc. All told, superconductivity is an extremely diverse field of research, with many unsolved puzzles. Even today its mechanism and behavior in many materials is almost entirely unknown, including many with unusually high superconducting transition temperatures (T_c).

In the experiments presented in this thesis, however, we only use one of the better understood superconductors, Niobium, which is heralded for its use in Josephson junctions,

possessing the highest T_c of any elemental superconductor (at atmospheric pressure), about 9.2 K. Even if we restrict our focus to the most commonly used and well understood superconductors, that subfield of superconductivity is still quite extensive. Therefore, in this chapter, we only discuss some basic theoretical aspects of elemental superconductors, such as Nb, and their applications in Josephson junctions and Superconducting QUantum Interference Devices (SQUIDs).

2.1 The Meissner-Ochsenfeld Effect and London Theory

If a metal is cooled below its superconducting transition temperature, T_c , the magnetic flux in its interior is expelled, an effect first discovered by Walther Meissner and Robert Ochsenfeld in 1932 [25]. Moreover, they discovered that a superconductor is a perfect diamagnet, if it is cooled in the presence of a magnetic field (but not in an excessively strong one) the field inside the superconductor will be spontaneously expelled.[†] At the point of the phase transition, a superconductor will acquire surface currents (which are thermodynamically stable) that act to perfectly cancel the magnetic field inside of it.

The brothers Fritz and Heinz London proposed a model of a superconductor in which Ohms' Law ($\mathbf{J} = \sigma\mathbf{E}$) was replaced with a relation that would hold for a perfect diamagnet [26,27]. Since the superconducting charges were required to be dissipationless (as found by Kamerling Onnes) they argued that one should instead use Newton's law of motion,

$$\partial\mathbf{J}/\partial t = \mathbf{E}/\Lambda, \tag{2.1}$$

[†]That behavior is quite different from a perfect conductor: if cooled to T_c in zero field, a perfect conductor will continue to have $\mathbf{B} = 0$ in its interior, even after the application of a magnetic field. However, if a perfect conductor is in the presence of a field while in the normal state and then cooled to T_c , it will not expel the magnetic field.

where the time derivative of the current density, \mathbf{J} , is related to the electric field, \mathbf{E} , and the factor, $\Lambda \equiv m/(e^2 n_s)$, with e the magnitude of the electron charge and m it's mass, and n_s the density of superconducting electrons.[†] This together with the Maxwell equation $\nabla \times \mathbf{E} = -\partial\mathbf{B}/\partial t$, where \mathbf{B} is the magnetic induction field, leads to

$$\frac{\partial}{\partial t} \left[\nabla \times \mathbf{J} + \frac{\mathbf{B}}{\Lambda} \right] = 0. \quad (2.2)$$

The results of Meissner and Oschenfeld suggested that inside the superconductor, $\mathbf{J} = 0$ and $\mathbf{B} = 0$, so in Eq. (2.2) the term in brackets must be conserved. Thus we arrive at what is known as the London equation,

$$\nabla \times \mathbf{J} + \frac{\mathbf{B}}{\Lambda} = 0. \quad (2.3)$$

This, together with the Maxwell relation, $\nabla \times \mathbf{B} = \mu_0 \mathbf{J} + \mu_0 \epsilon_0 (\partial\mathbf{E}/\partial t)$, assuming that the electric field \mathbf{E} is approximately constant in time, implies (taking the curl of both sides and using $\nabla \cdot \mathbf{B} = 0$),

$$\nabla^2 \mathbf{B} = \frac{\mu_0}{\Lambda} \mathbf{B} \quad (2.4)$$

$$\nabla^2 \mathbf{J} = \frac{\mu_0}{\Lambda} \mathbf{J}. \quad (2.5)$$

The prefactor determines the length scale over which the fields and currents can typically

[†]In Sec. 2.3, we'll see that supercurrent is carried by pairs of electrons, but replacing the variables with $m^* = 2m$, $e^* = 2e$, and $n_s^* = n_s/2$, doesn't change the London theory. The London theory assumed a so-called two fluid model, first described by Gorter and Casimir [28], where only a portion of the total number of electrons in a superconductor contribute to the supercurrent, but it was later described by Lev Landau that there aren't two types of fluids or particles, but rather more like two kinds of motions, superfluid flow versus normal flow.

exist on the surface of the superconductor, called the *London penetration depth*,

$$\lambda_L \equiv \sqrt{\Lambda/\mu_0} = \sqrt{m/\mu_0 e^2 n_s}. \quad (2.6)$$

Eq. (2.4) implies that the field will penetrate into a superconductor, decaying from its value at the surface in an exponential manner to zero over a short distance λ_L , which in most superconductors is about $0.1 \mu\text{m}$ at zero temperature.[†] This decay is a signature of the Meissner-Ochsenfeld effect.

2.2 Ginzburg–Landau Theory

A powerful yet simple way to explain many features of superconductivity from a phenomenological perspective, was developed by Vitaly Ginzburg and Lev Landau in 1950 [29], now called Ginzburg-Landau theory. In Ginzburg-Landau theory, we are not overly concerned with the microscopic details yet can obtain predictions of physical properties with high accuracy in many situations. Indeed, Ginzburg–Landau theory is in some sense a bridge linking the more empirical ideas of the previous section (Meissner-Ochsenfeld effect) with the full microscopic theory of the next section (BCS theory).

Ginzburg and Landau noted that while London’s theory explained some aspects of superconductivity, it couldn’t be used to understand why the superconducting state could be destroyed by large fields or currents (as experiments had shown), nor could it predict the surface energy of a superconductor-normal phase boundary. Instead, they started from the key insight that the transition to the superconducting state, at T_c , could be viewed analogously to Landau’s theory of second-order phase transitions.

[†]The penetration depth changes as a function of temperature, being largest at the critical point, T_c .

In the theory of second-order phase transitions, the equilibrium state of a system on either side of a phase-transition can be determined by minimizing its free energy, expressed in terms of an *order parameter*, whose value changes from zero above the critical point to a nonzero value below it.[†] In Ginzburg–Landau theory, the order parameter for superconductors is a complex quantity, $\Psi(r)$, related to the density of superconducting electrons ($|\Psi|^2 \propto n_s$), and plays the role of an “effective,” or averaged, wavefunction.

In the absence of a magnetic field, we can expand the free energy density of the superconducting electrons, F_s , in even powers of the order parameter,

$$F_s = F_n + \alpha|\Psi|^2 + \frac{1}{2}\beta|\Psi|^4 \quad (2.7)$$

where F_n is the free energy density of the normal state, and the variables $\alpha = \alpha(T - T_c)$ and $\beta > 0$ are phenomenological parameters, discussed in more detail later. The order parameter, Ψ , is assumed to be small and not varying too rapidly in space.

In the presence of a magnetic field, \mathbf{B} , since the order parameter is coordinate dependent, we’ll need to also consider terms corresponding to it’s gradient, $(\nabla\Psi)^2$, and properly maintain invariance under a change of gauge through the magnetic vector potential, \mathbf{A} , where $\mathbf{B} = \nabla \times \mathbf{A}$. Then, the free energy density takes the form,

$$F_s = F_n + \alpha|\Psi|^2 + \frac{1}{2}\beta|\Psi|^4 + \frac{1}{2m}|(-i\hbar\nabla + e^*\mathbf{A})\Psi|^2 + \frac{1}{8\pi}|\mathbf{B}|^2. \quad (2.8)$$

The procedure is then to minimize the total free energy, $\mathcal{F} = \int d\mathbf{r}F_s$, first with respect to the order parameter and then \mathbf{A} . In particular, minimizing with respect to Ψ^* yields a

[†]Landau used this same methodology to explain ferromagnetism, the subject of the next chapter.

nonlinear equation for Ψ , the first Ginzburg–Landau equation,

$$\frac{1}{2m^*} (-i\hbar\nabla + e^* \mathbf{A})^2 \Psi + \alpha\Psi + \beta\Psi|\Psi|^2 = 0, \quad (2.9)$$

while minimizing with respect to the vector potential \mathbf{A} yields an expression for the current density, the second Ginzburg–Landau equation,

$$\mathbf{J}_s = -\frac{i\hbar}{2m^*} (\Psi^* \nabla \Psi - \Psi \nabla \Psi^*) - \frac{e^{*2}}{m^*} |\Psi|^2 \mathbf{A}. \quad (2.10)$$

The two equations (2.9) and (2.10) are constrained by a boundary condition at the interface between a superconductor and vacuum,

$$\mathbf{n} \cdot (-i\hbar\nabla + e^* \mathbf{A}) \Psi = 0, \quad (2.11)$$

where \mathbf{n} is the unit vector normal to the boundary.

This set of equations, and their more generalized forms, can be used to understand a great number of phenomenon, for instance, the first term in Eq.(2.10) leads to the Josephson effect, while the second term leads to the Meissner effect. Beyond this they can be used to derive flux quantization, the behavior of type I and II superconductors, the proximity effect, and the surface energy of a superconductor/normal metal (S/N) interface, which determines whether it's favorable to form such a boundary. In type–II superconductors this is the determining factor for the formation of vortices. For now, we will only use Ginzburg-Landau theory to set the stage for the microscopic theory in the next section and use it to discuss some important length scales and the key differences between type–I and II superconductors; however we will return to it later.

As a simple case, consider a homogeneous superconductor without supercurrent, Eq. (2.9) reduces to,

$$\alpha\Psi + \beta|\Psi|^2\Psi = 0, \quad (2.12)$$

and has only two solutions: the trivial solution $\Psi = 0$, corresponding to the normal state, or the solution where the order parameter is nonzero and constant in space, $|\Psi|^2 = -\alpha/\beta$. The phenomenological parameters are given the restrictions, $\alpha = \alpha(T - T_c)$ and $\beta > 0$, to ensure that this second solution is only valid when $T < T_c$. Note that if $T > T_c$, then $\alpha(T - T_c)/\beta > 0$ makes the entire right-hand side of Eq. (2.12) positive, so in that case the only solution can be $\Psi = 0$. On the other hand, if $T < T_c$, the solution $|\Psi|^2 = -\alpha/\beta$ is valid.

There are two important two length scales that emerge from the Ginzburg–Landau equations: the London penetration depth λ_L , which we have already seen, and the coherence length ξ . The coherence length

$$\xi = \sqrt{\frac{\hbar^2}{2m^*|\alpha|}} \quad (2.13)$$

characterizes the decay of the order parameter near a S/N boundary. The ratio of these two length scales yields the dimensionless *Ginzburg–Landau parameter*, κ , the fundamental characteristic of a superconducting material. Its value determines whether a superconductor is type I or II. It turns out that κ is related to the critical magnetic field H_c , above which superconductivity vanishes,

$$\kappa = \frac{\lambda_L}{\xi} \propto H_c \lambda_L^2. \quad (2.14)$$

In addition, κ is related to the surface tension at the boundary between a normal and superconducting state. For superconductors with $\kappa < 1/\sqrt{2}$, the surface tension is positive so that

boundaries are energetically unfavorable. Such materials are called type I superconductors. On the other hand, the surface tension is negative when $\kappa > 1/\sqrt{2}$ allowing vortices to form between a certain range of fields. This is the case for type II superconductors including Nb.

While the Ginzburg–Landau theory works well within its limitations, it is not able to account for the microscopic origin of superconductivity, which is achieved using BCS theory. However, Lev Gor’kov established in 1959 that Ginzburg–Landau theory can be derived from BCS in certain regimes [30,31]. The physical understanding extracted from Ginzburg–Landau theory was instrumental in guiding the development of the full microscopic theory.

2.3 BCS Theory

Ginzburg–Landau theory is excellent at capturing many properties of superconductors, but it is unable to answer some questions that only a microscopic theory can address. For example, why can we describe some materials with a superconducting order parameter, Ψ , while others are not superconducting at all? We can distinguish between type I and II superconductors with the Ginzburg–Landau parameter, $\kappa = \lambda_L/\xi$, but what determines λ_L and ξ for one material versus another? What sets the precise values of the critical temperature, T_c , and the critical field, H_c ? How do the individual electrons behave in a superconductor? We won’t discuss all of these questions, but ask them merely to motivate the need for a microscopic theory.

The first complete microscopic theory for one class of superconductors, which included most elemental superconductors, including Nb and its diluted alloys, was put forth by John Bardeen, Leon Cooper, and Bob Schrieffer in 1957, and is now known as *BCS theory* [32,33]. BCS were motivated, in part, by several experimental results that came before, which showed

that below T_c there existed an energy gap in the excitation spectrum near the Fermi level. In 1950, C. A. Renolds *et al.* [34] and E. Maxwell [35] showed that the T_c in these materials varied with the mass of its isotopes ($T_c \propto 1/\sqrt{M_{\text{iso}}}$), which suggested superconductivity may be related to the interactions with the lattice of a material.

In 1956, Cooper showed that two electrons with oppositely aligned spins near the Fermi level will form a bound state if there is a weak attractive interaction between them [36]. Cooper assumed that the attractive potential felt by the electrons is only nonzero within a narrow band in k -space. Under these conditions, two electrons will form a bound state, called a *Cooper pair*, for any attractive interaction, regardless of how small.

An explanation for the physical origin of the attractive interaction was provided earlier by Fröhlich in 1952 [37] and by Bardeen and Pines in 1955 [38]. In most metals, the electrons interact with each other via the Coulomb force and with phonons, *i.e.* quantized lattice vibrations in the crystal. As they showed, when two electrons exchange virtual phonons they will generate a weak attractive interaction, usually of the order 10^{-3} eV. That attractive electron-phonon interaction together with Cooper's theory implied that Cooper pairs would form in a superconductor, provided that it was at low enough temperature, so that the weakly bound pairs could not be broken by thermal excitations.

The complete explanation for superconductivity came shortly thereafter. In 1957, Schrieffer, working with Bardeen and Cooper, proposed a macroscopic quantum state composed of electron pairs with opposite spins. Extending Cooper's two-particle results to an N -particle system, Schrieffer was able to obtain the energy gap for excitations from the ground state. In their model, the electron pairs begin to condense below the critical temperature T_c until the binding energy for an additional pair becomes zero.

One of the major triumphs of BCS theory was the determination of the temperature

dependence of the energy gap $\Delta(T)$. It can be obtained in the limit of weak coupling, $\hbar\omega_c/k_B T_c \gg 1$, where $\hbar\omega_c$ is a cutoff energy: between the range $-\hbar\omega_c$ to $\hbar\omega_c$, around the Fermi energy the interactions between the electrons is attractive, $-V$, while outside it is zero. Under those conditions BCS theory yields the equation,

$$1 = \frac{V}{2} \sum_{\mathbf{k}} \frac{\tanh(E_{\mathbf{k}}/(2k_B T))}{E_{\mathbf{k}}}, \quad (2.15)$$

where

$$E_{\mathbf{k}} = \sqrt{\xi_{\mathbf{k}}^2 + \Delta^2} \quad (2.16)$$

is the excitation energy of a quasiparticle of momentum $\hbar\mathbf{k}$ and $\xi_{\mathbf{k}} = \epsilon_{\mathbf{k}} - \mu$ is the single particle energy measured relative to the Fermi energy μ (also called the chemical potential).

From the expression (2.15), we can determine the critical temperature T_c when $\Delta(T) \rightarrow 0$. Noting that in this limit Eq. (2.16) reduces to $|\xi_{\mathbf{k}}|$ and replacing the sum in (2.15) with an integral (solved numerically) yields,

$$k_B T_c = 1.13 \hbar\omega_c e^{-1/N(0)V}. \quad (2.17)$$

The $T = 0$ density of states for electrons at the Fermi level, that are either spin-up or spin-down, is $N(0)$. Meanwhile, the energy gap turns out to be given by,

$$\Delta = \frac{\hbar\omega_c}{\sinh[1/N(0)V]} \approx 2\hbar\omega_c e^{-1/N(0)V} \quad (2.18)$$

As a consequence of Eqs. (2.17)–(2.18), the energy gap at zero temperature is

$$\Delta(0) = 1.764k_B T_c. \quad (2.19)$$

This result is consistent with many experimental tests with different materials, which have been shown to have a Δ between $1.5 k_B T_c$ and $2.25 k_B T_c$ [39].

The first direct observation of the energy gap predicted by BCS theory came with with the work of Ivar Giaever in 1960. While at General Electric, he demonstrated that electrons would quantum mechanically tunnel from a superconductor to a normal metal through an insulating barrier [40]. His experiment, which used an Al/AlO_x/Pb tunnel junction, showed that when the temperature was lowered below the T_c of Pb (7.2 K), at low bias, an energy gap appeared. He further realized that by measuring the differential conductance dI/dV versus voltage V , where I is the current, one would find a curve that would mimic the density of states predicted from BCS theory.

2.4 The Josephson Effect

In 1962 Brian Josephson predicted that a supercurrent I_s could pass between two superconductors that were separated by a thin barrier (sometimes also called a “weak link”), in what is now called a *Josephson junction*. The supercurrent can flow even without an external bias, known as the dc Josephson effect,

$$I_s = I_c \sin \phi, \quad (2.20)$$

provided that there is a non-zero phase difference ϕ across the junction and that the current is less than the critical current, I_c .

Eq. (2.20) can be derived from BCS theory or Ginzburg–Landau theory assuming that the coherence length is much larger than the thickness of the barrier, $\xi \gg l$. The gauge-invariant phase difference across the junction,

$$\phi \equiv \Delta\theta - \frac{2\pi}{\Phi_0} \int \mathbf{A} \cdot d\mathbf{s}, \quad (2.21)$$

is computed by integrating the vector potential \mathbf{A} along a path between the two superconducting electrodes. In the absence of magnetic fields, ϕ reduces to the phase difference $\Delta\theta \equiv \theta_2 - \theta_1$ of the complex Ginzburg-Landau order parameter, with form $\Psi_{1,2} = |\Psi_0| \exp(i\theta_{1,2})$, in the two electrodes.

If a finite voltage difference V exists across the junction, then the phase difference acquires a time dependence known as the ac Josephson effect,

$$\frac{d\phi}{dt} = \frac{2eV}{\hbar} = \frac{2\pi}{\Phi_0} V, \quad (2.22)$$

where $\Phi_0 = 2\pi\hbar/(2e)$ is the magnetic flux quantum. As a result, the supercurrent Eq. (2.20) oscillates at a frequency $\nu = 2eV/h$ and the energy of a Cooper pair traversing the junction changes by an amount $h\nu$.

The energy stored in the junction, the Josephson energy, is found by integrating the electrical work done by a current to change the phase,

$$E = \int I_s V dt = \frac{\hbar}{2e} \int I_c \sin \phi d\phi = E_J (1 - \cos \phi), \quad (2.23)$$

where we used Eq. (2.22) to change the integration variable from time t to the phase ϕ , and the Josephson coupling energy is

$$E_J = \frac{\hbar I_c}{2e}. \quad (2.24)$$

2.5 The RCSJ Model

To describe a physical Josephson junction, we consider an ideal junction described by Eqs. (2.20) and (2.22) that has been shunted by a resistance R , which accounts for dissipation at finite voltages, and a geometric capacitance C between the two electrodes.

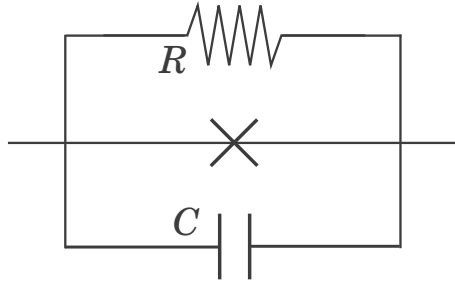


Figure 2.1: *The equivalent circuit for the RCSJ model of a physical Josephson junction. An ideal junction, at the center, is in parallel with a resistor R and capacitor C .*

A bias current I applied to the junction is split into three branches, as in Fig. 2.1, yielding an expression we can solve for the time dependence of the phase difference ϕ ,

$$C \frac{dV}{dt} + \frac{V}{R} + I_{c0} \sin \phi = I. \quad (2.25)$$

In practice, the critical current of the physical junction, I_c , can be different from that of the ideal junction, I_{c0} , in Eq. (2.20). Indeed, thermal fluctuations are known to suppress the observed critical current, $I_c < I_{c0}$ [41]. Using Eq. (2.22) to eliminate V , we can recast Eq. (2.25) in terms of ϕ to arrive at the second-order differential equation describing the

time dependence of the phase,

$$\left(\frac{\hbar}{2e}\right)^2 C \frac{d^2\phi}{dt^2} + \left(\frac{\hbar}{2e}\right)^2 \frac{1}{R} \frac{d\phi}{dt} = E_J \left(\frac{I}{I_{c0}} - \sin\phi\right). \quad (2.26)$$

Remarkably, this expression is analogous to the classical equation of motion for a particle of mass $\left(\frac{\hbar}{2e}\right)^2 C$ moving in a potential,

$$U = -E_J \left(\frac{I}{I_{c0}} \phi - \cos\phi\right), \quad (2.27)$$

under a linear drag force $\left(\frac{\hbar}{2e}\right)^2 \frac{1}{R} \frac{d\phi}{dt}$. The dimensionless Stewart and McCumber damping parameter [42, 43], which is the square of the junction's quality factor Q , is given by

$$\beta_c = Q^2 = \frac{(I_{c0}R)^2 C}{E_J} = (\omega_p RC)^2, \quad (2.28)$$

where ω_p is the plasma frequency.

When the bias current vanishes, the potential in Eq. (2.27) is a series of identical wells of depth $2E_J$ as a function of the phase difference ϕ (see Fig. 2.2). As the current is increased, the cosine begins to tilt and the barrier height shrinks, making it possible for the particle to escape the well via thermal fluctuations. When $I = I_{c0}$, the increasingly shallow minima become inflection points—unstable equilibria that, if subjected to perturbations, guarantee the particle will tumble down the washboard. In the absence of fluctuations, the solution to Eq. (2.27) is static, as the particle is confined to a particular well. In contrast, no stable equilibrium exists for a bias current higher than I_{c0} , and the phase difference ϕ necessarily becomes time dependent. According to Eq. (2.22), in such a case, the voltage V is no longer zero.

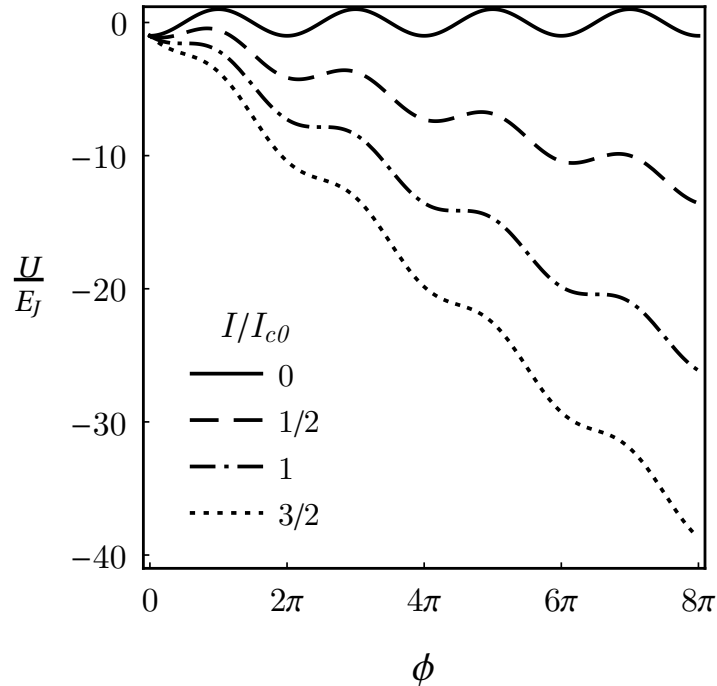


Figure 2.2: *The tilted washboard potential of the RCSJ model.* Static solutions to Eq. (2.27) exist for a bias current I less than or equal to the critical current I_{c0} (solid, dashed, and dot-dashed lines). As soon as $I > I_{c0}$, only solutions time-dependent in the phase ϕ exist (dotted line). This causes the voltage V to become nonzero, according to Eq. (2.22), and the junction to go normal.

2.5.1 Overdamped Junctions

When the capacitance C is small (the quality factor $Q \ll 1$), Eq. (2.26) for the phase reduces to a first-order differential equation

$$\frac{d\phi}{dt} = \frac{I_{c0}^2 R}{E_J} \left(\frac{I}{I_{c0}} - \sin \phi \right). \quad (2.29)$$

Evidently, the time-dependent solutions for ϕ , which we saw previously occur when $I > I_{c0}$, correspond to a positive $d\phi/dt$.

We can compute the voltage averaged over one period T of the phase by integrating

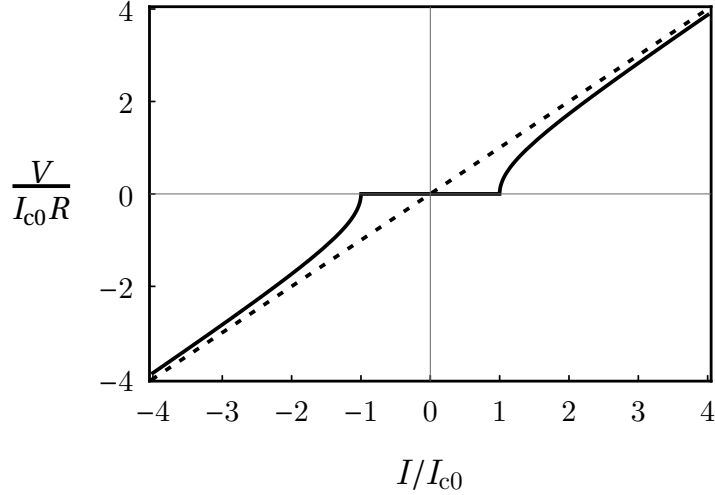


Figure 2.3: The time-average voltage difference, Eq. (2.32), across the overdamped junction in the RCSJ model (solid line). For $|I| \leq I_{c0}$, the voltage remains zero, but approaches Ohm's law (dashed line) when $|I| \gg I_{c0}$.

Eq. (2.29),

$$\int_0^{2\pi} \frac{d\phi}{I/I_{c0} - \sin \phi} = \int_0^T \frac{I_{c0}^2 R}{E_J} dt. \quad (2.30)$$

Solving this expression for the period T and inserting into Eq. (2.22),

$$\frac{2\pi}{T} = \frac{I_{c0} V}{E_J}, \quad (2.31)$$

yields the time-average voltage whose magnitude scales with the bias current as:

$$|V| = R \sqrt{I^2 - I_{c0}^2}. \quad (2.32)$$

The voltage, plotted in Fig. 2.3, remains zero for $|I| \leq I_{c0}$ (as only static solutions exist for the phase) and asymptotically approaches Ohm's law, $V = IR$, for $|I| \gg I_{c0}$.

2.6 Flux Quantization and SQUIDS

In this section we will discuss flux quantization and combine it together with the Josephson effect to describe Superconducting QUantum Interference Devices (SQUIDS). The experimental realization of flux quantization was observed independently in 1961 by the groups of Deaver and Fairbank at Stanford [44] and Doll and Naubauer at the Walther-Meibner Institute (WMI) [45]. They showed that since the macroscopic wavefunction must be single-valued while going around a closed superconducting loop, the flux is quantized in multiples of the flux quantum $\Phi_0 \equiv h/2e \approx 2.07 \times 10^{-15}$ Wb. Normally, without any fields present the phase difference ϕ is constant in the superconductor, but if the loop is threaded by a magnetic field, ϕ will change in discrete steps of $2\pi n$, with n being the number of flux quanta in the loop.

2.6.1 Magnetic Flux Quantization

The macroscopic quantum model of superconductivity postulates the existence of a macroscopic wavefunction describing an ensemble of Cooper pairs in a superconductor,

$$\Psi(\mathbf{r}, t) = \sqrt{n_s^*(\mathbf{r}, t)} e^{i\theta(\mathbf{r}, t)}. \quad (2.33)$$

The local density $n_s^*(\mathbf{r}, t) = |\Psi(\mathbf{r}, t)|^2$ yields the total number $\int \Psi^*(\mathbf{r}, t)\Psi(\mathbf{r}, t)dV = N_s^*$ of Cooper pairs with mass m^* and charge $q^* = -2e$. Subject to an electromagnetic field, the wavefunction Eq. (2.33) obeys the Schrödinger equation,

$$i\hbar \frac{\partial \Psi(\mathbf{r}, t)}{\partial t} = \frac{1}{2m^*} \left(\frac{\hbar}{i} \nabla - q^* \mathbf{A}(\mathbf{r}, t) \right)^2 \Psi(\mathbf{r}, t) + q^* \phi(\mathbf{r}, t) \Psi(\mathbf{r}, t), \quad (2.34)$$

for the vector potential \mathbf{A} and the scalar potential $\phi(\mathbf{r}, t)$ (not to be confused with the phase difference ϕ). It follows from Eq. (2.33) and Eq. (2.34) that the corresponding macroscopic quantum current density \mathbf{J}_s of the Cooper pairs is

$$\begin{aligned}\mathbf{J}_s &= q^* \text{Re} \left\{ \Psi^* \left(\frac{-i\hbar\nabla - q^*\mathbf{A}}{m^*} \right) \Psi \right\} \\ &= q^* n_s^*(\mathbf{r}, t) \left\{ \frac{\hbar}{m^*} \nabla\theta(\mathbf{r}, t) - \frac{q^*}{m^*} \mathbf{A}(\mathbf{r}, t) \right\}.\end{aligned}\tag{2.35}$$

Evidently, the velocity of the Cooper pairs is $\mathbf{v}_s = \hbar/m^* \nabla\theta(\mathbf{r}, t) - q^*/m^* \mathbf{A}(\mathbf{r}, t)$.

Expressing the current density Eq. (2.35) in terms of the London coefficient from Sec. 2.1,

$$\Lambda \equiv \frac{m^*}{n_s^* q^{*2}},\tag{2.36}$$

which assumes a constant Cooper pair density $n_s^*(\mathbf{r}, t) = \text{const}$, we can derive the quantization of magnetic flux enclosed by a superconducting ring. Indeed, we know from Stoke's theorem that an integral of the vector potential around a closed contour \mathcal{C} can be converted to an integral over a surface \mathcal{S} to yield the magnetic flux Φ ,

$$\oint_{\mathcal{C}} \mathbf{A} \cdot d\mathbf{l} = \int_{\mathcal{S}} (\nabla \times \mathbf{A}) \cdot d\mathbf{s} = \int_{\mathcal{S}} \mathbf{B} \cdot d\mathbf{s} = \Phi,\tag{2.37}$$

for a magnetic field \mathbf{B} piercing the surface. Replacing the vector potential in this expression with the current density (2.35) leads to a quantity Φ' ,

$$\Phi' = \Phi + \oint_{\mathcal{C}} \Lambda \mathbf{J}_s \cdot d\mathbf{l} = \frac{\hbar}{q^*} \oint_{\mathcal{C}} \nabla\theta \cdot d\mathbf{l},\tag{2.38}$$

termed the *fluxoid*.

To show that Φ' in Eq. (2.38) is quantized, we will study the integral of the phase θ . For an arbitrary path from \mathbf{r}_1 to \mathbf{r}_2 , the integral of the gradient of a scalar function is simply the difference of the function at the two locations

$$\int_{\mathbf{r}_1}^{\mathbf{r}_2} \nabla\theta \cdot d\mathbf{l} = \theta(\mathbf{r}_2, t) - \theta(\mathbf{r}_1, t), \quad (2.39)$$

which clearly vanishes for a closed loop, $\mathbf{r}_1 = \mathbf{r}_2$. However, the phase of the wavefunction Eq. (2.33) is only defined within modulo 2π ,

$$\theta(\mathbf{r}, t) = \theta_0(\mathbf{r}, t) + 2\pi n, \quad (2.40)$$

for a $\theta_0(\mathbf{r}, t)$ specified on $[-\pi, \pi]$, and an integer n to ensure that the wavefunction remains single valued. Therefore, an integral over a closed loop evaluates to $2\pi n$. This finding gives rise to the *flux quantum*,

$$\Phi_0 = \frac{h}{|q^*|} = \frac{h}{2e} \approx 2.067 \times 10^{-15} \text{ Wb}, \quad (2.41)$$

as the fluxoid, Eq. (2.38),

$$\Phi' = n \Phi_0, \quad (2.42)$$

becomes quantized.

When the superconducting ring thickness is much larger than the London penetration depth λ_L , our integration in Eq. (2.38) along a contour \mathcal{C} well within the superconducting ring has a negligibly small contribution from the current density \mathbf{J}_s . In this case, we find

that Eq. (2.38) reduces to

$$\Phi = \int_{\mathcal{S}} \mathbf{B} \cdot d\mathbf{s} = n \Phi_0, \quad (2.43)$$

so that the flux Φ through the ring is an integer multiple of the flux quantum. The measurement of this effect, mentioned earlier (Deaver and Fairbank [44], Doll and Nábauer [45]), served as further confirmation that superconducting electrons are paired according to BCS theory. Shortly after these findings, William Little and Roland Parks clearly showed in their experiment [46] that it is the fluxoid Φ' that is quantized in general, and that the flux Φ is only quantized when the contribution in Eq. (2.38) from the current density can safely be ignored.

2.6.2 SQUIDS

At this point, a natural question we might ask is whether we can combine the quantization of flux in a superconducting loop with the Josephson effect to elicit novel phenomena. The answer, of course, is that when a superconducting ring is interrupted by one or more Josephson junctions macroscopic quantum interference is observed. This now famous discovery was the pioneering work of Robert Jaklevic, John Lambe, James Mercereau, James Zimmerman, and Arnold Silver at the Ford Research Labs in the mid 1960s. The resulting Superconducting QUantum Interference Device, or SQUID, has a wide range of applications including superconducting electronics and quantum computing, and is so sensitive that it can be used as a magnetometer to measure extremely small magnetic fields in biological and medical research. In this thesis, we utilize SQUIDS in three different contexts to enable the development of near-term cryogenic memory devices: as magnetometers to characterize magnetic materials, for low-noise voltage measurements, and as phase-sensitive detectors.

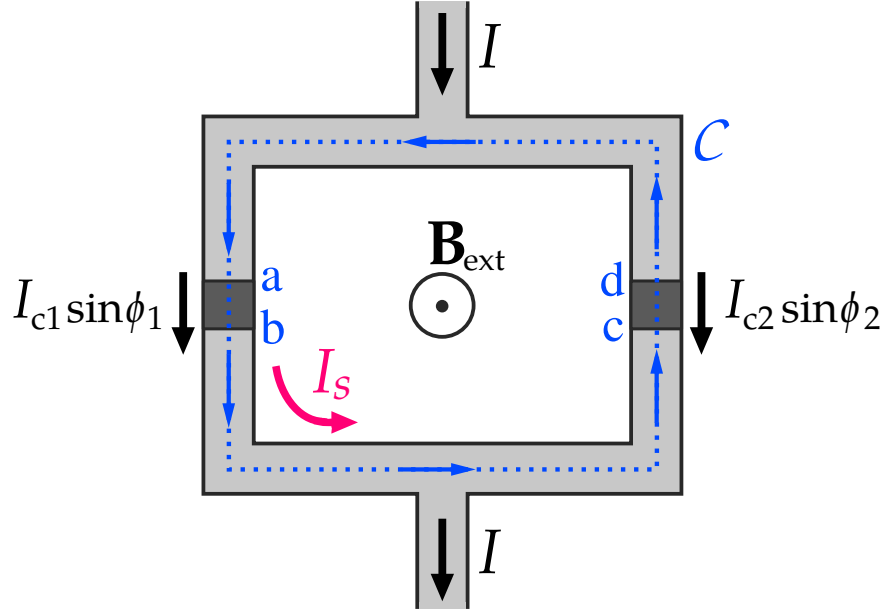


Figure 2.4: *The symmetric dc SQUID with total supercurrent I .* A superconducting loop (light gray) is interrupted by two weak links (dark gray) to form two Josephson junctions connected in parallel. Integration around the closed contour \mathcal{C} , shown in blue, yields Eq. (2.51) for the relation between the gauge invariant phase differences ϕ_1 and ϕ_2 . The circulating supercurrent I_s produces a screening flux that contributes, along with the flux from an external magnetic field \mathbf{B}_{ext} , to the total flux in the loop, Eq. (2.52).

Although SQUIDS can be formed from as little as one Josephson junction (the rf SQUID), a particularly useful variant is the dc SQUID invented in 1964. Here, two Josephson junctions are connected in parallel via a superconducting loop as shown in Fig. 2.4. We will see that the amplitude of the supercurrents through the two branches interfere, producing a modulation in the maximum total supercurrent of the SQUID.

As we saw previously in Sec. 2.6.1, an integral of the gradient of the phase over a closed contour is quantized. For the integration path shown in Fig. (2.4), we find

$$\begin{aligned}
 \oint_{\mathcal{C}} \nabla\theta \cdot d\mathbf{l} &= 2\pi n \\
 &= (\theta_b - \theta_a) + (\theta_c - \theta_b) + (\theta_d - \theta_c) + (\theta_a - \theta_d) + 2\pi n.
 \end{aligned}
 \tag{2.44}$$

where we've simply added $0 \bmod 2\pi$. Let's consider each term in parentheses in Eq. (2.44). The phase difference across the junctions can be written in terms of the gauge-invariant phase difference as

$$\theta_b - \theta_a = \phi_1 + \frac{2\pi}{\Phi_0} \int_a^b \mathbf{A} \cdot d\mathbf{l}, \quad (2.45)$$

$$\theta_d - \theta_c = -\phi_2 + \frac{2\pi}{\Phi_0} \int_c^d \mathbf{A} \cdot d\mathbf{l}. \quad (2.46)$$

The negative sign appearing in front of ϕ_2 is because we chose it to be defined in the opposite direction of the integration path, unlike ϕ_1 , which is in the same direction. For the remaining two terms in Eq. (2.44), recall from Sec. 2.6.1 that the gradient of the phase is related to the quantum current density \mathbf{J}_s through the expression

$$\nabla\theta = \frac{2\pi}{\Phi_0} (\Lambda\mathbf{J}_s + \mathbf{A}). \quad (2.47)$$

This means that we can write the last two expressions in Eq. (2.44) as

$$\theta_c - \theta_b = \int_b^c \nabla\theta \cdot d\mathbf{l} = \frac{2\pi}{\Phi_0} \int_b^c (\Lambda\mathbf{J}_s \cdot d\mathbf{l} + \mathbf{A} \cdot d\mathbf{l}), \quad (2.48)$$

$$\theta_a - \theta_d = \int_a^d \nabla\theta \cdot d\mathbf{l} = \frac{2\pi}{\Phi_0} \int_a^d (\Lambda\mathbf{J}_s \cdot d\mathbf{l} + \mathbf{A} \cdot d\mathbf{l}). \quad (2.49)$$

Combining all four terms and replacing the integration of the vector potential around the closed loop by the magnetic flux, we find

$$\phi_2 - \phi_1 = \frac{2\pi}{\Phi_0} \Phi + \frac{2\pi}{\Phi_0} \int_b^c \Lambda\mathbf{J}_s \cdot d\mathbf{l} + \frac{2\pi}{\Phi_0} \int_a^d \Lambda\mathbf{J}_s \cdot d\mathbf{l}, \quad (2.50)$$

$\bmod 2\pi$. Furthermore, as we saw in Sec. 2.6.1 regarding the flux quantization in a su-

perconducting cylinder, if the thickness of the junction is much greater than the London penetration depth λ_L , then the current density is approximately zero. In such a case, the final integrals can be neglected and we arrive at the simple relation for the difference in the two gauge-invariant phase differences,

$$\phi_2 - \phi_1 = \frac{2\pi}{\Phi_0} \Phi \pmod{2\pi}, \quad (2.51)$$

which show that the phases are related via the total flux through the loop.

From the result of Eq. (2.51), we can compute how the current in the SQUID varies with the total flux. In general, the flux Φ appearing in Eq. (2.51) has a contribution from an externally applied magnetic field \mathbf{B}_{ext} and from the inductance L of the loop,

$$\Phi = \Phi_{\text{ext}} + \Phi_s = \Phi_{\text{ext}} + LI_s. \quad (2.52)$$

The circulating supercurrent I_s that produces a screening flux Φ_s in the loop is

$$I_s = \frac{I_{c1} \sin \phi_1 - I_{c2} \sin \phi_2}{2}, \quad (2.53)$$

while the total current I in the SQUID is

$$I = I_{c1} \sin \phi_1 + I_{c2} \sin \phi_2. \quad (2.54)$$

With Eq. (2.51) and assuming both junctions have identical critical currents, $I_{c1} = I_{c2} = I_c$,

Eqs. (2.52) and (2.54) become

$$I = 2I_c \cos\left(\frac{\pi\Phi}{\Phi_0}\right) \sin\left(\phi_1 + \frac{\pi\Phi}{\Phi_0}\right) \quad (2.55)$$

$$\Phi = \Phi_{\text{ext}} - LI_c \sin\left(\frac{\pi\Phi}{\Phi_0}\right) \cos\left(\phi_1 + \frac{\pi\Phi}{\Phi_0}\right). \quad (2.56)$$

To find the maximum current I_{max} through the SQUID for a given Φ_{ext} , we maximize Eq. (2.55) with respect to ϕ_1 while accounting for the ϕ_1 dependence of Eq. (2.56).

We can consider a simple limiting case of this approach. To start, let's define a screening parameter $\beta_L = 2LI_c/\Phi_0$ to be the ratio of the maximum screening flux, corresponding to a maximum circulating current of I_c according to Eq. (2.53), to half a flux quantum $\Phi_0/2$. The limit we will study is $\beta_L \ll 1$ so that the screening flux is negligibly small and Φ_{ext} dominates the total flux. After a straightforward calculation, we find that the maximum current is

$$I_{\text{max}} = 2I_c \left| \cos\left(\frac{\pi\Phi_{\text{ext}}}{\Phi_0}\right) \right|, \quad (2.57)$$

for a given Φ_{ext} . The variation of I_{max} with Φ_{ext} is shown in Fig. 2.5.

Later, in Ch. 7, we will consider a more general version of the SQUID theory discussed here. In particular, we will allow for the two Josephson junctions to have different critical currents and accounting for possible geometric asymmetries in the SQUID whereby two inductances are needed to specify the loop. We will also treat both large and small screening parameters.

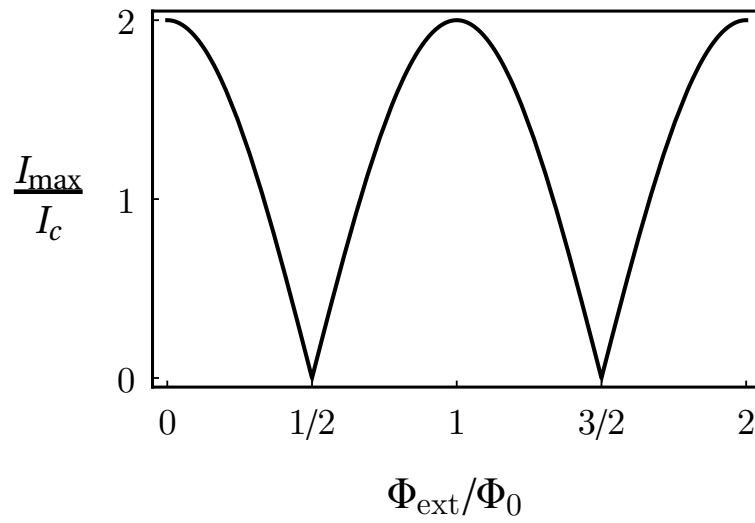


Figure 2.5: *Symmetric SQUID oscillations.* The maximum current I_{\max} in the SQUID oscillates as a function of the externally applied flux Φ_{ext} according to (2.57). Here, $\beta_L \ll 1$ so that $\Phi \approx \Phi_{\text{ext}}$.

Chapter 3

Ferromagnetism

Ferromagnetism is one of the most spectacular and readily observable physical phenomena. In this chapter we give a rapid-fire overview of ferromagnetic materials, insofar as to understand some aspects of their behavior relevant to ferromagnetic Josephson junctions, discussed later in Ch. 4.

3.1 Historical Overview

Magnetic materials are generally classified according to their magnetic susceptibility,

$$\chi_m = \mathbf{M}/\mathbf{H}, \tag{3.1}$$

the dimensionless ratio of the magnetization, \mathbf{M} , induced in a material and the magnetic field, \mathbf{H} , applied to it, as demonstrated by Pierre Curie in 1895. The sign of χ_m varies for paramagnetic ($\chi_m > 0$) and diamagnetic materials ($\chi_m < 0$). Curie observed that excessive thermal fluctuations will destroy magnetic ordering, reasoning that a paramagnetic or diamagnetic materials' magnetic susceptibility was inversely proportional to its temperature, now known as Curie's law. Curie was well aware of ferromagnetic materials, classifying them as a subset of paramagnetic materials with extremely large χ , though he could find no reason why their magnetic susceptibility was measured to be thousands of times larger than other typical paramagnets.

Then in 1906 Pierre Weiss, astonishingly, even without direct knowledge of the quantum mechanical origins of ferromagnetism, put forth two foundational postulates that have since dominated the theory of ferromagnetism for over a century: *spontaneous magnetization* and division into *magnetic domains* [47]. He found that if a ferromagnet, such as magnetite (Fe_3O_4) was cooled below a certain temperature, T_{Curie} , called the Curie temperature, it would spontaneously develop an ordered magnetic state with a net magnetization, even in the absence of an applied field. Weiss discovered that in an applied field (that is sufficiently weak), ferromagnetic materials deviated from Curie’s law, following instead what is now known as the Curie-Weiss law,

$$\chi_m = \frac{C}{T - T_{\text{Curie}}}, \quad (3.2)$$

where C is a constant, T is the temperature.[†] Above T_{Curie} the material will become paramagnetic. Weiss hypothesized that spontaneous magnetization in ferromagnetic materials was due to an additional strong molecular field generated within the magnetic materials, but its origin was somewhat of a mystery.

He tried to reconcile this theory with the well known fact that some ferromagnetic materials, such as single crystals of Fe, can often be found in a demagnetized state (clearly not “self-saturating”), but when placed in a small magnetic field will subsequently produce an extraordinarily large magnetic moment of (about 1.7 MJ/T per cubic meter), persisting long after the field is removed. Weiss posited that these unmagnetized ferromagnetic materials consisted of a scrambled network of many magnetic domain regions whose net magnetization was very nearly zero. He argued that the act of magnetizing the material, by placing it in a strong enough magnetic field, (which he discovered had to be applied in certain magneti-

[†]The Curie-Weiss law fails to describe the magnetic susceptibility of some materials very close to $T = T_{\text{Curie}}$. Rather, it follows $\chi_m \propto (T - T_{\text{Curie}})^{-\gamma}$, where γ is a critical exponent.

zation directions, but not others), would then cause the domains whose magnetization's are aligned with the applied field to grow at the expense of the domains who are anti-aligned to the field. The resulting contribution would then sum up to the very large values that had been observed experimentally.

The origin of Weiss's molecular field remained a mystery until the advent of quantum mechanics, and was explained independently by Werner Heisenberg [48] and Paul Dirac in 1926 [49], who showed that ferromagnets (as well as other materials) are strongly influenced by the *exchange interaction*. The exchange interaction is a consequence of Coulomb forces combined with the spin-statistics theorem applied to a joint system of Fermions (electrons). It results in an "effective" force (the exchange force) that causes the spins in a material to align themselves along some preferred axis.[†]

3.2 Magnetic Domains

While the dipolar interactions between the magnetic moments in a ferromagnet result in forces that are typically several orders of magnitude smaller than the strong exchange forces, they often play a crucial role in the materials' collective magnetic state. That is because the exchange interaction, while powerful over a few atomic spacings, is fairly short-ranged, decreasing exponentially with the distance between spins. In contrast, at large distances, the magnet moments will behave more like dipoles, and the resulting energy of those dipole-dipole interactions decreases as the inverse square of the distance between spins, a quantity that can become quite large after summing over the contributions from a large

[†]In the parlance of Hartree-Fock theory for many-electron systems, to satisfy the anti-symmetry property of the wavefunction of a Fermionic system, one must replace the trial wavefunction, originally a simple product of single electron states, by a Slater determinant (which is anti-symmetric), resulting in an extra term (the exchange term).

macroscopic collection. A ferromagnet can thus seek to reduce its dipolar energy by breaking up into uniformly magnetized *domains*, each of whose magnetizations are oriented in different directions. While conceptually proposed by Weiss, the first concrete theory to predict the shape and size of magnetic domains is attributed to the work of Lev Landau and Evgeni Lifshitz in 1935 [50].

A somewhat contrived model, but one that captures the essence of magnetic domains in real materials, is to imagine a number of individual spins arranged in a regular three-dimensional lattice with the restriction that the spins can only point along a few directions (e.g. $\pm\hat{x}$ and $\pm\hat{y}$). Then, one can write down the energy contributions associated with the short range exchange forces (like in the Heisenberg model), together with both the long-range dipolar forces and the magnetic induction field B that is created by all the spins. If the strength of the exchange coupling is large, and the dimensions (i.e. number of lattice sites) of the system are small, the most energetically favorable configuration is to align all of the spins into one large magnetic domain. In this limit the exchange field more than offsets the large magnetostatic energy, which goes as $\int_{\text{out}} B^2 dV$ with integration spanning the region outside the volume V of the solid. If, on the other hand, the strength of the exchange coupling is small and the size of the system is large, it becomes more energetically favorable for the system to separate into many domains so as to lower the magnetostatic energy, while at the expense of creating many magnetic interfaces.

Landau and Lifshitz showed that the resulting individual domains can be macroscopic in size and the collection of them are often arranged into rather complex structures. Some examples of possible magnetic domain configurations are shown in Fig. 3.1, but these depend strongly on the shape, size, and composition of the ferromagnet of interest. The boundary between domains, referred to as *domain walls*, can occur rapidly over only a few lattice sites,

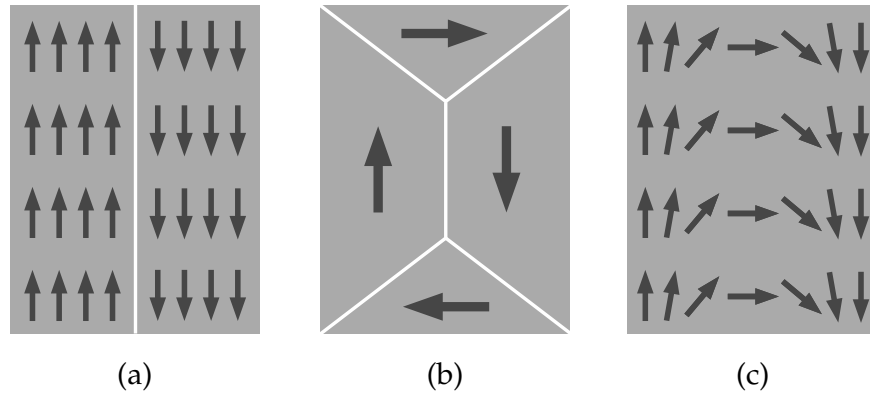


Figure 3.1: *Ferromagnetic domain structures*: A ferromagnetic material, seeking primarily to balance the competition between exchange forces and electrostatic dipolar forces between its electrons, will break up into regions of uniformly magnetized regions called domains. Fig. (a) shows a schematic of a ferromagnet with two domains separated by a single domain wall. Arrows indicate the direction of the magnetization in their respective regions. For larger size samples, or those with weaker exchange forces the system will typically break up into many domains as shown in (b). Many ferromagnets have more complicated magnetic structures, for instance, where the change in the direction of the spins occurs gradually over many lattice sites, as shown in (c), for a “C”-shaped configuration. Fig.(c) could also be a zoom in of the domain wall in (a).

as in Fig. 3.1, or the spin reversal can occur gradually over a large number of adjacent spins. In two-dimensions, for example, one will often find large-scale “C”-shaped domains, similar to those shown in Fig. 3.1(c), or “S”-shaped domains. While those types of structures appear complex at first glance, they turn out to be more energetically favorable than an abrupt domain wall. Magnetizing a ferromagnet in a strong field is the process of “sweeping out” domain walls to convert a multi-domain state into one with a single magnetic domain. As one can infer from the M vs. H loop of Fig. 3.4(b), starting at the origin and tracing the curve to the point M_{sat} , this initial magnetization process is irreversible, in that if the applied field is removed, the ferromagnet does not revert back to its original domain structure. Other factors such as defects in the ferromagnet or on its boundaries could cause some magnetic domains to become pinned regardless of the field applied, or revert back to their former

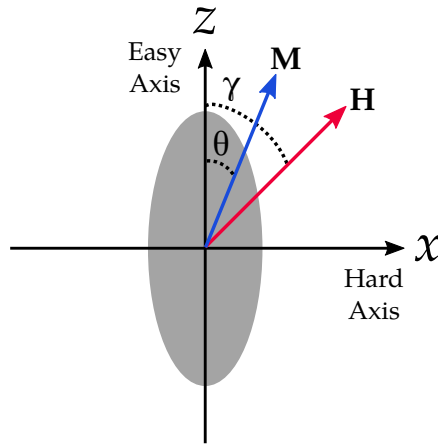


Figure 3.2: *Schematic setup for the Stoner-Wohlfarth model.* We consider a single magnetic domain with uniaxial anisotropy, shown in gray. The magnetization, \mathbf{M} , makes an angle θ with the easy axis and the applied magnetic field, \mathbf{H} , makes an angle γ with the easy axis.

orientations when the applied field is removed.

3.3 Magnetic Anisotropy

The magnetic properties of a ferromagnet are often directionally dependent, requiring the least amount of energy to magnetize it in one particular spatial direction, concurrent with the direction of spontaneous magnetization, commonly called the “easy axis” (as opposed to the least energetically favorable direction, called the “hard axis”). Such a ferromagnet is said to have *magnetic anisotropy*. The subject is of great practical interest, being exploited in many magnetic technologies, including the experiments presented in Chs. 6-9. There are many different types of magnetic anisotropy, but we’ll focus on only three: magneto-crystalline, shape, and exchange anisotropies, which will be discussed in more detail later.

3.3.1 The Stoner-Wohlfarth Model: Uniaxial Anisotropy

To model the magnetization of a single ferromagnetic domain with magnetic anisotropy, we'll consider the case of a general uniaxial anisotropy, which for example, could be due to magnetocrystalline or shape anisotropy. It is an example of the *Stoner-Wohlfarth model*, developed by Edmund Clifton Stoner and Erich Peter Wohlfarth in 1948 [51]. In this model, the ferromagnet of interest has one axis of high symmetry (the easy axis), which we will arbitrarily designate to point along $\hat{\mathbf{z}}$. The ferromagnet is placed in an external magnetic field, \mathbf{H} , that is applied in the xz -plane, as shown in Fig. 3.2.

A first order approximation is to write the energy per unit volume due to the anisotropy as

$$u_{\text{aniso}} = K(m_x^2 + m_y^2) = K \sin^2 \theta, \quad (3.3)$$

expressed in spherical polar coordinates, where θ is the angle that the magnetization \mathbf{M} makes with the z -axis, and $\mathbf{m} = \mathbf{M}/|\mathbf{M}|$, whose cartesian components obey $m_x^2 + m_y^2 + m_z^2 = 1$, and K is a constant called the anisotropy parameter. For convenience we'll define $K = \beta M^2/2$ where β is a dimensionless constant. The total energy density u is calculated by adding Eq. (3.3) to the energy density due to the applied field, u_{ext} , or

$$\begin{aligned} u &= u_{\text{aniso}} + u_{\text{ext}} \\ &= \frac{\beta}{2} M^2 \sin^2 \theta - \mu_0 \mathbf{M} \cdot \mathbf{H} \\ &= \frac{\beta}{2} M^2 \sin^2 \theta - \mu_0 M (H_x \sin \theta + H_z \cos \theta). \end{aligned} \quad (3.4)$$

How does this uniaxial anisotropy influence the magnetic state of the ferromagnet? Consider the simple case where $\mathbf{H} \parallel \hat{\mathbf{z}}$, so that $u = (\beta M^2/2) \sin^2 \theta - \mu_0 M H_z \cos \theta$. Initially, if $\mu_0 H_z = 0$, the energy density is minimal at $\theta = 0$ (and also degenerate with $\theta = \pi$, but let

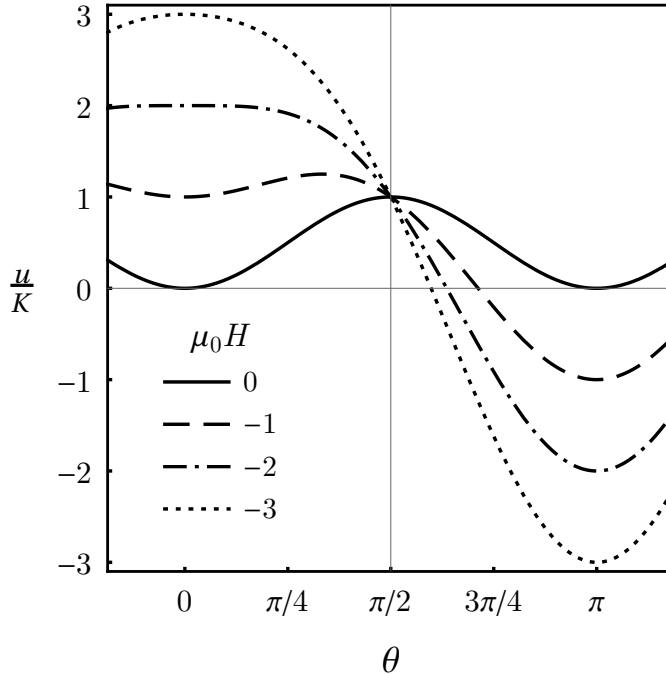


Figure 3.3: *Magnetization reversal in the Stoner-Wohlfarth model.* Energy density u , normalized to the anisotropy parameter, K , versus the angle of the magnetization to the easy axis θ , and the applied field $\mu_0 H$. We plot Eq. (3.4), for the case of $\mathbf{H} \parallel \hat{\mathbf{z}}$, for $K/M = \beta M/2 = 1$. With the magnetization initially aligned with the easy axis ($\theta = 0$), there is an energy minimum at small applied fields (solid line). As the magnitude of the field is increased in the $-\hat{\mathbf{z}}$ direction, the energy minima at $\theta = 0$ becomes metastable (when $\mu_0 \mathbf{H} = -\beta M \hat{\mathbf{z}}$), and eventually is unstable, with a new global energy minima at $\theta = \pi$. The magnetization has reversed direction.

us consider the system with the $\theta = 0$ solution). Next, let's say we wish to apply the field in the opposite direction, $-\hat{\mathbf{z}}$, to try and flip \mathbf{M} from $\theta = 0$ to $\theta = \pi$. In Fig. 3.3 we plot how the energy density changes with respect to θ for different values of the applied field.

It's easy to see that at small values of $|H_z|$ the solution at $\theta = 0$ is a stable local minimum ($\left. \frac{d^2 u}{d\theta^2} \right|_{\theta=0} > 0$). Further increasing $|H_z|$ until it reaches $\mu_0 H_z = -\beta M$, now one will find that the solution at $\theta = 0$ becomes metastable ($\left. \frac{d^2 u}{d\theta^2} \right|_{\theta=0} = 0$) and further increasing $|H_z|$ will force the magnetization to the new global energy minimum at $\theta = \pi$, as shown in Fig. 3.3. Therefore, by this field the magnetization suddenly reverses its direction.

The response of the magnetization \mathbf{M} versus the applied field \mathbf{H} is known as a *magne-*

tization curve. In ferromagnets, the magnetization curve is nonlinear with \mathbf{H} , rising until a sufficiently large field where the curve saturates to a constant value \mathbf{M}_s . Furthermore, reducing the applied field, the magnetization will not retrace over the same curve but remain nonzero even when \mathbf{H} is reduced to zero. In the last example (with $\mathbf{H} \parallel \hat{\mathbf{z}}$) the field had to be reduced to $\mu_0 H_z = -\beta M$ to get the magnetization to reverse. A similar behavior is also true sweeping the applied field back in the other direction.

The ferromagnet thus displays a hysteretic behavior, and in effect, retains some “memory” of its prior configuration history. We will often refer to magnetization curves as “hysteresis loops.” Examples of such curves are shown in Fig. 3.4 for the ideal ferromagnet (the example of the previous section using uniaxial anisotropy follows the curve in Fig. 3.4(a)) and a realistic ferromagnet, shown in Fig. 3.4(b). In realistic ferromagnets, the magnetization curve averages over potentially many magnetic domains, each reversing their orientations at slightly different fields, broadening and rounding the switching curve. In Fig. 3.4(b) the quantity M_r denotes the non-vanishing *remanent magnetization* that remains after the applied field is returned to zero. A *coercive field*, H_c , must be applied in the opposite direction to reverse the magnetization.

The magnetization curve can vary widely depending on the material, shape, and size of the ferromagnet. A material is said to be “magnetically soft” if it can be magnetized to saturation with a small applied field, typically a few mT or less. Some materials that fall into this category, which will be studied at length in later Ch. 6, are $\text{Ni}_{81}\text{Fe}_{19}$ (also known as Permalloy, which we will abbreviate as Py), or $\text{Pd}_{97}\text{Fe}_3$. Other materials, also discussed Ch. 6, such as Co, Ni, or $\text{Ni}_{65}\text{Fe}_{15}\text{Co}_{20}$, require much larger fields, typically tens or hundreds of mT, and are referred to as “magnetically hard”.

Let us return to Eq. (3.4) and our discussion regarding the stability of the solutions for

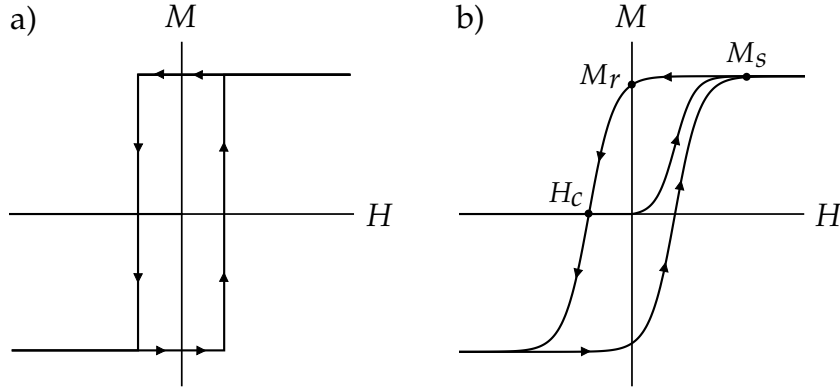


Figure 3.4: *Hysteresis loops showing the magnetization M vs. the magnetic field H applied along the easy axis of the ferromagnet.* a) The expected hysteresis curve of an ideal ferromagnet. b) The typical hysteresis curve of a real ferromagnetic material. When the applied field is increased the magnetization increases until it saturates to a maximum value M_s . The quantity M_r denotes the non-vanishing “remanent” magnetization that remains after the applied field is returned to zero. A “coercive field” field H_c must be applied in the opposite direction to reverse the magnetization.

the magnetization. By extremizing the total energy density we can determine the conditions for marginal stability, where $\partial^2 u / \partial \theta^2 = 0$. After a first derivative of Eq. (3.4) with respect to the angle θ , we find

$$\frac{\mu_0 H_x}{\sin \theta} - \frac{\mu_0 H_z}{\cos \theta} = \beta M. \quad (3.5)$$

Taking another derivative of this expression yields

$$\frac{\mu_0 H_x}{\sin^3 \theta} + \frac{\mu_0 H_z}{\cos^3 \theta} = 0. \quad (3.6)$$

Solving Eqs. (3.5) and (3.6) for the components of the external field, we find

$$\mu_0 H_x = \beta M \sin^3 \theta, \quad (3.7)$$

$$\mu_0 H_z = -\beta M \cos^3 \theta. \quad (3.8)$$

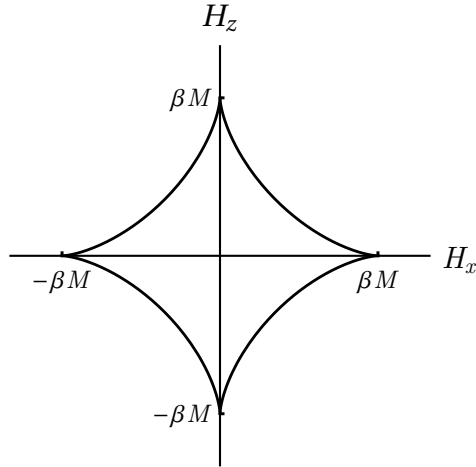


Figure 3.5: *Astroid diagram from the Stoner-Wolfarth model.* Extremizing the solutions to the total energy leads to Eq. (3.9), whose geometric representation is an astroid. Hysteretic solutions, of the type shown in Fig. 3.4, occur inside the asteroid, while nonhysteretic unique solutions occur outside it.

These expressions correspond to the metastable solutions for the magnetization, where $\partial^2 u / \partial \theta^2 = 0$, and can be combined into a single equation,

$$(\mu_0 H_x)^{2/3} + (\mu_0 H_z)^{2/3} = (\beta M)^{2/3}. \quad (3.9)$$

Eq. (3.9) traces out an astroid, shown in shown in Fig. 3.5, and is a geometric representation of the Stoner-Wohlfarth model, first proposed by John Slonczewski in 1956 [52]. The stable hysteretic behavior of the magnetization, shown in Fig. 3.4, is found within the astroid, while metastable solutions for \mathbf{M} exist on the line, and non-hysteretic unique solutions occur outside. At a given value of the field (H_x, H_z) , the magnetization will follow the vector lines that connect that point to lines that lie tangent to the astroid curve. The stable solutions which have tangent lines nearest to the easy axis cause \mathbf{M} to align with \mathbf{H} [52]. Traversing across the astroid line by modifying the field direction or strength, results in discontinuous

changes to the magnetization.

3.3.2 Types of Magnetic Anisotropy

The underlying crystalline structure of a ferromagnet is one of the ways that can preferentially set the direction of its magnetization. Such a ferromagnet is then said to have magnetocrystalline anisotropy, an effect which originates microscopically from spin-orbit coupling in the following manner. In a crystal of closely spaced atoms, whose electronic orbitals are anisotropically shaped, there will be more orbital overlap in certain directions than in others. Then, if the direction of the spin of an electron is strongly coupled to the orientation of those electronic orbitals (i.e. the crystal electric field), then strength of the exchange field will then too become anisotropic in space. Considering the number of diverse crystallographic structures found in the periodic table, it is evident there are many different types of magneto-crystalline anisotropy.

Even if a ferromagnetic material has no magneto-crystalline anisotropy, its shape can still influence its magnetization direction. For instance, an external field will equally magnetize a sphere in any direction, whereas a prolate ellipsoid will be easier to magnetize along its long axis than along its short axis. This *shape anisotropy* is due to the magnetostatic energy arising from so-called *demagnetizing fields*, generated by the object's own magnetization. The demagnetizing field for an arbitrary shaped ferromagnet varies spatially, in a manner that can be difficult to predict, but reduces to more simple forms for shapes such as ellipsoids, which we will mainly study. For example, a uniformly magnetized sphere has a uniform internal magnetic field,

$$\mathbf{H} = \mathbf{H}_{\text{ext}} - n_d \mathbf{M}, \quad (3.10)$$

if placed in a uniform external magnetic field \mathbf{H}_{ext} . The second term in Eq. (3.10) corresponds to the demagnetizing field, which points opposite to the direction of \mathbf{M} , where n_d is called the “demagnetizing factor,” which for a sphere equals $1/3$. In general, n_d is a tensor. For example, an extremely oblate ellipsoid, the components of the tensor along the principal axes are $\mathbf{n}_d = 1/2 \hat{a} + 1/2 \hat{b} + 0 \hat{c}$. In the notation of Sec. 3.3.1, this case is the same as taking $\beta/2 \rightarrow (n_a - n_c) = 1/2$.

Another type of magnetic anisotropy is *exchange anisotropy*, attributed to the exchange interaction near the interfaces between ferromagnetic and antiferromagnetic layers, and will be discussed briefly in Ch. 8. Among other features it can result in shifted magnetization curves, to the left or to the right along the field axis.

Finally, we mention only in passing some other considerations that may need to be taken into account when dealing with ferromagnetic samples. Stress applied to a ferromagnet can change its magnetic properties. Stress can cause the shape of the sample to change either mechanically, by thermal expansion or contraction, or by exposing the ferromagnet to a magnetic field (called magnetostriction), though the effects typically add small corrections to the magnetization curves. However, even if a ferromagnet has a Curie temperature above room temperature, it may have noticeably different magnetization curves at room temperature compared to at cryogenic temperatures. Stress can also change the shape and behavior of the magnetic domains in the sample.

Chapter 4

Interplay Between Superconductivity and Ferromagnetism

At first glance, one may balk at the prospect of combining ferromagnets and superconductors, given that ferromagnetism and superconductivity are inherently antagonistic forms of order. In a typical BCS-like superconductor the electrons bind into Cooper pairs with anti-aligned spins, while in a ferromagnet the exchange field acts to align the electron spins in one direction. Yet, combining and controlling the interplay between these two forms of competing order has proven to be a fertile arena for rich interesting physics, particularly near the interfaces of superconductors and ferromagnets. This situation stems from the fact that superconducting correlations can extend beyond the boundary of a superconductor into a non-superconducting material, called the superconducting *proximity effect*, which will be discussed in the next section. Many intriguing phenomena then emerge from how those superconducting correlations are modified in the presence of ferromagnetism.

In this chapter, after discussing the proximity effect and the physics of superconductor/ferromagnet (S/F) interfaces, we will explain how those effects modify the behavior of *ferromagnetic Josephson junctions*, for example $S/F/S$ junctions. Next, we discuss how different shaped junctions of that type behave in the presence of an externally applied magnetic field. Finally, we consider how using three ferromagnets (F' , F , and F'') with noncolinear magnetizations in Josephson junctions of the form $S/F'/N/F/N/F''/S$, where N is a normal metal, can be used to convert between spin-singlet Cooper pairs and an altogether differ-

ent form of spin-triplet pairing. This chapter will establish the theoretical background for the experiments that follow in Chs. 6–9, which involve each of the aforementioned types of Josephson junctions.

4.1 The Proximity Effect at S/N Interfaces

It has been known for a long time that superconductivity can extend beyond the boundary of a superconductor. For example, in 1932 R. Holm and W. Meissner found it was possible for two superconductors separated by a thin film of normal metal (an $S/N/S$ junction) to have zero resistance, the first observation of the superconducting proximity effect [53].[†] Further experiments in the 1960s on superconductor/normal metal (S/N) bilayers confirmed that superconducting pair correlations can extend into an adjacent non-superconducting material [54].

The proximity effect is simplest to understand (and observe) at S/N interfaces, shown schematically in Fig. 4.1, where it is possible for superconducting correlations to persist deep into the normal metal. The superconducting pair-correlation function Ψ decays in the normal metal, until coherence is lost via scattering and thermal fluctuations. For clean metals like Cu, Ψ typically decays on the order of 100s of nanometers. Correspondingly, on the superconducting side of the interface, the superconductivity is weakened due to the presence of the normal metal.

This behavior may be perplexing considering the electronic density of states on the two sides away from the interface. As we saw in Ch. 2, in a superconductor there is a finite energy gap Δ in the energy density of states near the Fermi energy quite unlike a normal metal as shown in Fig. 4.2(a). For single electrons in the normal metal, whose energy is

[†]Intriguingly, 30 years prior to the prediction of the Josephson effect.

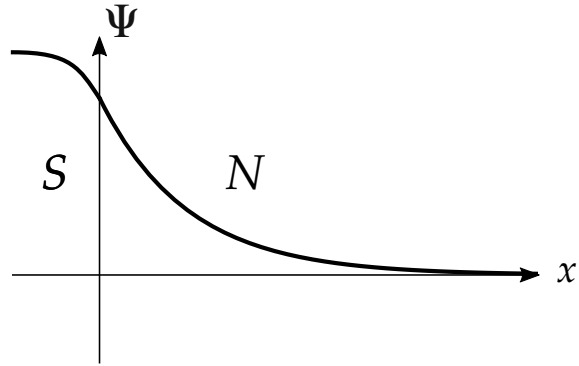


Figure 4.1: *Proximity effect near the interface of a superconductor and a normal metal.* Pair correlations from the superconductor (S) will penetrate into a normal metal (N) over a distance ξ_N , typically 100s of nm for clean metals like Cu at cryogenic temperatures. In N the superconducting pair-correlation function Ψ decays exponentially as thermal fluctuations and scattering events destroy the pairing. Likewise, on the S side of the interface, the leakage of Cooper pairs into the normal metal weakens the superconducting order parameter.

less than $E_F + \Delta$, transmission across the interface is forbidden due to the superconducting energy gap and the filled levels below. How then is current transferred across the interface (in either direction)?

The microscopic mechanism for the charge transfer process was explained by Alexander F. Andreev in 1964 [55]. Andreev showed that a double-charge transfer process called *Andreev reflection* is permissible. In this process, a single electron in the normal metal, close to the Fermi energy, can only be transferred into the superconductor when accompanied by a second electron (of opposite spin) and together form a Cooper pair in the superconductor. In the normal metal, the absence of this second electron is equivalent to a hole retro-reflected at the S/N interface, as shown in Fig. 4.2(b). For incident electrons moving in the other direction, due to time-reversal invariance the opposite process occurs, as shown in Fig. 4.2(c). Andreev reflection is the primary mechanism for Cooper pairs to be transferred into or out of the superconductor [56]. Perhaps the most important aspect of the Andreev reflection (with regards to this work) is that it preserves the phase coherence of the electrons. Like-

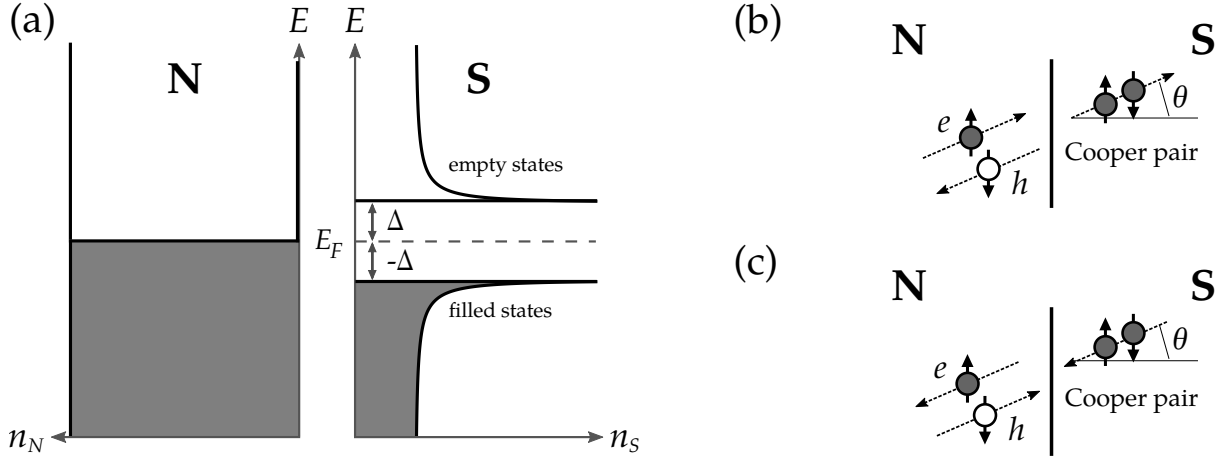


Figure 4.2: *Density of states at a superconductor/normal metal interface and Andreev reflection.* (a) The energy density of states on either side of a superconductor/ normal metal interface (n_S and n_N , respectively), prohibits single electron transfer at energies $E < E_F + \Delta$, where Δ is the superconducting gap and E_F is the Fermi energy, with filled states at $T = 0$ shaded. Instead, charge transport happens though Andreev reflection (b), where an electron near the Fermi level is converted into a retro-reflected hole in N and a Cooper pair in S . The inverse Andreev reflection process is shown in (c) for transferring Cooper pairs out of the superconductor. Both the Andreev processes conserve the total spin and the momentum in the direction parallel to the interface, all the while maintaining phase coherence.

wise, the reflected hole will retain phase information about the macroscopic phase of the superconductor.

In the Andreev reflection process, momentum is conserved in the directions parallel to the interface. At low energies, when the S/N interfaces are very clean and there is no potential energy barrier between them, practically all of the electrons near the interface are converted via Andreev reflection and electrons at the Fermi energy have perfect retro-reflection, which has been observed in experiments [56].

Finally, as seen in Fig. 4.2(b) Andreev reflection is dependent on the spin degree of freedom. If a spin-up electron in the normal metal enters the superconductor it needs to form a Cooper pair with a spin-down electron. Thus, to conserve the total spin in the process the reflected hole is in the spin-down band. Inside a normal metal, where the bands

associated with spin-up and spin-down electrons are the same, the spin degree of freedom for Andreev reflection is not usually important. However, the situation is drastically different in ferromagnetic materials, as we will see in the next section, where the two spin bands are mismatched.

These basic features of the proximity effect were described phenomenologically in terms of Ginzberg-Landau theory by Pierre-Gilles de Gennes in 1969, which we only briefly mention here, but is described in detail in several good references [54, 57]. Essentially, it amounts to solving Eqs. (2.9)–(2.11), where in the case of an S/N interface, the right-hand side of the boundary condition, Eq. (2.11), is replaced with $(1/t)\Psi$, where t is a material dependent property that is proportional to the superconducting coherence length.[†]

In actuality, the proximity effect results from the combination of the Andreev reflection process at the interface and how the superconducting correlations retain phase coherence once inside the non-superconducting material. The length scale over which the electrons keep their phase coherence varies with temperature and from material to material, and depends strongly on the presence of impurities. Nonetheless, that distance can be calculated in two important cases: the diffusive limit (sometimes called the “dirty limit”), where the electrons propagate via disorder scattering, *i.e.* the mean-free path is smaller than the sample dimensions, and the ballistic limit (sometimes called the “clean limit”), where the electrons propagate in relatively straight lines and their mean-free path is comparable to the size of the device.

When the electron transport is diffusive the propagation takes place over the distance

[†]We also note that there exist several more accurate and sophisticated theoretical quasiclassical methods for gaining practical solutions to the physics near S/N or S/F interfaces, or in simplistic situations involving diffusive motion or disorder, namely the Usadel and Eilenberger equations, but we will not dwell on them here.

that the pairs can remain correlated, called the *normal metal coherence length*[†]

$$\xi_{N, \text{diffusive}} = \sqrt{\frac{\hbar D}{2\pi k_B T}}, \quad (4.1)$$

where D is the electron diffusion constant that depends on the material, k_B is Boltzmann's constant, and T is the temperature.

Pure normal metals without disorder typically follow the ballistic limit, where the primary cause of scattering is at the boundaries of interfaces. In this case the normal metal coherence length takes the form

$$\xi_{N, \text{ballistic}} = \frac{\hbar v_F}{2\pi k_B T}, \quad (4.2)$$

where v_F is the Fermi velocity. The value of ξ_N is on the order of 100s of nanometers, typical for diffusive Cu samples below 10 K.

4.2 The Proximity Effect at S/F Interfaces

When the normal metal is replaced with a ferromagnet the Andreev reflection process is strongly altered on account of the incoming electron pairs (or reflected holes) occupying different spin bands. For instance, in the extreme example of a ferromagnet with perfect spin polarization, the Andreev reflection process will be completely suppressed [56, 57]. If there is a large mismatch between the spin-up and spin-down bands along the relevant Fermi wavevector in k -space it will result in a very short correlation length in the ferromagnet, as we will show below.

Besides the rapid decay with thickness, the pair correlation function in a ferromagnet

[†]There are many interesting questions that can be explored here, regarding how the superconducting correlations can endure the averaging over many disordered scattering events. So-called weak localization effects, or other signatures such as coherent backscattering, can be investigated in S/N interfaces.

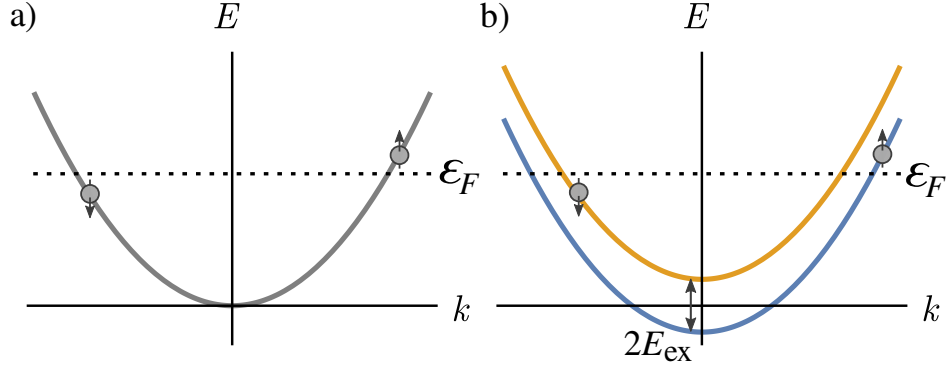


Figure 4.3: *A simplified toy model of a normal metal and a ferromagnet.* Consider a model where the Bloch bands are assumed to have a parabolic dispersion relation (Energy E vs. wavevector k). In a normal metal (a) the spin-up and spin-down bands are degenerate, while in a ferromagnet (b) the spin bands (blue and yellow lines) are shifted with respect to one another by twice the exchange energy. In the ferromagnet, oppositely aligned spin pairs that enter those respective bands near the Fermi energy E_F will have a nonzero difference between their respective Fermi wavevectors, so the pair acquires a net center-of-mass momentum. That leads to a spatial oscillation of the pair correlation function, as described in Eq. (4.6). A similar situation occurs in real ferromagnets, although the band structure is typically more complex.

is strongly modified in another manner that is dependent on the particular structure of the spin-bands. Accurately modeling the band structure in realistic ferromagnets can be quite complex. However, we can discuss some of the more salient features by considering a “toy model” of a ferromagnet, similar to that described by E. Demler, G. Arnold, and M. Beasley [58]. Consider a situation in which the spin bands are parabolic in k -space, separated by twice the exchange energy E_{ex} , shown in Fig. 4.3. Via Andreev reflection, oppositely aligned spin pairs enter the ferromagnet near the Fermi level, but occupy different spin bands. The correlated pairs thus have different Fermi wavevectors, k_F^\uparrow and $-k_F^\downarrow$, which we will initially consider to be perpendicular to the S/F interface. Their difference is,

$$(k_F^\uparrow - k_F^\downarrow) \equiv Q \approx 2E_{ex}/\hbar v_F. \quad (4.3)$$

Thus the pair acquires a net center-of-mass momentum, $\hbar Q$. Quantum mechanically, accord-

ing to the anti-symmetry property of fermions, in the wavefunction $|\Psi\rangle$ we are also required to consider the case where the particles are interchanged. That is a spin pair with the state $|\uparrow\downarrow\rangle$ will acquire a center-of-mass momentum $\hbar Q$, while a pair with the state $|\downarrow\uparrow\rangle$ will acquire a center-of-mass momentum $-\hbar Q$. Arranging these two pairs in a spin-singlet configuration (as imposed by the memory of their pairing from the BCS-type superconductor) we write the spin and center-of-mass contributions to the wavefunction as,

$$|\Psi\rangle = \frac{1}{\sqrt{2}} \left(|\uparrow\downarrow\rangle e^{iQX} - |\downarrow\uparrow\rangle e^{-iQX} \right), \quad (4.4)$$

where X is the coordinate describing the center-of-mass of the electron pair. Rearranging Eq. (4.4) with Euler's formula yields

$$|\Psi\rangle = \frac{1}{\sqrt{2}} \left[\left(|\uparrow\downarrow\rangle - |\downarrow\uparrow\rangle \right) \cos(QX) + i \left(|\uparrow\downarrow\rangle + |\downarrow\uparrow\rangle \right) \sin(QX) \right], \quad (4.5)$$

$$= |0, 0\rangle \cos(QX) + i |1, 0\rangle \sin(QX), \quad (4.6)$$

where the states $|s, m\rangle$ are labeled according to their total spin quantum number s and projection m . From Eq. (4.6) we see that the pair-correlation function in a ferromagnet contains two terms: the first corresponding to the spin-singlet correlations, and the second corresponding to the spin-triplet correlations with $m = 0$, which each oscillate in the direction perpendicular to the interface. The oscillation of the pair-correlation function was first predicted, not in S/F systems, but for bulk superconductors in the presence of an exchange field by Fulde and Ferrell in 1964 and independently by Larkin and Ovchinnikov a year later, but nonetheless is often referred to as the *FFLO state* in their namesake [58–61].

Note that Eq. (4.4) did not account for the full angular dependence of the pair-correlation

function. In general, we ought to consider the case where the incident electrons make an angle θ with the interface normal, so in the ballistic limit the difference in the Fermi wavevectors is $(k^\uparrow - k^\downarrow) \cos(\theta) = Q \cos(\theta) = 2E_{ex}/(\hbar v_F)$. For example, if we consider only the amplitude of the first term in Eq. 4.5 and integrate over all angles we find that the spin-singlet pair-correlation function decays algebraically in X ,

$$\int_0^1 d(\cos \theta) \cos\left(\frac{2E_{ex}X}{\hbar v_F \cos \theta}\right) \approx \frac{\sin(X/\xi_F)}{X/\xi_F} \quad (4.7)$$

where we have defined,

$$\xi_{F, \text{ballistic}} = \frac{\hbar v_F}{2E_{ex}}. \quad (4.8)$$

which corresponds to the coherence length in the ferromagnet [58–61] and the integration in Eq. (4.7) is only valid for $X \gg \xi_F$. A similar calculation for the second term in Eq. (4.6), shows that the spin-triplet correlations (with $m = 0$), being composed of oppositely aligned spin pairs, also oscillate and decay rapidly with thickness.

In the diffusive limit, the spin-singlet pair correlation function oscillates and decays exponentially with distance [57]

$$|\Psi\rangle \propto \exp(-x/\xi_F) \sin(X/\xi_F), \quad (4.9)$$

where the coherence length is

$$\xi_{F1, \text{diffusive}} = \sqrt{\frac{\hbar D_F}{E_{ex}}}, \quad (4.10)$$

and D_F is the diffusion constant in the ferromagnet. In Fig. 4.4 we plot Eq. (4.9) vs. X . Due to the large exchange energy in typical ferromagnets, the coherence length is several orders

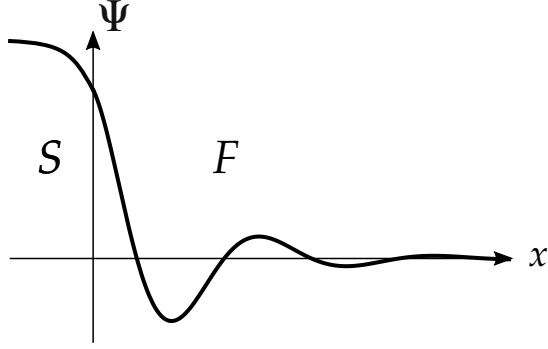


Figure 4.4: *Proximity effect near the interface of a superconductor and a ferromagnet.* Pair correlations from the superconductor (S) penetrate into a ferromagnet (F), quickly decaying over a distance ξ_F , which in weak ferromagnets like $\text{Cu}_{48}\text{Ni}_{52}$ is on the order of 10 nanometers at cryogenic temperatures. Since ξ_F depends on the strength of the exchange energy, in strong ferromagnets, like Fe or Co, the decay is on the order of a nanometer. In addition to the decay, the pair-correlation function oscillates spatially in the direction perpendicular to the interface.

of magnitude smaller in S/F systems than in S/N systems. Taking the expressions for the ballistic limit, Eq. 4.2 and Eq. 4.8, and assuming the Fermi velocities are similar in the two materials, and $E_{ex} \approx k_B T_{\text{Curie}}$ to be proportional to the ferromagnet's Curie temperature, we find the ratio of the two coherence lengths to be

$$\xi_N/\xi_F = \frac{E_{ex}}{\pi k_B T} \approx \frac{T_{\text{Curie}}}{\pi T}. \quad (4.11)$$

For example, consider Co, which has $T_{\text{Curie}} = 1388$ K [62]; if the sample temperature is $T = 4$ K, then $\xi_N/\xi_F \approx 110$. In typical ferromagnets ξ_F is usually on the order of a nanometer.

The spatial oscillation of the pair-correlation function can be detected experimentally through several different means. For instance, it can cause measurable oscillations in the critical temperature of S/F bilayers [63,64]. It can also be measured by probing the tunneling density of states, via differential conductance measurements, in a $S/F/I/N$ structure, where I is an insulator [65,66]. In those experiments the thickness of the F-layer was varied until

the pair correlation function changed sign, resulting in an inversion of the measured density of states. Another method, which we will discuss in the next section, as well as in Ch. 6, is to measure the oscillation of the critical current in $S/F/S$ Josephson junctions versus the ferromagnetic layer thickness.

4.3 π -Phase Josephson Junctions

The oscillation of the pair-correlation function can be combined with the Josephson effect to make a so-called π – *junction*, *i.e.* an $S/F/S$ junction in which the equilibrium phase difference between the two superconducting electrodes is π . This effect was predicted in 1977 by Bulaevskii *et al.* who considered what would happen if magnetic impurities were inserted into the central layer of an $S/I/S$ Josephson junction [67]. The first experimental verification of π -junction physics was not achieved until the early 2000's with the works of V. Ryazanov *et al.* and T. Kontos *et al.* [65,68].

The absolute value of the pair correlation function is related to the critical current in a Josephson junction. As we found in Eq. (2.23), the energy stored in a conventional Josephson junction is

$$E = \frac{\hbar I_c}{2e}(1 - \cos \phi), \quad (4.12)$$

and is normally minimized when the phase difference across the junction is $\phi = 0$. In an $S/F/S$ junction, if one can set the thickness of the F -layer such that the oscillating pair correlation function is negative, then

$$E = \frac{\hbar I_c}{2e}(1 - \cos(\phi - \pi)), \quad (4.13)$$

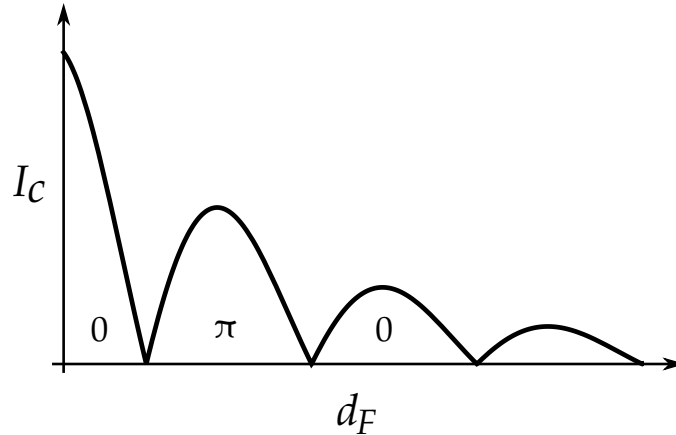


Figure 4.5: $0-\pi$ phase oscillations in an $S/F/S$ Josephson junction. The critical current I_c oscillates as a function of the ferromagnetic layer thickness d_F . The minima signal the transition between the 0 and the π -phase states, as the labels indicate.

which forces the minimal energy state to occur at $\phi = \pi$. Emphasis should be placed on the important feature that in these types of junctions only two distinct values of ϕ are allowed, 0 or π , as showed by Buzdin *et al.* in 1982 [61].

Experimentally, by measuring I_c for many $S/F/S$ junctions, each with a different F -layer thickness, d_F , we can directly trace out the oscillations in the pair-correlation function as shown in Fig. 4.5, and from those measurements extract the coherence length, the period of the oscillations, and the critical current magnitude for an F -layer of interest. We will discuss experiments of this type in Ch. 6 for a number of different ferromagnets with both long and short coherence lengths. Experiments demonstrating the $0 - \pi$ oscillations have been performed on a wide expanse of materials by many groups, including ours, in the last two decades [19, 69–77].

4.4 Fraunhofer Patterns in Ferromagnetic Josephson Junctions

A key method for probing both the ferromagnetic and superconducting properties of Josephson junctions is to measure them in the presence of an external magnetic field applied perpendicular to the direction of the supercurrent. In small ferromagnetic Josephson junctions, one can simultaneously measure both the Josephson physics of Ch. 2 and the Stoner-Wohlfarth physics of Ch. 3. In this section, first we return to the Josephson effect and examine how standard Josephson junctions of finite area behave in the presence of magnetic flux. Then, we discuss how the situation changes for ferromagnetic Josephson junctions.

4.4.1 The Josephson Effect in the Presence of Magnetic Flux

We consider the case of “short” Josephson junctions, the relevant limit for all the experiments that follow, where the distance between the superconducting electrodes d , is small compared to the lateral dimension of the junction. We assume that the thickness t of each superconducting electrode is larger than the London penetration depth λ_L , and that the critical current density J_c through the junction is homogeneous. First, we will assume that there is no contribution from the magnetization \mathbf{M} of the material between the electrodes (if any), so that an externally applied field $\mu_0\mathbf{H}_{\text{ext}}$ equals the field induced inside the junction \mathbf{B} .

Recall from Eq. (2.51) that the difference in the gauge invariant phase differences ϕ between two points along a closed path is proportional to the flux threading the loop. Consider two sets of such points P and Q shown in Fig. 4.6, which are separated by an infinitesimal distance dz on the z -axis and lie along a closed path (Q_1, Q_2, P_3, P_4) that extends deep

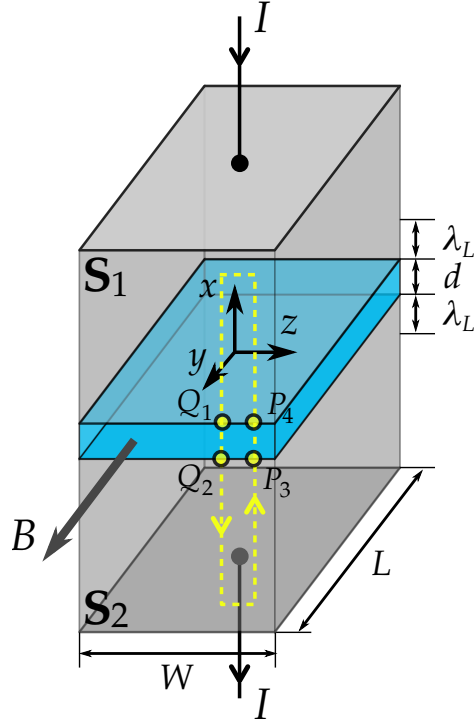


Figure 4.6: *Geometry for calculating the Fraunhofer pattern in a Josephson junction with rectangular cross-section of area LW . The superconducting electrodes are separated by a distance d , which for example could be the thickness of a normal metal spacer. The integration path is shown with a yellow dotted line and extends deep into each superconductor, taking into account the London penetration depth λ_L , near both interfaces. The field \mathbf{B} in the junction is assumed to have only a component along \hat{y} .*

($\gg \lambda_L$) into the superconducting electrodes. Following a calculation analogous to what we did for Eq. (2.51), we arrive at

$$\phi_P - \phi_Q = 2\pi \frac{\Phi}{\Phi_0}, \quad (4.14)$$

where ϕ_Q is the gauge invariant phase difference from point Q_1 to Q_2 and ϕ_P is from P_3 to P_4 . There are no contributions to this expression from the current density \mathbf{J}_s since both integrations along the z -direction vanish deep in the superconductor and the integrations along the x -direction cancel the contributions from the adjacent paths dz away.

The flux penetrating the closed yellow path in Fig. 4.6

$$d\Phi = B t dz, \quad (4.15)$$

where the magnetic field inside the junction $\mathbf{B} = B\hat{y}$ is only along the y -direction, the distance $t = d + 2\lambda_L$ is the sum of the separation between the electrodes d and the London penetration depth of each electrode, and dz is the width of the integration path along \hat{x} . Combining Eqs. (4.14) and (4.15), we can write $\phi_P - \phi_Q = \Delta\phi$ as

$$\Delta\phi = \frac{\partial\phi}{\partial z} dz = 2\pi \frac{Bt}{\Phi_0} dz, \quad (4.16)$$

so that $\partial\phi/\partial z = 2\pi Bt/\Phi_0$.[†] Integrating this expression over z we see that the gauge invariant phase difference varies linearly along z as

$$\phi(z) = \frac{2\pi t B}{\Phi_0} z + \phi(0). \quad (4.17)$$

As a result of Eq. (4.17), the supercurrent density is

$$\begin{aligned} J_s(z) &= J_c \sin \phi(z) \\ &= J_c \sin(kz + \phi(0)), \end{aligned} \quad (4.18)$$

where $k = 2\pi t B/\Phi_0$ describes the period $2\pi/k$ of the supercurrent density oscillations in the z -direction.[‡] Integrating the supercurrent density over the junction area A yields the total

[†]In general, we can write the gradient of ϕ as $\nabla\phi = 2\pi t/\Phi_0 \mathbf{B} \times \hat{x}$, where \hat{x} is the unit vector perpendicular to the junction area and, in this case, opposing the direction of the current flow.

[‡]For one complete oscillation of the supercurrent density along the z -axis, the corresponding flux enclosed is precisely equal to a flux quantum: $\Phi = (2\pi/k)tB = \Phi_0$.

supercurrent,

$$I_s = \int J_s(z) dA. \quad (4.19)$$

We now consider two specific junction shapes—rectangular and circular—and determine how the maximum supercurrent (at a given flux) I_c^{\max} varies with the total flux Φ through the junction.

The schematic of a Josephson junction with a rectangular cross section of length L and width W is shown in Fig. 4.6. Integrating the supercurrent density in Eq. (4.18) along y and x yields the total supercurrent,

$$\begin{aligned} I_s &= \int_{z=-L/2}^{L/2} \int_{y=-W/2}^{W/2} J_c \sin(kz + \phi(0)) dy dz \\ &= J_c W L \frac{\sin(kL/2)}{kL/2} \sin \phi(0), \end{aligned} \quad (4.20)$$

where k was defined previously in Eq. (4.18). The total flux penetrating the junction is $\Phi = B(d + 2\lambda_L)$. With the replacements $kW/2 = \pi\Phi/\Phi_0$ and $J_c W L = I_c$, it follows that the maximum supercurrent at a given value of the flux is

$$I_c(\Phi) = I_{c0} \left| \frac{\sin(\pi\Phi/\Phi_0)}{\pi\Phi/\Phi_0} \right|, \quad (4.21)$$

which traces out a *Fraunhofer pattern*[†] with respect to the total magnetic flux. This function is shown in Fig. 4.7, normalized to the maximum critical current I_{c0} .

For a junction with a circular cross section of radius R , the integration of the supercurrent density is performed in polar coordinates $z = r \cos \alpha$ and $y = r \sin \alpha$. Namely, Eq. (4.19) is

[†]This is directly analogous to the Fraunhofer diffraction pattern in optics for light incident on a slit of finite width.

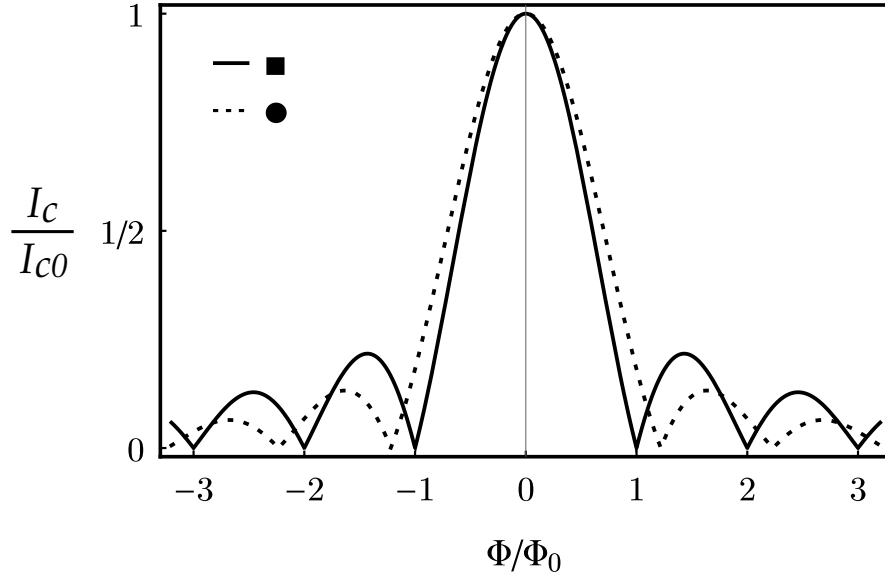


Figure 4.7: Fraunhofer patterns for rectangular and circular Josephson junctions. The critical current $I_c(\Phi)$ oscillates as a function of the applied flux Φ . Rectangular shaped junctions (solid) follow a Sinc function (Eq. (4.21)), while circular junctions (dashed) follow an Airy function (Eq. (4.23)). The current axis is normalized to the maximum critical current I_{c0} and the flux axis to the flux quantum Φ_0 .

written as

$$\begin{aligned}
 I_s &= \int_{r=0}^R \int_{\alpha=0}^{2\pi} J_c \sin(kr \cos \alpha + \phi(0)) r dr d\alpha \\
 &= 2J_c \pi R^2 \frac{J_1(kR)}{kR} \sin \phi(0).
 \end{aligned}
 \tag{4.22}$$

Comparing to Eq. (4.20), we see that instead of a sine function, which appeared for the rectangular junction, we have a first order Bessel function of the first kind, $J_1(kR)$. With $kR = \pi\Phi/\Phi_0$ and $J_c \pi R^2 = I_c$, the maximum supercurrent for a circular junction is

$$I_c = 2I_{c0} \left| \frac{J_1(\pi\Phi/\Phi_0)}{\pi\Phi/\Phi_0} \right|.
 \tag{4.23}$$

This function, which traces out an *Airy pattern*, is also shown in Fig. 4.7 for comparison to the result obtained for a rectangular junction. In the Chs. 6-9, we fabricate Josephson

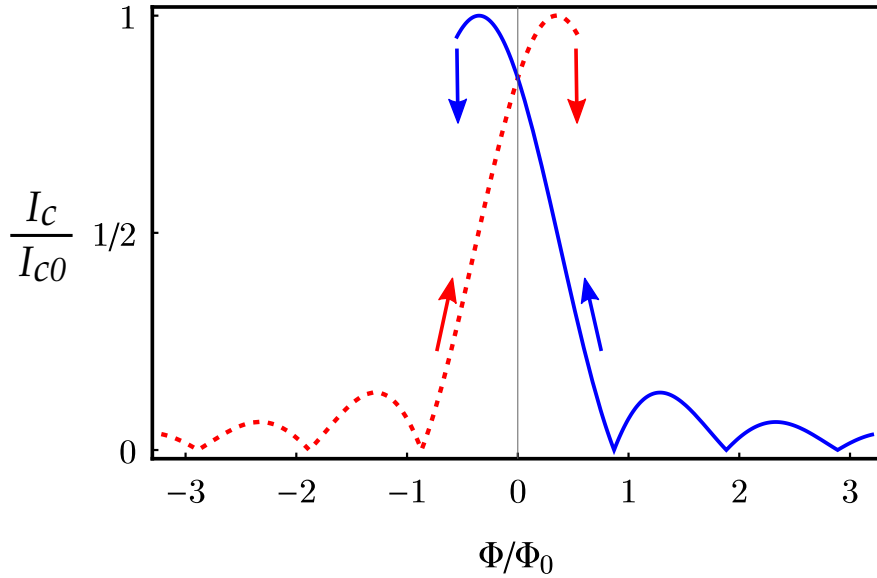


Figure 4.8: *Fraunhofer patterns for a ferromagnetic Josephson junction.* The critical current I_c follows Fraunhofer patterns that are shifted with respect to the applied flux Φ , by an amount corresponding to the flux added (or subtracted) to the junction due to the magnetization of the ferromagnetic layer. The behavior of the ferromagnet is hysteretic with the applied flux, so the solution jumps between the two Fraunhofer patterns when the applied flux corresponds to the ferromagnet’s coercive field.

junctions with elliptical cross-sections which also follow Eq. (4.23). We will refer to all curves of this type in general, as “Fraunhofer patterns”, even when they correspond to Airy functions or some other similar looking function.

4.4.2 Adding a Ferromagnetic Layer

We will now examine how the Fraunhofer physics is modified by the presence of a ferromagnetic layer in an $S/F/S$ Josephson junction. In addition to the assumptions discussed in the previous section, we consider the ideal case of an elliptical junction in which the ferromagnetic layer consists of a single magnetic domain, and follows the Stoner-Wohlfarth model discussed in Ch. 3.

The total magnetic flux in the junction is

$$\Phi_{\text{tot}} = \Phi + \mu_0 M w d_F, \quad (4.24)$$

where w is the width of the junction (minor axis) and d_F is the thickness of the ferromagnetic layer. The magnetization of the ferromagnet, M , which is assumed to be uniform and initially point along the same direction as Φ , produces a flux (the second term in Eq. 4.24) that adds to the external flux in the junction. In Eq. 4.24 we neglect the small contributions to Φ_{tot} from the uniform demagnetizing field and any magnetic field from the ferromagnetic layer that returns inside the junction. From Eq. 4.24 it is clear that the Fraunhofer pattern will be shifted along the field axis by an amount,

$$H_{\text{shift}} = -\frac{M d_F}{2\lambda_L + d}. \quad (4.25)$$

If the external flux starts at a large positive value and is slowly reduced through zero, the Fraunhofer pattern traces out the blue curve shown in Fig. 4.8. Due to the hysteresis in the magnetization curve, shown previously in Fig. 3.4, once the applied flux becomes sufficiently negative to exceed the coercive field of the ferromagnetic layer the magnetization will change sign. Thus the solution abruptly switches to another Fraunhofer curve that is shifted in the opposite direction (the red curve in Fig. 4.8). Increasing the applied flux from a large negative value towards positive flux produces the opposite effect, as in the Stoner-Wohlfarth model.

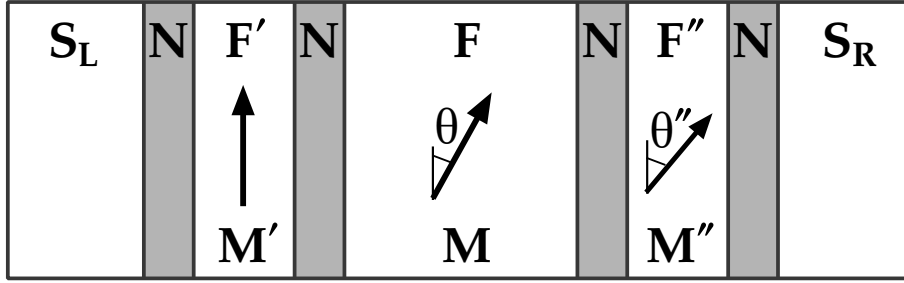


Figure 4.9: *Schematic for the generation of long-range spin-triplet correlations using noncollinear magnetizations.* The angles θ and θ'' lie in the same plane parallel to the interfaces and describe the orientation of the magnetizations of the second and third ferromagnets.

4.5 Generating Long-Range Spin-Triplet Correlations with Ferromagnetic Barriers

What would happen if the electrons inside a Josephson junction could somehow be paired with the same spin-orientation, that is $|\uparrow\uparrow\rangle$ or $|\downarrow\downarrow\rangle$? In that case, both electrons enter the same spin band and can remain correlated in the ferromagnet over much longer distances. In a Josephson junction there is thus an overall slower decay in the critical current and no oscillation of the supercurrent with the thickness of the ferromagnet [78]. While spin-triplet superconductivity is not commonly found in nature, it was predicted in the early 2000s by S. Bergeret, M. Eschrig and others that it could be engineered in multi-layered ferromagnetic systems having noncollinear magnetizations or magnetic inhomogeneity [78–82]. Since then, demonstrations of spin-triplet proximity effects have been reported by many groups using a variety of experimental techniques [83–104].

Our group has focussed on spin-triplet Josephson junctions (JJs) of the form suggested by Houzet & Buzdin [105], containing three magnetic layers $S/F'/N/F/N/F''/S$ [85, 90, 106, 107]. A schematic of a junction of this type is shown in Fig. 4.9, in which all the ferromagnets,

F' , F , and F'' have in-plane magnetization (parallel to the layer interfaces). Normal metal layers are inserted between the various layers to prevent them from magnetically coupling to one another in an undesirable manner. Such a Josephson junction converts between spin-singlet and long-range spin-triplet supercurrent in the following manner [108]:

1. Spin-singlet pairs from the superconductor on the left (S_L) enter the first ferromagnet (F') and acquire a net center-of-mass momentum, generating a short-range ($m = 0$) spin-triplet component, as previously described in Eq. (4.6), which we repeat here for convenience

$$|\Psi\rangle = |0, 0\rangle \cos(QX) + i |1, 0\rangle \sin(QX). \quad (4.26)$$

Both the spin-singlet and the $m = 0$ spin-triplet terms decay rapidly and oscillate with the thickness of the F' layer.

2. The electron pairs enter a second ferromagnet (F) with magnetization noncolinear to the first and the $m = 0$ spin-triplet states undergo a basis rotation as the quantization direction (set by \mathbf{M}) changes. The spin-singlet state $|0, 0\rangle$ is rotationally invariant, however the $|1, 0\rangle$ state is not. Expression of the $|1, 0\rangle$ state in the rotated basis includes the long-range ($m = \pm 1$) spin-triplet states. For example, if the angle between F' and F is θ then in the new basis,

$$|1, 0\rangle = \cos(\theta) |1, 0\rangle_\theta + \frac{\sin(\theta)}{\sqrt{2}} |1, 1\rangle_\theta - \frac{\sin(\theta)}{\sqrt{2}} |1, -1\rangle_\theta \quad (4.27)$$

where $|s, m\rangle_\theta$ denotes the basis rotated by θ . The conversion to the $s = 1$ spin-triplet states, $|1, 1\rangle = |\uparrow\uparrow\rangle$ and $|1, -1\rangle = |\downarrow\downarrow\rangle$, is maximized when the magnetizations are perpendicular (e.g. $\theta = \pi/2$ or $3\pi/2$). The spin-singlet states and $m = 0$ spin-

triplet states decay quickly in F , as described previously, but the ($m = \pm 1$) states can propagate much further, and thus are referred to as *long-range triplet correlations* (LRTC). Since the spin pairs are aligned in these states both electrons enter the same spin band and have no center-of-mass momentum, implying that the pair correlation function will not oscillate in space. Analogous to that of a normal metal, the correlation length for the LRTC is much larger than it would be inside a single ferromagnet with constant magnetization. In the dirty limit it has the same form as Eq. (4.1),

$$\xi_{F, \text{LRTC}} = \sqrt{\frac{\hbar D_F}{2\pi k_B T}} \quad (4.28)$$

where D_F is the diffusion constant in the central ferromagnet.

3. Since the final superconducting electrode (S_R) can only accept spin-singlet states, a third ferromagnetic layer (F'') is needed to convert the long-range triplet states back into spin-singlet. That occurs similarly through another basis rotation and that conversion process is optimal when the magnetization of F'' is perpendicular to that of F .

The phase across such a *spin-triplet junction* will take on different values depending on the relative orientation of the three magnetizations. The simplest case is when each of the adjacent ferromagnetic layers have their magnetization directions at 90 degrees to one another, for example in Fig. 4.10, where $\theta = \pi/2$ and θ'' is either 0 or π . When the direction of rotation between the F' and the F layers is the same as that between the F and the F'' layers (*i.e.* $\theta'' = \pi$, Fig. 4.10(a)), then the phase across the junction will be 0. On the other hand, if the relative direction of rotation reverses from the F' and the F layers versus the F and the F'' layers (*i.e.* $\theta'' = 0$, Fig. 4.10(b)) then the phase across the junction will be π .

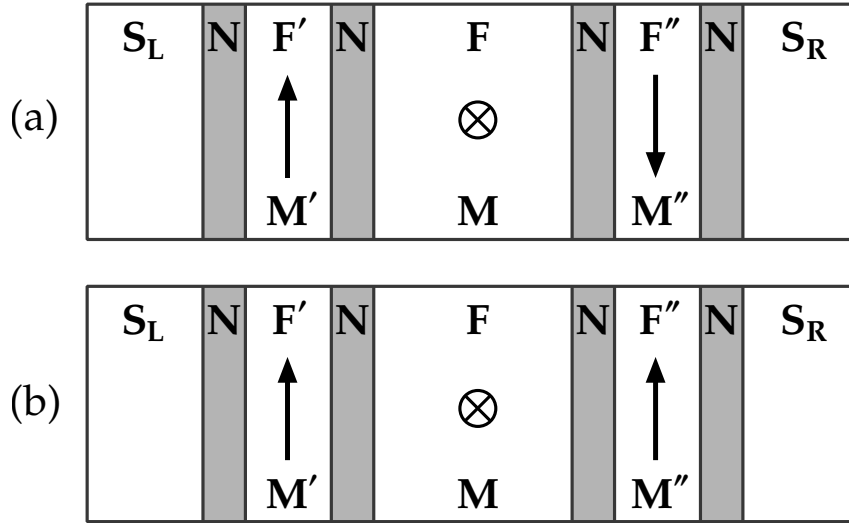


Figure 4.10: *Schematic for the generation of 0 and π phase junctions using long-range spin-triplet correlations.* When the chirality of the rotation angle between the F' and F layers is the same as between the F and F'' layers, shown in (a), the phase across the junction is 0 . When the relative rotation angle is reversed, as in (b), the phase across the junction is π .

In the past, our group has made spin-triplet Josephson junctions in which all the magnetic layers have in-plane magnetization [85], as in Fig. 4.10, and when some of the layers have out-of-plane magnetization, such as the geometry shown in Fig.4.11 [21, 106].

By fixing the magnetization direction of two of the ferromagnetic layers and controllably toggling the direction of the the third, one can conceivably switch between the 0 and the π phase states, a proposition that was partially realized by our group in 2014, spearheaded by the work of Eric Gingrich [109]. In Ch. 9 we will discuss a variant of this controllable switching experiment.

Recently, another Birge group member William Martinez successfully implemented another scheme to manipulate the LRTC states, whereby rotating the magnetization of the F'' layer so that it was either \parallel or \perp to that of the F layer, the long-range triplet supercurrent could be controllably toggled “on” or “off” as evidenced by large amplitude changes in the

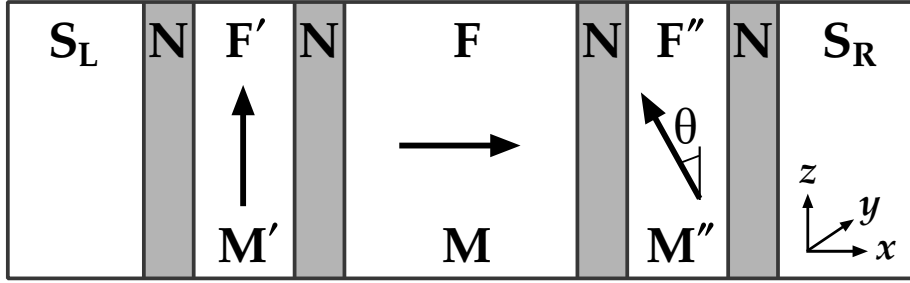


Figure 4.11: *Schematic for the generation of long-range spin-triplet correlations using non-collinear magnetizations* The angle θ with respect to the z -axis lies in the $y - z$ plane and describes the orientation of the magnetization of the third ferromagnet.

critical current [107]. This experiment was an excellent display of spin-triplet physics, and the “on” and “off” states could serve as the basis for a superconducting memory. However, when the current control scheme is in the “off” state, the device is in the resistive state. If one’s aim is to build devices with high energy efficiency the more advantageous method is to control the phase of the junction, all the while keeping it in the superconducting state so as to prevent resistive energy losses.

Finally, for spin-triplet Josephson junctions of the type discussed in this section to work as advertised, one must contend with a whole host of challenges beyond just controlling the orientation of the magnetic layers. Some of those issues, many of which can be resolved with the proper selection of materials and fabrication techniques, will be discussed in the remaining chapters. One notable consideration, for instance, is the proper matching of the band structure between the adjacent ferromagnetic materials in a junction. This will be discussed further in Ch. 8.

Chapter 5

Experimental Techniques

In this chapter we discuss the experimental methods used in the fabrication and measurement of Josephson junctions and SQUIDs for the experiments presented in the following chapters.

5.1 Sputtering

We use sputtering almost exclusively for the deposition of uniform metallic thin-films during sample fabrication. Sputtering is a kinetic process where energetic particles, in our case ionized Ar atoms, are bombarded into a metallic target material of interest, ejecting a vapor of metallic atoms onto a nearby sample. The deposition rate can be made appreciable by confining the Ar ions using magnetrons that produce strong magnetic and electric fields. The ions undergo helical cyclotron motion along the magnetic field lines, leading to a cascading chain of ionization events with the surrounding gas, which at moderately low pressures ($< 10^{-2}$ Torr) can form a sustained plasma.

Our main sputtering chamber, shown in Fig. 5.1 contains up to four large DC triode magnetron guns, each of which can be equipped with 2.25 inch diameter sputtering targets, in addition to three small DC magnetron guns that carry 1 inch diameter targets. In total, one can sputter any combination of layers composed of up to seven different materials in a single run. The chamber also contains a small 1 cm ion mill, which will be discussed later in the next section.

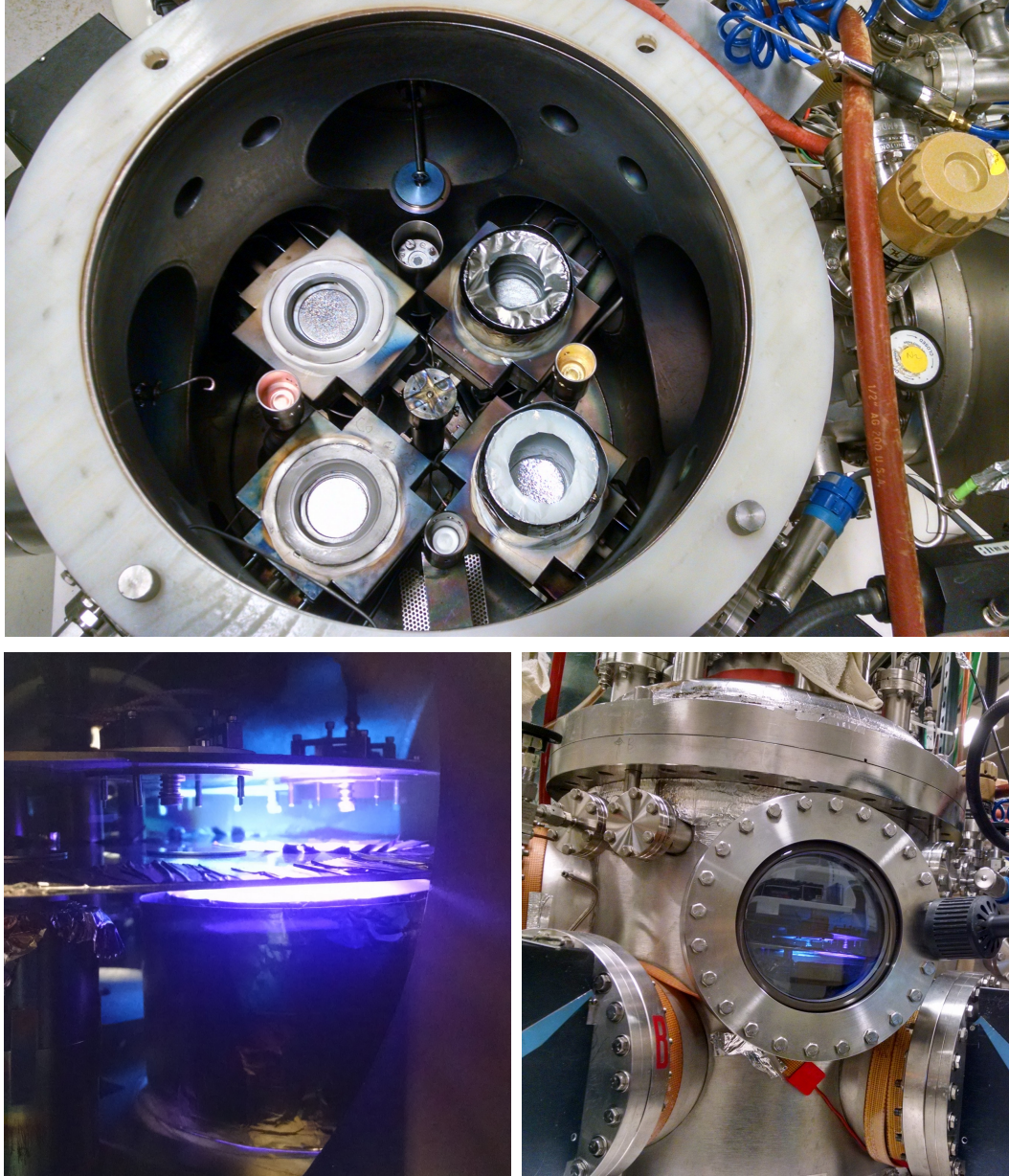


Figure 5.1: *7-target sputtering chamber with active plasma.* (top) The interior of the sputtering chamber showing: the four large DC magnetron guns loaded with the targets (starting at 2 o'clock, moving clockwise) Nb, Al, Co, Pd; the three small DC magnetrons loaded with the targets (starting at 3 o'clock, moving clockwise) Au, Ru and Cu. There is also a small ion mill located at the 12 o'clock position. Examples of the foil chimney collimators can be seen on top of the Nb and Al targets. (bottom) The sputtering process in action, showing the ignited plasma (purple and blue in color) over the Al (front) and Nb (far back) targets. One can see the sample holder plate and film thickness monitor on top, the shutter plate wrapped in Al foil in the center, and on the bottom the chimney around the Al target as observable from the front viewing window. The images were taken during the run to fabricate one of the sets of samples in Ch. 8

A photograph showing the sputtering process in action can be found in Fig. 5.1, showing the glowing plasmas above Al and Nb targets. The system was originally designed by William Pratt and has been extensively modified and maintained by Reza Loloee.

The sputtering deposition rate is controlled by changing the strength of the negative voltage bias of the target, which attracts the positively charged Ar ions. The density of the plasma near the triode magnetrons, which is also related to the sputtering rate, can be controlled by modifying the current driven through a Tungsten filament used to ionize the Ar atoms. The sputtering rate is measured using a crystal film thickness monitor attached to the sample plate accurate to $\pm 0.1 \text{ \AA/s}$, and calibrated using a tooling factor dependent on the density of target material of interest. The target voltage, filament current, and corresponding sputtering rates for all the materials used in this thesis are listed in Table 5.1.

To produce high-quality films the sputtering process needs to take place in an extremely clean environment, thus the sputtering chamber is equipped with a cryopump (assisted by a mechanical roughing pump) used to reduce the pressure in the chamber before the run to $\approx 2 \times 10^{-8}$ Torr. Those low pressures are achieved by baking the entire chamber to $\approx 100 \text{ }^\circ\text{C}$ (using thermal tapes attached to the outside of the chamber) for eight hours, releasing water molecules trapped on the inner walls to be captured by the cryopump.[†] Afterward, the cryopump continuously pumps on the chamber, in total for around 48 hours. Furthermore, to reduce the partial pressure of contaminant water molecules, just prior to the run the vacuum chamber is cooled by circulating liquid nitrogen through a Meissner trap housed in the lid. The sputtering run is typically performed with the Argon pressure near 1.3×10^{-3} Torr and the sample temperature held between $-30 \text{ }^\circ\text{C}$ and $-20 \text{ }^\circ\text{C}$. The partial pressure of

[†]Attached to the cold head of the cryopump is a sorption pump of activated charcoal pellets to assist in the adsorption of gases.

Table 5.1: *Sputtering parameters used for the various metallic targets.* The target voltage, filament current and the approximate sputtering rate used for all the materials used in this thesis. The 2.25 in targets are used with the DC triode magnetron guns, and the 1 in targets in the small DC magnetron guns. The sputtering is performed in the presence of Argon gas at 1.3×10^{-3} Torr.

Sputtering Target (2.25 in)	Target Voltage (V)	Filament Current (A)	Sputtering Rate ($\text{\AA}/s$)
Nb	600	0.60	4.1
Al	400	0.50	2.1
Pd	130	0.44	1.9
Co	250	0.35	1.1
Ni	350	0.30	1.8
Ni ₈₁ Fe ₁₉ (Py)	500	0.50	4.5
Ni ₆₅ Fe ₁₅ Co ₂₀	500	0.50	3.0
Pd ₉₇ Fe ₃	245	0.45	4.9
Sputtering Target (1 in)	Target Power (W)		Sputtering Rate ($\text{\AA}/s$)
Cu	18		3.4
Ru	18		1.2
Au	19		5.0

various contaminant materials can be monitored using a residual gas analyzer attached to the chamber.

To limit cross contamination, the chamber contains an aluminum foil wrapped shutter plate attached to a stepper motor, controlled to open or close off access between the samples above and the sputtering targets below as shown in Fig. 5.1. Also, around each gun a chimney wrapped with aluminum foil helps collimate the sputtered material toward the opening in the properly aligned shutter plate. The sputtered material is deposited on 0.5×0.5 in² Si substrates that are firmly isolated in stainless steel sample holders each with their own individual shutters. The sample shutters can be manually manipulated from outside the vacuum chamber wall via a wobble stick with flexible bellows that allows for linear and angular motions along a cone of movement. After manually opening the individual sample shutters, the timing and movement sample plate, the shutter plate, and the film thickness monitors with respect to each of sputtering targets is computer controlled using the LabVIEW software package. In total, the system can be programmed to produce a different layer sequence for each of the possible 16 samples that can be supported during a single run.

In between sputtering runs, the sample holders and sample shutter parts are thoroughly cleaned in a 1:3 solution of deionized (DI) water and nitric acid for approximately 10 minutes, followed by a manual scrubbing with steel brushes to remove all remaining residual metal films. Next, the parts are separately agitated in an ultrasonic bath while immersed in acetone, isopropanol, and then DI water, each for 10 minutes, and blown dry with an industrial heat dryer.

5.2 Photolithography

Photolithography is one of the techniques we use to define the circuit layout by shining ultraviolet light through a geometric mask onto a photosensitive material coating the sample in order to reveal a pattern. In this process, we use a viscous light-sensitive chemical substance called *photoresist* that can be spin-coated onto the sample substrates. It is subsequently baked, driving off the solvent in the photoresist to form a firm uniform coating. For “positive” photoresists, which we use most frequently, when this hardened material is exposed to an ultraviolet light source it becomes soluble in a chemical “developer.” On the other hand, unexposed regions are left untouched (“negative” photoresists work in the opposite manner). A pattern with fine features down to several microns can be achieved when the sample is pressed close against a glass plate with a chrome-plated pattern of the desired circuit geometry and is exposed to the ultraviolet light on the other side.

For photolithography, we use an ABM mask aligner that exposes the sample to light of wavelengths peaked near 405 and 365 nm. A weak vacuum holds down the sample to a stage that can be adjusted with a set of micrometers to achieve the necessary three cardinal-axis and rotational alignment with the glass photomask. In the corners and center of the photomask we incorporate Vernier marking features in order to align the top and bottom wiring layers with one another. Alignment markings are also included on the bottom wiring layer photomask for electron-beam lithography, described in the next section.

For high-quality lithography, it is essential to use very clean substrates during the photolithography process. In addition to performing all of the lithography steps in a class-100 cleanroom, we typically clean the bare Si substrates in an ultrasonic bath of acetone, isopropyl alcohol, and DI water for ten minutes each. The samples are subsequently blown

dry with a nitrogen gun. The positive photoresist that we typically use is called Microposit S1813 (hereafter referred to as S1813) and is spun onto the substrates at 5000 rpm for 50 seconds. It is then immediately baked at 110 °C for two minutes. The photoresist is exposed to an ultraviolet lamp on the mask aligner for 11 seconds. We configure the resist to have a slightly undercut edge profile using the following process: we immerse the exposed sample into chlorobenzene for five minutes, which acts to harden the top surface of the previously unexposed regions of photoresist, and blow dry with a nitrogen gun. Then, we immediately immerse the sample in a developer (called 352 solution) for 45 seconds, rinse in DI water for at least 30 seconds, and finally blow dry with a nitrogen gun. The regions that had already been exposed to the ultraviolet light are dissolved away in the developer.

The resulting photolithographically-defined pattern can act as a mask during sputtering. Metals deposited onto the surface of the sample adhere to the bare regions of the substrate,[†] while the material deposited on top of the photoresist is removed later using a *lift-off process*. During lift-off the sample is immersed in acetone and the hardened photoresist dissolves away along with the metal on top of it. The undercut profile of the resist previously mentioned is useful in obtaining a clean lift-off of the resist.

For photomasks with very small features of only a few microns, or with long thin wire lines, such as those used in the SQUID samples that will be discussed in Ch. 9, a few steps are modified in the photolithography process. After the same cleaning procedure the sample is baked in an oven at 110 °C for 15 minutes to remove any water on the surface of the substrate. Next, the sample is coated in an HMDS adhesion primer, which forms a hydrophobic surface that improves the wetting of the resist to the substrate surface. It is important to cover the

[†]Some materials such as Cu adhere poorly to Si, however we typically use Nb as the first sputtered layer, which does not suffer from that issue.

entire substrate and beyond, breaking the surface tension with the edge of the chip before spinning the sample at 5000 rpm for 50 seconds. This is immediately followed by the S1813 spin-coating process, again completely coating the entire substrate followed by the baking procedure.

Finally, we note that for the so-called “Anacostia” SQUID mask used for the samples in Ch. 9, which was designed by Eric Gingrich at Northrop Grumman Corporation, after applying the HMDS procedure the S1813 photoresist is only exposed for 6 seconds, followed by the treatment in the chlorobenzene for 5 minutes and developed in the 352 solution for only 35 seconds.

5.3 Electron-Beam Lithography

To define even smaller features with dimensions less than a few microns, a much more accurate form of lithography using electron beams is utilized. Analogous to photolithography, an electron-sensitive resist coated on a sample can be exposed to a fine electron beam which the user can trace or raster over an area to make a pattern of interest. We typically use the “negative” electron beam resist ma-N 2401, which when exposed to an electron beam is hardened, while the unexposed resist can be dissolved away in a chemical developer, revealing the pattern.

Several electron-beam lithography systems have been assembled and maintained in the Keck Microfabrication Facility at Michigan State University by Baokang Bi, who outfitted a commercial scanning electron microscope (SEM) with a beam blanker and computer control using the Nanometer Pattern Generation System (NPGS) software developed by Joe C. Nability.

During the course of the work presented in this thesis two different SEM systems were used for lithography: a legacy JEOL 840A (no longer in operation at Michigan State University) and a new Hitachi SU5000 Schottky Field Emission SEM. The latter SEM, which we also use for fine resolution imaging as shown in Fig. 5.2, can be programmed to pattern individual junctions of any desired shape using the following process.

The ma-N 2401 is spin-coated onto the substrates at 3000 rpm for 40 seconds and baked for two minutes at 90°C. After transferring the samples into the SEM, the beam current is set to 68 pA (using aperture 4, spot size 1, and intensity 30) and the z -height of the stage to a working distance of 15 mm. Next, the focus and stigmation needs to be properly adjusted, which is typically done in a non-critical region of the sample at high magnification *e.g.* 300,000X. Returning to a low magnification setting (200X), we locate the desired writing area on the sample by finding the electron-beam alignment markings present on the bottom wiring layer. So as to not expose the resist in the area of interest the electron beam is blocked by manipulating the beam blanker with the NPGS software, except for a small window of interest used to align the beam while at higher magnification (1000X). Next, at this magnification elliptical Josephson junction patterns with $\approx 0.5 \mu\text{m}^2$ area are written onto the resist on the bottom wiring layer via an area dose of $550 \mu\text{C}/\text{cm}^2$. In addition, a pinwheel or wagon wheel shaped feature is written off to the side using a line dose of $2.5 \text{ nC}/\text{cm}$, which is used to monitor the quality of the stigmation and focus adjustments previously mentioned. Finally, the samples are removed from the SEM and developed in AZ MIF solution for 30 seconds and washed with DI water for 30 seconds before being blown dry with a nitrogen gun.

The electron beam resist can be used as an ion mill mask, discussed in the next section. Afterward, a lift-off process is performed by immersing the samples in PG remover for at

least 15 minutes. Depending on the type of process, especially with Josephson junctions, the lift-off at this stage is the most unreliable part of the fabrication process. These issues will be discussed in more detail later.

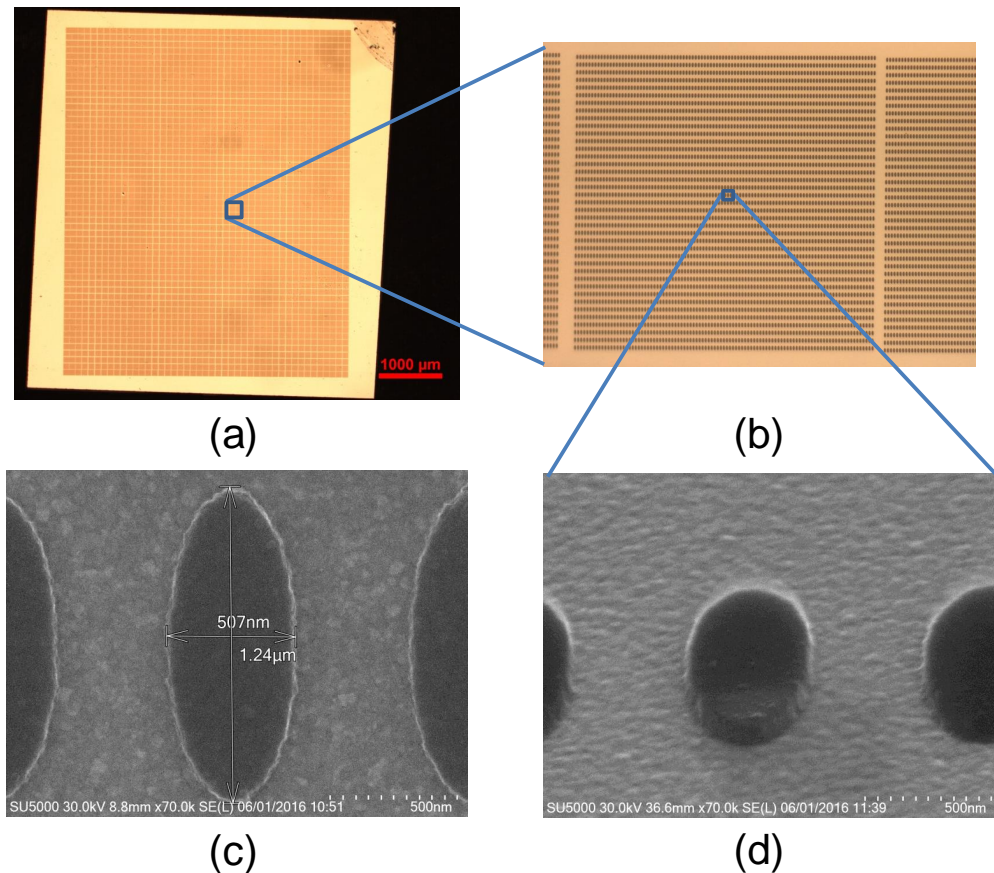


Figure 5.2: *Bit arrays written with electron-beam lithography.* We pattern sub-micron scale features for SQUID magnetometry or Josephson junction experiments using electron-beam lithography and the resist ma-N 2401. In the bottom two images we show images of $\approx 0.5 \mu\text{m}^2$ area elliptical bits taken with a scanning electron microscope. Images (c) and (d) are taken at 90 degrees and 60 degrees to the sample plane, respectively. For SQUID magnetometry experiments, we have developed a method to pattern $100 \mu\text{m} \times 100 \mu\text{m}$ sized arrays containing 99×39 bits, shown in (b), which are then repeatedly stamped over a $0.45 \text{ cm} \times 0.55 \text{ cm}$ area, shown in (a). The total number of bits is ≈ 9.5 million, necessary for an appreciable signal in the SQUID magnetometer.

Additionally, as shown in Fig. 5.2, Victor Aguilar and I developed a method for the patterning of large arrays of magnetic bits onto a single substrate. By programming the

stage of the Hitachi SU5000, one can repeatedly stamp a large pattern (e.g 99×39) of $0.5 \mu\text{m}^2$ area elliptical bits densely over the surface of a substrate. We showed that a $0.45 \text{ cm} \times 0.55 \text{ cm}$ area can be automated and written overnight in the SEM over the course of about 9 hours. The total number of bits is ≈ 9.5 million to achieve the necessary signal to noise for measurement and characterization in our SQUID magnetometer system, discussed later.

The spacing of the adjacent stamped patterns needs to account for the drift and back-action of the stage. The most severe of those effects can be prevented by ensuring that the motion of the stage does not reverse its direction by 180° at any point during the writing process. Additional developments are currently underway by Josh Willard to lessen the discrete edge effects caused by the rapid rastering of the electron beam, possibly by using a finer line spacing during the raster.

5.4 Ion Milling

Ion milling is a process used both for the etching of metal layers to define our Josephson junctions, or for cleaning the surface of our films prior to sputtering. Ion milling is essentially the opposite of sputtering, and consists of bombarding Argon atoms directly into the sample to remove atoms on the top surface. In the ion milling process, ionized Argon atoms are produced by passing a current through a Tungsten cathode filament and are then transported across the inner part of the ion mill (by the “beam voltage”) and then linearly accelerated out of the ion mill by a graphite grid (called the “accelerator”) that is biased with a negative voltage. Another filament, called the “neutralizer,” is held about a centimeter above the accelerator and injects electrons back into the outgoing ion beam to reduce spreading caused by the otherwise mutual repulsion of the ions. The emerging Argon atoms collide with the

Table 5.2: *Ion mill settings*. Depending on the purpose listed, we use one of two ion mills in the presence of Argon gas at a pressure of 1.9×10^{-4} Torr with the following settings. The voltage of the ion beam, and that applied to the accelerator and the anode (discharge) are V_{beam} , V_{acc} , and V_{dis} , respectively. The currents applied to the cathode and the neutralizer filaments are I_{beam} and I_{neut} , respectively.

Ion Mill	Purpose	V_{beam} (V)	V_{acc} (V)	V_{dis} (V)	I_{beam} (mA)	I_{neut} (mA)
3 in	Deep etching	300	-30	39	9.0	9.5
1 in	Pre-clean	175	-50	40	1.3	1.8

sample positioned directly above the ion mill and slowly remove the atoms on the top surface.

Similar to sputtering, the etching or “milling” rate depends on the chamber pressure, the cathode current, and the accelerator voltage, each of which we keep fixed run to run for our two ion mills. In the etching process, used for Josephson junction design, we use a large 3 inch ion mill from Commonwealth Scientific in a separate vacuum chamber, while for pre-cleaning prior to sputtering we use a smaller 1 inch ion mill, shown in Fig. 5.1. The various voltage and current settings for typical use are listed in Table 5.2.

The ion mill etching rate is highly material dependent. Beforehand, extensive testing was performed by myself and other group members over the years to accurately calibrate the etching rates of the various materials shown in Table 5.3, which are listed relative to the standard etching rate of Au. Those tests comprise of the following process:

1. Sputter many samples of a given material or a repeated multilayer of materials to a specific thickness.[†] Also, fabricate several independent control Au film samples in the same run.
2. For each of the samples, ion mill for a set time interval using the standard condi-

[†]We’ll often cap the test samples with a thin layer of Au to avoid the formation of an oxide after exposure to air. Oxides will typically mill much slower than the metals themselves, modifying the extracted etching rate.

Table 5.3: *Ion mill conversion factors for various materials.* The unitless inverse ratio of the etching rates for various materials to the standard rate of Au (*k*-factors). One can see, for example, that Nb etches ≈ 6.71 times slower in the ion mill than Au, whereas a material such as Cu etches only about twice as slowly as Au. The listed numbers are obtained using the calibration procedure described in the text. A repeated [Pd/Co] multilayer, used in Chs. 8–9, was also calibrated, with the individual layer thicknesses (in parentheses) listed in nanometers.

	Nb	Co	Ni	Ni ₈₁ Fe ₁₉	Ni ₆₅ Fe ₁₅ Co ₂₀	Cu	Au	Ru	Pd ₉₇ Fe ₃	[Pd(0.9)/Co(0.3)] _n
<i>k</i> -factor	6.71	3.5	3.905	2.695	3.64	1.9	1.0	3.5	1.89	1.63

tions listed in Table 5.2 to form a narrow series of channels, typically defined by a photolithographic ion mill mask.

3. Accurately measure the depth of the etched channel(s) using, for example, atomic force microscopy. Repeat for a number of samples, preferably some of which have been ion milled for different amounts of time (*e.g.* 1, 2, and 3 minutes).
4. From the measured depth and the known mill time, calculate the effective mill rate. Determine the conversion factor or “*k*-factor,” defined as the inverse ratio of the etching rate for a given material relative to that for Au.

Once all the “*k*-factors,” shown in Table 5.3, are known we can accurately ion mill down to a desired depth even for very complicated samples, such as Josephson junctions with a large number of layered materials. This is achieved by depositing Au onto a crystal film thickness monitor, placing it directly over the ion mill, and measuring the etching rate of Au. Then, we simply multiply the thickness of each layer in the sample of interest by the corresponding “*k*-factors,” and divide by the measured Au milling rate to determine the milling time. We typically measure the etching rate of Au with the film thickness monitor before and after the sample is ion milled and average those rates to improve the accuracy. Evidence of the precision of our milling process, even in complex samples, using this “on-

the-fly” measurement scheme can be obtained afterward by more accurate techniques such as Transmission Electron Microscopy (TEM), as shown in Chs. 6 and 8.

5.4.1 Ion Mill and Thermal Evaporation Chamber

The deposition chamber we use primarily for ion mill etching is equipped with a continuously operating turbomolecular pump (and a supporting mechanical pump) that allows us to reduce the chamber pressure to $\approx 2 \times 10^{-8}$ Torr. The primary volume is kept at high vacuum, while samples can be easily added or removed from the chamber via a load lock, a small volume that can be independently sealed, vented to atmosphere, loaded with a sample, and evacuated via a second mechanical pump. The sample can then be transferred into the primary chamber volume via a transfer arm, without adversely effecting the high vacuum of the system. In this manner, up to five samples can be transferred into the main chamber during a single run. Usually within an hour or two the turbomolecular pump will have the system back down at base pressure (2×10^{-8} Torr), so that the ion milling process previously described can begin. The vacuum chamber is equipped with the 3 inch ion mill and one Au sputtering gun, enabling us to perform the ion mill calibration scheme. The chamber was designed by William Pratt and has been modified and maintained over the years by Reza Loloee.

In addition, for the fabrication of Josephson junctions discussed further in the next section, the chamber also allows us to thermally evaporate SiO_x onto the samples, which we can immediately deposit after ion milling to electrically isolate the circuit of interest and protect the sidewalls of the remaining material. The thermal evaporation process simply amounts to passing a current through a small baffle boat filled with SiO_x pellets. When the SiO_x pellets get hot enough to sublimate a vapor of the oxide is deposited on to the samples positioned



Figure 5.3: *The ion milling and thermal evaporation vacuum chamber.* The vertical transfer arm (top) is attached to a small load lock used for transferring samples in and out of the system. The main volume of the chamber (bottom) contains a 3 in ion mill, a Au sputtering gun, and a baffle boat for SiO_x thermal evaporation (not shown). The turbomolecular pump and the main gate valve is also visible (left).

directly above the boat. The deposition rate can be actively monitored with a film thickness monitor, whose tooling factor adjusts for the throw distance of SiO_x particles from the boat, to reflect the true deposition rate. The sample is rotated back and forth during the SiO_x deposition to help with film uniformity.

5.5 Josephson Junction Sample Fabrication

In this section, we give a brief outline of our scheme for fabricating Josephson junctions. The fabrication details for each specific experiment are provided in Chs. 6–9.

The Josephson junction fabrication proceeds as follows. Photolithography is first used to define the bottom wiring layer of a circuit. Then, as shown in Fig. 5.4, sputtering is used to deposit the base superconducting electrode followed by a series of normal metal and or ferromagnetic layers. The last layer is typically a thin film of Au to prevent oxidation. After removing the photoresist with a liftoff process, a second series of electron-sensitive negative resist is spun and baked onto the sample. After being exposed to an electron beam in the pattern of the desired Josephson junction (e.g. a sub-micron ellipse with a given aspect ratio) the sample is developed, revealing a lithographic mask that protects the material below. Next, ion milling is used to etch down through the ferromagnetic materials of interest, followed by an *in situ* deposition of SiO_x .

As previously mentioned, the lift-off process following the SiO_x deposition is a critical step. We have found that excessive exposure to the ion mill or the thermal evaporation processes can cause heat and damage to photoresist or electron beam resist. The edges of the resist can begin to droop, melt, or disturb the desired undercut profile, and sometimes prevent the resist from lifting off at all. As a general rule of thumb we never ion mill or deposit SiO_x onto a sample for more than 120 seconds at a time, instead we break up the process into several steps with cooldown stages if necessary.

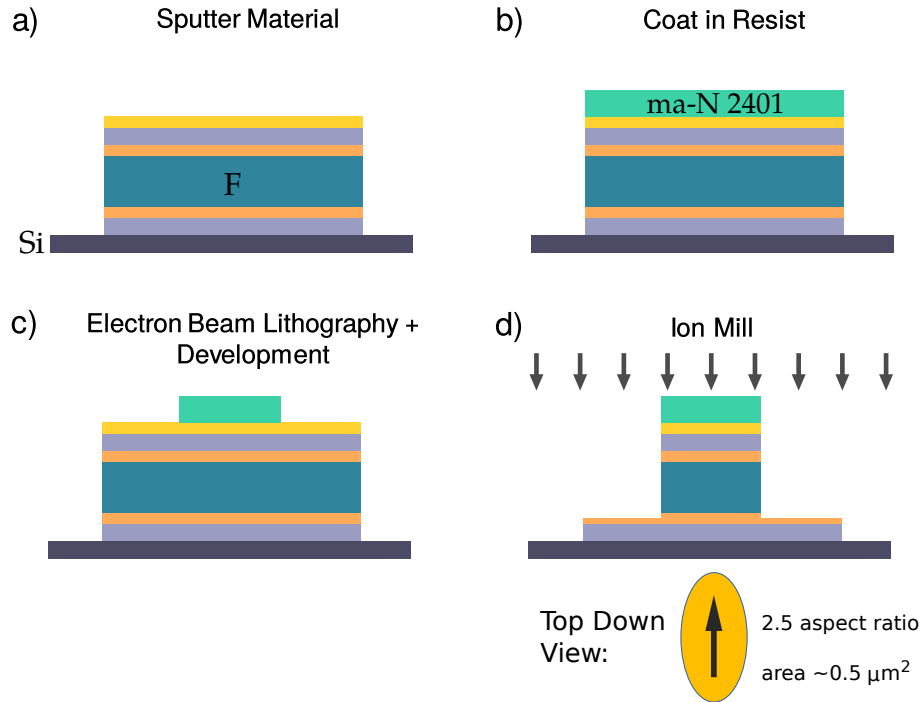


Figure 5.4: *Josephson junction fabrication steps, part 1.* (a) Sputtering is used to deposit the superconducting base layer (violet), the ferromagnetic layers (blue), and the normal metal spacers (orange and gold) onto a Si substrate (dark blue). (b) A negative tone resist ma-N 2401 (green) is spun onto the sample and baked. (c) The resist is exposed to an electron beam and after a subsequent development process forms a resistant cap in the pattern of the desired Josephson junction. (d) Ion milling etches back the metal layers that are not covered by the resist. We ion mill completely through the ferromagnetic layers to form elliptical nanomagnets, utilizing shape anisotropy to orient the magnetization along a preferred axis. Prior to the first metalization step (not shown) the bottom lead circuit geometry is patterned with photolithography (similar to the process shown in Fig. 5.5 (h)-(i)).

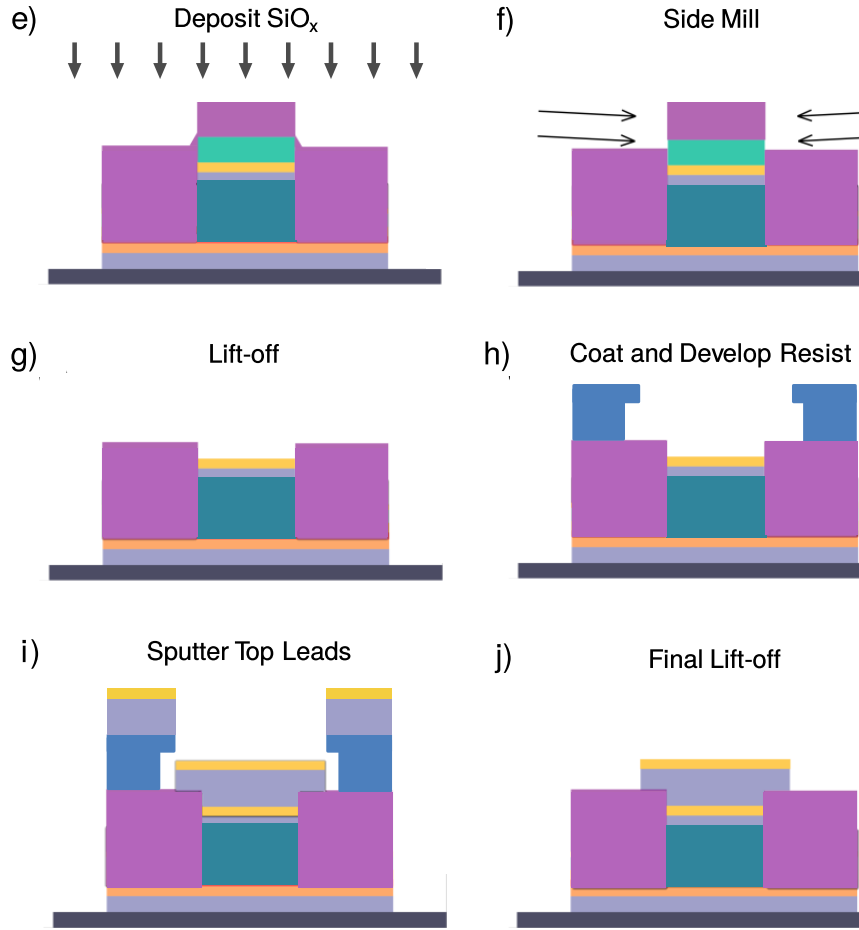


Figure 5.5: *Josephson junction fabrication steps, part 2.* Following the processes shown in Fig. 5.4, the nanopillar is electrically isolated (e) with a thermally evaporated layer of SiO_x . (f) To break through the sidewall of the nanopillar we rotate the sample and ion mill at grazing angle (3°) of incidence. (g) That allows the chemical liftoff-process to access and dissolve the resist. (h) The top lead circuit geometry is patterned with photolithography using a positive tone resist (S1813), that is hardened in chlorobenzene and developed to create an undercut in the resist profile. (i) Sputtering deposition is used to deposit the top superconducting electrode and Au protective cap. (j) The resist is lifted-off chemically and the completed ferromagnetic Josephson junction is ready for measurement.

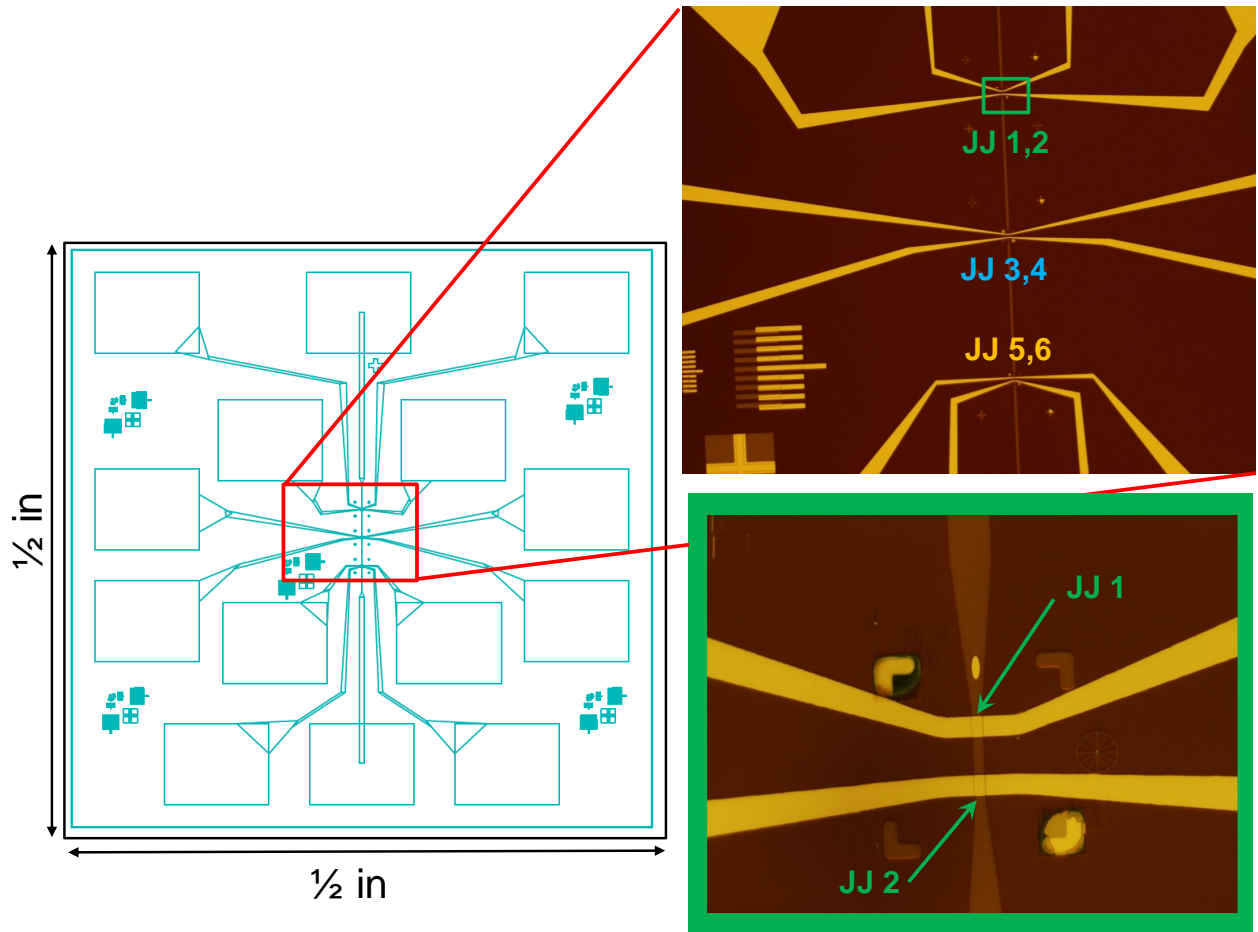


Figure 5.6: *Josephson junction sample design and images.* The left sketch shows an overlay of the two photolithography masks used to define the bottom and top leads of the Josephson junction circuit. The bottom lead consists only of the vertical line down the center of the image, the two rectangular contact pads attached to it, and several alignment marks that are not electrically connected. The top leads consist of all the lines with a horizontal component and the associated contact pads. The mask can accommodate up to six independent Josephson junctions, which reside at the intersection of the two lead patterns (JJ 1-6). The optical images on the right show magnified views (red and green boxes) of a finished sample made with the mask. In those images, the Au of the top leads stands out as a bright yellow, the surrounding SiO_x layer is reddish brown in color (at this thickness of 50 nm), and the bottom leads underneath it appear light brown. In the highest magnification image in the lower right (green box) one can see the L-shaped alignment marks used for electron-beam lithography. In that image the large ellipse is written above JJ-1 to help tell if the electron-beam resist lifted off properly. The total chip size is $0.5 \times 0.5 \text{ in}^2$.

To improve the possibility of a successful lift-off, next we perform two additional ion milling steps (2 minutes each) at a grazing angle of incidence of 3° to the sample plane,

as shown in Fig. 5.5. The purpose of this “side-mill” step is to use the ion mill to break through any SiO_x that may have been deposited onto the sidewall of the electron-beam resist (or metal redeposited during the ion milling process). Breaking through the side wall allows the lift-off solution to dissolve the resist. The circuit geometry of the underlying bottom wiring layer must be considered when deciding the direction to side-mill the samples from. Generally, one should avoid side-milling at 90° to edges in the bottom wiring layer because it can cause those layers to become electrically shorted to overlapping regions of the top electrode (sputtered later). If the lift-off process fails, one can very carefully swipe the junction area a few times with a cotton Q-tip while immersed in the lift-off solution. While this procedure is not “ideal,” the mechanical force from the Q-tip is usually enough to break through the side-wall, allowing for a successful lift-off and saving an otherwise ruined sample.

Finally, as shown in Fig. 5.5, a second photolithography process is used as a pattern for the top wiring layer. Prior to depositing the top electrode, any residual hydrocarbons are removed from the surface of the junctions using a commercial March3 oxygen plasma etcher. After inserting the samples into the sputtering chamber, we use the small 1 cm ion mill to clean the top surface of the samples again immediately before sputtering the top superconducting electrode. A final lift-off process removes the photomask, leaving a finished sample. To fabricate one full set of samples (16 substrates) the entire process usually takes between 2-3 weeks.

In Fig. 5.6 we show images from an optical microscope of a completed sample containing six Josephson junctions, alongside the superimposed outline of the mask layout for both the top and the bottom electrodes. In Fig. 5.6, some of the Vernier and electron-beam alignment markings used in both photo and electron-beam lithography are visible.

5.6 Measurement Probes and Low Noise rf SQUID Electronics

Our samples are typically measured at 4.2 K by immersing the sample into a Dewar of liquid helium using low-temperature measurement probes built by William Pratt. The simplest of these probes can be used to make four-terminal measurements of the I - V characteristic curves of our Josephson junction samples. The workhorse probe used for most of the measurements in this thesis is called Quick Dipper I (QD-I) and is equipped with several additional improvements. To measure extremely small voltages down to 10's of pV, the probe contains a rf SQUID comparator circuit, shown in Fig. 5.7.

The scheme works as follows: the sample represented by the resistor R_s is connected in a loop with an inductor and a reference resistor, $R_{\text{ref}} = 126 \mu\Omega$, shown at the bottom of Fig. 5.7. That loop is inductively coupled through a transformer to an rf SQUID, which consists of a single Josephson junction in a superconducting loop. The goal is to try and sense a small change in the voltage of the sample. For example, if the sample is a Josephson junction (or a DC SQUID) it will begin to develop a voltage when a current comparable to the sample's critical current is driven through it. A dynamic change in the voltage across the sample will induce a current in the rf SQUID loop. The resulting flux change in the rf SQUID loop is detected by the SQUID electronics attached to the top of the probe outside the Dewar. The SQUID electronics system is a commercial Quantum Design 2010 SQUID control circuit and amplifier. After sensing a change in the rf SQUID, the SQUID electronics system outputs a feedback voltage V_{out} which is reduced by a voltage divider composed of R_{ref} and a feedback resistor $R_{\text{FB}} = 2 \text{ k}\Omega$. The feedback in the SQUID control circuit acts to maintain a voltage across R_{ref} that matches the voltage across R_s . Since the voltage across the sample and reference resistor is balanced, we can infer the voltage across the sample

using the simple formula for a voltage divider with the feedback and reference resistors:[†]

$$V_s = V_{\text{out}} \left(\frac{R_{\text{ref}}}{R_{\text{ref}} + R_{\text{FB}}} \right). \quad (5.1)$$

Plugging in the values for R_{ref} and R_{FB} , we see that V_s can be very small in principle even for appreciable V_{out} values (the gain is on the order of 10^7), while the rf SQUID is sensitive to changes in flux on the order of $\Phi_0 = 2.067 \times 10^{-15}$ Wb. This causes the system to have extremely good rms voltage noise, which we have measured to be approximately 6 pV per 10 power line cycles.

QD-I has several other features. In addition to the current and voltage wiring leads, the probe contains several extra sets of wire leads. Those leads can be used, for example, to control an on-chip flux line for SQUID experiments as done in Chs. 7 and 9.

Furthermore, around the sample, at the end of the probe, there is a solenoid coil that can be used to apply a uniform magnetic field parallel to the plane of the sample. To achieve a very stable magnetic field value, the solenoid is made of superconducting wire and is shorted by a controllable superconducting *persistent switch*. If a current is present in the solenoid and the persistent switch is closed, the supercurrent will “persist” in the loop made by the short across the solenoid, producing a very stable magnetic field. To change the value of the magnetic field, a resistive heater nearby the persistent switch can warm the persistent switch and drive it into the normal state, breaking the short. The circuit to control the current supplied to the solenoid coil, the persistent switch heater, the current supplied to the sample, and the voltage detected from the SQUID electronics is all automated using the LabVIEW package. Significant improvements to the computer control software were

[†]In Eq. (5.1) we have neglected the ≈ 0.06 % correction to V_s due to the finite open-loop gain of the feedback circuit.

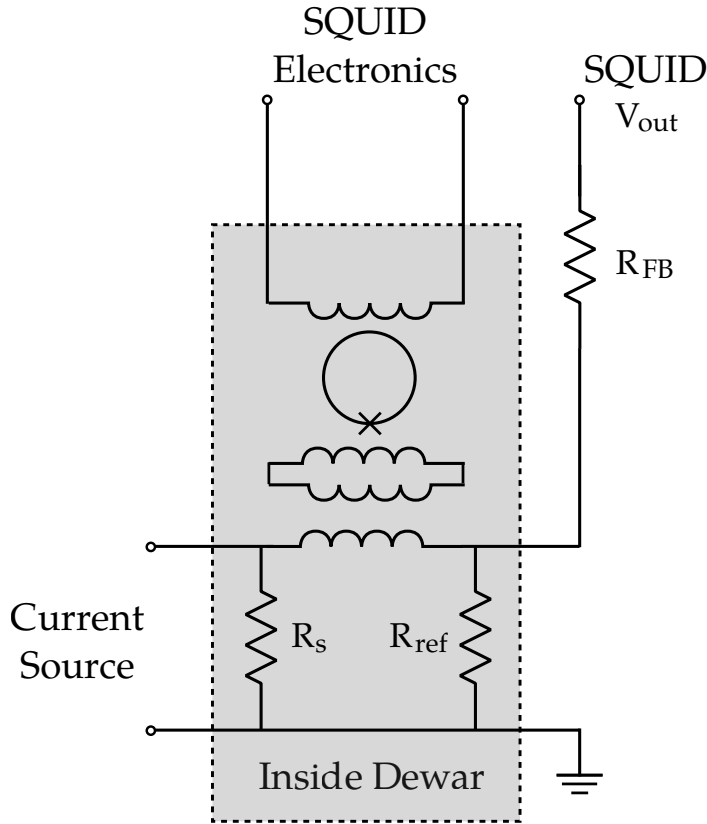


Figure 5.7: *rf-SQUID comparator measurement circuit.* An rf SQUID, composed of a single Josephson junction is inductively coupled through a transformer to an LC circuit that contains the sample (R_s) and a reference resistor R_{ref} . Commercial SQUID electronics, described in the text sense the state of the rf SQUID and provide a voltage V_{out} passed through a feedback resistor R_{FB} . The system allows for large amplification of very small voltage changes in the sample, with extremely low rms voltage noise.

developed by Victor Aguilar, which enabled us to measure I - V curves at a much faster rate.

Victor also improved the code to allowed us to iterate various magnetic field sweep sequences.

5.7 SQUID Magnetometry

We used two different SQUID magnetometers for our measurements. Both are Magnetic Property Measurement Systems (MPMS) built by Quantum design, one an older model built in the 1980s and the other a more state of the art system, the MPMS3. The MPMS3 can measure over temperature ranges of 1.8 - 400 K and is equipped with a magnet capable of

generating fields up to 7 T, with accuracy of ± 0.005 mT.

In addition to acting as a DC SQUID magnetometer, the MPMS3 can also act as a Vibrating Sample Magnetometer (VSM), in which the sample is mechanically vibrated in a field while measuring the induced voltage in a pickup coil that is proportional to (magnetic moment) \times (vibration frequency) \times (vibration amplitude). This method is combined with SQUID magnetometry to achieve more sensitive measurements.

As previously shown in Fig. 5.2, we have developed a process for patterning arrays of nanomagnets using electron-beam lithography for magnetic characterization in the SQUID magnetometer. As opposed to measuring large continuous films of various magnetic materials whose magnetic behavior is dominated by domain wall motion, the magnetic bit arrays will allow us to better characterize the behavior of magnetic bits of the actual dimensions that are used in our Josephson junction and SQUID experiments. This allows us to observe the spread in the magnetic switching and quantify the effects of shape anisotropy.

Chapter 6

S/F/S Josephson Junctions: Materials

Characterization

Josephson junctions containing ferromagnetic materials (*S/F/S* junctions) have been under intense study for the past 15 years. As discussed in Ch. 4, the experimental breakthrough that triggered such intense interest was the demonstration that the ground-state phase difference across the junction can be either 0 or π , depending on the thickness of the ferromagnetic layer(s) in the junction [65, 68]. That result has been confirmed by numerous groups since the initial discovery, using a wide variety of weak and strong ferromagnetic materials [69–75]. In this spirit, with this chapter we present four separate experimental studies of Nb-based micron-scale elliptically-shaped Josephson junctions containing central ferromagnetic layer of either $\text{Ni}_{65}\text{Fe}_{15}\text{Co}_{20}$, Py (the alloy $\text{Ni}_{81}\text{Fe}_{19}$), $\text{Pd}_{97}\text{Fe}_3$, and Ni. Throughout this chapter, we'll examine the comparative advantages and disadvantages that these materials offer as potential components in cryogenic memory devices. This chapter encompasses Refs. [19, 20] where these results were first published, including some additional findings.

Before using a new magnetic material in a memory device, one would like to know how it behaves by itself inside a Josephson junction. Most importantly, at what *F*-layer thickness, d_F , does the junction transition from the 0 state to the π state? Secondly, how does I_c decay as d_F increases? Thirdly, how much does the field generated by the magnetization affect the junction properties? And lastly, does the material exhibit single-domain switching behavior when it is patterned into a micron-scale elliptical nanomagnet? All of those questions can

be answered by fabricating and measuring micron-scale $S/F/S$ junctions containing only a single magnetic layer [77].

By applying an external magnetic field, the critical current of the junctions are found to follow characteristic Fraunhofer patterns. The high quality of the Fraunhofer patterns typically enables us to extract the maximum value of the critical current even when the peak is shifted significantly outside the range of the data due to the magnetic moment of the ferromagnetic layer. Indeed, we observe that the maximum value of the critical current oscillates as a function of the ferromagnetic barrier thickness, indicating transitions in the phase difference across the junction between values of zero and π . We compare the data to previous work and to models of the 0 - π transitions based on existing theories.

6.1 Role of π -Junctions in Cryogenic Memory

Josephson junctions that exhibit a ground-state phase shift of π for certain ranges of ferromagnetic layer thickness are of considerable interest for the development of practical cryogenic memory and superconducting qubits. There have been several proposals to use π -junctions as new components in either classical or quantum information processing circuits [110–116]. Our current work in this area focuses on the development of cryogenic random access memory [18, 77].

Numerous ideas have been presented in the literature regarding how $S/F/S$ junctions might be used as practical memory devices [12, 14, 16, 17, 22, 117, 118]. The ferromagnetic layer influences the properties of the junction both through the magnetic field and the exchange field it generates, and ideas have been presented using either of those mechanisms. In addition, either the critical current magnitude, I_c , or the ground-state phase difference

across the junction, ϕ , can be used as the physical quantity associated with information storage. Without trying to summarize the whole field, we can nonetheless make two general observations:

1. Proposals that rely on the internal magnetic field of the junction tend to become less viable as junction size decreases, since the relevant physical parameter defining the effect of the field is the magnetic flux, Φ , threading the junction area. If the junction area is reduced to the point where $\Phi \ll \Phi_0 = h/2e = 2.07 \times 10^{-15} \text{ Tm}^2$, then the magnetic field has negligible effect on the junction properties. For that reason, we have chosen to emphasize the effect of the exchange field in our work.
2. Proposals that rely on the magnitude of I_c invariably require that the $S/F/S$ junction switch from the zero-voltage state into the voltage state when the memory is read. That switching process takes a time of order $\tau_{\text{switch}} \approx \hbar/(eI_cR_N)$, where R_N is the junction resistance in the voltage state. For standard $S/F/S$ junctions, τ_{switch} is much too long to be useful for memory applications. One can shorten τ_{switch} somewhat by increasing R_N via the introduction of an insulating barrier to make an $S/I/F/S$ junction [14, 72]. Suppression of I_c by the insulating layer can be mitigated by adding a thin auxiliary nearly-superconducting (s) layer, to form an $S/I/s/F/S$ junction with very large values of I_cR_N [15, 119–121].

An alternative scheme, proposed by workers at Northrop Grumman Corporation, shown in Fig. 6.1, envisions a memory cell consisting of a SQUID loop that contains a phase-controllable Josephson junction and two conventional $S/I/S$ junctions with much smaller I_c 's [22, 23]. The critical current of the SQUID loop is determined by the phase state of the controllable junction, either 0 or π , which correspond to the logical 0 or 1 of the memory.

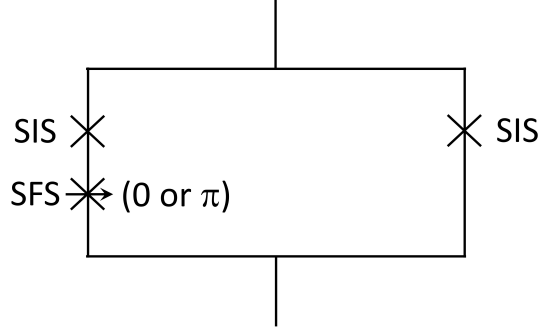


Figure 6.1: *Cryogenic phase-sensitive memory cell proposed by Northrop Grumman Corporation.* The memory cell is composed of a phase-controllable ferromagnetic Josephson junction together with two $S/I/S$ junctions in a SQUID loop. The critical current of the SQUID will oscillate as a function of the flux threading the loop. Depending on the state of the phase-controllable junction, it will contribute either an additional 0 or π -phase into the loop, resulting in a larger or smaller total critical current, respectively, in the SQUID. The $S/I/S$ junctions are added to facilitate a fast switching time (set by their large $I_c R_N$ product) while reading out the state of the memory. Figure taken from [18].

During the read operation, only the $S/I/S$ junctions may switch into the voltage state, providing a fast τ_{switch} , while the controllable junction remains in the superconducting state. As a result, high $I_c R_N$ is not a critical requirement for the controllable junction in the Northrop Grumman design. This is the memory design we are currently pursuing.

What we want, then, is a Josephson junction whose ground-state phase difference can be controllably switched between the 0 and π states. It is advantageous that one or both of the nanomagnets in such a junction be single-domain, so that the magnetizations are uniform and magnetic switching is clean and reproducible. One method of accomplishing these goals is to make a junction containing a “spin valve”, i.e. two F layers whose relative magnetization directions can be switched between parallel and antiparallel [12,16,17]. These type of memory devices contain a spin valve with one “hard” magnetic layer and one controllable “soft” layer.

We demonstrated such a controllable 0 - π junction, which is the subject of Ch. 7, using Ni and $\text{Ni}_{81}\text{Fe}_{19}$ (referred to as NiFe or Py) as the two ferromagnetic materials [18]. Thin

Ni films are magnetically “hard”, whereas NiFe is “soft”, hence it was possible to reverse the magnetization direction of the NiFe without changing that of the Ni. However, due to the poor magnetic properties of Ni, discussed later in this chapter, we have been searching for a material to replace it as the hard magnetic layer. In addition, we have been exploring other possible alternatives for the soft layer as well.

6.2 Sample Fabrication and Characterization

Our $S/F/S$ Josephson junctions are fabricated using high-vacuum sputtering deposition on 0.5×0.5 in² silicon chips. The geometry of the bottom leads was defined via optical photolithography and the positive photoresist S1813, using the liftoff process.

Before the sputtering deposition, the chamber was baked for eight hours and reduced to a base pressure of 2×10^{-8} Torr with a cryopump. The chamber was then cooled by circulating liquid nitrogen through a Meissner trap to reduce the partial pressure of water in the chamber to $< 3 \times 10^{-9}$ Torr as confirmed by an *in-situ* residual gas analyzer. The films were deposited via dc sputtering in an Argon plasma with pressure 1.3×10^{-3} Torr. During deposition the sample temperature was held between -30°C and -20°C measured with a thermocouple affixed to the back of one of the substrates.

In a single run, a rotating sample plate and shutter system passes up to 16 chips over a sequence of triode sputtering guns containing 2.25-inch diameter targets of Nb, Al, NiFe, NiFeCo, PdFe or Ni and magnetron guns containing 1-inch diameter targets of Au and Cu. The thicknesses of the various deposited materials were controlled by measuring the deposition rates (accurate to $\pm 0.1/\text{s}$) using a crystal film thickness monitor and a computer controlled stepper motor that operates the position of the shutter and sample plate.

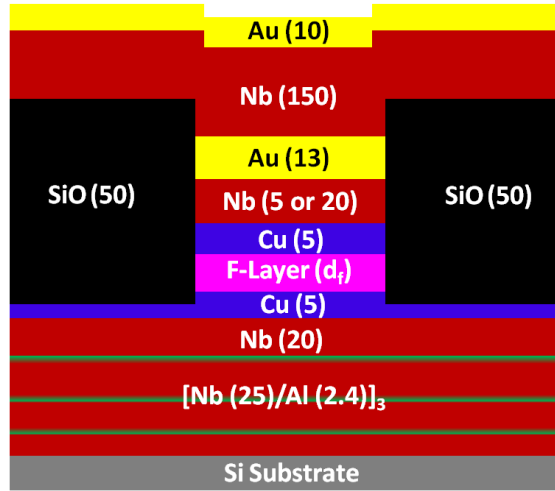


Figure 6.2: A schematic representation of the cross-sectional structure of our $S/F/S$ Josephson junctions. The F layer is either $\text{Ni}_{65}\text{Fe}_{15}\text{Co}_{20}$, $\text{Ni}_{81}\text{Fe}_{19}$, $\text{Pd}_{97}\text{Fe}_3$, or Ni . The thickness d_F ranges from 0.8 to 3.8 nm for the $\text{Ni}_{65}\text{Fe}_{15}\text{Co}_{20}$, $\text{Ni}_{81}\text{Fe}_{19}$, and Ni samples. The much weaker ferromagnet, $\text{Pd}_{97}\text{Fe}_3$, is thicker, ranging from 9 to 36 nm. The ferromagnets are grown on a smooth superconducting Nb/Al base electrode, set between Cu spacer layers. The lateral shape of the junctions are elliptical with aspect ratio of 2.5 and area of either 0.1, 0.25 or 0.5 μm^2 . The patterned region is isolated by SiO. All thicknesses listed in nm. Figure taken from [19].

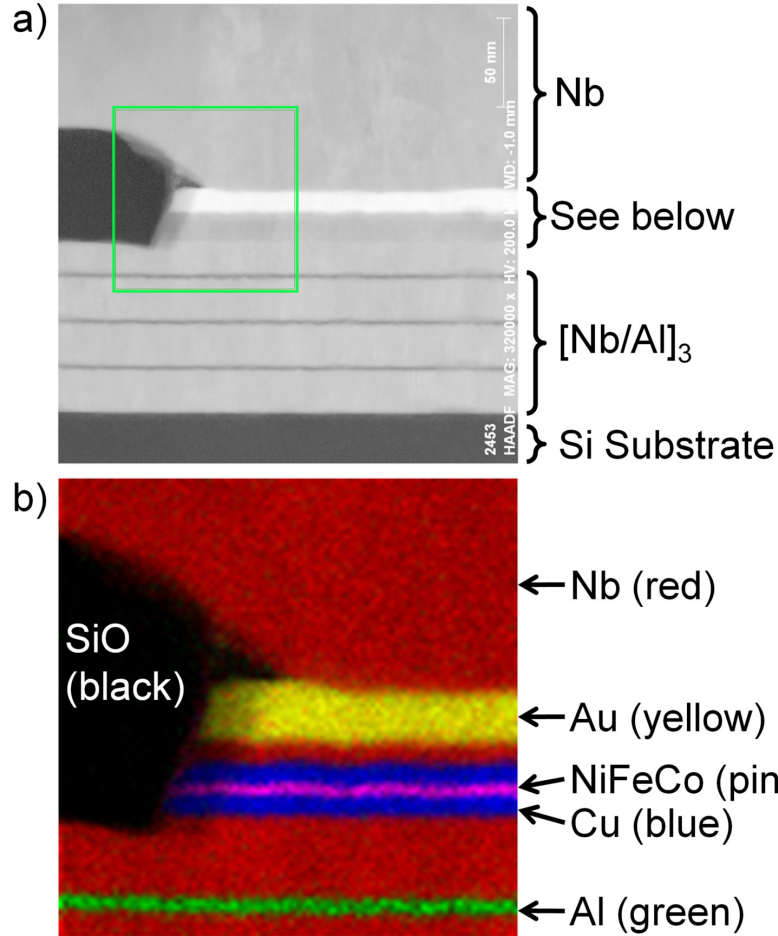


Figure 6.3: *Cross-sections through the center of our S/F/S Josephson junctions prepared with focused ion beam (FIB) milling and imaged with Scanning Transmission Electron Microscopy (STEM) to validate the fabrication process. In (a) the STEM image shows where our [Nb/Al] bottom electrode meets the left edge of the patterned junction area and SiO barrier. Energy dispersive x-ray spectroscopy (EDX) was used to map out the elemental composition of the individual layers within. In (b) we show the EDX analysis for the region outlined by the green square, which clearly shows a continuous NiFeCo layer ($d_F=1.6$ nm). Figure taken from [19], courtesy of P. Kotula and N. Missert, Sandia National Laboratory.*

The bottom wiring layer, which was deposited without breaking vacuum, consists of the sequence $[\text{Nb}(25)/\text{Al}(2.4)]_3/\text{Nb}(20)/\text{Cu}(5)/F(d_F)/\text{Cu}(5)/\text{Nb}(5 \text{ or } 20)/\text{Au}(10)$, with thicknesses given in nanometers. A schematic of the sample structure is shown in Fig. 6.2.

In order to verify the fabrication process, for the junctions containing NiFeCo, cross-sectional areas of the junctions were investigated by high-resolution scanning transmission electron microscopy (STEM) and energy dispersive x-ray spectroscopy (EDX). Since we do not have these capabilities at Michigan State University, we sent samples to our collaborators Paul Kotula and Nancy Missert at Sandia National Laboratories to help us with the STEM preparation and imaging.

The cross-sections were prepared using a FEI Helios focused ion beam (FIB) with a Ga ion source, and transferred to a Ti grid for imaging in a FEI Titan G2 80-200 aberration-corrected STEM operated at 200kV and equipped with four silicon drift X-ray detectors. The high-angle annular dark field STEM image in Fig. 6.3(a) shows the left hand side of one of the NiFeCo junction stacks.

To achieve quality magnetic switching it is crucial to grow the ferromagnets on a smooth underlayer. The low surface roughness of the $[\text{Nb}/\text{Al}]$ multilayer [122–124] provides a smooth template for subsequent growth of the Cu spacer and ferromagnetic layer, where the Al is thin enough to be superconducting through the proximity effect with Nb. We independently measured the roughness of the $[\text{Nb}/\text{Al}]$ multilayer to be $\approx 2.3 \text{ \AA}$ using atomic force microscopy (AFM), smoother than a single Nb(100) film ($> 5 \text{ \AA}$). Significant diffusion of Al along Nb grain boundaries was not observed. The superconducting transition temperature of $[\text{Nb}(25)/\text{Al}(2.4)]_3/\text{Nb}(20)$ films, was measured independently with a SQUID magnetometer to be 8.0 K, well above the temperature at which we measure our $S/F/S$ junctions (4.2 K).

Due to the crystal lattice mismatch between the fcc ferromagnetic materials and the

bcc Nb we add a 5-nm Cu spacer on either side of the F layer. STEM diffraction patterns show that the Cu layer grows with a [111] orientation on Nb [011]. Grains with favorable orientation relative to the beam direction show lattice fringes extending through the entire Cu/ferromagnetic layer/Cu thickness. In comparison to films grown on only Nb the spacer improves the magnetic properties of the F layers: decreasing the coercive field, and increasing the sharpness of hysteresis loops. Also, smooth normal metal spacer layers will be used in cryogenic memory to magnetically decouple the multiple F layers.

EDX phase maps were created by performing a multivariate statistical analysis of the spectra from each individual pixel, and color-coding pixels containing the same spectrum [125]. The phase map shown in Fig. 2b corresponds to the area within the green square in Fig. 2a. The 1.6 nm NiFeCo layer is clearly uniform and continuous, consistent with the magnetic behavior discussed below.

To set the direction of the magnetocrystalline anisotropy of the ferromagnetic alloys, the NiFeCo and PdFe samples were sputtered in a magnetic-field of ≈ 80 mT (whose direction points along what will become the major axis of our elliptical junctions) generated by small NdFeB magnets affixed directly on the back of the substrates. The NiFe and Ni samples, made in separate sputtering runs, were sputtered in a magnetic-field of ≈ 50 mT. Finally the samples were capped with a thin layer of Nb and Au to prevent oxidation.

The junctions were patterned by electron-beam lithography followed by ion milling in Argon. We use the negative e-beam resist ma-N2401 as the ion mill mask. The junctions are elliptical in shape with an aspect ratio of 2.5 and area of either 0.1, 0.25 or 0.5 μm^2 , all sufficiently small to ensure that the magnetic layer is single domain (not including the junctions containing Ni). Elliptically-shaped junctions have the advantages that the modulation of the critical current through the junction versus the applied magnetic field, known

as a Fraunhofer pattern, follows an analytical formula while the (small) demagnetizing field is nearly uniform when the magnetization is uniform.[†]

Outside the mask region, we ion milled through the capping layer, the F layer, and nominally half-way into the underlying Cu spacer layer. Figure 6.3 confirms our patterning of the F layer, though it is clear this sample was slightly over-milled; the step edge extends through the second Cu layer and just into the underlying Nb. After ion milling, a 50 nm thick SiO layer was deposited by thermal evaporation to electrically isolate the junction and the bottom wiring layer from the top wiring layer. During thermal evaporation the sample was rotated to improve the uniformity of the oxide and reduce pinhole formation.

To prevent the e-beam resist from over-heating during the ion milling and SiO deposition the back of the substrate is placed against a Cu heatsink with a small drop of vacuum grease or silver paste to improve thermal contact. A capping layer containing 20 nm Nb was used in some of the NiFe-based samples, but was later reduced to 5 nm in the remaining NiFe and NiFeCo-based samples for two main reasons: i) During ion milling a veil of Nb can be backspattered onto the edge of the e-beam resist, preventing the e-beam resist from lifting-off properly, or at all. Reducing the Nb thickness reduces the extent of the veil. ii) Since Nb has the slowest etching rate of all our materials, reducing the Nb thickness drastically reduces the total time required to ion mill. Reducing the Nb thickness in the capping later improved our lift-off success rate, likely due to less damage and distortion of the resist under the heat of the ion mill and during SiO deposition.

Finally, the top Nb wiring layer was patterned using the same photolithography and lift-off process as the bottom leads. Residual photoresist on the surface is cleaned with oxygen

[†]Strictly speaking, the field is uniform only inside a uniformly magnetized ellipsoid. Because the elliptical nanomagnets in our junctions are very thin, there is very little difference between an ellipse and an ellipsoid.

plasma etching followed by *in-situ* ion milling in which 2 nm of the top Au surface is removed prior to sputtering. We deposited top leads of Nb(150 nm)/Au(10 nm), ending with the Au to prevent oxidation.

6.3 Critical Current Oscillations of Josephson Junctions

6.3.1 Junctions Containing $\text{Ni}_{65}\text{Fe}_{15}\text{Co}_{20}$

The alloy $\text{Ni}_{65}\text{Fe}_{15}\text{Co}_{20}$ is a promising candidate for the “hard layer”: like NiFe, it has a small magneto-crystalline anisotropy whose direction can be set by depositing the material in the presence of a magnetic field, but its anisotropy is somewhat larger than that of NiFe. Using NiFeCo as the hard layer should allow us to use initialization fields of only a few tens of mT.

First we describe the measurement scheme in detail for the junctions containing NiFeCo, but the process is similar for all of the $S/F/S$ samples that follow in this chapter. Each device was connected to the wire leads of a dip-stick probe with pressed indium. The samples were immersed at 4.2 K in a liquid-He dewar outfitted with a Cryoperm magnetic shield and placed inside a shielded room to reduce noise from external sources of electromagnetic radiation. The dipping probe is equipped with a superconducting solenoid used to apply uniform magnetic fields over a range of -60 to 60 mT along the long-axis of the elliptical junctions in the plane of the sample. The current-voltage characteristics of the junctions were measured at 4.2 K in a four-terminal configuration using one or both of the following methods: 1) a Yokogawa current source provides a bias current to the Josephson junction while voltage measurements were made with a Keysight nanovoltmeter or 2) a commercial Quantum Design rf SQUID in a self-balancing potentiometer comparator circuit (described in Ch. 5) measures the voltage

across the junction, while the measurement current is provided by a battery-powered ultra-low noise programmable current source [126]. Data taken independently from the two setups agree with one another, however the rf SQUID comparator scheme has lower RMS voltage noise of only 6 pV compared to 11 nV for the commercial nanovoltmeter, with both systems measuring over 10 power line cycles. Typical I - V curves, shown in Figs. 6.4 and 6.5, have the expected behavior of overdamped Josephson junctions [127]. Figure 6.4 shows how the I - V curve shape changes while being measured in applied magnetic fields ranging from 0-50 mT. The entire data collection process is automated using the LabVIEW software package.

The sample resistance in the normal state R_N was determined by the slope of the linear region of the I - V curve when $|I| \gg I_c$. While the sensitivity of the rf SQUID measurement system allows us to measure junctions with small I_c , it operates only over a restricted voltage range. Thus, depending on the resistance of the sample, one may be limited in the extent to which the linear tail of the I - V curve can be measured. In these cases, independent measurements using both measurement schemes are necessary to accurately determine both I_c and R_N . Measurements of the area-resistance product in the normal state yield consistent values of $AR_N = 5\text{-}10 \text{ f}\Omega\text{-m}^2$ for junctions of different areas – an indicator of the reproducible high quality interfaces. This total specific resistance is close to twice the Nb/F interface resistance, determined in separate current-perpendicular-to-plane giant-magnetoresistance studies [128].

The critical current I_c was extracted by fitting the I - V curves to a square root function of the form,

$$V = R_N \sqrt{I^2 - I_c^2}, \quad I \geq I_c. \quad (6.1)$$

We occasionally observe that I_c is slightly different in the positive and negative current

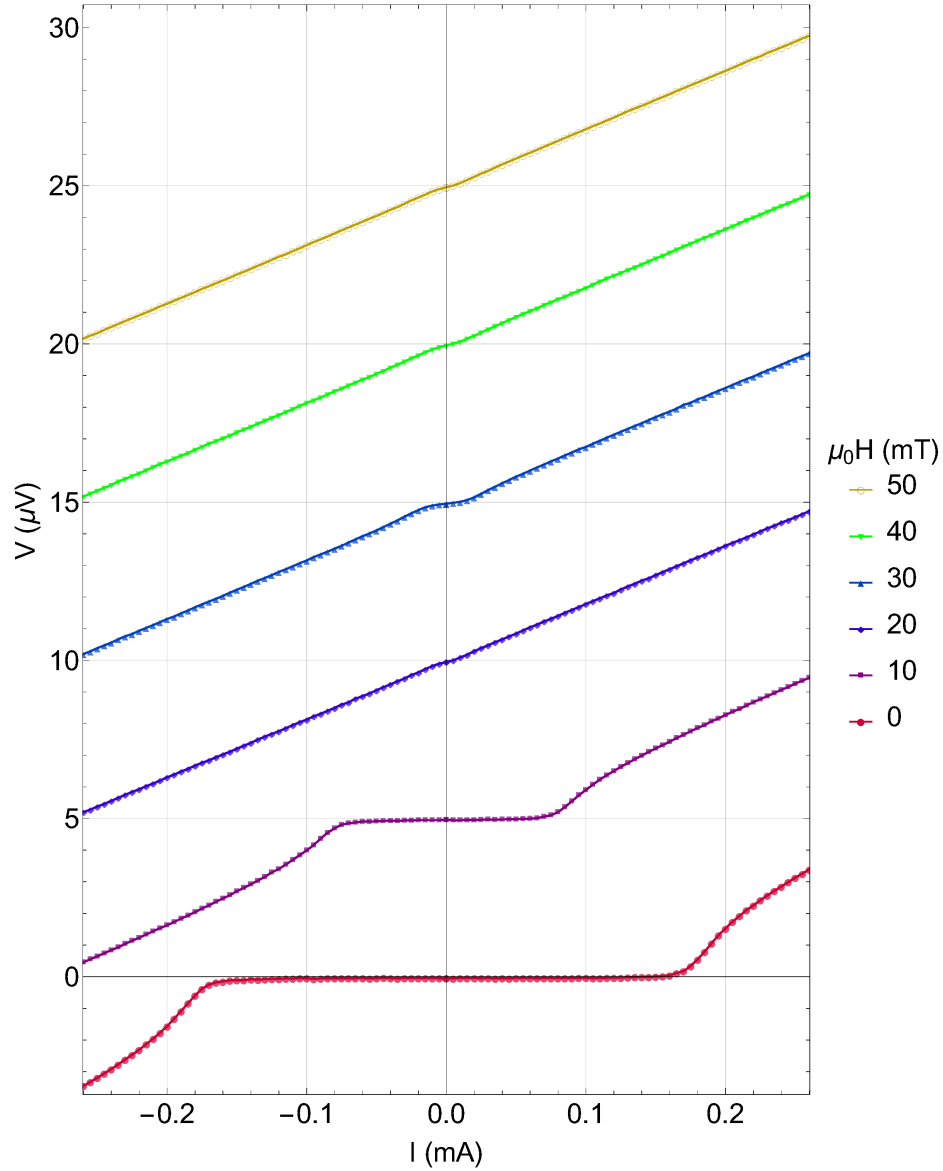


Figure 6.4: *The voltage across an overdamped S/F/S Josephson junction containing 2 nm layer of NiFeCo, versus the applied current. The data are measured via standard four-terminal measurement in an external magnetic field of 0 - 50 mT as indicated. The critical current I_c , extracted from I - V curves above, is used to produce the Fraunhofer pattern shown in Fig. 6.6 (b). For clarity, each successive curve is shifted along the voltage axis in steps of 5 μ V. Figure taken from [19].*

directions. That does not violate any symmetry given the presence of the ferromagnetic material in the junctions, but we find it puzzling given the rather small value of mutual inductance between the electrical leads and the junction proper. In those cases we define I_c to be the average value of the critical currents in the two directions.

When the critical current of the junctions is small, there is a noticeable amount of rounding of the I - V curves as I approaches I_c . Ivanchenko and Zil'berman (IZ) and Ambegaokar and Halperin developed a theory to fit such data when the rounding is due to thermal fluctuations [129,130]. (In the “tilted-washboard” potential of the RCSJ model from Ch. 2, thermal fluctuations cause the particle to escape out of the potential wells when $I < I_c$.) When the rounding is caused by fluctuations in the electromagnetic environment coupled to the junction (usually from the measurement apparatus), the temperature in the IZ model becomes an effective temperature, which can be much larger than the actual sample temperature. In the IZ model the I - V curve has the analytical solution [129]

$$V(I_c, R_N, T_{\text{eff}}) = I_c R_N \left(\frac{I}{I_c} - \mathcal{I}_- + \mathcal{I}_+ \right), \quad I \geq 0, \quad (6.2)$$

where $\mathcal{I}_{\pm} = \left(\frac{\mathcal{I}_{(1 \pm i)\gamma(\gamma c)}}{2i\mathcal{I}_{\pm i\gamma(\gamma c)}} \right)$, $\gamma = I\hbar/(2ek_B T_{\text{eff}})$ and $\gamma_c = I_c\hbar/(2ek_B T_{\text{eff}})$. $\mathcal{I}_{\nu}(z)$ are modified Bessel functions of the first kind with ν a non-integer complex number, where e is the electron charge, k_B is the Boltzmann constant, and T_{eff} is the effective noise temperature.

Figure 6.5 shows fits of the IZ function to data from a sample at magnetic fields where I_c is rather small, hence the rounding is apparent. Data are presented both for the nanovoltmeter-based measurement system and for the rf-SQUID-based system. The noise temperature, T_{eff} , is ≈ 95 K for the former, versus ≈ 37 K for the latter, as shown in Table 6.1. The table shows that the values of I_c extracted from the fits are comparable despite the difference in

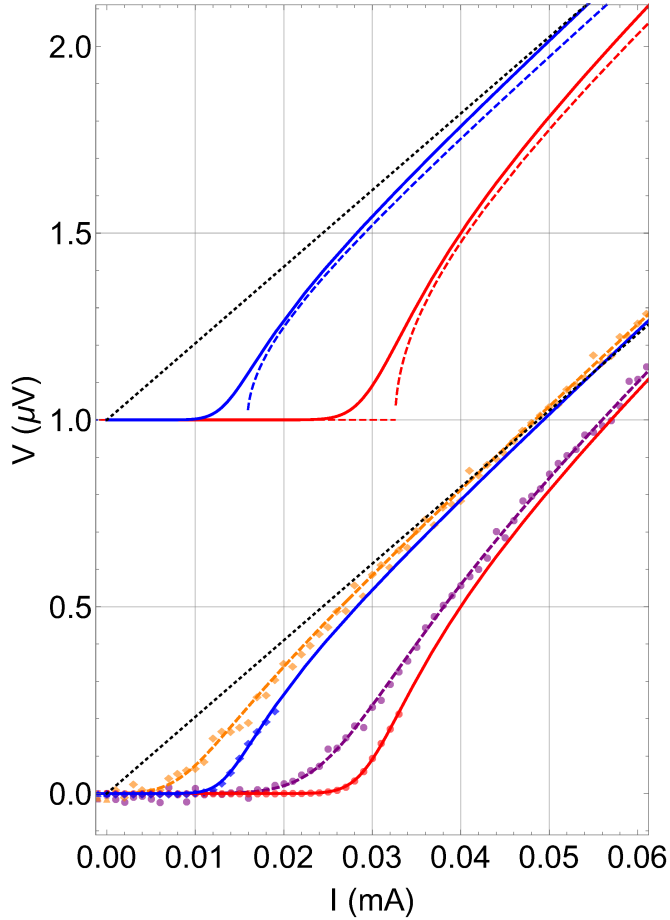


Figure 6.5: *The voltage across an S/F/S Josephson junction versus the applied current at applied magnetic fields of 18 mT (circles) and 36 mT (diamonds), using two different measurement schemes. The orange and purple colored data points are measured with a commercial nanovoltmeter while the blue and red colored data points are measured with an rf SQUID in a self-balancing potentiometer comparator circuit. The data are fit to the Ivanchenko-Zil'berman function, Eq. (6.2), which accounts for noise-induced rounding and allows us to extract the noise temperature of our measurement systems. The upper set of curves (shifted along the voltage axis by 1 μV for clarity) compares the two different fitting methods: to the square root function (Eq. (6.1), dashed lines) and to the Ivanchenko-Zil'berman function (Eq. (6.2), solid lines). The dotted black line represents Ohms' law for the measured normal state resistance. This junction contains a 1 nm layer of NiFeCo. Figure taken from [19].*

Table 6.1: *Parameters obtained from fits of the Ivanchenko-Zil'berman function to the data shown in Fig. 6.5.* The normal-state resistance R_N was measured to be 20.5 m Ω , and was not used as a free fitting parameter.

Method	Field (mT)	I_c (μ A)	T_{eff} (K)
nanovoltmeter	18	31.0 ± 0.1	98.6 ± 4.8
	36	12.6 ± 0.3	85.3 ± 12.9
rf SQUID	18	32.6 ± 0.05	37.4 ± 0.7
	36	15.9 ± 0.1	36.5 ± 2.8

T_{eff} . However, due to its much lower RMS voltage noise, the SQUID-based measurement system was used for samples whose maximum value of I_c is less than about 10 μ A.

Measuring I_c as a function of the applied magnetic field, we map out so-called ‘‘Fraunhofer’’ diffraction patterns, shown in Fig. 6.6. To compare junctions with different cross-sectional areas we normalized our data by multiplying I_c by R_N . For elliptical junctions the functional form is an Airy function [127], as described in Eq. (4.23) but is repeated here for convenience,

$$I_c = I_{c0} |2J_1(\pi\Phi/\Phi_0) / (\pi\Phi/\Phi_0)|, \quad (6.3)$$

where J_1 is an unmodified Bessel function of the first kind (whose order is a real integer, unlike the modified Bessel functions of Eq. (6.2)) and I_{c0} is the maximum critical current and $\Phi_0 = h/2e$ is the flux quantum. The magnetic flux through the junction is [76]

$$\Phi = \mu_0 H w (2\lambda_L + 2d_N + d_F) + \mu_0 M w d_F, \quad (6.4)$$

where H , w , λ_L , d_N and d_F are the applied field, the width of the junction (minor axis), the London penetration depth of the Nb electrodes, and the thicknesses of the normal metal and

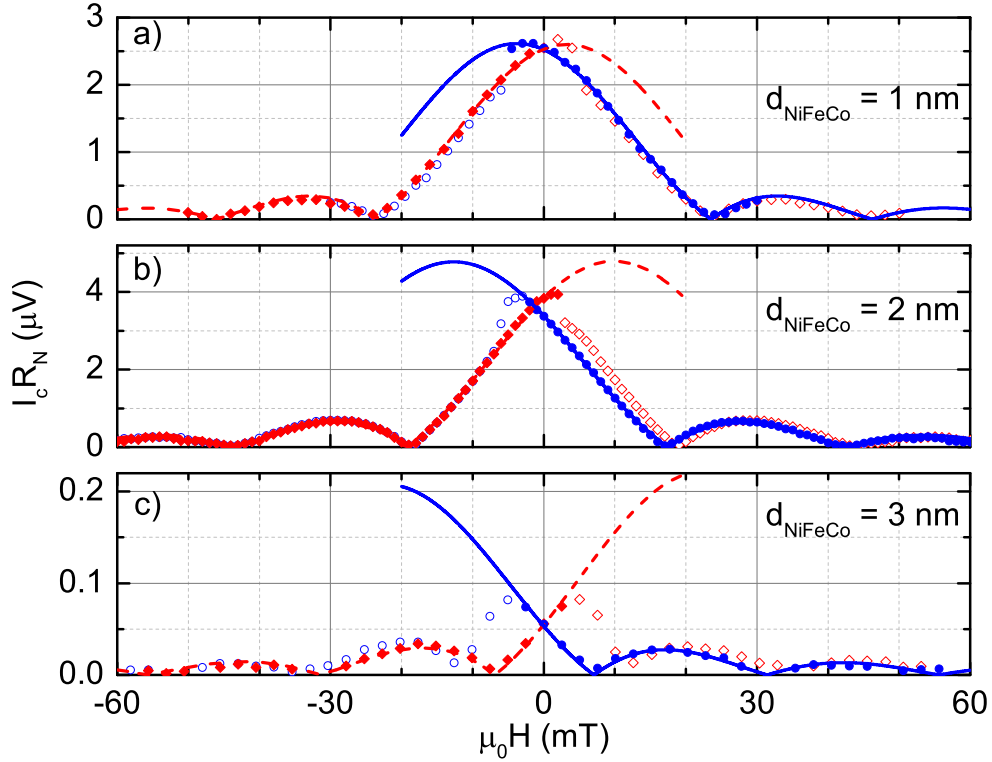


Figure 6.6: *Fraunhofer patterns of Josephson junctions containing NiFeCo.* Critical current times the normal state resistance, $I_c R_N$, is plotted versus the applied field H , for three samples with $d_{\text{NiFeCo}} =$ (a) 1 nm, (b) 2 nm, (c) 3 nm. The data before H_{switch} , the field at which the NiFeCo magnetization reverses direction (solid markers), and the corresponding fits (lines) to Eq. (6.3) show excellent agreement for both the positive (red, dashed) and negative (blue) field sweep directions. The hollow circles are the corresponding data points after H_{switch} . The Fraunhofer patterns display magnetic hysteresis and are increasingly shifted with larger d_{NiFeCo} . Figure taken from [19].

F layers. The last term in Eq. (6.4) arises from the magnetization M of the single-domain ferromagnet, and is valid only if M is uniform and points along the same direction as the applied field H . Equation (6.4) neglects the small contributions to Φ from the uniform demagnetizing field and any magnetic field from the nanomagnet that returns inside the junction. From Eq. (6.4) it is clear that the Fraunhofer pattern will be shifted along the field axis by an amount $H_{\text{shift}} = -Md_F/(2\lambda_L + d_F + 2d_{\text{Cu}})$.

The data shown in Fig. 6.6 were acquired as follows: we first applied a field of -60 mT to fully magnetize the nanomagnet, then the field was slowly ramped to +60 mT in steps of typically 1.5 mT. At a critical value $H_{\text{switch}} > 0$, the ferromagnet undergoes a rapid reversal of its magnetization direction. The data then transition to another Fraunhofer pattern shifted in the opposite direction. The applied magnetic field was then swept in the reverse orientation to observe the magnetic hysteresis. Similar magnetic hysteresis loops in Josephson junctions have been previously studied [17, 77], and are well understood.

We fit the data starting from the initialization field to H_{switch} with Eq. (6.3), where I_{c0} and H_{shift} are fitting parameters. Allowing the sample width, w , to be a free fitting parameter gives rise to large uncertainty in H_{shift} for data sets with large values of H_{shift} . Hence we fixed w to its nominal value in all the fits presented here. We keep λ_L fixed at 85 nm, as determined by data obtained in our group over many years [76]. In Fig. 6.6 the corresponding fits (lines) show excellent agreement with the fitted data (solid markers), for the positive (red) and negative (blue) sweep directions. The hollow data points after H_{switch} , whose fits are not plotted for clarity, match well with the Fraunhofer pattern from where the field is swept in the opposite direction. The nodes in the Fraunhofer patterns closely approach $I_c = 0$, which illustrates that there are no shorts in the SiO. This and the lack of distortion in the pattern at large field values indicates that there is little if any trapped flux

in the junction electrodes.

The excellent quality of the Fraunhofer patterns starting at high field and extending past zero field to H_{switch} indicates that the remanent magnetization in the junctions is uniform, suggesting that the ferromagnetic layers are probably single-domain. In many cases, the magnetic switching is abrupt, which also supports that interpretation. The excellent quality of the fits allows us to extract the peak value of I_c even in cases where the peak is inaccessible in the data because it lies beyond the field where the magnetic layer switches. The uncertainties in peak height and position in such cases, are, of course, larger than when the peak is directly visible in the data.

Some Fraunhofer patterns, such as those shown in Figs. 6.6 (b)-(c), show that the reversal of the magnetization occurs over a range of field values, implying that our junctions do not strictly follow the abrupt switching behavior predicted by the Stoner-Wolfarth model. For those samples, magnetization reversal takes place through a non-uniform intermediate state, for example an “S-shaped” state or a multi-domain state. This could be exacerbated by a number of factors including nonuniform magnetocrystalline anisotropy, surface or edge roughness, or magnetostriction.

The thickness at which the junctions transition from a 0 to π -phase state is determined by plotting $I_c R_N$ for many samples spanning a range of ferromagnet thicknesses d_F , and looking for deep local minima where I_c theoretically passes through zero. This is shown in Fig. 6.7(a) where I_c denotes the maximum critical current obtained from the Fraunhofer pattern fits. The transition from a 0 to π -phase state occurs at a thickness of $d_{\text{NiFeCo}}=1.2$ nm.

Theoretical predictions for the behavior of $I_c R_N$ versus thickness of the ferromagnetic layer describe an oscillating function with either an algebraic decay for ballistic transport [61]

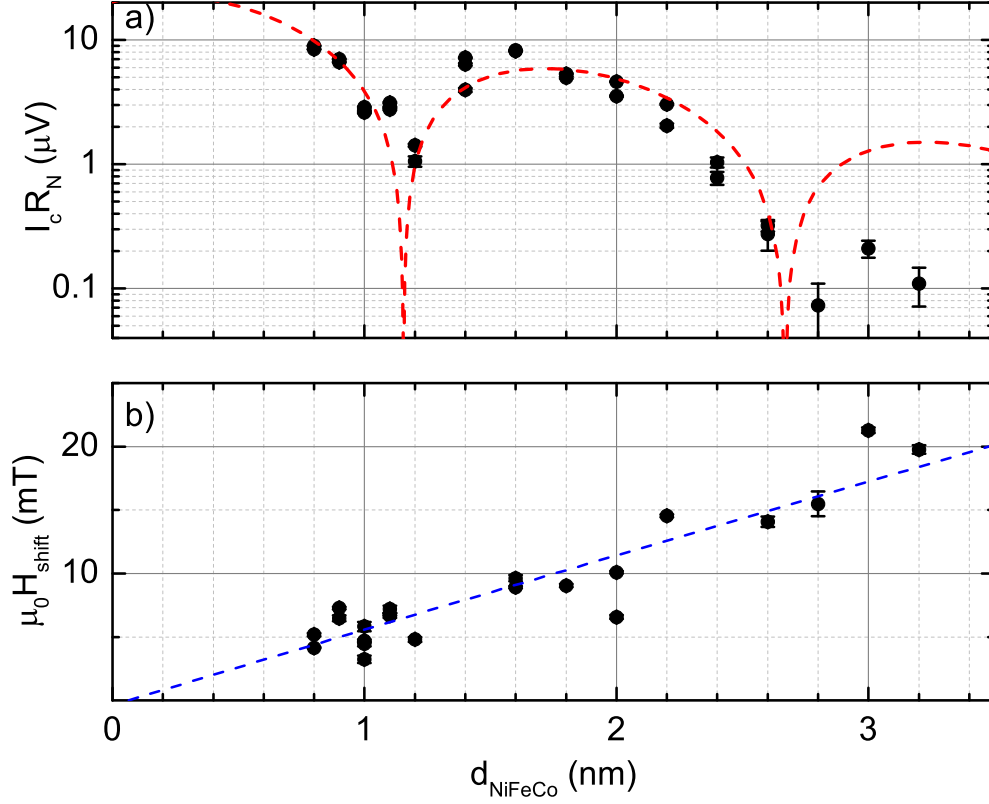


Figure 6.7: *Critical current oscillations and Fraunhofer pattern shifts in Josephson junctions containing NiFeCo.* a) The maximal I_c times R_N is plotted versus d_{NiFeCo} for many samples, with the error bars determined by the goodness of fit parameters of the individual Fraunhofer patterns. The data are fit to Eq. (6.5), and the best fit parameters are shown in Table 6.2. The first minima indicates that at a critical NiFeCo thicknesses of 1.15 ± 0.02 nm there is a transition between the 0 and π -phase states. b) The Fraunhofer pattern field shift H_{shift} is shown to increase with d_{NiFeCo} . The fit to Eq. (6.6) yields a magnetization of 855 ± 81 kA/m and an x-intercept which corresponds to no discernible magnetic dead layer ($d_{\text{dead}} = 0.06 \pm 0.17$ nm). Figure taken from [19].

or an exponential decay for diffusive transport [131]. The crossover from the ballistic to the diffusive limit has also been addressed in several theoretical works [78, 132]. In the diffusive limit the behavior is governed by the Usadel equations [57] in cases where the majority and minority spin bands have nearly identical properties. For strong ferromagnetic materials, the Usadel equations are not adequate [78]. In principle, one should take into account the Fermi-surface mismatch at each interface, as well as the different densities of states, mean free paths, and diffusion constants for the majority and minority spin bands. Microscopic calculations based on the Bogoliubov-deGennes equations and taking into account the finite interface transparency, have been performed for ballistic systems [133, 134], and could, in principle, be extended to systems with disorder. But there have been no theoretical calculations of the supercurrent that take into account the complex band structure of transition-metal ferromagnetic materials such as those discussed in this chapter. Nevertheless, several previous experimental works have used existing theoretical formulas to fit data from strong ferromagnetic materials. For instance, the ballistic form was used by Robinson *et al.* to fit data from junctions containing elemental ferromagnets, Ni, Co, and Fe, but data from junctions containing NiFe appeared to show a crossover from ballistic to diffusive behavior at a thickness of about 2 nm [73, 74]. We also attempted to fit our data to the ballistic limit used in Ref. [74], but did not find good agreement.

The data shown in Figs. 6.7(a) roughly follow an exponential decay, which is not surprising given the short mean free paths of minority carriers in NiFeCo [135]. It should be emphasized however that with our thin F layers, the concept of a mean free path may not be a valid notion when considering that the dominant scattering occurs at the F-layer/Cu interfaces. We estimate that ratio of interfacial minority-majority scattering for our F-layer materials

Table 6.2: *Best-fit parameters from Eq. (6.5) corresponding to the data in Figs. 6.7(a) and 6.11(a).*

F-layer	$d_{0-\pi}$ (nm)	V_0 (μV)	ξ_{F1} (nm)	ξ_{F2} (nm)
NiFeCo	1.15 ± 0.02	30 ± 6	1.11 ± 0.16	0.48 ± 0.03
NiFe	1.76 ± 0.05	69 ± 19	1.50 ± 0.38	0.58 ± 0.10

to be ≈ 6 [135]. Regardless, we fit the data to the diffusive limit case with the function,

$$I_c R_N = V_0 e^{-d_F/\xi_{F1}} \left| \sin \left(\frac{d_F - d_{0-\pi}}{\xi_{F2}} \right) \right|, \quad (6.5)$$

where ξ_{F1} and ξ_{F2} are length scales that control the decay and oscillation period of I_c with d_F , and $d_{0-\pi}$ is the $0-\pi$ transition thickness. The simplest model of a diffusive $S/F/S$ Josephson junction based on the Usadel equation [57] predicts that $\xi_{F1} = \xi_{F2} = \sqrt{\hbar D_F/E_{ex}}$ where D_F and E_{ex} are the diffusion constant and exchange energy of F, respectively, and has an overall phase offset $\phi \equiv (d_{0-\pi}/\xi_{F2}) - \pi/2 = \pi/4$. In the presence of spin-orbit or spin-flip scattering [136], or when the F-layer contains domain walls [137], one expects to find $\xi_{F1} < \xi_{F2}$. For strong ferromagnetic materials with large exchange energy, however, one often finds that $\xi_{F1} > \xi_{F2}$ [74], a result that can be explained from a semi-ballistic calculation starting from the Eilenberger equation [78, 132]. In addition, the phase offset, ϕ , has been shown by Heim *et al.* [138] to vary sensitively with the type and thickness of normal-metal spacer layers or insulating barriers included in the junction.

Equation (6.5) fits the data reasonably well our NiFeCo based junctions. Table 6.2 lists the best-fit parameters for the data in Fig. 6.7(a), and shows that, in spite of the significant scatter in the data, the thickness corresponding to the first $0-\pi$ transition can be extracted with reasonable precision. Despite this, Eq. (6.5) does not fit so well for the the thickest

subset of the NiFeCo samples, where one would have expected a better fit in this more-diffusive regime. The junctions appear to have $\xi_{F1} > \xi_{F2}$.

In Fig. 6.7(b), for each junction we plot the average of the H_{shift} values obtained from Fraunhofer pattern fits in each sweep direction versus the F layer thickness. Indeed, H_{shift} vs. d_F increases proportional to the magnetic flux in the junction contributed by the uniform magnetization of the ferromagnet. The trend is approximately linear due to the fact that our $\lambda_L \gg d_F$. We fit these data to:

$$H_{\text{shift}} = M(d_F - d_{\text{dead}})/(2\lambda_L + d_F + 2d_{\text{Cu}}), \quad (6.6)$$

with M and d_{dead} as free parameters. The resulting fits for NiFeCo give $M = 855 \pm 81$ kA/m with no discernable dead layer, $d_{\text{dead}} = 0.06 \pm 0.17$ nm.

In Fig. 6.8 we plot the average of the switching field H_{switch} for the two sweep directions from each Fraunhofer pattern versus d_F . In general NiFeCo has a larger H_{switch} than NiFe-based junctions (to be discussed in the next section) and their difference increases as d_F approaches 1 nm. Stoner-Wohlfarth theory predicts that H_{switch} should grow linearly with d_F , though that trend is clearly violated by the NiFeCo data at small d_F . The large scatter in the data as well as that violation, are probably the result of extrinsic factors such as surface roughness, magnetostriction, or defects in the film. The large switching field could be advantageous if NiFeCo is used as a fixed layer, since a sufficient difference between the switching fields of the free and the fixed F layers is important for controlling a cryogenic memory device.

To further characterize the magnetic properties of our NiFeCo we fabricated samples for SQUID magnetometry measurements. Unpatterned thin films of Nb(25)/Cu(5)/NiFeCo(d_F)

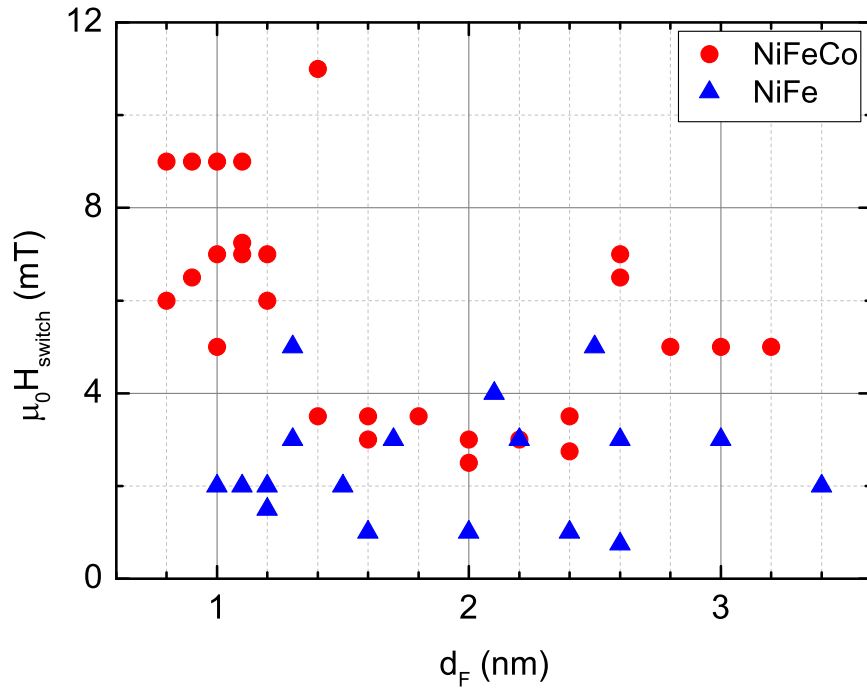


Figure 6.8: *Switching field distribution for both the NiFeCo and NiFe based S/F/S junctions.* The average of the switching field H_{switch} for the two sweep directions from each Fraunhofer pattern versus ferromagnet thickness d_F . The large increase in H_{switch} for NiFeCo at small values of d_F is due to extrinsic factors such as strain, surface roughness, or defects. Figure taken from [19].

/Cu(5)/Au(5), with thicknesses in nanometers, were sputtered under the same conditions as for the $S/F/S$ junctions. The samples were measured at 10 K in a Quantum Design SQUID magnetometer, with the applied magnetic field parallel to the plane the films. The hysteresis loops of films with $d_{\text{NiFeCo}} = 1\text{-}5$ nm are shown in Fig. 6.9. When accounting for the F layer thickness the saturization magnetization per unit volume is nearly constant for all samples 934 ± 8 kA/m and is similar to the results in Figs. 6.7(b), while the x-intercept shows $d_{\text{dead}} = -0.06 \pm 0.03$ nm. Note that these unpatterned films contain many magnetic domains that switch predominantly by domain-wall motion, and should not be viewed as a direct comparison to the single-domain nanomagnets in our $S/F/S$ junctions. Nonetheless, as d_{NiFeCo} is reduced from 5 nm to 1 nm, the coercive field increases from ≈ 2 mT to ≈ 6 mT. The Curie temperature of NiFeCo was measured to be >400 K, so our NiFeCo samples should not require cooling in a field to set their magnetization direction.

6.3.2 Junctions Containing Permalloy

To maximize energy-efficiency in a memory application, it is desirable to use a free layer whose magnetization direction can be controllably switched by a very low applied field. Permalloy (NiFe) has very sharp magnetic switching at low magnetic fields (< 2 mT), high Curie temperature, and other advantageous properties, thus it is standardly used in magnetic memory technologies such as magnetoresistive random access memory (MRAM). Similarly, we envision using it as a switchable layer in future controllable JJ-based memory devices. While NiFe has already been studied by other groups [16, 74], there is no guarantee that we can safely rely on those previous results. The $0\text{-}\pi$ transition thickness of NiFe was reported to be 1.2 nm by Robinson *et al.* [74] and 2.3 nm by Qader *et al* [16]. Since we continue to use NiFe in our spin-valve junctions, it is important for us to characterize the NiFe grown in

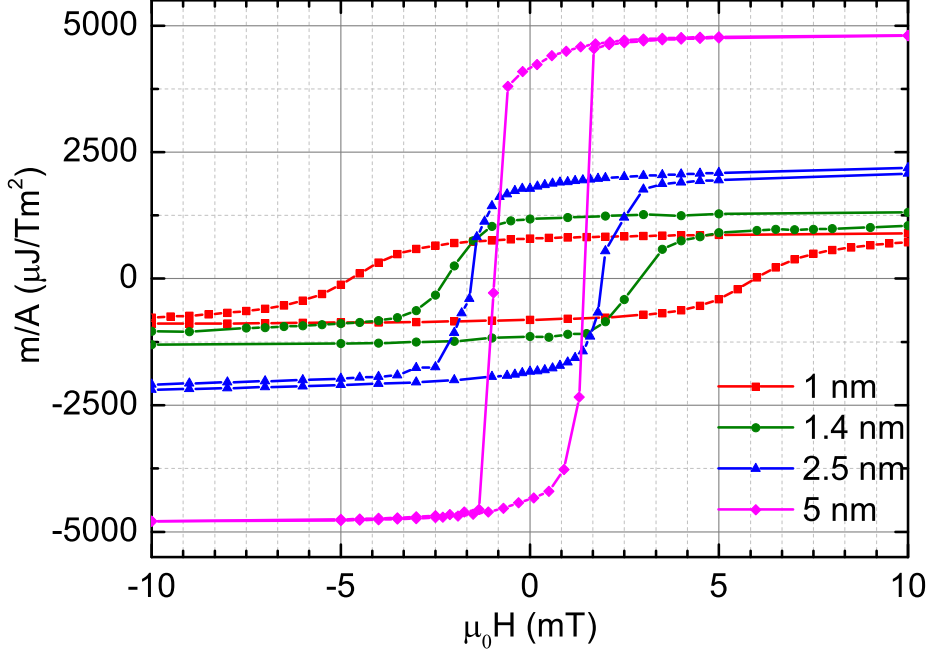


Figure 6.9: *NiFeCo* hysteresis loops of unpatterned films with d_{NiFeCo} ranging from 1-5 nm. Plotted is the sample magnetic moment divided by the area versus the applied field, measured using SQUID magnetometry. Note that dividing the ordinate by the thickness in nm will give magnetization in kA/m or emu/cm³. As d_{NiFeCo} is reduced, the switching field increases and the squareness decreases. Figure taken from [19].

our lab.

A set of samples with varying NiFe thickness was fabricated identically as described in Section 6.2 over the course of several three separate runs by myself, Mazin Khasawneh, Bethany Niedzielski and Eric Gingrich. The bottom wiring layer sequence consisted of [Nb(25)/Al(2.4)]₃/Nb(20)/Cu(5)/NiFe(d_F)/Cu(5)/Nb(5)/Au(15), with top-leads of Nb(150)/Au(10), as described in Fig. 6.2.

Measurements of the resulting area-resistance product in the normal state yielded consistent values of $AR_N = 5\text{-}10 \text{ f}\Omega\text{-m}^2$. Following the same procedure as before, we then measured Fraunhofer patterns, shown in Fig. 6.10, by first applying a field of -60 mT to fully magnetize the nanomagnet, then slowly ramped the field to +60 mT in steps of typically 1.5

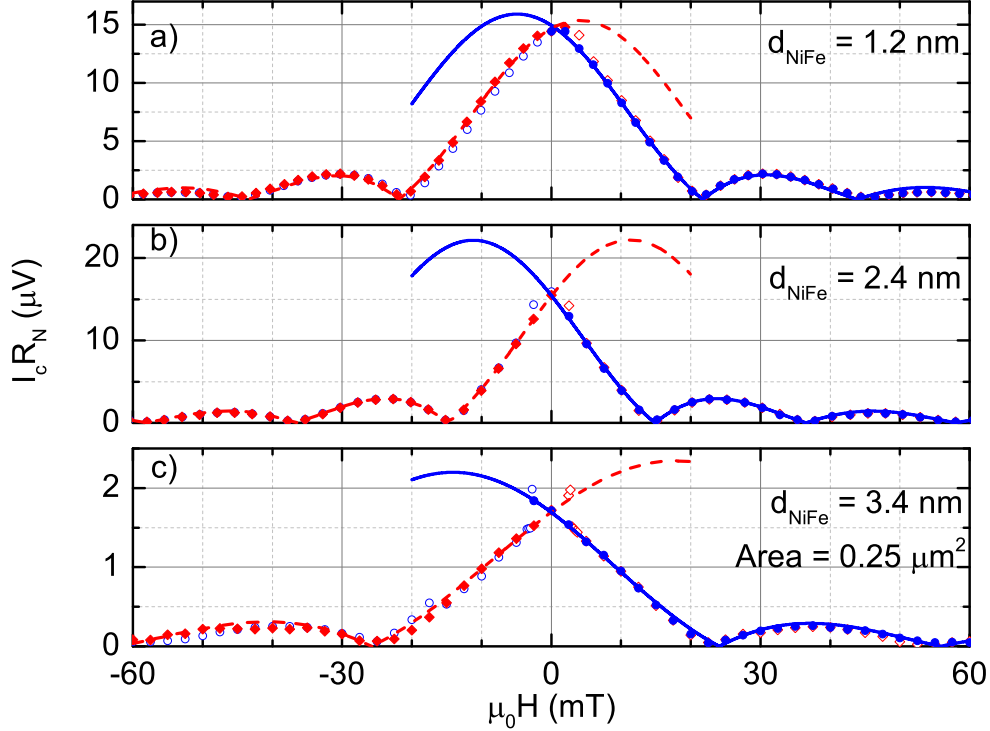


Figure 6.10: *Fraunhofer patterns of Josephson junctions containing NiFe.* $I_c R_N$ vs applied field H , varying d_{NiFe} from (a) 1.2 nm, (b) 2.4 nm, and (c) 3.4 nm. The nominal junction area in (a) and (b) is $0.5 \mu\text{m}^2$, and in (c) is $0.25 \mu\text{m}^2$, as evidenced by (c)'s comparatively wider Fraunhofer pattern. Figure taken from [19].

mT.

In Fig. 6.10 the corresponding fits (lines) show excellent agreement with the fitted data (solid markers), for the positive (red) and negative (blue) sweep directions. The hollow data points after H_{switch} , whose fits are not plotted for clarity, match well with the Fraunhofer pattern from where the field is swept in the opposite direction.

The $0-\pi$ transition plot for NiFe, extracted from the Fraunhofer patterns, is shown in Fig. 6.11(a) where I_c denotes the maximum critical current obtained from the Fraunhofer pattern fits. The transition from a 0 to π -phase state occurs at thickness of $d_{\text{NiFe}}=1.76 \pm 0.05$ nm. That thickness is between the values found by Robinson *et al.* [73,74] and by Qadar *et al.* [16]. As in the NiFeCo junctions, the data shown in Fig. 6.11(a) roughly follow an

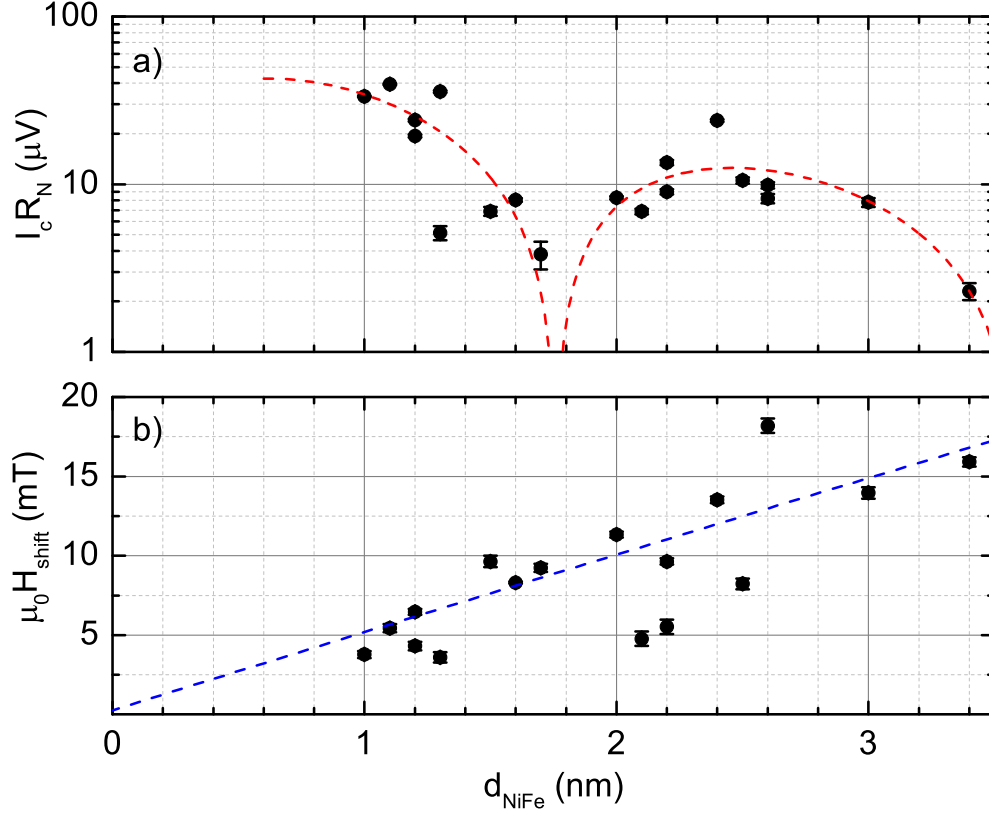


Figure 6.11: *Critical current oscillations and Fraunhofer pattern shifts in Josephson junctions containing NiFe.* a) The maximal I_c times R_N is plotted versus d_{NiFe} for many samples, with the error bars determined by the goodness of fit parameters of the individual Fraunhofer patterns. The data are fit to Eq. (6.5), and the best fit parameters are shown in Table 6.2. The first minima indicates that at a critical NiFe thicknesses of 1.76 ± 0.05 nm the junctions transition between the 0 and π -phase states. b) Despite some scatter the Fraunhofer pattern field shift H_{shift} increases with d_{NiFe} . The fit to Eq. (6.6) yields a magnetization of 711 ± 144 kA/m and no discernible magnetic dead layer ($d_{\text{dead}} = -0.05 \pm 0.55$ nm). Figure taken from [19].

exponential decay. We fit the data to the diffusive limit case with Eq. (6.5).

Equation (6.5) fits the data reasonably well for both our NiFe based junctions. Table 6.2 lists the best-fit parameters for the data in Fig. 6.11(a), and shows that, in spite of the significant scatter in the data, the thickness corresponding to the first $0-\pi$ transition can be extracted with reasonable precision. Similar to the NiFeCo samples, the NiFe-based junctions appear to have $\xi_{F1} > \xi_{F2}$. In the case of NiFe, the values are similar to those found by Robinson *et al.* ($\xi_{F1} = 1.4$ nm, $\xi_{F2} = 0.46$). Combining our results on NiFe and NiFeCo with those of Robinson *et al.*, one might conclude that $\xi_{F1} > \xi_{F2}$ is a generic condition for Josephson junctions containing strong transition-metal ferromagnetic materials. That is not true, however, as the thickness dependence of $I_c R_N$ in junctions containing NiFeMo was fit very well by Eq. (6.5) but with $\xi_{F1} < \xi_{F2}$, presumably due either to the very short mean free path or very short spin diffusion length in that material [77].

In Fig. 6.11(b), for each junction we plot the average of the H_{shift} values obtained from Fraunhofer pattern fits in each sweep direction versus the F layer thickness. We fit these data to Eq. (6.6), with M and d_{dead} as free parameters. The resulting fits for NiFe give $M = 711 \pm 143$ kA/m and $d_{\text{dead}} = -0.05 \pm 0.55$ nm. As previously mentioned, in Fig. 6.8 we plot the average of the switching field H_{switch} for the two sweep directions from each Fraunhofer pattern versus d_F .

6.3.3 Junctions Containing Pd₉₇Fe₃

To achieve low switching fields, it is advantageous for the free layer to have low magnetization and low magnetocrystalline anisotropy. Another candidate class of materials that fulfills these criteria is the Pd_{1-x}Fe_x alloy system with low Fe concentrations. We present studies of micron-scale elliptically-shaped Josephson junctions containing Pd₉₇Fe₃ layers of

varying thickness.

Dilute PdFe alloys have been known for several decades to have very low magnetocrystalline anisotropy [139], and previous work from our group on the alloy with 1.3% Fe concentration found it to have a spin diffusion length of 9.6 ± 2 nm [140]. Josephson junctions containing PdFe with a lower Fe concentration of $\approx 1\%$ have already been studied by other groups [13–15] with an eye toward applications in cryogenic memory. In the past our group has tried using Pd_{98.7}Fe_{1.3} as the free layer in controllable spin-triplet Josephson junctions [109], but the poor magnetic switching characteristics of the PdFe led to unreliable control over the phase state of the junctions. That work provided the main motivation for studying PdFe alloys with somewhat higher Fe concentrations.

We first characterized the magnetic properties of unpatterned continuous Pd₉₇Fe₃ films via SQUID magnetometry. Thin films of Nb(5)/Cu(5)/PdFe(d_F)/Cu(5)/Nb(5), with thicknesses in nanometers, were deposited via dc sputtering under the same conditions as described in Section 6.2.

The samples were measured using a Quantum Design SQUID magnetometer at 5 K, with the applied magnetic field parallel to the film plane. The hysteresis loops of films with $d_{\text{PdFe}} = 8\text{--}16$ nm are shown in Fig. 6.12. The saturation magnetization per unit volume is nearly constant for the three samples. Plotting the saturation magnetic moment divided by the sample area versus d_{PdFe} and fitting to a straight line gives a slope which corresponds to a magnetization of $M = 90 \pm 9$ kA/m. Meanwhile, the x-intercept $d_{\text{dead}} = 2.8 \pm 0.9$ nm, indicates the thickness over which the PdFe has no net magnetization, known as the magnetic dead layer. Note that these unpatterned films contain many magnetic domains so that the switching mechanism is governed by domain-wall motion; hence the film results should not be directly compared to the switching behavior of the nanomagnets in our $S/F/S$ junctions,

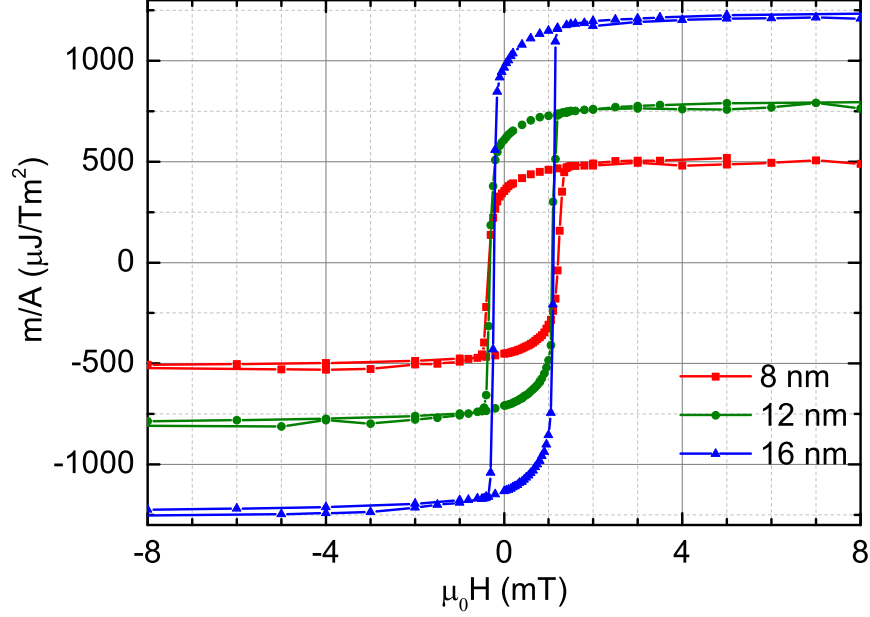


Figure 6.12: *Hysteresis loops of unpatterned films containing PdFe with thickness spanning 8-16 nm.* Plotted is the magnetic moment divided by the sample area versus the applied field, measured using SQUID magnetometry. For the three samples the magnetization is approximately constant, $M = 90 \pm 9$ kA/m. The data are slightly shifted along the field axis due to a small amount of trapped flux in the solenoid of the SQUID magnetometer. From the data we extract a magnetic dead layer thickness of $d_{\text{dead}} = 2.8 \pm 0.9$ nm, discussed in the text. Figure taken from [20].

discussed later.

In a separate sputtering run we fabricated $S/F/S$ Josephson junctions containing PdFe using the same techniques described in Section 6.2. The bottom wiring layer consists of the sequence $[\text{Nb}(25)/\text{Al}(2.4)]_3/\text{Nb}(20)/\text{Cu}(5)/\text{PdFe}(d_F)/\text{Cu}(5)/\text{Nb}(5)/\text{Au}(15)$, and the top wiring layer is $\text{Nb}(150)/\text{Au}(10)$ as shown in Fig. 6.2. The junctions have an aspect ratio of 2.5 and area of $0.5 \mu\text{m}^2$.

The samples I - V curves were measured at 4.2 K using the same methods as in Sections 6.3.1 and 6.3.1. The sample resistance in the normal state, R_N , measured from the I - V curves and was independently confirmed using a lock-in amplifier. Measurements of the area-resistance product in the normal state yielded consistent values of $AR_N = 11 \pm 1$

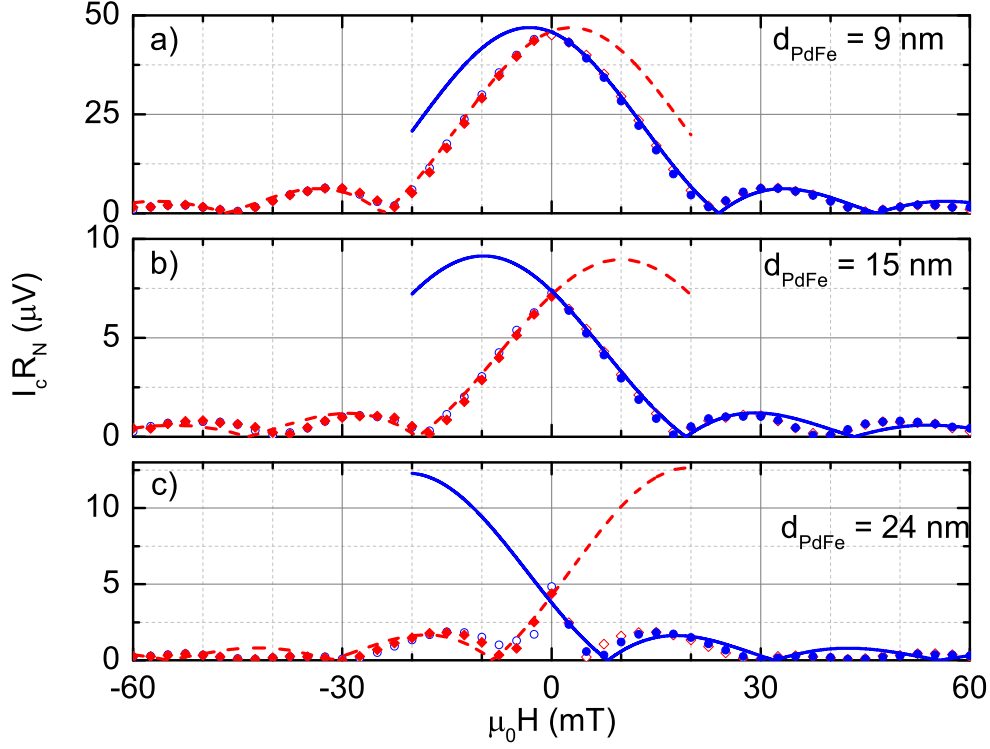


Figure 6.13: *Fraunhofer patterns of Josephson junctions containing PdFe.* Critical current times the normal state resistance, $I_c R_N$, is plotted versus the applied field H , for three samples with d_{PdFe} equal to (a) 9 nm, (b) 15 nm, and (c) 24 nm. The data before H_{switch} , the field at which the PdFe magnetization vector reverses direction (solid markers), and the corresponding fits (lines) to Eq. (6.3) show good agreement for both the positive (red, dashed) and negative (blue) field sweep directions. The hollow circles are the corresponding data points after H_{switch} . The Fraunhofer patterns display magnetic hysteresis and are increasingly shifted with larger d_F . Figure taken from [20].

$\text{f}\Omega\text{-}m^2$, an indicator of reproducible high quality interfaces.

To acquire the Fraunhofer patterns in Fig. 6.13, first we fully magnetized the nanomagnet with an applied field of -60 mT along the long-axis of the elliptical junctions, then ramped the field to +60 mT in steps of 2.5 mT, measuring I_c at each step.

The data follow the expected Airy function from Eq. (6.3) from the initialization field up to the beginning of a small field range, $H_{\text{switch}} > 0$, during which the ferromagnet switches the direction of its magnetization vector. Beyond H_{switch} the data jump to another Fraunhofer pattern that is shifted in the opposite direction. The magnetic flux through

the junction is given by Eq. (6.4). The Fraunhofer pattern will be shifted by an amount $H_{\text{shift}} = -Md_F/(2\lambda_L + d_F + 2d_{\text{Cu}})$ along the field axis due to Eq. (6.4). To measure the magnetic hysteresis, we then swept the applied field in the opposite orientation.

The data prior to the magnetic switching event were fit to Eq. (6.3) with I_{c0} and H_{shift} as fitting parameters, while w is fixed at the nominal sample width of $0.5 \mu\text{m}$. In Fig. 6.13, for both the positive (red) and negative (blue) sweep directions, the corresponding fits (lines) show excellent agreement with the data (solid markers). The hollow markers denote the data after H_{switch} , and closely correspond to the Fraunhofer pattern in which the field is swept in the opposite orientation. The excellent nature of the Fraunhofer patterns allow us to obtain a value for I_{c0} , albeit with a larger uncertainty, even when the central peak in the Fraunhofer pattern is shifted far outside the range of the data as shown in Figs. 6.13(b)-(c). The nodes in the Fraunhofer pattern nearly approach $I_c = 0$, indicating a robust SiO barrier around the junction. The data typically follow the Airy function through zero field before the relatively sharp magnetic switching event, but for a few samples did not. Therefore, it appears that not all of the samples are single-domain near zero field.

The switching characteristics of the PdFe layer were maintained even when smaller initialization fields were used. After returning the field to zero, we measured the Fraunhofer pattern again, sweeping the field from only $\pm 5 \text{ mT}$ in both directions at finer field steps of 0.5 mT , as shown in Fig. 6.14 (green and orange points), where we have zoomed-in on the central peak. It is clear that the junctions switch the direction of their magnetization over a range of field values. To characterize the magnetic switching we use two parameters: $H_{\text{switch},1}$, denoting the beginning of the switching event, is the field at which I_c begins to deviate from the initial Airy function, and $H_{\text{switch},2}$, denoting the end of the switching event, is the field at which I_c joins the corresponding shifted Airy function. Across the range of

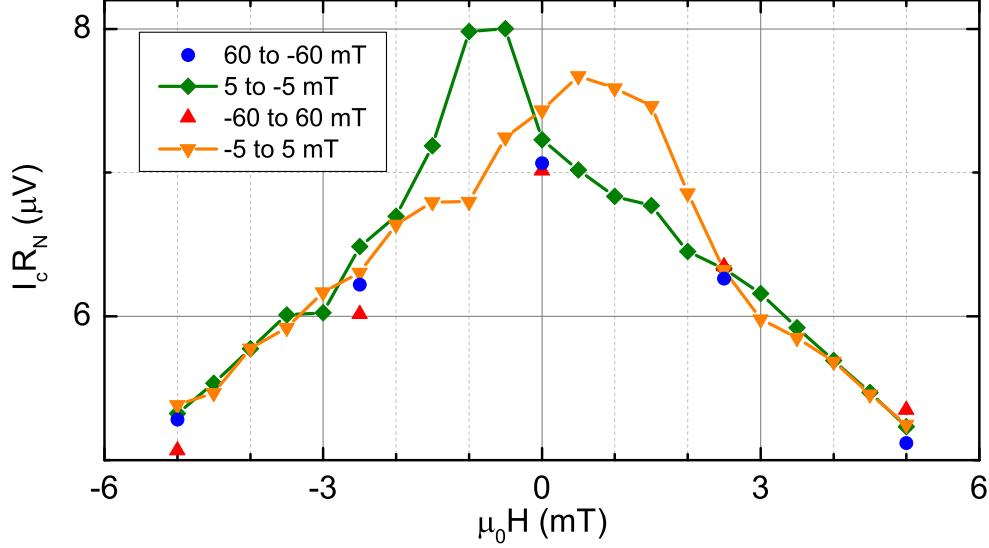


Figure 6.14: *Magnetic switching of PdFe Josephson junctions at small applied fields.* $I_c R_N$ is plotted versus the applied field H for the same Josephson junction shown in Fig. 6.13(b), zoomed-in on the central peak. Separate measurements using small initialization fields of ± 5 mT and finer step size (green and orange data points) show the behavior of the magnetic switching. The reversal of the PdFe magnetization direction for the two sweep directions begins at $H_{\text{switch},1} = 1.0$ mT (orange) and -0.5 mT (green) and ends at $H_{\text{switch},2} = 2.5$ mT (orange) and -2.0 mT (green). During the switching event the data deviate from the expected Fraunhofer pattern fit. As the field approaches $H_{\text{switch},2}$ the data converge with the corresponding measurements from Fig. 6.13(b) where much larger ± 60 mT initialization fields were used (blue and red points). Lines connect the adjacent finer spaced data for clarity. Figure taken from [20].

thicknesses studied, on average the junctions began to switch at a very low field $|H_{\text{switch},1}| = 0.4$ mT with standard deviation 0.6 mT, and completed the switching process at $|H_{\text{switch},2}| = 2.4$ mT with standard deviation 0.9 mT. The value of $|H_{\text{switch},1}|$ for PdFe is smaller than found in $\text{Ni}_{81}\text{Fe}_{19}$ -based junctions of similar construction measured by our group [19], however $|H_{\text{switch},2}|$ is comparable. The low Fe concentration in the $\text{Pd}_{97}\text{Fe}_3$ alloy may give rise to this gradual switching behavior. Prior work on an alloy with lower Fe concentration, $\text{Pd}_{99}\text{Fe}_1$, showed that the ferromagnetic behavior of thin films is controlled by the presence of weakly coupled ferromagnetic clusters [141].

Repeating the measurement at even lower initialization fields (3 mT) sometimes caused

irregular and irreproducible changes to I_c and H_{shift} . We surmise that too low of an initialization field allows domain walls to form within the junction, which disturb the magnetic switching. Hence, if Pd₉₇Fe₃ layers are used in cryogenic memory, an initialization field of at least 5 mT would be necessary to reproducibly magnetize the nanomagnet.

In Fig. 6.15(a) we plot $I_c R_N$ for many samples of varying ferromagnet thicknesses d_F . The junctions transition from a 0 to π -phase state at the value of d_F where the first deep local minimum occurs. In Fig. 6.15(a) I_c denotes the maximum critical current obtained from the Fraunhofer pattern fits. The data are of sufficient quality to determine the location of the the 0- π transition with high precision, as we will show below.

As discussed earlier, theoretical predictions describe the behavior of $I_c R_N$ versus d_F as an oscillating function with either an exponential decay for diffusive transport or an algebraic decay for ballistic transport [57]. Bergeret *et al.* have shown that $\xi_{F1} > \xi_{F2}$ is a persistent feature in the semi-clean limit where $\xi_{F1} = l_e$, the mean free path [78]. We find that the diffusive limit agrees best with our Pd₉₇Fe₃ data in Fig. 6.15, after fitting the points to Eq. (6.5). The best-fit parameters are: $V_0 = 102 \pm 12 \mu\text{V}$, $\xi_{F1} = 16.2 \pm 1.4 \text{ nm}$, $\xi_{F2} = 7.2 \pm 0.6 \text{ nm}$, and $d_{0-\pi} = 16.3 \pm 0.2 \text{ nm}$, which corresponds to $\phi = 0.7 \pm 0.1$. The fits show that the junctions have $\xi_{F1} > \xi_{F2}$, which was also the case for a PdNi alloy studied previously [76].

In Fig. 6.15(b), we plot the average of H_{shift} from the Fraunhofer pattern fits for each sweep direction versus d_F . We fit these data to Eq. (6.6), with M and d_{dead} used as fitting parameters. The fit yields $M = 85 \pm 9 \text{ kA/m}$ and $d_{\text{dead}} = -0.6 \pm 2.2 \text{ nm}$. The values of both the magnetization and the dead layer thickness, obtained from Fig. 6.15(b) are consistent with those from the SQUID magnetometry data shown in Fig. 6.12.

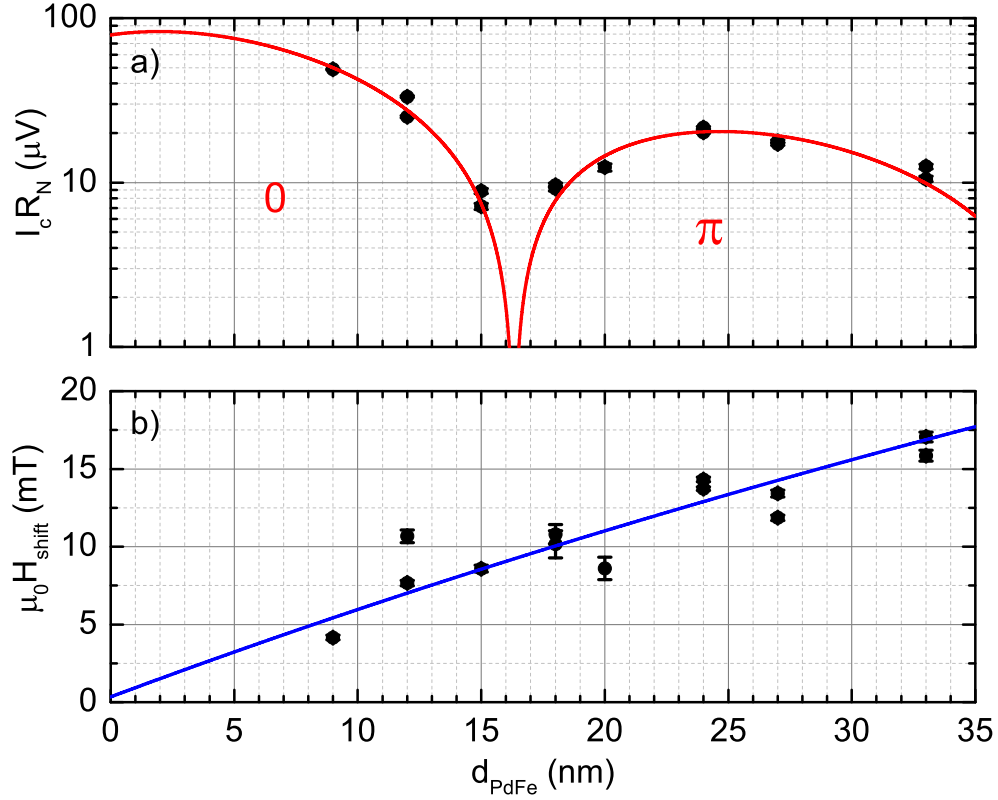


Figure 6.15: *Critical current oscillations and Fraunhofer pattern shifts in Josephson junctions containing PdFe.* a) The maximal I_c times R_N is plotted versus d_{PdFe} for many samples, with the error bars determined by the goodness of fit parameters of the individual Fraunhofer patterns. For many data points the uncertainty is smaller than the symbol size. The minimum indicates the critical PdFe thickness at which the junctions transition between the 0 and π -phase states. The solid red line is a fit to the data using Eq. (6.5). b) The Fraunhofer pattern field shift H_{shift} increases with d_{PdFe} . The blue line is the fit to Eq. (6.6), which yields $M = 85 \pm 9$ kA/m and $d_{\text{dead}} = -0.6 \pm 2.2$ nm. Figure taken from [20].

6.3.4 Junctions Containing Ni

We also attempted to carry out a study of $S/F/S$ junctions containing Ni, using the same fabrication process as described previously. The layer configuration was sputtered without breaking vacuum as follows, $[\text{Nb}(25)/\text{Al}(2.4)]_3/\text{Nb}(20)/\text{Cu}(5)/\text{Ni}(d_F)/\text{Cu}(5)/\text{Nb}(20)/\text{Au}(15)$, with d_F ranging from 1.2 to 3.8 nm in samples from three different sputtering runs. The samples have top electrode of $\text{Nb}(150)/\text{Au}(10)$, as shown in Fig. 6.2.

Measuring the samples I - V curves at 4 K, we found the area resistance product of the samples to be slightly larger than usual with a moderate amount of scatter, $A \times R_N = 15 \pm 14 \text{ f}\Omega\text{m}^2$. Measuring the samples in the presence of an applied external field oriented along the long-axis of the junctions ranging from $\pm 60 \text{ mT}$, we found the resulting Fraunhofer patterns to be of generally poor quality, thought to be attributed to the Ni layer containing multiple magnetic domains for each of the three junction sizes measured. We subsequently attempted to magnetize the junctions in a large field of 260 mT along the long axis of the junctions. To remove any possible flux trapped in the Nb electrodes, we subsequently raised the sample probe in the dewar until it was just above the liquid helium level, above the T_c of Nb, as monitored via changes in the sample resistance using a multimeter. After the magnetization procedure we again measured the Fraunhofer patterns, which improved somewhat, but were still of less than ideal quality. Over a year later, we found that other groups use even larger fields ($> 400 \text{ mT}$) to magnetize their junctions containing Ni [142].

Despite some scatter in the measured values of $I_c R_N$ and a relatively small number of data points (due in part to low yield from this sample set), we nonetheless can map out a rough picture of how $I_c R_N$ decays with thickness, shown in Fig. 6.16. Perhaps the most important observation is that the $I_c R_N$ values are quite large in comparison to most of

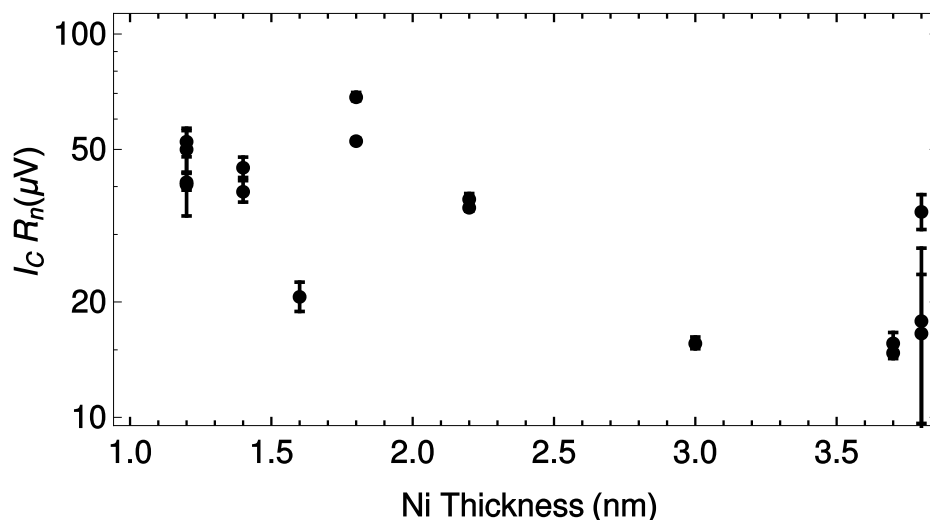


Figure 6.16: *Critical current oscillations in Josephson junctions containing Ni.* The maximal I_c times R_N is plotted versus d_{Ni} for many samples, with the error bars determined by the goodness of fit parameters of the individual Fraunhofer patterns. The data are compatible with a minima between a Ni thickness of 3.0-3.6 nm, as measured later by groups at NIST [143] and Northrop Grumman Corporation [23]. Overall, $I_c R_N$ does not appear decay substantially with increasing Ni thickness.

the other materials presented in this chapter. Also, the critical current in the Ni junctions appears to decay quite slowly with the Ni thickness. Although the magnetic properties evidenced in the Fraunhofer patterns are of less than desired quality, Ni appears to be one of the rare ferromagnetic materials that both switches at a large magnetic field and transmits large critical currents in Josephson junctions. While the data is by no means definitive it is compatible with a minima between a Ni thickness of 3.0-3.6 nm, which was later measured by groups at the National Institute of Standards and Technology (NIST), Boulder [143] and Northrop Grumman Corporation [23]. Given the large scatter we did not fit the data in Fig. 6.16 to the previously discussed theoretical predictions.

6.4 Conclusion

This section provides a study of the magnetic and transport behaviors of $S/F/S$ Josephson junctions containing the ferromagnets NiFeCo, NiFe, PdFe, and Ni. Systematic studies of the material properties of such junctions, including the $0-\pi$ transition thickness, switching fields, and shifts in the Fraunhofer patterns versus F -layer thickness are crucial for the advancement of cryogenic memory technologies. To develop phase-controlled $S/F/N/F'/S$ memory devices one would need to fix either the F or F' layer to a thickness near its respective $0-\pi$ transition, while the other layer could be kept much thinner to avoid substantial decay in I_c . Then, by tuning the relative orientation of the F and F' magnetization vectors between parallel and anti-parallel configurations, the junction can be controllably toggled between the π and 0 phase states [18].

We have shown that NiFeCo is a potential candidate for such a fixed layer. If positioned near the first $0-\pi$ transition at 1.2 nm, it has a reasonable switching field, $H_{\text{switch}} \approx 7$ mT, which is somewhat larger than NiFe, but not as unwieldy as Ni (260 mT). However, from Fig. 6.8, it is not clear if the relatively small difference in the switching fields of NiFeCo and NiFe would allow them to be successfully used together as the fixed and free layers in a single device. One could attempt to use another material with a lower switching field than NiFe, or possibly tune the relative concentrations of Ni, Fe, and Co to optimize the switching characteristics for the situation desired.

In addition we have studied the magnetic and transport behavior of Josephson junctions containing Pd₉₇Fe₃. If used as a “free” magnetic layer in cryogenic memory, Pd₉₇Fe₃ is advantageous in that its $0-\pi$ transition occurs at a thickness of ≈ 16.5 nm, much greater than for NiFe, making Pd₉₇Fe₃ much less sensitive to small thickness variations. Meanwhile,

junctions with Pd₉₇Fe₃ maintain a relatively low switching field $|H_{\text{switch},2}| = 2.4$ mT (with standard deviation 0.9 mT). As a “free” layer Pd₉₇Fe₃ has some disadvantages– the magnetic switching can occur over a range of fields, possibly due to the existence of weakly coupled ferromagnetic clusters. For reproducible magnetic switching, the junctions had to be magnetized at an initialization field of 5 mT or greater. Preliminary magnetometry measurements on Pd_{1-x}Fe_x films with $x = 7\text{-}13\%$ suggest that those alloys with higher Fe concentration may have better magnetic properties. In the future, we plan to test the behavior of those alloys in Josephson junctions.

Looking forward, the addition of extra magnetic layers could pose a number of new complications: i) The surface roughness may grow with the number of layers; one would need to ensure that both the F and F' layers remain single domain. ii) An additional spacer layer would be required between the F and F' layers to keep them magnetically decoupled. As shown by Heim *et al.* [138], spacer layers could cause modifications to the precise value of d_F at which the $0\text{-}\pi$ transition occurs. iii) Magnetostriction, edge roughness and other effects should be minimized so that the magnetic switching behavior of the junction is dominated primarily by shape anisotropy.

Chapter 7

Controllable Phase SQUIDs: Spin-Singlet

Here we discuss the first experimental demonstration that the phase state of a Josephson junction can be controllably switched between 0 and π , i.e. a phase-sensitive cryogenic one-bit memory device [18]. That feat was achieved by adding two ferromagnetic Josephson junctions to a superconducting loop to form a Superconducting QUantum Interference Device (SQUID), which is sensitive to the relative phase between the two junctions. While the sample fabrication and measurement of these samples was undertaken primarily by Bethany Niedzielski and Eric Gingrich, the former whose dissertation [144] explains the experiment and the development thereof in greater detail, my main contribution to that effort was to extract from the data unambiguous proof that the junction(s) had indeed switched between the 0 and π phase states. As described below, this confirmation required that the data from the various states of the junctions be self-consistently fit to a general SQUID theory accounting for asymmetries in both the critical current and the geometric inductance on either side of the loop.

To avoid treading over the same ground, after outlining the experimental approach and relevant SQUID physics, in this chapter we focus mainly on the methods of the data analysis. The techniques described here will lay the groundwork for Chapter 9, where they will be utilized again to analyze controllable phase-sensitive SQUIDs that carry spin-triplet supercurrent.

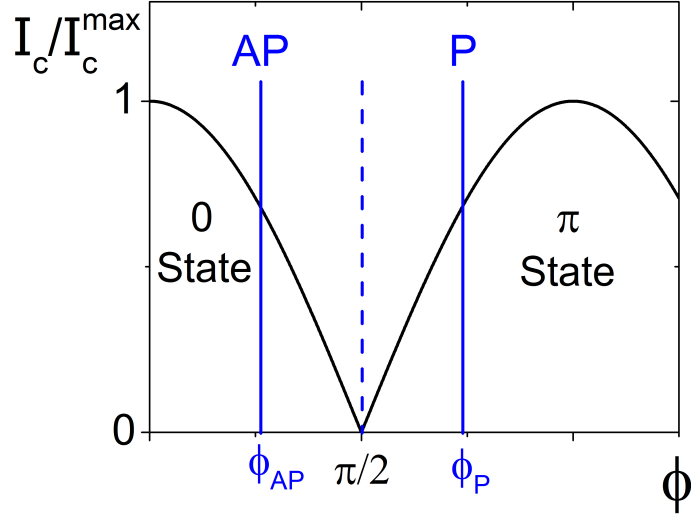


Figure 7.1: *Scheme to control the phase-state of a spin-valve Josephson junction.* The critical current will oscillate as a function of the phase accumulated across the junction ϕ ; the ground-state phase of the junction can be either 0 or π . If the layer thicknesses of the two ferromagnets are properly adjusted, the ground state phase of the junction will be π if the two layers are parallel ($\phi_P = \phi_1 + \phi_2$), where ϕ_1 and ϕ_2 are the phases accumulated in each of the two ferromagnetic layers respectively, and 0 if the two layers are antiparallel ($\phi_{AP} = \phi_1 - \phi_2$). In this simplified picture, the decay of the supercurrent versus the ferromagnetic layer thickness is ignored. Figure taken from [18].

7.1 Spin-Valve Josephson Junctions and SQUIDS

Consider a Josephson junction, similar to those discussed in Chapter 6, but with two different ferromagnetic layers, F_1 and F_2 whose magnetizations are in-plane and either parallel or antiparallel with respect to one another, arranged in the configuration $S/F_1/N/F_2/S$ [12, 16, 17, 145], called a *spin-valve* Josephson junction. As discussed in Ch. 4.3, in a ferromagnetic Josephson junction the pair correlation function will oscillate and decay as a function of the thickness of a ferromagnet. The pair correlation function will accumulate a total phase

shift of,

$$\begin{aligned}\phi &= \phi_1 \pm \phi_2, \\ &= (Q_1 \times d_{F_1}) \pm (Q_2 \times d_{F_1}),\end{aligned}\tag{7.1}$$

where $\phi_1 = Q_1 \times d_{F_1}$ and $\phi_2 = Q_2 \times d_{F_1}$ are the individual phase shifts acquired from traversing the F_1 and F_2 layers. In Eq. (7.1), the thicknesses of F_1 and F_2 are d_{F_1} and d_{F_2} , respectively, and Q_1 and Q_2 are related to the center-of-mass momentum of the spin pairs, given by,

$$Q_1 = (k_{F_1}^\uparrow - k_{F_1}^\downarrow)\tag{7.2}$$

$$Q_2 = (k_{F_2}^\uparrow - k_{F_2}^\downarrow),\tag{7.3}$$

where $k_{F_{1,2}}^\uparrow$ and $k_{F_{1,2}}^\downarrow$ are the Fermi wavevectors in the majority and minority bands, respectively. The presence of the minus sign in Eq. (7.1) originates from the fact that if the magnetizations of F_2 and F_1 are antiparallel, then from one ferromagnet to the next the majority and minority bands will reverse their roles, leading the pair correlation function to acquire the opposite phase, $-\phi_2$.

Controlling the phase state of these types of junctions depends crucially on the precise layer thicknesses of F_1 and F_2 . As shown schematically in Fig. 7.1, if we choose the thickness of F_1 such that ϕ_1 is close to $\pi/2$ and the thickness of F_2 such that $\phi_2 \leq \pi/2$, then when the layers are parallel, $\phi = \phi_P = \phi_1 + \phi_2$, the junction is in the π -state, whereas when the layers are antiparallel, $\phi = \phi_{AP} = \phi_1 - \phi_2$, the junction is in the 0-state. Or, in the language of Ch. 6, we need to fabricate the two ferromagnetic layers such that one is near its 0- π transition thickness while the other is far away from its 0- π transition thickness. It

is because of this restriction that we went to such lengths to characterize the $0-\pi$ transition thicknesses of the various ferromagnetic materials in Ch. 6.

The free layer in both junctions was chosen to be $\text{Ni}_{81}\text{Fe}_{19}$ (Py) of thickness 1.5 nm, which switches at a low field and puts the junction close to the $0-\pi$ transition, as indicated by Fig. 6.11 [19]. The fixed layer in both junctions was chosen to be Ni of thickness 1.2 nm, which according to Fig. 6.16, is away from its $0-\pi$ transition thickness. Moreover the Ni should not significantly decay the critical current and should add or subtract a small component to the phase [17, 69, 73]. The ferromagnetic layers are prevented from coupling magnetically by a Cu spacing layer. The full structure of the junctions is: $[\text{Nb}(40)/\text{Al}(2.4)]_3/\text{Nb}(20)/\text{Cu}(5)/\text{NiFe}(1.5)/\text{Cu}(10)/\text{Ni}(1.2)/\text{Cu}(5)/\text{Nb}(20)/\text{Au}(15)/\text{Nb}(150)/\text{Au}(10)$. For all other details about the sample fabrication, including work on the development and study of smooth normal metal spacers, studies regarding the smoothness of the bottom Nb/Al electrodes, and how those layers effect the magnetic properties of the ferromagnetic layers, see Bethany's dissertation [144].

While only a single junction is required for the phase change to occur, to observe such a change requires a phase-sensitive measurement. One way to accomplish that is to set up an interference experiment between two spin-valve junctions in a SQUID loop, as shown in Fig. 7.2. The SQUID loop was fabricated to have inner dimensions of $10\ \mu\text{m} \times 10\ \mu\text{m}$, and the wire leads composing the loop were $5\ \mu\text{m}$ wide. The junctions was fabricated to have elliptical cross-sections, each with different aspect ratios (2.2 and 2.8), to help control the coercive fields of the magnetic layers via shape anisotropy. In this way the more eccentric junction has a larger coercive field than the less eccentric junction.

The idea is to set up the following scenario: The sample is initialized by applying an in-plane magnetic field using a solenoid coil around the sample to align the magnetizations

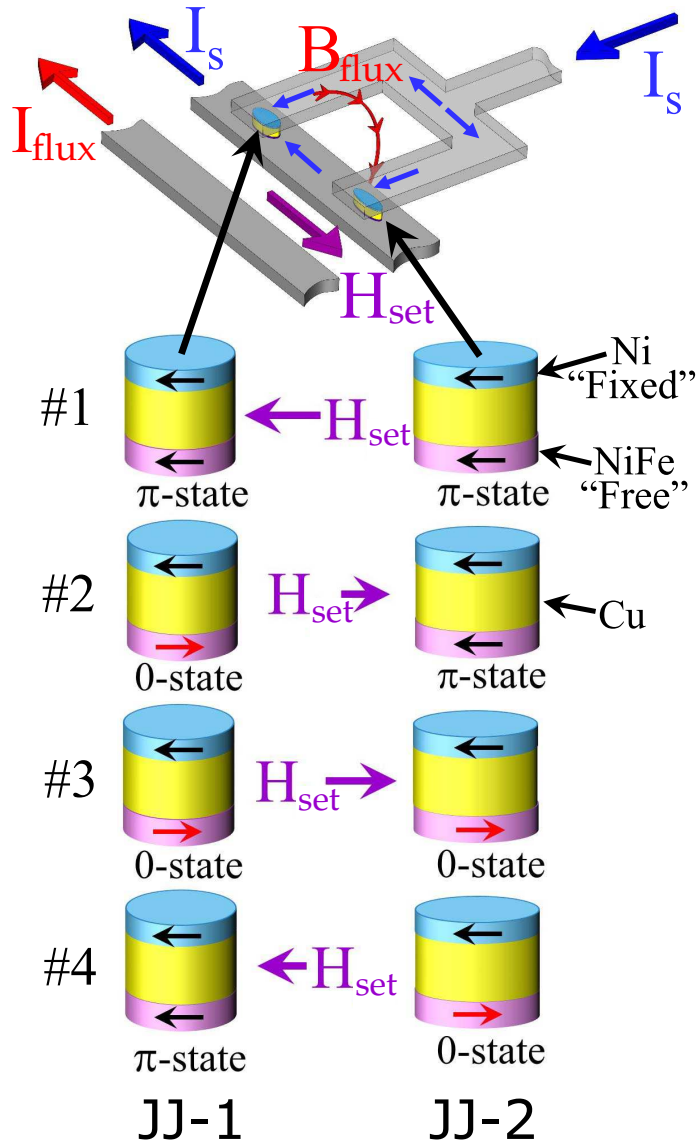


Figure 7.2: *Spin-valve SQUID schematic and the configuration of the four magnetic states.* The circuit layout for the asymmetric SQUID (top) is composed of a superconducting loop intersected by two spin-valve Josephson junctions (small yellow ellipses). The critical current in the SQUID (probed by the measurement current I_s) oscillates as a function of the flux inside the loop, provided in part by a current I_{flux} through a nearby superconducting flux-line to add a field B_{flux} to the loop. The magnetic state of the junctions is controlled via an external in-plane magnetic field H_{set} . The (bottom) diagrams show the four possible orientations of the F_1 and F_2 magnetizations, whose configuration sets the phase across the junctions to be either 0 or π . The junctions are elliptical in shape, one with a smaller aspect ratio (JJ-1) and the other, with a larger aspect ratio (JJ-2), each with area $0.5 \mu m^2$. The length of the purple arrows indicate the magnitude of H_{set} for each state. Figure modified from [18].

of all the magnetic layers in both junctions. Next, a small set field H_{set} is applied in the reverse direction, which will cause the “free”-layer in the less eccentric junction to reverse its magnetization direction relative to that of the “fixed”-layer. If H_{set} is not too large, then both magnetic layers in the more eccentric junction will remain parallel. The net result is a relative total phase shift of π between the two junctions in the SQUID.

The phase shift between the two magnetic states was detected by adding flux to the SQUID loop, accomplished by driving a small current I_{flux} through a nearby superconducting line, which we refer to as the “flux-line.” The total critical current of the SQUID oscillates as a function of the applied flux, as shown in Fig. 7.3, allowing for the detection of phase shifts by comparing the curves before and after the magnetic switching. The sudden phase shifts in Fig. 7.3 are also generally accompanied by sudden shifts in the critical current (mainly because the P and AP states do not have perfect alignment about $\phi = \pi/2$, as in Fig. 7.1).

After applying H_{set} the external field is always returned to zero before measuring the SQUID oscillations versus I_{flux} . Further increasing H_{set} will eventually cause the Py layer in the more eccentric junction to also reverse its magnetization, returning the total phase shift in the SQUID to 0. Reversing the direction of the set field, one can then trace out a full magnetic major-loop, as shown in Fig. 7.3.

From a careful inspection of the current paths through the SQUID in Fig. 7.2, one will notice that the path length traversed by the current in the two arms the SQUID is not equal. Current exiting one of the junctions into the straight bottom electrode must then travel (in the bottom electrode) between the “fork” opening in the top electrode, whereas current coming from the other junction does not. This leads to an asymmetry in the geometrical inductance of the two arms of the SQUID that distorts the resulting oscillations of the critical current versus the applied flux.

Moreover, the magnitude of the critical current may divide in an asymmetric manner through the two junctions. These two features were not fully appreciated by our group until high-resolution SQUID data was obtained and the shape of the resulting oscillations was investigated. As it turns out, the two effects mentioned above complicate the analysis by contributing new “effective” phase shifts to the resulting SQUID oscillations, but can be properly accounted for using the theory that follows.

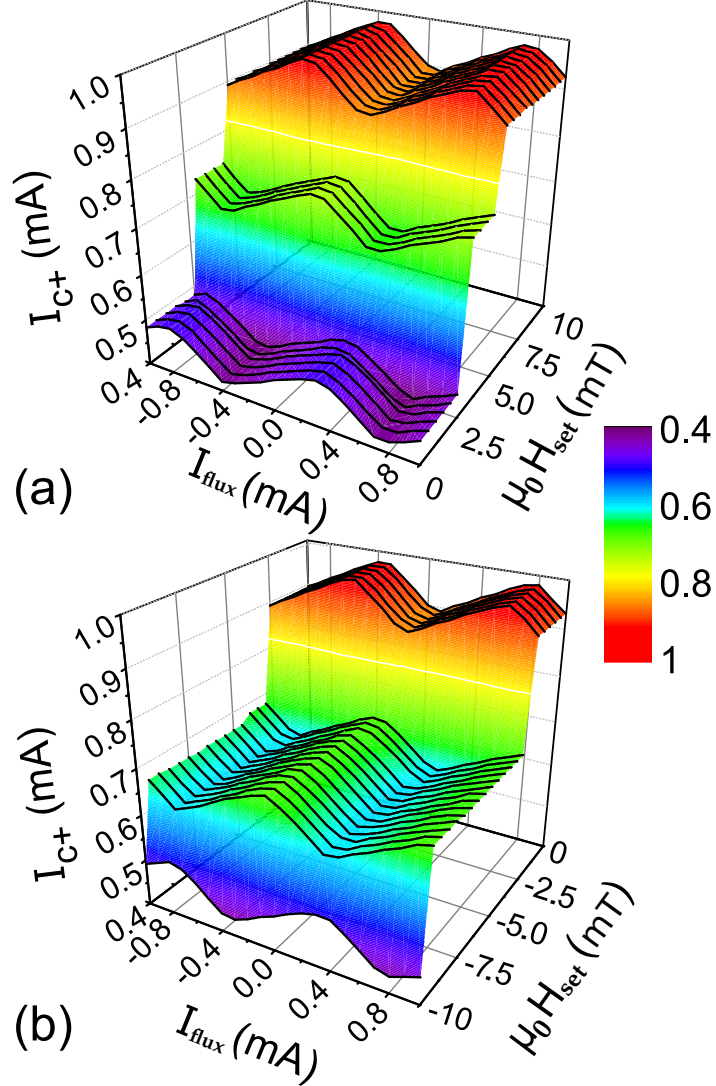


Figure 7.3: *Oscillations in the critical current versus the current applied to the flux-line and the in-plane set field used to control the magnetic state of the SQUID.* After initializing all of the magnetic layers in the SQUID to have parallel alignment using a large negative in-plane field, next a small positive set field H_{set} is momentarily applied to the sample. Current is then applied to the flux line, causing the positive critical current I_{c+} to oscillate versus the applied flux, corresponding to the lower purple colored state in (a). The SQUID oscillations are always measured in zero external field. Further increase of H_{set} will cause the free magnetic layer in one of the junctions to change its magnetization, resulting in a π -phase shift relative to the other junction, the green colored state in (a). At even larger values of H_{set} , the free layer in the second junction will flip the direction of its magnetization and a second phase shift occurs, the red colored state in (a). Reversing the direction of H_{set} , one can switch the two junctions back to their original orientations, as shown in (b), completing a magnetic major-loop. The sudden jumps in the relative phase correspond to the four magnetic states, whose layer configurations are shown in Figure 7.2. The sudden phase changes are also accompanied by changes in the magnitude of I_{c+} . Figure modified from [18].

7.2 Theory of the Asymmetric DC SQUID

We now return to the theory of the DC SQUID, but consider it in a more general sense, one that accounts for asymmetries in both the critical currents in the two junctions and in the geometric inductance of the two arms of the SQUID loop. We follow and extend upon a clever method first described by W.T. Tsang and T. Van Duzer in 1975 [146]. Consider the SQUID shown in Fig. 7.2, containing two junctions, which we assume are small enough to contain only a small fraction of a flux quantum. As in Eq. (2.54), the total current in the SQUID is the sum of the currents in the two arms according to the Josephson effect,

$$I(\phi_1, \phi_2) = I_{1c} \sin(\phi_1) + I_{2c} \sin(\phi_2), \quad (7.4)$$

where ϕ_1 and ϕ_2 are the gauge-invariant phase differences across Josephson junctions 1 and 2, respectively, with I_{1c} and I_{2c} their critical currents. The phase differences are subject to the constraint of Eq. (2.51),

$$\phi_2 - \phi_1 = \frac{2\pi}{\Phi_0} \Phi \pmod{2\pi}. \quad (7.5)$$

The goal is to determine the dependence of the total current in the SQUID on an externally applied flux.

As we saw previously in Eq. (2.52), the total magnetic flux Φ in the SQUID is the sum of the contributions from an externally applied magnetic field, Φ_a , and from the self-inductance L of the loop,

$$\Phi = \Phi_a + \Phi_s. \quad (7.6)$$

Generalizing to an asymmetric inductance, we define L_1 and L_2 to be the inductances of the two arms of the SQUID, such that $L = L_1 + L_2$. Thus, we rewrite the second term in

Eq. (7.6) to be

$$\Phi_s(\phi_1, \phi_2) = L_1 I_{c1} \sin(\phi_1) - L_2 I_{c2} \sin(\phi_2). \quad (7.7)$$

The phase difference between the two junctions, Eq. (2.51), becomes

$$\phi_1 - \phi_2 = \theta_a + \alpha_1 \sin(\phi_1) - \alpha_2 \sin(\phi_2), \quad (7.8)$$

where for convenience we have defined three parameters corresponding to the applied flux, θ_a , and the flux generated by the flow of the two currents, α_1 and α_2 , defined to be:

$$\theta_a \equiv \frac{2\pi}{\Phi_0} \Phi_a, \quad (7.9)$$

$$\alpha_1 \equiv \frac{2\pi}{\Phi_0} L_1 I_{c1}, \quad (7.10)$$

$$\alpha_2 \equiv \frac{2\pi}{\Phi_0} L_2 I_{c2}. \quad (7.11)$$

The problem of finding how the current $I(\phi_1, \phi_2)$ relates to the external flux, θ_a , amounts to finding the maxima and minima of Eq. (7.4) with respect to the constraint imposed on ϕ_1 and ϕ_2 by Eq. (7.8). The solution proposed by Tsang and Van Duzer is to apply the method of Lagrange multipliers by introducing a new parameter λ to Eq. (7.4),

$$\begin{aligned} I(\phi_1, \phi_2, \lambda) = & I_{1c} \sin(\phi_1) + I_{2c} \sin(\phi_2) \\ & + \lambda[\phi_2 - \phi_1 + \theta_a + \alpha_1 \sin \phi_1 - \alpha_2 \sin \phi_2], \end{aligned} \quad (7.12)$$

which is permissible as the term in square brackets, from Eq (7.8), is equal to zero. We then solve for the critical points of Eq. (7.12) with respect to ϕ_1 , ϕ_2 , and λ . By finding the partial derivatives $\partial I/\partial\phi_1$, $\partial I/\partial\phi_2$, $\partial I/\partial\lambda$, and setting them each to zero, the resulting

three equations can be used to eliminate λ , leaving us with two equations that relate the critical values of ϕ_1 and ϕ_2 (denoted with subscript c 's):

$$\phi_{2c} = \cos^{-1} \left(\frac{-1}{I_{c2}/(I_{c1} \cos(\phi_{1c})) + \alpha} \right), \quad (7.13)$$

$$\theta_a = \phi_{2c} - \phi_{1c} + \alpha_2 \sin \phi_{2c} - \alpha_1 \sin \phi_{1c}, \quad (7.14)$$

where $\alpha = \alpha_2 + \alpha_1(I_{c2}/I_{c1})$. To obtain the critical current at a fixed value of the applied flux, θ_a , one needs to find the set of values (ϕ_{1c}, ϕ_{2c}) , that satisfy Eqs. (7.13) and (7.14). In order to quickly find the critical current over the entire θ_a axis, first we solve for all of the (ϕ_{1c}, ϕ_{2c}) pairs that satisfy Eq. (7.13): a locus of solutions in the ϕ_1 - ϕ_2 plane. Examples of these solutions are shown in the left panel of Fig. 7.4. The shape of the locus of solutions varies depending on the input physical parameters I_{c1} , I_{c2} , α_1 , α_2 , forming either discrete loops or continuous oscillations in the ϕ_1 - ϕ_2 plane due in part to the argument of the \cos^{-1} in Eq. (7.13) being bounded by ± 1 , discussed later. Next, we insert the (ϕ_{1c}, ϕ_{2c}) pairs into Eq. (7.14) to find θ_a , while the same pairs are correspondingly inserted into Eq. (7.4) to find $I_c(\theta_a)$. This results in the curves shown in the middle panel of Fig. 7.4. The periodic SQUID oscillations shown in the right panel of Fig. 7.4 are obtained by shifting the $I_c(\theta_a)$ solutions by integer multiples of π and finding the intersections of the resulting curves.

Closer inspection of Eq. (7.13) reveals that for certain values of the parameters α and the ratio I_{c2}/I_{c1} , the locus of solutions will become an open continuous curve along the ϕ_1 or ϕ_2 axis, such as in Fig. 7.5, when either one of the following two conditions is satisfied:

$$(I_{c2}/I_{c1} + \alpha \leq 1) \quad (7.15)$$

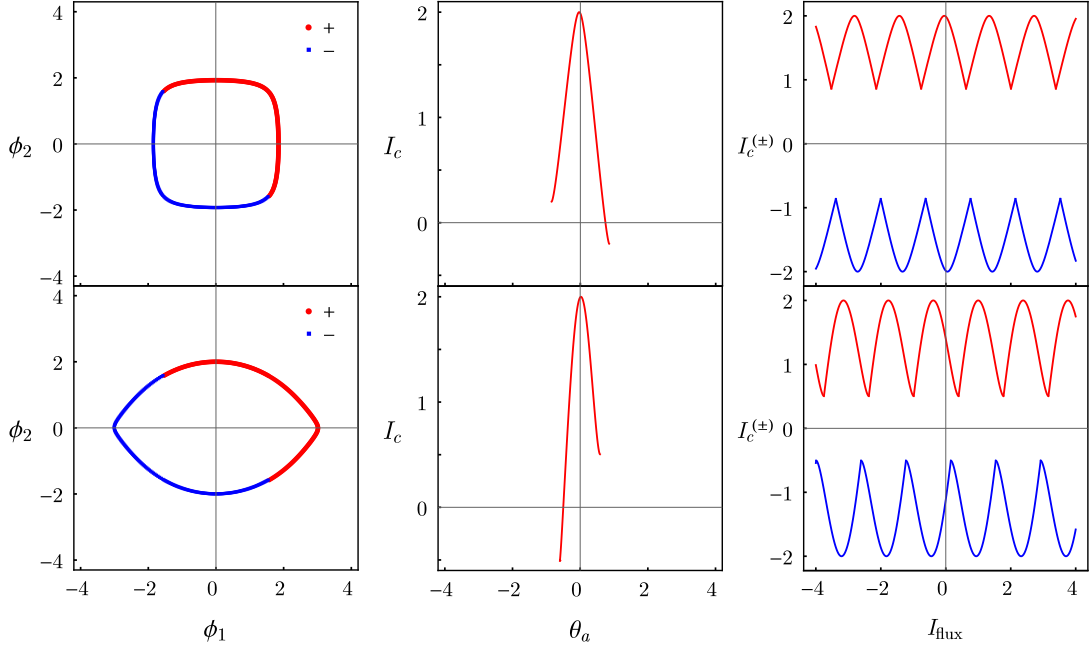


Figure 7.4: *Asymmetric SQUID theory, closed solutions.* The left panel shows the locus of solutions to Eq. (7.13), where the independent variable is taken to be either ϕ_1 (red) or ϕ_2 (blue). For the set of the input parameters, listed below, the locus of solutions are discrete closed rings in the ϕ_1 - ϕ_2 plane. Inserting the (ϕ_1, ϕ_2) pairs into Eq. (7.14) and Eq. (7.6), yields solutions for the critical current I_c versus the flux applied to the SQUID, θ_a , shown in the middle panel. Shifting the $I(\theta_a)$ solution by integer multiples of π , and finding the intersections of the resulting curves, and restoring the physical units, determines the SQUID oscillation curves versus the applied flux current, I_{flux} , shown in the right panel. Units of the flux current are in mA for a SQUID where $I_{\text{flux}} = 1.7$ mA puts a flux of Φ_0 in the SQUID loop. Input parameters (top): $I_{c1} = 1.1$, $I_{c2} = 0.9$, $\alpha_1 = 1.209$, $\alpha_2 = 0.989$, (bottom): $I_{c1} = 0.748$, $I_{c2} = 1.252$, $\alpha_1 = 0.205$, $\alpha_2 = 0.344$.

$$(I_{c2}/I_{c1} - \alpha \geq 1). \quad (7.16)$$

The nature of these “open” solutions presents a minor additional complication. For instance, as $\phi_{c1} \rightarrow 0$, the \cos^{-1} will become imaginary when the condition $(I_{c2}/I_{c1}) + \alpha < 1$ is satisfied. In this case, we rearrange Eq. (7.13), solving for ϕ_{1c} ,

$$\phi_{1c} = \cos^{-1} \left(\frac{-(I_{c2}/I_{c1})}{(1/\cos(\phi_{2c})) + \alpha} \right), \quad (7.17)$$

and take ϕ_{2c} to be the independent variable. Likewise, as $\phi_{c2} \rightarrow 0$, Eq. (7.17) will become imaginary when $(I_{c2}/I_{c1}) - \alpha > 1$, so we use Eq. (7.13), where ϕ_{1c} is the independent variable. What's more is that very close to the boundary of either of the two conditions $(I_{c2}/I_{c1}) \pm \alpha \approx 1$ the solution for $I_c(\theta_a)$ does not increase monotonically. Figure 7.5 shows the shape of the locus of solutions and the resulting solutions for the SQUID oscillations for all the cases of the open solutions and near the edge of the discontinuity.

From this general construction, we can analyze several important features present in the SQUID oscillation curves. As previously discussed in Ch. 2, the depth of the modulation decreases as the total inductance or critical current in the SQUID increases, defined by the screening parameter, which now becomes,

$$\beta_L = \frac{LI_c}{\Phi_0} = \frac{(L_1 + L_2)(I_{c1} + I_{c2})}{\Phi_0}. \quad (7.18)$$

In addition, the asymmetries due to the inductance and critical current cause the curves to have several new features. The inductance asymmetry distorts the oscillations into a tilted “ratchet”-like shape. The extent of the skewness increases according to the parameter

$$\alpha_L = \frac{L_2 - L_1}{L_2 + L_1}. \quad (7.19)$$

A ratchet leaning to the right indicates that the SQUID has $\alpha_L > 0$, or $L_2 > L_1$.

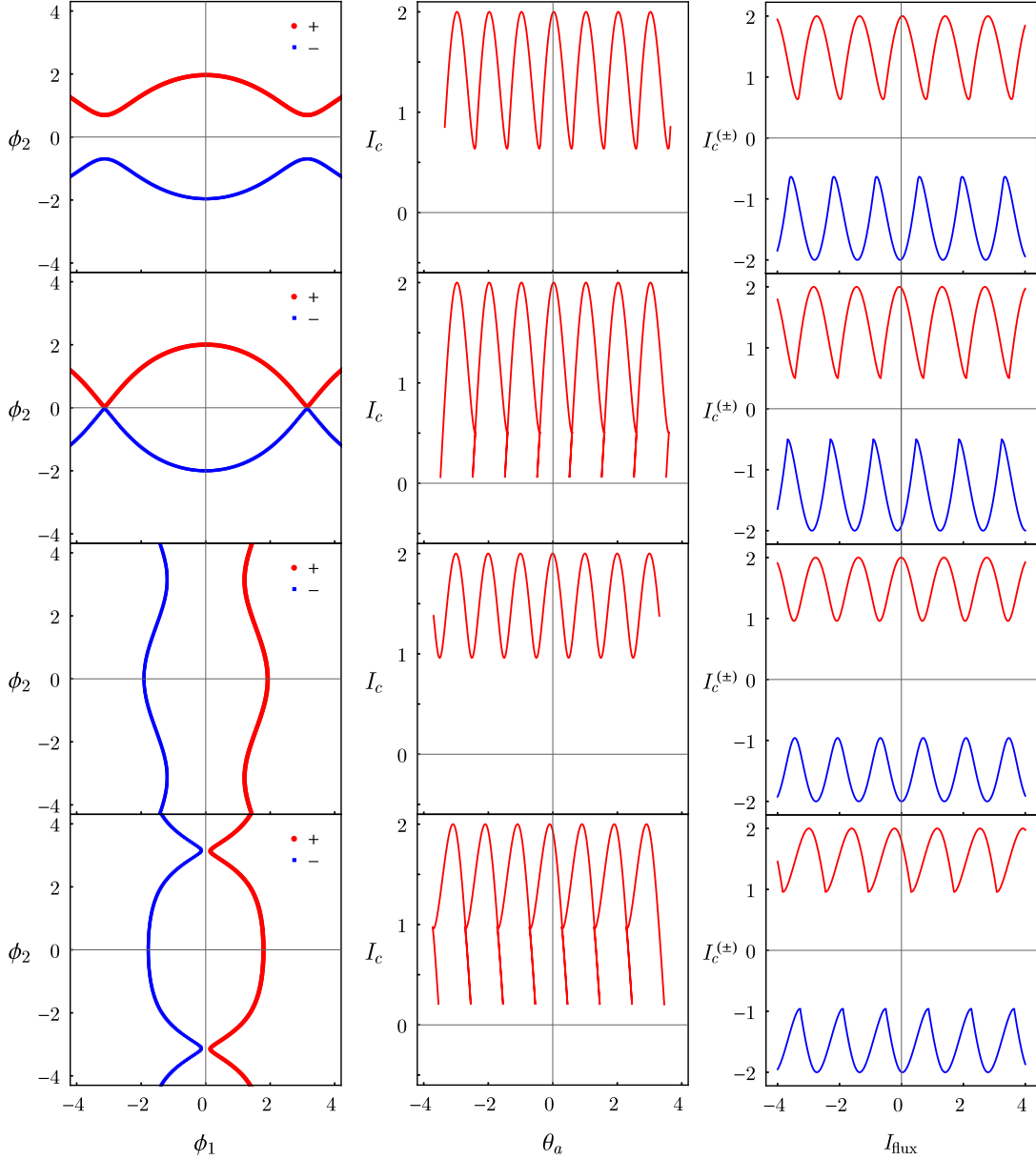


Figure 7.5: *Asymmetric SQUID theory, open solutions.* Similar to Fig. 7.4, but using input parameters, listed below, which result in the locus of solutions in the ϕ_1 - ϕ_2 plane that are continuous (“open”) curves of either ϕ_1 or ϕ_2 . Close to the cross over point between open and closed solutions, as shown in the 2nd and 4th rows, the solutions for $I_c(\theta_a)$ do not always increase monotonically with θ_a , as mentioned in the text. Nonetheless the SQUID oscillations can still be computed. Input parameters: (1st row): $I_{c1} = 0.682$, $I_{c2} = 1.318$, $\alpha_1 = 0.157$, $\alpha_2 = 0.317$; (2nd row): $I_{c1} = 0.748$, $I_{c2} = 1.252$, $\alpha_1 = 0.200$, $\alpha_2 = 0.336$; (3rd row): $I_{c1} = 0.682$, $I_{c2} = 1.318$, $\alpha_1 = 0.157$, $\alpha_2 = 0.317$; (4th row): $I_{c1} = 1.48$, $I_{c2} = 0.52$, $\alpha_1 = 0.046$, $\alpha_2 = 0.016$. Units of the flux current are in mA, for a SQUID where $I_{\text{flux}} = 1.7$ mA puts a flux of Φ_0 in the SQUID loop.

Moreover, the critical current asymmetry causes the oscillations for the positive (I_{c+}) and negative (I_{c-}) critical current curves to become shifted with respect to one another in opposite directions along the flux axis, according to the parameter[†]

$$\alpha_I = \frac{I_{c2} - I_{c1}}{I_{c2} + I_{c1}}. \quad (7.20)$$

The origin of those shifts can be understood from the following description, which was first pointed out to us by our collaborator, Don Miller from Northrop Grumman Corporation. Consider the peak value of the critical current, from Eq. (7.4), $I = I_{c1} + I_{c2}$, which occurs when the phase across each junction is $\phi_1 = \phi_2 = \pi/2$. The maximum self-induced flux through the SQUID loop, from Eq. (7.7), is $\Phi_s^{\text{peak},+} = L_2 I_{c2} - L_1 I_{c1}$, a quantity that must be balanced by the externally applied flux. Thus, the peak of the maximum positive critical current I_{c+} occurs at a flux $\Phi^{\text{peak},+} = -\Phi_s^{\text{peak},+}$. On the other hand, the maximum negative critical current occurs at a flux $\Phi^{\text{peak},-} = -\Phi^{\text{peak},+}$, and hence the positive and negative critical current curves are shifted with respect to each other by an amount

$$\Delta\Phi^{\text{peak}} \equiv \Phi^{\text{peak},+} - \Phi^{\text{peak},-} = 2(L_2 I_{c2} - L_1 I_{c1}). \quad (7.21)$$

Since the critical current is periodic with respect to flux the relative phase shift, $\Delta\Phi^{\text{peak}}$, can only be determined modulo Φ_0 . However, it is still possible to determine which value of $\Delta\Phi^{\text{peak}}$ corresponds to the physically relevant value by self-consistently fitting the data from the four magnetic states. From the best-fit parameters one can then observe that after a magnetic switching event, one of the junction's critical currents will change, while the other's remains approximately constant. Finally, between the four magnetic states one

[†]The value of α_I can also cause changes in the depth of the modulation.

should extract a self-consistent set of parameters for the inductances L_1 and L_2 , which are set by the sample geometry. In general, if one finds the wrong value of $\Delta\Phi^{\text{peak}}$, it typically results in an unphysical value of L_1 and L_2 .

These considerations allowed us to write a generalized nonlinear least-squares SQUID fitting program using the Mathematica software package that that can quickly compute the solutions for any combination of input parameters. For the shift, we define a parameter ϕ_{shift} that describes how far the nearest peak of the I_{c+} curve is shifted away from zero. In the fitting program we work in terms of the dimensionless set of parameters just described (β_L , α_L , α_I , ϕ_{shift}), but one can equivalently use the set $(I_{c1}, I_{c2}, \alpha_1, \alpha_2)$. For reference, the conversion between the two sets of parameters is given by:

$$\alpha = \pi\beta_L(1 + \alpha_I), \quad (7.22)$$

$$\alpha_1 = \pi\beta_L(1 - \alpha_L)(1 - \alpha_I)/2, \quad (7.23)$$

$$\alpha_2 = \pi\beta_L(1 + \alpha_L)(1 + \alpha_I)/2, \quad (7.24)$$

with peak shift, $\Phi_s^{\text{peak},+} = L_2I_{c2} - L_1I_{c1} = \beta_L(\alpha_L + \alpha_I)\Phi_0/2$.

The code can perform a simultaneous global fit of both the positive (I_{c+}) and negative (I_{c-}) critical current data from the experiment. The user can choose, depending on the nature of the data, to use any number of the parameters listed above either as fixed inputs or as free parameters to be optimized in the fit, and find the standard errors on each of the free parameters. Using the code, the fitting of typical SQUID oscillation data takes between 2-10 minutes depending on the step size and accuracy desired (and the specifications of the machine used).

Table 7.1: *Best-fit parameters for the four magnetic states using the asymmetric SQUID theory.* The uncertainties are extracted via the “NonlinearModelFit” routine in Mathematica, and do not account for possible correlations between the fitting parameters. The difference between the individual phase shifts ϕ_{shift} for adjacent rows in the table is $\approx \pm\pi$ (the values in the last two columns are listed in units of 2π). For convenience we define a global phase shift, $\phi_{\text{global}} = -0.1271$, which is the average of the values $(\phi_{\text{shift}} - 0.5)$ in the $(0-\pi)$ and $(\pi-0)$ states.

State	β_L	α_L	α_I	I_{c+} (μA)	$ I_{c-} $ (μA)	ϕ_{shift}	$\phi_{\text{shift}} - \phi_{\text{global}}$
$(\pi-\pi)$	4.207 ± 0.023	0.330 ± 0.006	-0.147 ± 0.006	506.0 ± 0.2	510.7 ± 0.3	-0.1195 ± 0.0007	0.0076
$(0-\pi)$	6.296 ± 0.030	0.335 ± 0.005	-0.472 ± 0.005	771.2 ± 0.2	762.8 ± 0.2	$+0.3517 \pm 0.0006$	0.4788
$(0-0)$	8.198 ± 0.033	0.345 ± 0.004	-0.150 ± 0.004	985.5 ± 0.2	987.8 ± 0.2	-0.1360 ± 0.0005	-0.0089
$(\pi-0)$	5.957 ± 0.020	0.339 ± 0.004	$+0.176 \pm 0.004$	707.7 ± 0.2	719.6 ± 0.2	$+0.3955 \pm 0.0004$	0.5226

7.3 SQUID Oscillation Data: Comparison to Theory

For the same SQUID shown in Fig. 7.3, higher resolution data in each of the four magnetic states was measured and fit using the general SQUID theory described above. As shown in Fig. 7.6(a), the theoretical fits for the positive (I_{c+}) and negative (I_{c-}) critical current oscillations versus the applied flux show excellent agreement with the measured data.

Those oscillations clearly show the tilted ratchet shape of the curves due to the inductance asymmetry of the SQUID.[†] The effective phase shifts between the curves make it hard to discern by eye whether or not a relative 0 or π -phase shift has occurred between two of the magnetic states, but can be unequivocally extracted from the best-fit parameters.

As shown in Table 7.1, the analysis produces only one consistent set of best-fit parameters, with rather small error bounds. When these variables are converted into the physical parameters for the inductances and the critical currents, shown in Table 7.2, the values are in agreement with those expected from the design geometry based on simulations using the

[†]We verified that rewiring the sample, so that the flux current flows in the opposite direction, reverses the direction that the ratchet leans, as expected by the theory.

Table 7.2: *Inductances and critical currents extracted from the least-squares fits.* After fitting the four magnetic states with the asymmetric SQUID theory, the best fit parameters from Table 7.1 were converted into the physical parameters below. Note that the two inductances in the two arms of the SQUID L_1 and L_2 are very consistent between the four states. Also, between adjacent states in the table the critical current noticeably changes in the junction whose magnetic state was modified, whereas in the other junction the critical current is approximately constant.

State	L_1 (pH)	L_2 (pH)	I_{c1} (μA)	I_{c2} (μA)
$(\pi-\pi)$	5.73 ± 0.05	11.38 ± 0.08	291.6 ± 1.5	216.8 ± 1.5
$(0-\pi)$	5.64 ± 0.04	11.33 ± 0.07	564.5 ± 1.8	202.5 ± 1.8
$(0-0)$	5.63 ± 0.03	11.56 ± 0.06	567.3 ± 2.0	419.3 ± 2.0
$(\pi-0)$	5.71 ± 0.03	11.56 ± 0.05	294.0 ± 1.3	419.7 ± 1.3

FastHenry software package. The most important finding of the fitting analysis is that the phase shifts between the adjacent magnetic states in the Table 7.1 all differ by $\approx \pm\pi$.

Another way to better visualize the relative phase shifts between the magnetic states is to compare the plots of their average critical current $I_c^{\text{avg}} = (I_{c+} - I_{c-})/2$ versus the applied flux, as shown in Fig. 7.6(b). The particular shape of the I_c^{avg} curves is determined by the misalignment between the I_{c+} and I_{c-} curves, but clearly shows that the I_c^{avg} curves transition between maxima and minima for each of the four magnetic states.

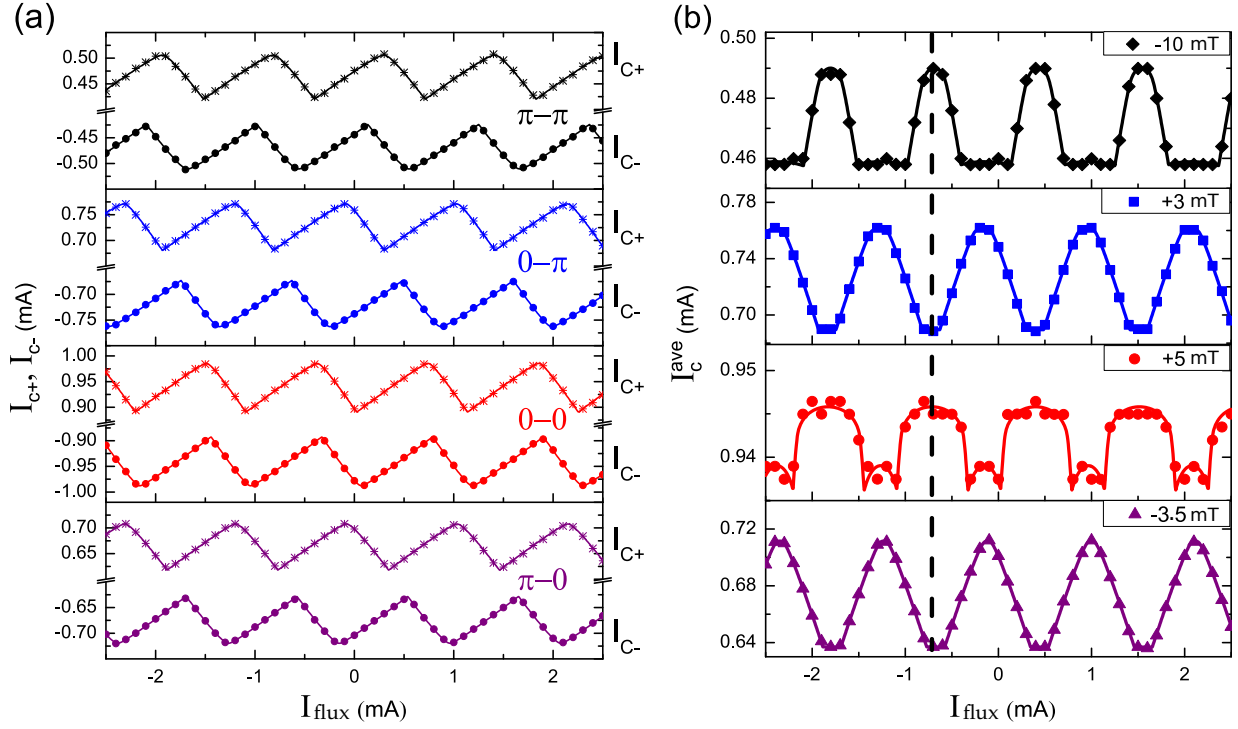


Figure 7.6: *Using asymmetric SQUID theory to fit the SQUID oscillation data from the four magnetic states.* In (a) the measured positive and negative critical current data (I_{C+} and I_{C-}) are plotted versus the flux-line current, I_{flux} , for the four magnetic states. The states are labeled $\pi - \pi$, $0 - \pi$, etc., according to the phase states of JJ-1 and JJ-2, as in Fig. 7.2. The lines are the theoretical least-squares fits to the data. In b) the average critical current, $I_c^{avg} = (I_{C+} - I_{C-})/2$ is plotted versus the applied flux to more clearly see the relative π phase-shifts between the four magnetic states. The solid lines in (b) are determined by the best-fit curves from (a). At a fixed value of the flux current (dashed line) one can see that the states transition from maxima to minima. The labels denote the switching field for each magnetic state. Figure modified from [18].

Chapter 8

Spin-Triplet Josephson Junctions Containing a PMA

SAF

In this chapter we present measurements of Josephson junctions containing three magnetic layers with noncolinear magnetizations carrying spin-triplet supercurrent [21]. The junctions are of the form $S/F'/N/F/N/F''/S$, where S is superconducting Nb, F' is either a thin Ni or Permalloy layer with in-plane magnetization, N is the normal metal Cu, F is a synthetic antiferromagnet (SAF) with magnetization perpendicular to the plane, composed of Pd/Co multilayers on either side of a thin Ru spacer, and F'' is a thin Ni layer with in-plane magnetization. The supercurrent in these junctions decays more slowly as a function of the F -layer thickness than for similar spin-singlet junctions not containing the F' and F'' layers. The slower decay is the prime signature that the supercurrent in the central part of these junctions is carried by spin-triplet pairs. The junctions containing $F' = \text{Permalloy}$ are suitable for experiments, such as those discussed in Ch. 9, where either the amplitude of the critical current or the ground-state phase difference across the junction is controlled by changing the relative orientations of the magnetizations of the F' and F'' layers.

As we discussed in Ch. 4, the theory of spin-triplet Josephson junctions predicts that the ground-state phase difference across a junction of the form described above depends on the relative orientations of the three magnetizations [80–82, 105, 147, 148]. Spin-triplet junctions where the magnetization of all three ferromagnetic layers are coplanar exhibit complementary 0 and π -phase states dependent only on whether the outer two magnetizations are parallel

or antiparallel.

In principle, there are many ways to design a Josephson junction to test that prediction. We have focused on designs where the magnetizations of the outer F' and F'' layers both lie in-plane; the junctions are given an elliptical shape to set the directions of those in-plane magnetizations by shape anisotropy. But the elliptical junction shape makes it difficult to achieve non-colinear magnetization in the central F layer, if it is also in-plane. A solution is to use out-of-plane magnetization for F , which is easily accomplished using a magnetic material with strong perpendicular magnetic anisotropy (PMA) [106]. Then, one can utilize shape anisotropy to preferentially orient the magnetization direction of the F' and F'' layers, all the while preserving the optimal 90 degree relative magnetization angle between each successive ferromagnetic layer. Previous efforts by our group, primarily undertaken by Eric Gingrich, to detect the Josephson junction phase change using such a design were only partially successful, however [109]; while a π phase change appeared in some experiments, the magnetic behavior of the junctions was poor and irreproducible. We suspected at the time that stray fields from the domain walls in the PMA F layer penetrated the F' and F'' layers and ruined their magnetic properties. A possible solution to that problem is to replace the central PMA layer with a PMA synthetic antiferromagnet (SAF), in which each magnetic domain in the lower half of the SAF is coupled to a domain with opposite-pointing magnetization in the upper half of the SAF. Such a system should produce minimal stray fields in the F' and F'' layers that are located above and below the SAF [149].

The main result of this chapter is that the critical current in these junctions decays more slowly with increasing thickness of the PMA SAF than it does in junctions that do not contain the F' and F'' layers. That result represents strong evidence that the supercurrent in the central part of these junctions is carried by spin-triplet pairs, whereas it is carried

only by the short-range components in the control samples. The results of this chapter lay the groundwork for Ch. 9, where the spin-triplet Josephson junctions presented here will be implemented into phase-controllable SQUID devices.

8.1 Magnetic Properties of Pd/Co Multilayers and Synthetic Anti-Ferromagnets With Perpendicular Magneto-Anisotropy

Thin multilayers of Pd and Co can be grown to have perpendicular magnetic anisotropy, i.e. with magnetization perpendicular to the sample plane, as reported by Chang *et al.* [150]. Moreover, when two such Pd/Co multilayers are separated by a thin normal metal spacer (such as Ru, Rh, Ir, or Cu), they may couple via the exchange interaction to form a SAF, in which the magnetizations on either side of the spacer align in an antiparallel fashion. The outstanding PMA and SAF properties of such layers have attracted interest for their use in spin-transfer-torque magnetic random access memories [151] and other applications. Spurred by the initial suggestion of Mike Schneider at the National Institute of Standards and Technology, Boulder, we decided to investigate if PMA SAFs could be advantageous for spin-triplet Josephson junctions with phase control. For the PMA SAF to serve as the central F layer and optimize the generation of long-range spin-triplet supercurrent its magnetization needs to remain pinned perpendicular to the sample plane over the range of measurement fields used in the experiments.

To characterize the Pd/Co multilayers and verify that they have PMA, we sputtered films of: Nb(5)/Cu(5)/[Pd(d_{Pd})/Co(0.3)] $_n$ /Pd(d_{Pd})/Cu(5)/Nb(5), where the layer thicknesses in nanometers are shown in parentheses and the sequences in brackets are repeated $n = 10$ or 20 times. Similar to Chang *et al.* [150] we fix the Co thickness to 0.3 nm while the Pd

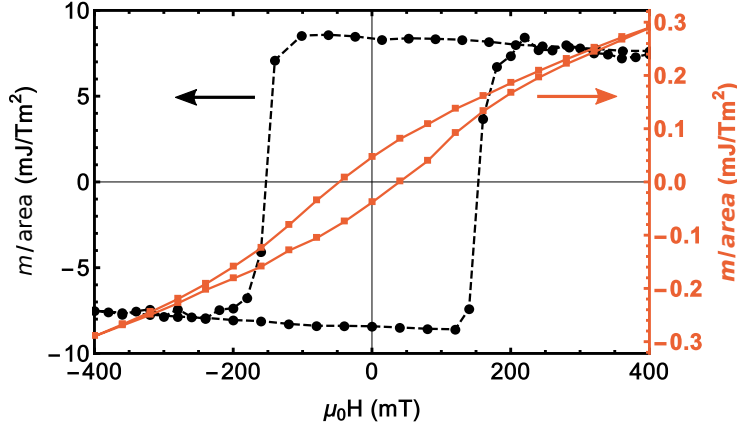


Figure 8.1: *Hysteresis loops of a Pd/Co multilayer film measured at 5K using a SQUID magnetometer.* The data are expressed as total magnetic moment m per unit area. With the applied magnetic field perpendicular to the sample plane (black, left axis), the loop is square-like indicating the Pd/Co multilayer has perpendicular magento-anisotropy (PMA), with a large coercive field of over 160 mT. With the applied field parallel to the sample plane (red, right axis) the hysteresis is only slightly discernable, thus the magnetization has a very small in-plane component. Also, note the comparatively smaller scale on the right axis. The sample is composed of Nb(5)/Cu(5)/[Pd(0.9)/Co(0.3)]₁₀/Pd(0.9)/Cu(5)/Nb(5) with thicknesses in nanometers. Lines are to guide the eye.

thickness, d_{Pd} , was varied from 0.8 - 1.0 nm. All the samples throughout this chapter were fabricated using high-vacuum sputtering deposition, using the same procedure and growth conditions as used in Ch. 6.2.

We measured the films' magnetic moment m per unit area vs. the applied magnetic field (M - H loop), using a Quantum Design dc-SQUID magnetometer at 5 K. Sweeping an applied magnetic field that is perpendicular to the sample plane results in square-like M - H loops, as shown in Fig. 8.1 (black data points), confirming that the Pd/Co multilayer has PMA. The sample with $d_{\text{Pd}} = 0.9$ nm had the best magnetic properties: a coercive field of over 160 mT and the largest squareness. With H applied parallel to the sample plane, the M - H loops show only a slight hysteresis with small remanent magnetization, indicating a very small in-plane moment (red data points). Note that dividing the m/area values by the

total Co thickness of 3.0 nm gives a saturation magnetization of about 2.7×10^6 A/m (=2700 emu/cm³) which is about twice the saturation magnetization of bulk Co. This is because the Co partially polarizes the surrounding Pd layers [152].

8.1.1 Synthetic Anti-Ferromagnets

Next, we characterized the magnetic behavior of two such Pd/Co multilayers arranged on either side of a thin Ru spacer to form a SAF with PMA. The coupling of the Pd/Co multilayer into a SAF structure arises due to interlayer exchange coupling (IEC) between the two multilayers. The energy density of the IEC can be modulated by tuning the thickness of the spacer layer and depends strongly upon which material(s) it forms interfaces with. We arranged the Ru spacer to have adjoining Co layers on either side, similar to Chang *et al.* [150].

To optimize the antiferromagnetic coupling in the SAF, we sputtered a set of samples with an “unbalanced” SAF configuration of the form: Nb(5)/Cu(5)/[Pd(0.9)/Co(0.3)]₁₂/Ru(d_{Ru})/[Pd(0.9)/Co(0.3)]₁₀/Cu(5)/Nb(5), varying the Ru thickness between $d_{\text{Ru}}=0.7, 0.8, \dots, 1.1$ nm. We measured the samples’ magnetic response in a dc-SQUID magnetometer with H perpendicular to the sample plane. As shown in Fig. 8.2, at a Ru thickness of 0.7 nm the Pd/Co multilayers are ferromagnetically coupled, since only a single (slightly distorted) loop is observable. As the Ru thickness increases, the M - H loops have an intermediate step with a flat plateau in the magnetization, indicating stable antiferromagnetic exchange coupling at applied fields less than ± 250 mT. The maximum width of the intermediate plateau, and hence the maximum antiferromagnetic coupling measured, was obtained for the samples with $d_{\text{Ru}} = 0.9$ and 1.0 nm (not shown). Therefore, in the Josephson junction samples presented in the next section we choose to fix $d_{\text{Ru}} = 0.95$ nm.

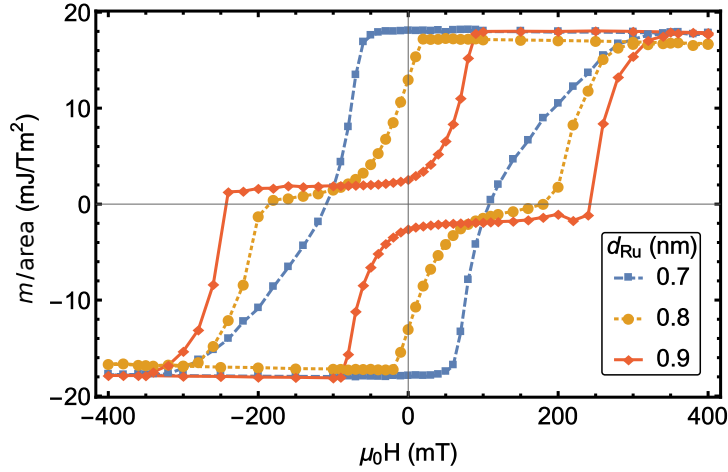


Figure 8.2: *Hysteresis loop measurements of synthetic antiferromagnet (SAF) films measured using a dc-SQUID magnetometer.* The samples are measured at 5K with the applied field perpendicular to the sample plane, with the data expressed as the total magnetic moment m per unit area. The SAF is composed of Pd(0.9 nm)/Co(0.3 nm) multilayers separated by a thin Ru spacer, whose thickness, d_{Ru} , was varied from 0.7 to 1.1 nm (0.7-0.9 nm shown). At a Ru thickness of 0.7 nm (blue) the Pd/Co multilayers are ferromagnetically coupled out-of-plane, since only a single loop is observable. However, as the Ru thickness increases, the out-of-plane M - H loops have an intermediate step with a flat plateau in the magnetization (yellow, red). The width of the intermediate plateau is maximal near $d_{\text{Ru}} = 0.9$ (red), indicating stable antiferromagnetic exchange coupling at applied fields less than ± 250 mT. Lines are to guide the eye.

Note that the extra two repeats of the Pd/Co multilayer in the data presented in Fig. 8.2 are added merely to accentuate the separation between the two corresponding hysteresis loops, allowing us to more easily determine the optimal Ru thickness. In spin-triplet Josephson junctions, it is desirable to maximize the flux cancelation within the PMA SAF. Thus, in the experiments that follow, we used a balanced SAF structure which has an equal total thickness of Pd and Co on either side of the Ru spacer.

We briefly mention that we tested another, similar type of PMA SAF which was composed of Ni/Co multilayers of the form: $[\text{Co}(0.3)/\text{Ni}(0.6)]_n/\text{Co}(0.3)/\text{Ru}(d_{\text{Ru}})/[\text{Co}(0.3)/\text{Ni}(0.6)]_m/\text{Co}(0.3)$, where $n = 4$ and $m = 3$ or 4 . The magnetic behavior of these PMA SAFs was quite similar to the data in Fig. 8.2, with strong antiferromagnetic pinning, PMA, and square-shaped M - H loops. However, after a visitor to our group Demet Korucu fabricated them into Josephson junctions, we found the Ni/Co SAFs to be rather unsatisfactory from a device perspective in that they suffered from extremely small critical current. The same was not true for the Pd/Co based PMA SAFs which will be discussed in the next section.

8.2 Josephson Junctions

We next seek to address the following questions: 1) how does the Pd/Co PMA SAF structure behave as a barrier to current transport in Josephson junctions (JJs)? 2) can a PMA SAF of this nature be utilized in a JJ device with ferromagnetic layers to generate spin-triplet supercurrent? Both questions can be answered by measuring how the critical current in these type of junctions varies with the number of Pd/Co layers on either side of the Ru spacer. To this end we fabricated three sets of JJs. The first is a series of control samples that contain only the Pd/Co PMA SAF, shown in Fig. 8.3 (a), and are meant to measure

the decay of the short-range spin-singlet supercurrent. The second and third series of JJs are designed to carry long-range spin-triplet supercurrent. They contain a Pd/Co PMA SAF centered between two additional ferromagnetic layers with in-plane magnetization, shown in Fig. 8.3 (b). In the second set both the bottom ferromagnet, F' , and the top ferromagnet, F'' , are Ni with thickness 1.6 nm. The third set of JJ's is similar, but the F' layer is Permalloy (Py = Ni₈₁Fe₁₉) with thickness 1.25 nm and the F'' layer is Ni(1.6 nm), as shown Fig. 8.3 (b).

Due to Permalloy's sharp magnetic switching at low magnetic field, we envision using it in controllable JJs [17,107,153]. However, from previous experience we know that Py's magnetic properties degrade if grown on a rough surface. Thus, in the third series of JJ's, the Py layer is intentionally placed near the bottom of the stack where it will be the least effected by upward-propagating surface roughness, as discussed in more detail later in Fig. 8.4. Nickel, while harder to control magnetically, is the ferromagnetic material we and others have found to be the least detrimental to the propagation of supercurrent [143]. Thus, it was used as both F' and F'' in the second set of samples in case the critical currents in the JJs with Py were too small to measure. The role of the other layers in Fig. 8.3 will be discussed later.

8.2.1 Sample Fabrication

The sample fabrication proceeds similarly to other nanopillar junctions made by our group [19, 77], such as in Ch.6, with a few noted differences. The geometry of the bottom leads was defined via optical photolithography and a lift-off process. The bottom electrode is a sputtered Nb/Al multilayer of form [Nb(25)/Al(2.4)]₃/Nb(20), which is much smoother than a continuous Nb layer [122–124], and is capped with a thin 2 nm layer of Au to prevent oxidation. We then had to break vacuum and exchange sputtering targets. Ideally one would

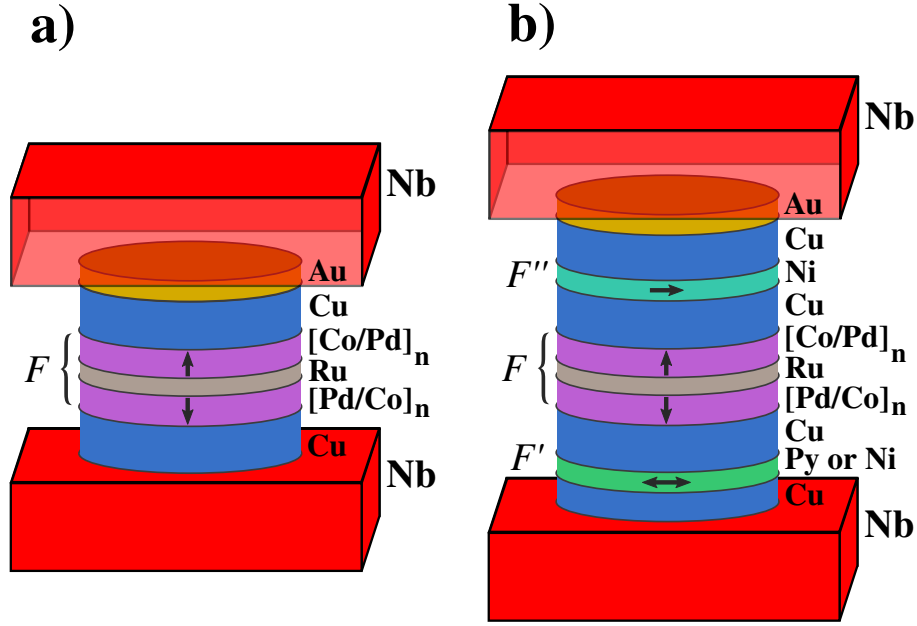


Figure 8.3: A schematic representation of the vertical cross sectional structure of our Josephson junctions (not to scale). The central F layer is composed of two sets of n [Pd(0.9 nm)/Co(0.3 nm)] bilayers with perpendicular magnetic anisotropy (PMA), on either side of a Ru(0.95 nm) spacer to form a synthetic antiferromagnet (SAF). (a) With only the PMA SAF in the center, the supercurrent is carried by short-range spin-singlet pairs. (b) When combined with the two other ferromagnets, F' and F'' , with in-plane magnetization, the supercurrent in F is carried by long-range spin-triplet pairs. In this study, the F' layer is either Ni(1.6 nm), which maximizes the spin-triplet supercurrent, or Py (1.25 nm), which can act as a “free” layer, switching it’s magnetization at a low field.

sputter the entire stack *in situ*, however, we are limited to seven sputtering targets in our chamber. During the target exchange, which takes less than 10 minutes, the samples are contained in a bag filled with continuously flowing N₂ gas to limit contamination. After another bakeout, pump down, and liquid nitrogen cooling, we ion mill away the protective Au layer before continuing the sputtering process. All the ferromagnetic layers are then deposited *in situ* in the following sequence: for the “spin-singlet” samples of Fig. 8.3(a), Cu(4)/PMA-SAF/Cu(4)/Au(2); and for the “spin-triplet” samples of Fig. 8.3 (b) we sputter, Cu(2)/[Ni(1.6) or Py(1.25)]/Cu(4)/ PMA-SAF /Cu(4)/Ni(1.6)/Cu(7)/Au(2), where PMA-SAF = [Pd(0.9)/Co(0.3)]_n/ Ru(0.95)/ [Co(0.3)/Pd(0.9)]_n. Due to the crystal lattice mismatch between the fcc ferromagnetic materials and the bcc Nb we add a Cu(2) spacer before the (Py or Ni) *F'* layer. Meanwhile, between the *F'*, *F*, and *F''* layers, Cu(4) buffers are inserted to prevent them from coupling magnetically. Finally, the stack is capped with a thin layer of Cu and Au to prevent oxidation.

The junctions were patterned by electron-beam lithography followed by ion milling in Argon. We use the negative e-beam resist ma-N2401 as the ion mill mask. The junctions are elliptical in shape with an aspect ratio of 2.5 and area of 0.5 μm², sufficiently small for the Py layers to be mostly single domain [19]. Elliptically-shaped junctions have the advantage that the Fraunhofer patterns follow an analytical formula while the (small) demagnetizing field is nearly uniform when the magnetization is uniform.

Outside the mask region, we ion milled from the capping layer through the *F'* layer, and nominally half-way into the underlying Cu spacer layer. After ion milling, a 50-nm-thick SiO layer was deposited by thermal evaporation to electrically isolate the junction and the bottom wiring layer from the top wiring layer.

Finally, the top Nb wiring layer was patterned using the same photolithography and

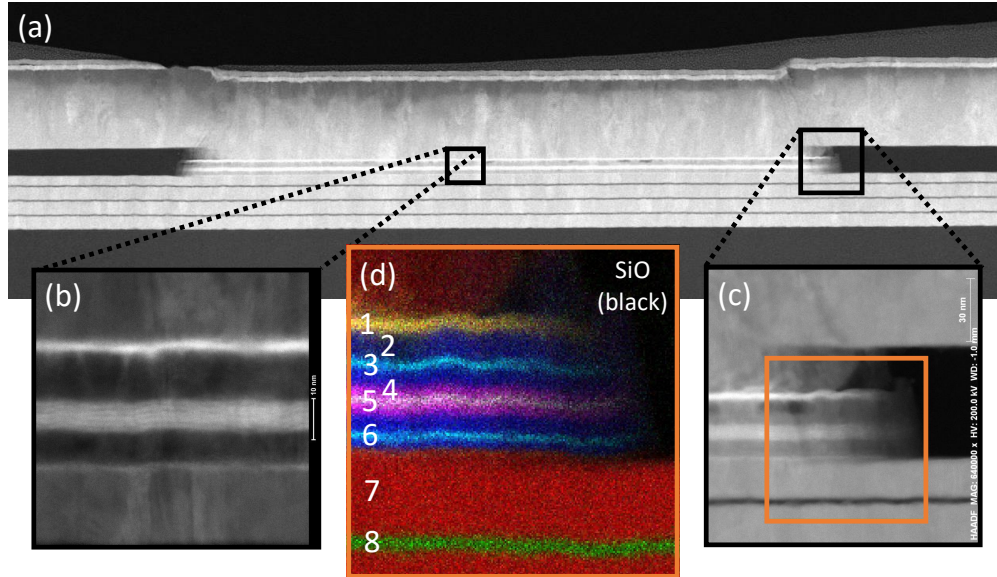


Figure 8.4: Vertical cross sections of the junctions described in Fig. 6.2 (b) prepared using a focused ion beam (FIB) were investigated by high-resolution scanning transmission electron microscopy (STEM) and energy dispersive x-ray spectroscopy (EDX). Panel (a) shows an STEM image of the full extent of the junction, including the smooth Nb/Al bottom electrode. Expanded views of the individual ferromagnetic layers are shown in panels (b) and (c) near the center and side of the junction, respectively. The EDX phase map shown in panel (d) corresponds to the area within the orange square in panel (c). The multivariate statistical analysis of the spectra from each individual pixel are color coded and numbered in the figure as follows: Au (yellow, 1), Cu (blue, 2), Ni + Fe (cyan, 3 and 6), Pd + Co (magenta, 4), Co + Ru (white, 5), Nb (red, 7), Al (green, 8), SiO (black). Figure courtesy of P. Kotula and N. Missert, Sandia National Laboratory.

lift-off process as the bottom leads. The surface is cleaned with oxygen plasma etching followed by *in-situ* ion milling in which 1 nm of the top Au surface is removed immediately before sputtering. We deposited top leads of Nb(150 nm)/Au(10 nm), ending with the Au to prevent oxidation.

In order to verify the fabrication process, vertical cross sections of the junctions were investigated by high-resolution scanning transmission electron microscopy (STEM) and energy dispersive x-ray spectroscopy (EDX) by our collaborators Paul Kotula and Nancy Missert at Sandia National Laboratories. The cross sections were prepared using a FEI Helios focused

ion beam (FIB) with a Ga ion source, and transferred to a Ti grid for imaging in a FEI Titan G2 80-200 aberration-corrected STEM operated at 200kV and equipped with four silicon drift X-ray detectors.

The high-angle annular dark field STEM image in Figs. 8.4(a)-(c) show cross sections of a junction with the same structure as Fig. 8.3 (b) with $n = 3$. The Nb/Al bottom electrode, seen at the bottom of Fig. 8.4(a), is a smooth and continuous surface that provides a good growth template for the layers grown on top. Fourier transforms of regions of the high-resolution STEM image show that the Cu layer directly above grows with a [111] orientation on Nb [011]. Grains with favorable orientation relative to the beam direction show lattice fringes extending through the entire Cu/ferromagnetic layer/Cu thicknesses. In the top Cu(7 nm) layer there appear to be three to four isolated regions (width ≈ 5 nm) with lower Cu density than the rest of the layer (one such dark patch can be clearly seen in Fig. 8.4(c)). The origin of those low-density Cu regions is unknown. The individual Pd and Co layers inside the SAF, shown in Fig. 8.4(b), near the center of the junction, appear relatively smooth and continuous. Furthermore, the STEM image shows that the ion milling procedure used in the sample fabrication to define the junction area is accurately calibrated to mill down to the desired depth.

Identifying the elemental composition of the layers is achieved through EDX phase maps, created by performing a multivariate statistical analysis of the spectra from each individual pixel, and color-coding pixels containing the same spectral shape [154]. The phase map shown in Fig. 8.4(d) corresponds to the area within the orange square in Fig. 8.4(c). The Py layer (cyan, labeled as layer 6) is clearly uniform and continuous. The individual layers inside the SAF are not distinguishable due to their sub-nanometer thickness and the lower spatial resolution of EDX compared to STEM. However, we clearly show a difference between

the component Pd/Co X-ray peaks from the outer regions of the SAF (magenta, labeled as layer 4) compared to its center, where component Ru/Co peaks are more prominent (white, labeled as layer 5). The Ni layer (cyan, labeled as layer 3), while continuous, has some observable roughness, consistent with the magnetic behavior discussed in the next section.

8.3 Transport Measurements and Analysis

Each device was connected to the wire leads of a dip-stick probe and measured at 4.2 K using the rf SQUID comparator circuit, setup in the same manner as in Ch. 6. Typical I-V curves have the expected behavior of overdamped Josephson junctions [127]. The critical current I_c was extracted by fitting the I-V curves to a square root function, Eq. (6.1), where the sample resistance in the normal state R_N was determined by the slope of the linear region of the I-V curve when $|I| \gg I_c$.

Measurements of the area-resistance product in the normal state typically yield consistent values of AR_N , with a median value of $22.5 \text{ f}\Omega\text{-m}^2$, an indicator of the reproducible high quality interfaces. The AR_N values for the full set of samples are shown in Fig. 8.8(b). The junction area typically varies by less than 10% from the nominal value of $0.5 \text{ }\mu\text{m}^2$, and can be accurately extracted from the Fraunhofer pattern measurements discussed later. It is thought that R_N is dominated by the interfacial resistance between the various layers. It is therefore noteworthy that, although these junctions contain many interfaces, the AR_N products are (on average) only about twice those of similarly-sized junctions containing only a single ferromagnetic layer [19, 77], which had 5-10 $\text{f}\Omega\text{-m}^2$. The junctions with $F' = F'' = \text{Ni}$ with $n = 3$ or 4 Pd/Co repeats have slightly larger AR_N than those with $n = 1$ or 2. Otherwise, the average value of AR_N does not appear to be correlated with n .

When I_c is less than a few μA , the I-V curves exhibit noticeable rounding due to thermal effects and instrumental noise. Such rounding is accommodated by the theories of Ivanchenko and Zil'berman (IZ) and of Ambegaokar and Halperin [129,130]. Fitting the I-V curves with the IZ function, Eq. (6.2) instead of the square-root function of Eq. (6.1) results in values of I_c that are somewhat larger – typically 30% for $I_c \approx 1\mu\text{A}$ [19]. However, fitting every I-V curve with the IZ function is computation-intensive and not practical, so we used the simpler square-root fits for the Fraunhofer data shown in Figs. 8.5-8.7. For the summary shown in Fig. 8.8, we used the values obtained from fitting the IZ function to the data near the peaks of the individual Fraunhofer patterns.

8.3.1 Fraunhofer Patterns

Measuring I_c as a function of the applied magnetic field, we map out “Fraunhofer” diffraction patterns, shown in Figs. 8.5-8.7 for the three JJ types described in Fig. 8.3.

Fig. 8.5 shows data from three spin-singlet samples with $n = 1, 2,$ and 3 . Those data were acquired by applying a field of 60 mT then slowly ramping the field to -60 mT in steps of typically 2 mT (blue data points). We then repeated this procedure in the other field direction (red data points) and observed very little magnetic hysteresis since the F layer’s magnetizations are aligned perpendicular to the applied field.

For the spin-triplet samples with the additional F' and F'' layers, we first measured the critical current near zero field to monitor the “virgin” or as-grown state of the various nanomagnets. Initially sweeping the field from (± 60 mT) the critical current was typically small and any semblance of “Fraunhofer patterns” were rather irregular, as shown in Fig. 8.6 (a). Successively expanding the applied field sweep range ($\pm 60, \pm 90, \pm 120, \pm 150$ mT) to help align the F' and F'' layers resulted in significant improvements in the Fraunhofer quality

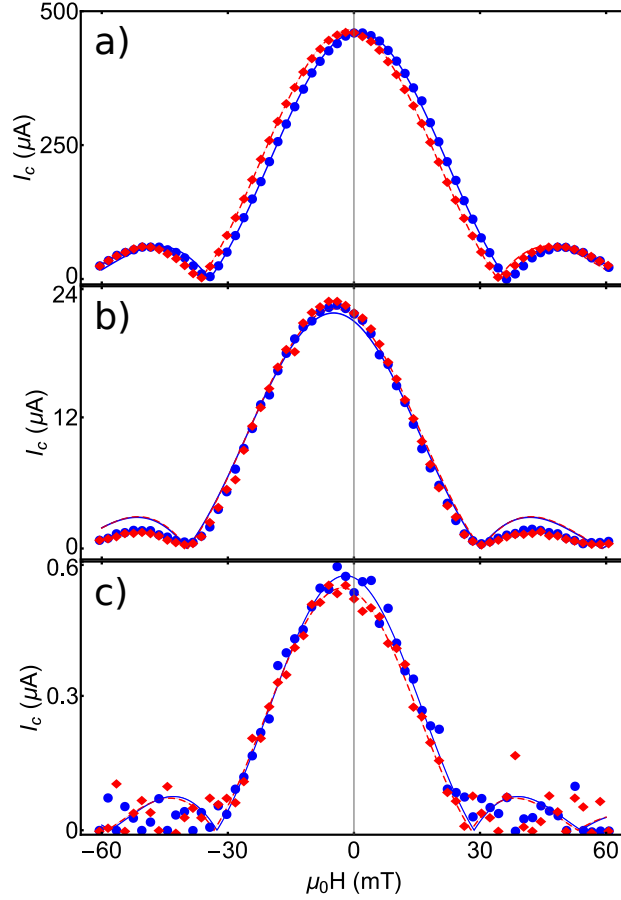


Figure 8.5: The critical current, I_c , is plotted versus the applied in-plane field H for junctions with the structure shown in Fig. 8.3 (a) (without F' and F''). The supercurrent is carried primarily by spin-singlet pairs. Increasing the number of Pd/Co layer repeats: (a) $n = 1$, (b) $n = 2$, (c) $n = 3$, causes I_c to decay rapidly. Since the magnetization of the SAF is perpendicular to the plane there are only slight horizontal shifts in the Fraunhofer patterns and very little magnetic hysteresis. The corresponding fits to Eq. (6.3) (lines) show excellent agreement for both the positive (red, dashed) and negative (blue) field sweep directions.

and enhanced the peak value of I_c (near zero field), shown in Fig. 8.6 (b)-(c). After initializing the samples at ± 150 mT the peak value of I_c appears to saturate, and the Fraunhofer pattern closely follows the theoretical curve described later in Eq. (6.3). This detailed “initialization” behavior was reproducible on five separate junctions from various chips. Therefore, for the data presented in Figs. 8.6-8.7, we determined that a large initialization field of 150 mT was required to help set the initial orientation of the Ni layer(s). Ideally, an even larger initialization field would be beneficial to fully magnetize the Ni [142], however, too large a field might disturb the magnetic properties of the PMA SAF. Based on the results of Figs. 8.1-8.2, as a precautionary measure any external magnetic fields were kept at 150 mT or below.

After the initialization procedure, we removed any flux trapped in the junction or in the Nb leads by lifting the dip-stick probe slightly in the Dewar until the sample lay just above the liquid Helium bath, such that the Nb ceased to be superconducting as monitored by an Ohmmeter connected to the sample leads. After reinserting the sample into the liquid Helium we next applied a field of 90 mT and slowly ramped the field to -90 mT, in steps of 2 mT. Finally, the field was slowly swept in the opposite direction, after reinitializing the sample at -150 mT, measuring I - V curves with the field from -90 mT to 90 mT, observing any hysteretic effects from the in-plane ferromagnets.

Fraunhofer pattern measurements such as these contain information about the magnetic state of the in-plane ferromagnetic layers, the behavior of the critical current, and the dimensions of the junction. For elliptical junctions the functional form of the Fraunhofer patterns are the Airy functions from Eq. (6.3). Since the magnetization of the F -layer is parallel to the current flow, it does not contribute to the flux Φ in Eq. (6.3). The in-plane magnetizations of F' and F'' do contribute, however, and cause shifts in the Fraunhofer pattern along the

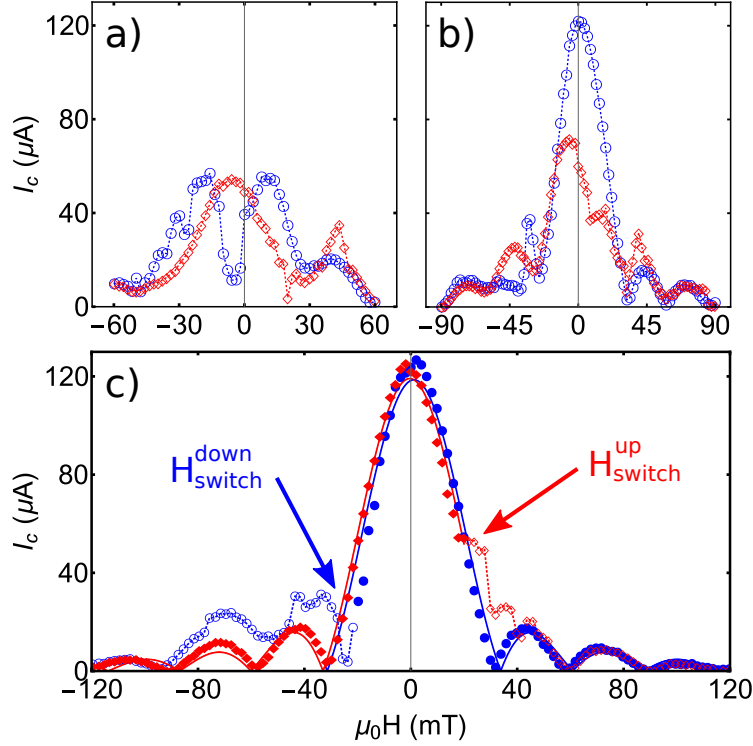


Figure 8.6: Critical current, I_c , vs. the applied in-plane field H , for a sample with $F' = F'' = \text{Ni}$ (1.6 nm), and $n=1$, similar to Fig. 8.3 (b). If the initialization field is too small, e.g. (a) $H_{\text{init}} = 60$ mT or (b) $H_{\text{init}} = 90$ mT, and the magnetizations of the two Ni layers are not aligned, the “Fraunhofer” patterns are of poor quality. With an initialization field of 150 mT (c) the Ni layers are fully magnetized, and the data before H_{switch} (solid markers) show good agreement with the expected form for both the positive (red) and negative (blue) field sweep directions. Solid lines are fits to Eq. (6.3). Hence we initialized all our spin-triplet samples at 150 mT. In (c) the hollow markers represent the data points after H_{switch} and the dashed lines are only to guide the eye. The Ni layers, while amenable to large supercurrents, contain multiple magnetic domains and switch magnetization over a broad field range.

field axis [17, 19, 76, 77, 153, 155]. Hence the horizontal Fraunhofer pattern shifts will differ for the three types of samples outlined in Fig. 8.3.

If the in-plane F' and F'' layers are uniform and colinear with H , and the F layer is assumed to be perpendicular to H , then similar to the discussion in Ch. 6 the magnetic flux through the junction is [76, 153],

$$\Phi = \mu_0 H w (2\lambda_L + d_{\text{tot}}) + \mu_0 w (M' d_{F'} + M'' d_{F''}), \quad (8.1)$$

where H , w , and λ_L are the applied field, the width of the junction (minor axis), and the London penetration depth of the Nb electrodes. The total thickness between the Nb electrodes is $d_{\text{tot}} = d_N + d_{F'} + d_F + d_{F''}$, where d_N is the total thickness of all the normal metal layers (including the Ru in the SAF) and $d_{F'}$, d_F , and $d_{F''}$ are the thicknesses of the three ferromagnetic layers F' , F , and F'' , respectively (d_F being the total thickness of all the Pd/Co multilayers). The last term in Eq. (8.1) arises from the in-plane magnetization's M' and M'' corresponding to the ferromagnets F' and F'' , respectively. Eq. (8.1) neglects the small contributions to Φ from the uniform demagnetizing field's and any magnetic field from the nanomagnets that returns inside the junction. From Eq. (8.1) it is clear that the Fraunhofer pattern will be shifted along the field axis by an amount $H_{\text{shift}} = -(M' d_{F'} + M'' d_{F''}) / (2\lambda_L + d_{\text{tot}})$ in the direction opposite of the junctions' net in-plane magnetization.

For samples without the F' and F'' layers there should be very little shift, resulting only from any canting of the [Pd/Co] perpendicular magnetization into the plane. That expectation is born out by the data shown in Fig. 8.5. For samples with the F' and F'' layers the shifts will be more pronounced. The shifts should be largest when M' and M'' have the same sign (parallel alignment) and smaller when they have opposite signs (antiparallel

alignment) [153].

The complex nature of these Fraunhofer pattern shifts, combined with the possibility that the Ni layers do not switch abruptly or behave as a single magnetic domain, make a comprehensive analysis difficult. For the samples with $F' = F''$, the two Ni layers may not switch at the same field due to the upward propagating surface roughness, making it impractical to fit all the data points in the Fraunhofer patterns shown in Figs. 8.6 and 8.7. Therefore we only attempt to fit the clean sections of the Fraunhofer patterns before the first magnetic switching event occurs. We fit Eq. (6.3) to the data starting from the initialization field to H_{switch} . The free parameters in the fit are I_{c0} , the junction width transverse to the field direction, and the field shift of the central peak. In Figs. 8.5 - 8.7 the corresponding fits show excellent agreement with the data, for the positive (red) and negative (blue) sweep directions. In Figs. 8.6(c) and 8.7 the hollow data points denote the data after H_{switch} . Those data show that the reversal of the Ni magnetization occurs over a range of fields, consistent with the behavior of Ni seen in previous work by us and others [17, 153]. Most of the junctions display full magnetic remanence, continuing to follow Eq. (6.3) though zero applied field before H_{switch} .

8.3.2 Critical Current vs Thickness

In Fig. 8.8(a) we plot the maximum measured I_c times R_N on a log scale versus the number of Pd/Co repeats n on either side of the Ru spacer. In Fig. 8.8 (b) we plot the area-resistance product for the entire data set. The $I_c R_N$ products of the spin-singlet samples (blue circles) decay much more rapidly with increasing n than do the spin-triplet samples with $F' = \text{Ni}$ (orange triangles) and those with $F' = \text{Py}$ (red diamonds). The three data

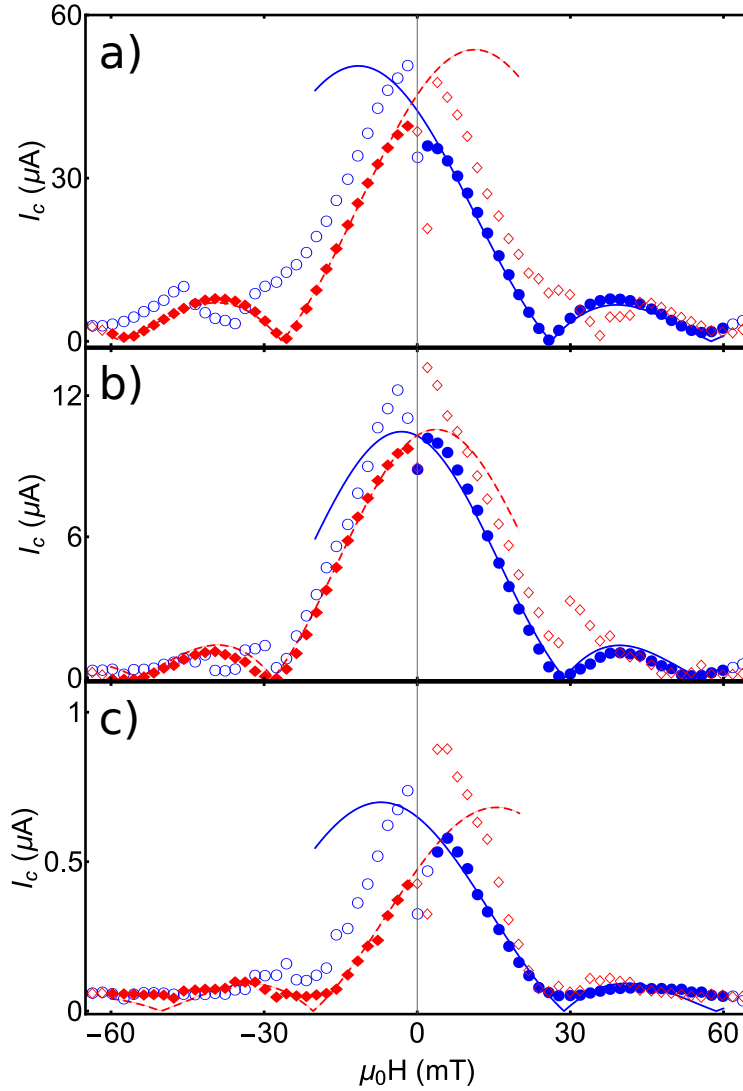


Figure 8.7: I_c is plotted vs. the applied in-plane field H , for junctions with the structure shown in Fig. 8.3 (b) with $F' = \text{Py}$, $F'' = \text{Ni}$. Increasing the number of repeats of Pd/Co: (a) $n=1$, (b) $n=2$, (c) $n=3$, causes I_c to decay, but more slowly than without the F' and F'' layers (Fig. 8.5). The horizontal shifts in the Fraunhofer patterns are indicative of the magnetic state of the in-plane ferromagnets. The data before H_{switch} , the field at which the Py magnetization reverses direction (solid markers), and the corresponding fits to Eq. (6.3) (lines) show excellent agreement for both the positive (red, dashed) and negative (blue) field sweep directions. The hollow circles are the corresponding data points after H_{switch} . The Py typically switches abruptly at low fields (< 2 mT), whereas the Ni is thought to contain multiple magnetic domains and gradually switches over a broad range of fields.

Table 8.1: *Fitting the data in Fig. 8.8 to Eq. (8.2) yields the best-fit parameters:*

Sample Set	A_0 (μV)	\bar{n}
Spin-singlet, only F	89 ± 28	0.70 ± 0.04
Spin-triplet, $F'=F''=\text{Ni}$	14 ± 3	1.38 ± 0.07
Spin-triplet, $F'=\text{Py}$, $F''=\text{Ni}$	4.1 ± 0.6	1.53 ± 0.07

sets are fit to the total number of bilayers ($2n$) with a simple exponential decay,

$$I_c R_N(n) = A_0 * e^{-(2n/\bar{n})}. \quad (8.2)$$

The best-fit parameters are listed in Table 8.1. The decay length expressed as a number of [Co/Pd] bilayers is 1.38 ± 0.07 and 1.53 ± 0.07 for the spin-triplet samples, whereas it is only 0.70 ± 0.04 for the spin-singlet samples. That observation is the main result of this work.

It is instructive to compare the data in Fig. 8.8(a) with data from the only other study of spin-triplet Josephson junctions containing PMA layers, namely ref. [106]. In that work the central F layer consisted of a [Ni/Co] multilayer with strong PMA, but not a SAF. In those junctions the decay of the spin-triplet samples was much slower than the decay of the control samples that did not contain the F' and F'' layers. (The ratio of the spin-triplet to spin-single decay lengths in that work was about 4.5, whereas it is only about 2.1 in the present work.) Later, our group measured a series of junctions containing [Ni/Co] PMA SAFs, and found not only that they carried much smaller critical currents, but that the decay with the number of repeats was also much steeper than in the non-SAF [Ni/Co] junctions [156]. To explain the sharp decay of the spin-triplet supercurrent in the [Ni/Co] SAFs, we propose the following explanation. It is known from giant magnetoresistance (GMR) studies [157] that the [Ni/Co] interface has strong spin-scattering asymmetry – i.e. minority-band electrons are

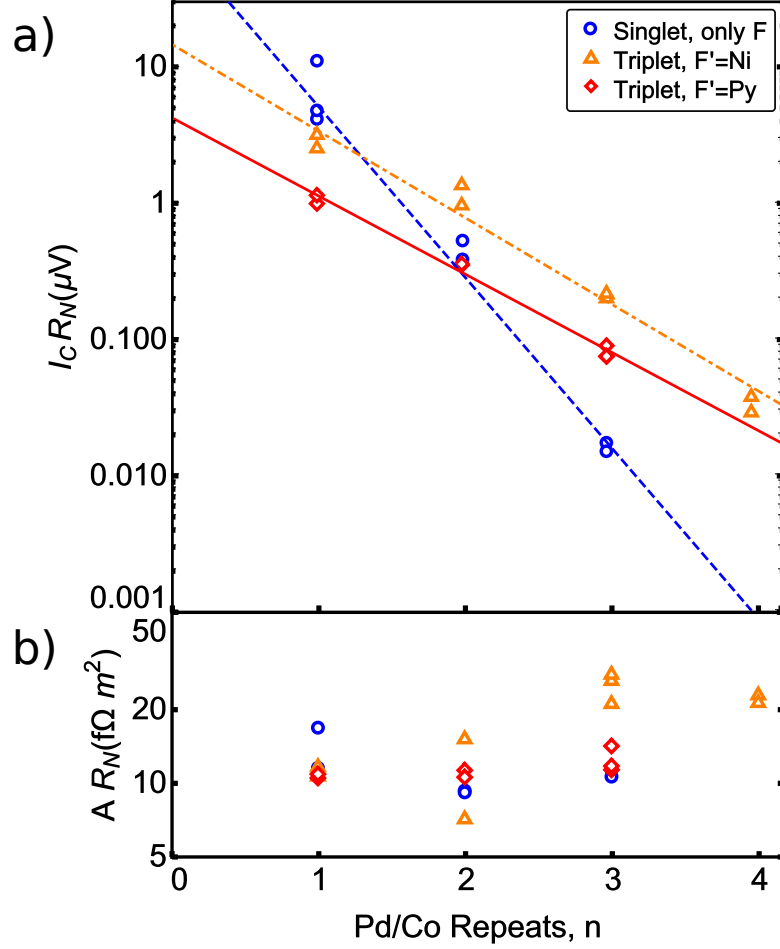


Figure 8.8: Comparison of the critical current decay in spin-triplet and spin-singlet samples and their area-resistance products. (a) The maximum measured I_c times R_N is plotted vs. the number of Pd/Co repeats n in the PMA SAF. The $I_c R_N$ of the spin-singlet samples (blue circles) decays more rapidly with increasing Pd/Co thickness than do the spin-triplet samples with $F' = \text{Ni}$ (orange triangles) and those with $F' = \text{Py}$ (red diamonds). The data are fit to the total number of Pd/Co bilayers according to Eq. (8.2), with the best-fit parameters shown in Table 8.1. (b) The area-resistance product of the junctions vs. n does not appear to be correlated to the number of Pd/Co interfaces, and is on average $11.4 \text{ f}\Omega \text{m}^2$ across all the datasets, with the exception of the $F' = \text{Ni}$ chips with $n = 3$ and 4 , which have slightly larger resistances.

scattered more strongly than majority-band electrons. Hence in a $[\text{Ni}/\text{Co}]_n$ multilayer, the current will become more strongly spin-polarized as the number of repeats n increases. In a $[\text{Ni}/\text{Co}]$ SAF, the majority electrons in one half of the SAF become minority electrons in the other half and vice versa. Hence all electrons passing through the SAF are strongly scattered at some point. This effect increases with n , hence causing a steep decay of critical current as a function of n . We note that this mechanism affects both spin-singlet and spin-triplet supercurrents; but the former already face a steep decay due to the standard S/F physics discussed in the introduction, whereas for the spin-triplet supercurrent the presence of the SAF becomes the dominant decay mechanism.

Our decision to use $[\text{Pd}/\text{Co}]$ multilayers was a direct result of the discussion above. Unfortunately, the degree of spin-scattering asymmetry at the $[\text{Pd}/\text{Co}]$ interface has not been measured, as far as we know. (Our own attempts to do so using GMR techniques were thwarted by our inability to achieve reproducible in-plane magnetic states for any thickness combination in the $[\text{Pd}/\text{Co}]$ system.) From comparing the results shown in Fig. 8.8(a) with our unpublished data on junctions containing $[\text{Ni}/\text{Co}]$ PMA SAFs, we infer that the spin-scattering asymmetry in $[\text{Pd}/\text{Co}]$ is weaker than in $[\text{Ni}/\text{Co}]$. Nonetheless, we believe that the spin-scattering asymmetry in $[\text{Co}/\text{Pd}]$ underlies the fact that the decay of the spin-triplet supercurrent is only a factor of two less steep than the decay of the spin-singlet supercurrent.

An alternative explanation for the unusually steep decay of the spin-triplet supercurrent in our samples is the strong spin-orbit interaction in the Co/Pd system [158]. It should be possible to distinguish between these two explanations by comparing the decay of the supercurrent in spin-triplet JJs containing $[\text{Pd}/\text{Co}]$ plain multilayers in the center, with the decay we observe in our JJs containing $[\text{Pd}/\text{Co}]$ multilayer SAFs. Our group intends to carry out such a study in the near future.

The next question to address is, at what value of n can we be certain that the spin-triplet component of the supercurrent in the spin-triplet samples is the dominant contribution? A straightforward interpretation of the data shown in Fig. 8.8(a) might lead one to conclude that the point where the spin-triplet curves cross the spin-singlet curve is the point where the spin-singlet and spin-triplet contributions to the supercurrent are equal in the spin-triplet samples. Those crossings occur approximately at $n = 1$ for the Ni-Ni samples and at $n = 2$ for the Ni-Py samples. But that interpretation is wrong. The magnitude of the spin-singlet supercurrent in the spin-triplet samples is surely far less than the supercurrent we measure in the spin-singlet samples, because the spin-singlet supercurrent will be further suppressed when it has to pass through the additional F' and F'' layers. That suppression would effectively shift the entire spin-singlet curve down vertically, thus the blue data set can only be considered as a generous upper bound on the magnitude of the spin-singlet supercurrent that can pass through the spin-triplet samples. We do not know how large that suppression is, but we can guess that the suppression is roughly three times greater in the Py-Ni samples than in the Ni-Ni samples, from the vertical offset between the two spin-triplet curves.

8.4 Conclusion

In conclusion, we have measured the critical current in Josephson junctions of the form $S/F'/N/F/N/F''/S$, where F is a synthetic antiferromagnets consisting of [Pd/Co] multilayers with perpendicular anisotropy. The critical currents in those junctions decay less steeply with the number of [Pd/Co] bilayers than in junctions without the F' and F'' layers. That result represents strong evidence that the 3-layer junctions carry spin-triplet supercurrent. Furthermore, by choosing F' to be a soft magnetic material such as Permalloy, while F'' is a

hard magnetic material such as Ni, the relative magnetization directions of those two layers can be controlled. Such junctions are utilized in Ch. 9 to make cryogenic memory devices in which the ground-state phase difference across the junctions is controlled on-demand by changing the magnetic configuration of the ferromagnetic layers.

Chapter 9

Controllable Phase SQUIDs: Spin-Triplet

It is now well established that spin-triplet supercurrent can be generated from conventional spin-singlet superconductors using ferromagnetic layers with an inhomogeneous magnetization profile [85–87, 90–98, 100–104], resulting in several important consequences, such as the extension of superconducting properties deep into strongly ferromagnetic materials, as discussed in Ch. 4. Surprisingly, one of the most salient predictions of the spin-triplet theory has yet to be verified experimentally, namely that a Josephson junction containing three magnetic layers with noncolinear magnetizations should exhibit a ground-state phase shift of either 0 or π depending on the relative orientations of those magnetizations.

In this chapter, we verify that prediction experimentally, using the same type of junctions presented in Ch. 8. The junctions are of the form $S/F'/N/F/N/F''/S$, which contain three ferromagnetic layers, F' and F'' both with in-plane magnetization, and the central layer F with magnetization perpendicular to the plane. Detection of the ground-state phase across these spin-triplet Josephson junctions is achieved using similar techniques to those employed in Ch. 7, in which we measure the relative phase-shift between two such junctions in a SQUID loop.

We demonstrate a scheme by which the magnetization direction of the F' layer can be controllably switched by 180° without disturbing the F and F'' layers, thereby allowing the phase state of the junction to be set to 0 or π on demand. We show that the phase can be reliably switched between the zero or π states for seven different spin-triplet SQUID

devices measured, several of which we were able to switch between the two states over a thousand times without error. Finally, we study the temperature dependence of the critical current in these types of junctions below 4.2 K using a dilution refrigerator. This type of phase-controllable junction could be used as a memory element in a fully-superconducting computer.

9.1 SQUID Sample Fabrication

The samples are of similar construction to the individual spin-triplet junctions from Ch. 8 where the in-plane ferromagnets are $F' = \text{Py}$ and $F'' = \text{Ni}$ and the central F layer is a Pd/Co-based synthetic antiferromagnet with perpendicular magnetic anisotropy. Thus, the spin-triplet SQUID sample fabrication proceeds similarly to that detailed in Ch. 8, aside from a few notable changes discussed below.

We designed a new SQUID layout, shown schematically in Fig. 9.1, which has nominally equal inductances on either side of the loop, unlike the asymmetric SQUIDs discussed in Ch. 7. This modification was aimed at simplifying the data analysis, in the sense that the output SQUID oscillations will be symmetric (not “ratchet” shaped), though the critical currents in the two junctions may still be asymmetric. The design uses a pitchfork shaped bottom wiring layer, which contains the bottom electrode and all of the magnetic layers, intersected by a “T-shaped” superconducting top wiring layer, making a SQUID loop with an inner area of $6 \times 6 \mu\text{m}^2$. There is an on-chip superconducting flux line, similar to that used in the SQUIDS from Ch. 7, through which we pass current to add flux to the SQUID loop. The design layout accommodates up to four independent and identical SQUIDs on a single $0.5 \times 0.5 \text{ in}^2$ chip.

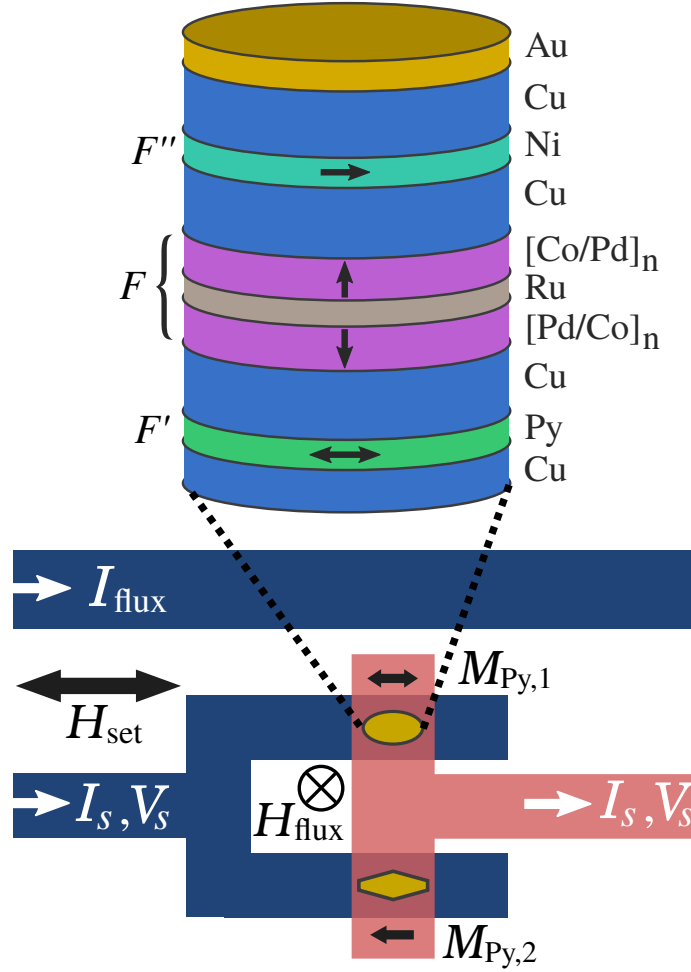


Figure 9.1: *Spin-triplet Josephson junction structure and SQUID loop design.* (Top) A schematic cross-section of the central layers in our Josephson junctions (not to scale). The central F layer is composed of two sets of n alternating layers of Pd (0.9 nm) and Co (0.3 nm), with perpendicular magnetic anisotropy (PMA), on either side of a Ru (0.95 nm) spacer to form a synthetic anti-ferromagnet (SAF). When combined with another ferromagnetic layer, F' (Py (1.25 nm)), with in-plane magnetization, the PMA SAF provides the 90 degree basis rotation to generate long-range spin-triplet pairing. The third ferromagnet, F'' (Ni (1.6 nm)), converts the spin-triplet pairs back to spin-singlet supercurrent to be accepted by the top Nb electrode. One junction has an elliptical cross-section (aspect ratio 2.0) to make its F' layer switch at a low field, while the other is an elongated hexagon (aspect ratio 3.0), both have area $0.5 \mu\text{m}^2$. (Bottom) The superconducting electrodes and the junctions are arranged into a SQUID loop, used to measure the relative phase between the two junctions. An external field H_{set} is used to set and control the magnetization directions of the F' layers inside the junctions, while the current I_s through the SQUID and voltage V_s across it are typically measured after returning $H_{\text{set}} = 0$. The flux current I_{flux} is driven through a nearby superconducting line to inject flux into the SQUID loop, causing the total critical current in the SQUID to modulate with the flux current.

The geometry of the bottom leads was defined via optical photolithography using the HMDS and S1813 procedure described at the end of Section 5.2. The bottom electrode is a sputtered Nb/Al multilayer of form $[\text{Nb}(25)/\text{Al}(2.4)]_3/\text{Nb}(20)$, where all thicknesses are listed in nanometers, and is capped with a thin 2 nm layer of Au to prevent oxidation. As in Section 8.2.1, we then had to break vacuum and exchange sputtering targets, due to the limited number of sputtering guns in our chamber. During the target exchange, which typically takes about 10 minutes, the samples are contained in a bag filled with continuously flowing N_2 gas to limit contamination. After another bakeout, pump down, and liquid nitrogen cooling, we ion mill away the protective Au layer before continuing the sputtering process. All the ferromagnetic layers are then deposited *in situ* in the following sequence, shown at the top of Fig. 9.1: $\text{Cu}(2)/\text{Py}(1.25)/\text{Cu}(4)/\text{PMA-SAF}/\text{Cu}(4)/\text{Ni}(1.6)/\text{Cu}(7)/\text{Au}(2)$, where $\text{PMA-SAF} = [\text{Pd}(0.9)/\text{Co}(0.3)]_n/\text{Ru}(0.95)/[\text{Co}(0.3)/\text{Pd}(0.9)]_n$, and $n = 2$ or 3 , corresponding to a total number of $[\text{Pd}/\text{Co}]$ bilayers of 4 or 6. The stack is capped with a thin layer of Cu and Au to prevent oxidation.

Next, using electron-beam lithography and ion milling in Argon, we patterned $0.5 \mu\text{m}^2$ area junctions onto each of the arms of the forked bottom lead. The goal is to be able to control the magnetic state of the “soft” layer ($F'=\text{Py}$) in the first junction with a small external field, while the magnetic state of the other layers in the first junction, and all the layers in the second junction, are left unperturbed. To accomplish that we patterned the two junctions to have different shapes and aspect ratios, to take advantage of shape anisotropy. The “controllable” first junction, is elliptical in shape with an aspect ratio of 2.0. Our colleague, Nick Rizzo at Arizona State University, suggested the stability of the “fixed” second junction could be improved by making its shape an elongated “hexagon” (*i.e.* a diamond with the edges chopped off, hereafter referred to as a “hex” bit) rather than an

ellipse. His idea was backed-up with micromagnetics simulations using the Landau-Lifshitz-Gilbert equations, which showed that a hex bit of a $0.5 \mu\text{m}^2$ would, in theory, have a somewhat larger switching field than an ellipse of the same size and aspect ratio. Following his suggestion, we patterned the second junction into a hex shape and with a larger aspect ratio of 3.0. The junctions are placed on either side of the SQUID loop, as shown in Fig. 9.1, with their long-axes aligned parallel to one another.

We used the negative e-beam resist ma-N 2401 as the ion mill mask and outside the mask region, we then ion milled from the capping layer through the F' layer, and nominally half-way into the underlying Cu spacer layer. After ion milling, a 50 nm thick SiO layer was deposited by thermal evaporation, followed by a liftoff process, to electrically isolate the junction area. Finally, the top Nb wiring layer was patterned using the same photolithography process as the bottom leads. The surface was cleaned with oxygen plasma etching followed by *in-situ* ion milling, in which 1 nm of the top Au surface was removed immediately before sputtering. We deposited top leads of Nb(150 nm)/Au(10 nm), ending with the Au to prevent oxidation.

9.2 Measurement of SQUID Oscillations

The sample was connected to the end of a dipping probe and immersed into a Dewar of liquid helium that is outfitted with a Cryoperm magnetic shield and placed inside a shielded room to reduce exposure to external sources of electromagnetic radiation. As in Ch. 8 the junctions are initialized with a -150 mT field, to align the magnetizations of all the in-plane ferromagnetic layers. Any flux trapped in the Nb leads is subsequently removed by lifting the probe in the dewar until the sample temperature rises just above the T_c of Nb,

Measurement Flowchart

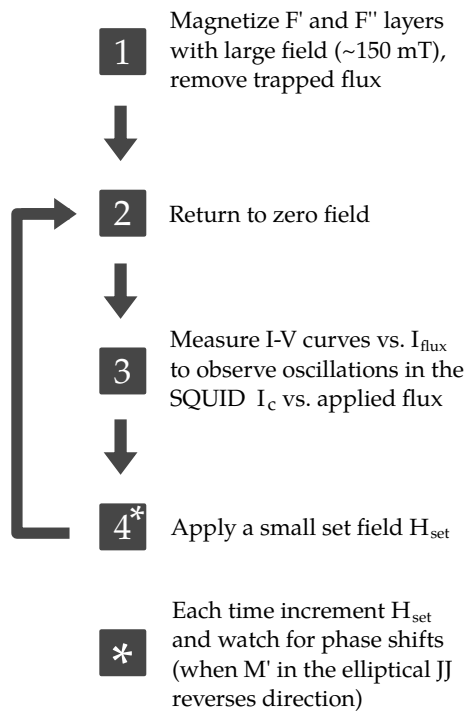


Figure 9.2: Flowchart describing the measurement process for probing the two main aspects of the SQUID samples. (1) oscillations in the SQUID's maximum I_c versus the flux in the SQUID loop (proportional to the current applied to the flux line), and (2) the magnetic state of the two junctions in the SQUID as modified by an external field. The relative phase shifts in the SQUID oscillations associated with the states before and after a magnetic switching event can be used to characterize the device as a magnetic memory.

monitored with an ohmmeter attached across the leads of the flux line. Re-immersing the sample in the liquid He, we measure the voltage across the SQUID (V_s) with the rf SQUID comparator circuit discussed in Ch. 5.6, while varying the current supplied to the sample (I_s) using a battery-powered ultra-low noise programmable current source [126]. The resulting I - V curves are representative of overdamped Josephson junctions and are fit to either the square root function (Eq. (6.1)) or the Ivanchenko-Zil'berman function (Eq. (6.2)), the latter of which accounts for thermal rounding. Either of those methods allows us to extract the normal state resistance R_N of the SQUID and the total critical current in the SQUID at positive or negative bias, I_{c+} and I_{c-} , respectively. $I_{c,\text{Avg}}$ is defined to be the average of I_{c+} and I_{c-} .

The procedure to measure the relative phase of the two junctions in the SQUID is outlined in Fig. 9.2. A separate Yokogawa current source drives a current I_{flux} through the flux line, which produces a very small out-of-plane field that induces a magnetic flux Φ through the SQUID loop. The I_c data exhibit oscillations as a function of I_{flux} with a period corresponding to one flux quantum $\Phi_0 = h/2e$ through the SQUID loop. A flux line current of ± 3 mA is sufficient to observe just over three periods in I_c . We call the initial state of the SQUID at zero field after being magnetized the ‘‘P-state’’, since the magnetizations of the Py layers in the two junctions have parallel alignment. The measured oscillations in $I_c(I_{\text{flux}})$ for one representative sample are shown in Fig. 9.3 and 9.4 and many others are presented in the Appendix.

A variable in-plane ‘‘set field’’ $\mu_0 H_{\text{set}}$ is used to control the magnetization directions of the F' layers in the junctions, however the SQUID oscillations, $I_c(I_{\text{flux}})$, are measured with the junctions in their remnant magnetization state to avoid convolving the SQUID physics with the Fraunhofer effect. Therefore, after applying a field $\mu_0 H_{\text{set}} = 0.5$ mT in the positive

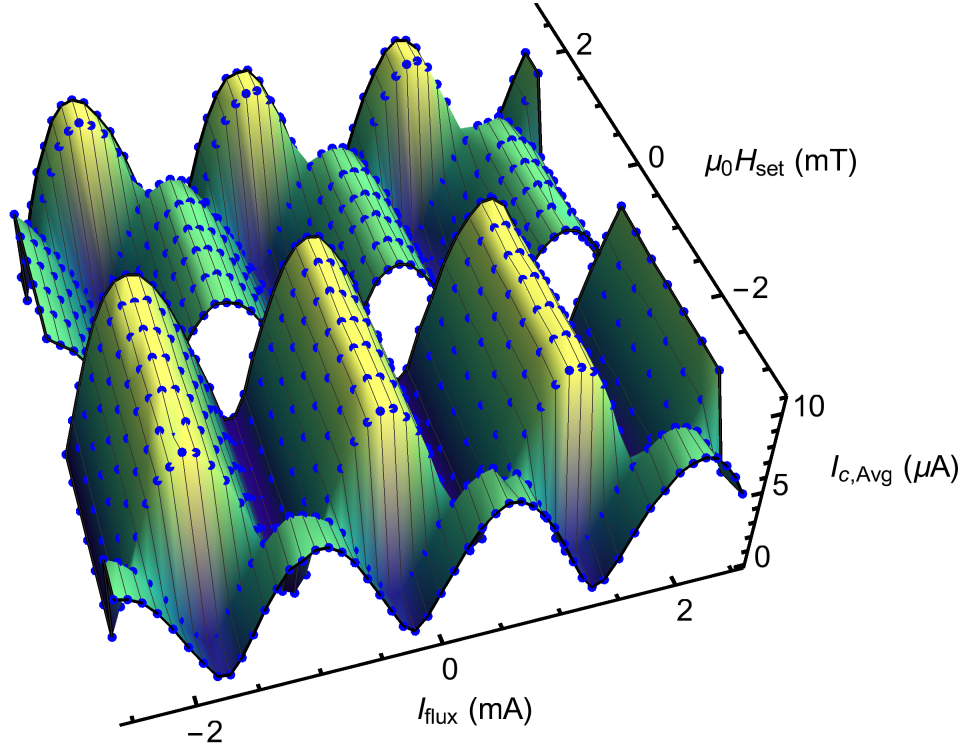


Figure 9.3: A 3D plot of a complete minor magnetization loop, for SQUID 2A-4. We show the oscillations in $I_{c,Avg}$ versus the flux line current, I_{flux} , measured after applying different values of the set field, $\mu_0 H_{set}$. All the SQUID oscillations are measured at zero field. Starting at zero field and increasing $\mu_0 H_{set}$ in the positive direction, the SQUID switches from the P to the AP state at +2.4 mT, and will remain in that state even if $\mu_0 H_{set}$ is increased or decreased slightly in either direction. Next, returning to zero field, $\mu_0 H_{set}$ is applied in the negative field direction until -2.4 mT, where the SQUID switches from the AP state back into the P state. The phase of the SQUID can thus be controllably set to either 0 or π on demand, and that behavior is reproducible over a large number of magnetic switches.

direction, the field is returned to zero before measuring $I_c(I_{\text{flux}})$. The process is repeated increasing $\mu_0 H_{\text{set}}$ in steps of 0.5 mT, as described in Fig. 9.2.

Initially, if $\mu_0 H_{\text{set}}$ is less than the coercive field of the Py layers in either junction, the data shows that the state of the SQUID is unchanged by $\mu_0 H_{\text{set}}$. Then, when $\mu_0 H_{\text{set}}$ exceeds the coercive field of the Py layer in the elliptical junction, $\mu_0 H_{\text{set}} \approx 2.4$ mT, that layer suddenly reverses its magnetization direction and the resulting SQUID oscillation curve shifts in phase (relative to the P-state) by almost exactly $\Phi_0/2$. The half period (or “ π ”) phase shift is immediately recognizable in the data for either either $I_{c,\text{Avg}}$, I_{c+} , and I_{c-} . We refer to the state after the phase-shift the “AP-state”, since the magnetizations of the Py layers in the junction are now aligned anti-parallel to each other. Across the full set of samples, shown in the Appendix, the SQUIDs typically switch into the AP-state for values of H_{set} between 1.6–2.8 mT, which agrees well with separate SQUID magnetometry measurements of the coercive field of Py, for junctions of this size, made in our lab [144].

As shown in Fig. 9.3, we observe that the I_c amplitude of the AP-state is typically slightly larger than that in the P-state, and is sometimes accompanied by a vertical offset in I_c . However, the difference between the amplitudes of the P and AP state critical currents is considerably smaller in these spin-triplet SQUIDs than in the samples from Ch. 7 that carry only spin-singlet supercurrent. According to the theory of spin-triplet Josephson junctions discussed in Ch. 4, the pair correlation function describing the long range spin-triplet pairs in the F layer, unlike the spin-singlet pair correlation function, does not oscillate in sign versus the accumulated phase shift through the junction. Furthermore, if the F' layer magnetization reverses direction, the theory predicts that the critical currents in the P and the AP states will be nearly identical.

Indeed, we did observe nearly identical critical currents in the very first run of the first

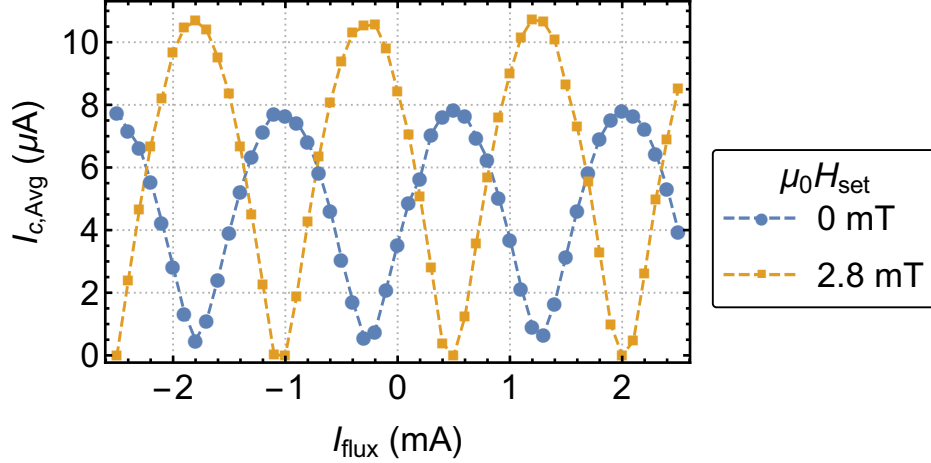


Figure 9.4: The average critical current $I_{c,\text{Avg}}$ oscillates with the current applied to the flux line I_{flux} for the P and AP states of SQUID 2A-4. After initializing the sample with an in-plane field of -150 mT, the SQUID oscillation corresponds to the P-state (blue). Applying successively larger set fields H_{set} the SQUID will switch abruptly into the AP-state (yellow) with a relative π -phase shift. The points are the values of $I_{c,\text{Avg}}$ extracted from the I - V curves using a simple square root fit, Eq. (6.1), while the dashed lines are only to guide the eye.

SQUID we measured (2A-1), as shown in Fig. 9.5. But in all of the other samples, and in subsequent runs of that sample, the critical currents were slightly different in the P and AP states. We do not understand the source of that small difference. We initially surmised that there might be a small amount of spin-singlet supercurrent traversing the samples, so that the total observed supercurrent would be the superposition of the spin-singlet and spin-triplet parts. If only the latter switches sign, then the total amplitudes would be different in the two states.

To test that hypothesis, in our lab Victor Aguilar is currently studying a set of junctions, similar to those described here, but with the order of the F and F'' layers exchanged. This “shuffled” configuration does not permit the conversion to long range spin-triplet supercurrent and thus will be a direct measurement of the spin-singlet contribution to the supercurrent.

We observe that the AP-state is magnetically stable even if $\mu_0 H_{\text{set}}$ is slightly increased

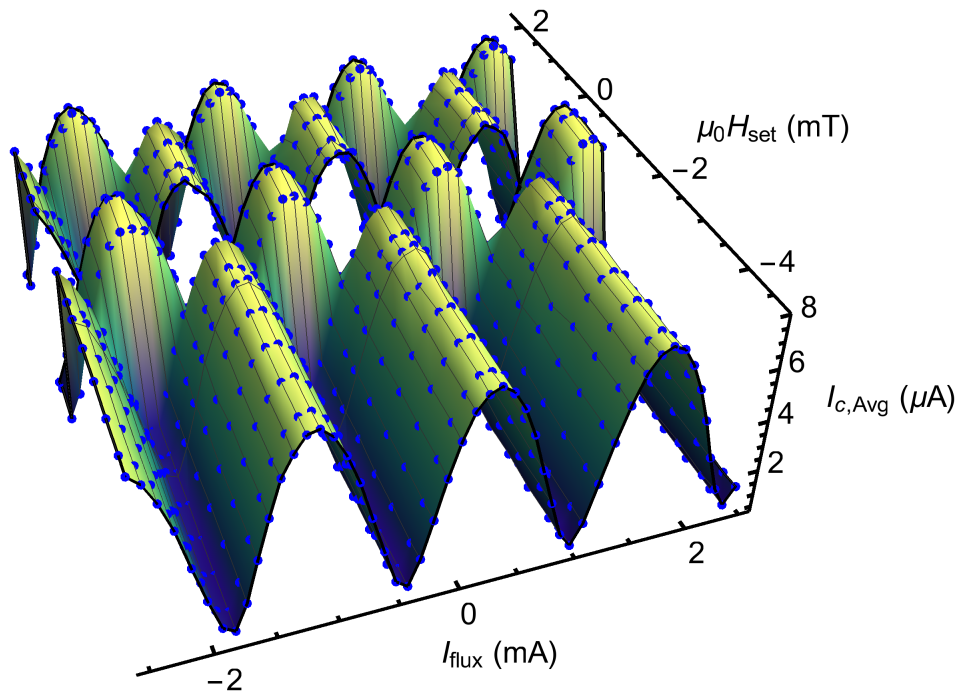


Figure 9.5: A 3D plot of a complete minor magnetization loop, for SQUID 2A-1. We show the oscillations in $I_{c,\text{Avg}}$ versus the flux line current, I_{flux} , measured after applying different values of the set field, $\mu_0 H_{\text{set}}$. All the SQUID oscillations are measured at zero field. Starting at zero field and increasing $\mu_0 H_{\text{set}}$ in the positive direction, the SQUID switches from the P to the AP state at +2.0 mT, and will remain in that state even if $\mu_0 H_{\text{set}}$ is increased or decreased slightly in either direction. Next, returning to zero field, $\mu_0 H_{\text{set}}$ is applied in the negative field direction until -1.6 mT, where the SQUID switches from the AP state back into the P state. However, in this SQUID the amplitude of the critical current is approximately the same in the two states. The phase of the SQUID can thus be controllably set to either 0 or π on demand, and that behavior is reproducible over a large number of magnetic switches.

or decreased in either direction. Assuming that the Py layers behave similarly to the Stoner-Wohlfarth model discussed in Ch. 3, the magnetic state of the SQUID should remain stable over a range of fields between $\mu_0 H_{Py_1} < \mu_0 H_{set} < \mu_0 H_{c,Py_2}$, where $\mu_0 H_{c,Py_1}$, and $\mu_0 H_{c,Py_2}$ are the coercive fields of the Py layer in the elliptical and hex junctions, respectively.[†] We observe that after switching into the AP-state, the state is stable over a narrow range of fields, typically around 1-2 mT, but if $\mu_0 H_{set}$ is increased further ($> \mu_0 H_{c,Py_2}$) then a second switching event is observed, evidenced by another abrupt phase shift. We infer that the range of fields over which the AP-state is stable is representative of the difference between the coercive fields of the Py layers in the two junctions ($\mu_0 H_{c,Py_2} - \mu_0 H_{c,Py_1}$). The value of $\mu_0 H_{c,Py_1}$ and $\mu_0 H_{c,Py_2}$ may vary slightly from sample to sample, due to differences in lithography, surface roughness, or defectivity during growth, so it is important to characterize each SQUID individually and determine the mean value and variance of these two fields.

To further demonstrate that the state of the SQUID is magnetically controllable, after setting the SQUID into the AP state we apply $\mu_0 H_{set}$ in the negative direction to switch the Py magnetization back to its original orientation, completing a minor magnetic loop. The data shows that SQUID oscillations remain stable in the AP-state until $\mu_0 H_{set} \approx -2.4$ mT, at which point the magnetization of the Py in the elliptical junction is reversed and the original P-state SQUID oscillation curve is recovered. For comparison we plot the complete set of SQUID oscillations, for both directions of the set field in the 3D plot of Fig. 9.3. One can see that the SQUID oscillations in the P and AP-states for both positive and negative values of $\mu_0 H_{set}$ are functionally equivalent, but we often observe that the values of $\mu_0 H_{c,Py_1}$ on either side of zero are not always symmetric. Typically, we observe that the coercive field

[†]The tacit assumption being that the coercive field of the Ni layers in either of the junctions exceeds that of the Py layers in both of the junctions.

in the negative direction (or the initial direction of the magnetization) is slightly larger in magnitude than the coercive field in the positive direction.

In total, nine SQUIDs were measured from four chips (two chips with $n = 2$ and two chips with $n = 3$, corresponding to a total number of [Pd/Co] bilayers of 4 or 6, respectively). The full set of those data can be found in the Appendix, where the sample numbering convention (*e.g.* 2A-4) is listed by the chip name (2A, 3A, etc.) followed by the number of the SQUID (each chip contains four SQUIDs). As we will discuss in the next section, in seven of the SQUIDs we measured complete minor loops with reproducible $0-\pi$ state switching between the P and AP states, confirmed by fitting the data to SQUID theory from Ch. 7. The average normal state resistance of those samples was $R_N = 13.4 \pm 0.9$ m Ω , about half the resistance of the individual spin-triplet junctions from Ch. 8, a reasonable number given that the SQUID samples have twice the total area (two junctions per SQUID). Minor loops were measured in most of those seven samples multiple times and displayed $0-\pi$ phase changes even after different thermal cycles, *i.e.* bringing the sample up to room temperature and subsequently reinserting it into the Dewar and repeating the measurement process as previously described. Several of the SQUIDs, while having the same qualitative behavior (complete minor loops, oscillations in I_c , etc.), were measured to have slightly different magnetic switching fields $\mu_0 H_{c, PY1}$ or I_c amplitudes after different thermal cycles. We surmise that these small changes over different thermal cycles are attributable to the Ni layers not being completely magnetized by the -150 mT field in the same way for each measurement.[†]

Overall the SQUID oscillation data from samples with $n = 3$ are very similar to those

[†]As discussed in Ch. 9, we kept the initialization field below ± 150 mT, even though it is known that this field may not be sufficient to completely magnetize all of the Ni domains at this thickness.

with $n = 2$, aside from a universal reduction in the critical current that is consistent with the decay from the single junctions observed in Fig. 8.8. The $n = 3$ SQUIDs were also measured to have reproducible $0-\pi$ switching, however the overall decrease in amplitude of the SQUID oscillations typically makes the data noisier.

The last two of the nine samples measured did not behave as expected. One of those samples exhibited SQUID oscillations, but had poor magnetic behavior with the phase appearing to move continuously rather than switching abruptly. The final sample had very large resistance of $> 1\Omega$ and very small I_c , presumably due to a liftoff issue during fabrication.

9.3 SQUID Oscillation Data: Comparison to Theory

The critical current data analyzed using the square root function (*e.g.* Fig. 9.4) can be easily fit to the SQUID theory from Ch. 7, to confirm the relative $0-\pi$ phase shifts between the P and AP states. However, we find that due to the relatively small critical current and noticeable thermal rounding in the $I-V$ curves of these samples, more accurate critical current values can be extracted using the Ivanchenko-Zil'berman function, Eq. (6.2).

The SQUID oscillations produced by fitting the fits to the Ivanchenko-Zil'berman function, shown in Fig. 9.6, generally have less scatter in I_{c+} and I_{c-} and allow us to extract the values of the thermal noise temperature T_{eff} . Fitting all the data in a full three dimensional plot such as Fig. 9.3 with Eq. (6.2) is rather time-intensive, so we fit the P and AP states at only two values of $\mu_0 H_{\text{set}}$. As shown in Fig. 9.6, the resulting SQUID oscillations have larger amplitude and maximum critical current compared with the data fit using the square root function (Fig. 9.4). Typically $T_{\text{eff}} \approx 40-80$ K in the Ivanchenko-Zil'berman fits, which is slightly larger than the values measured in individual Josephson junctions discussed in Ch. 6

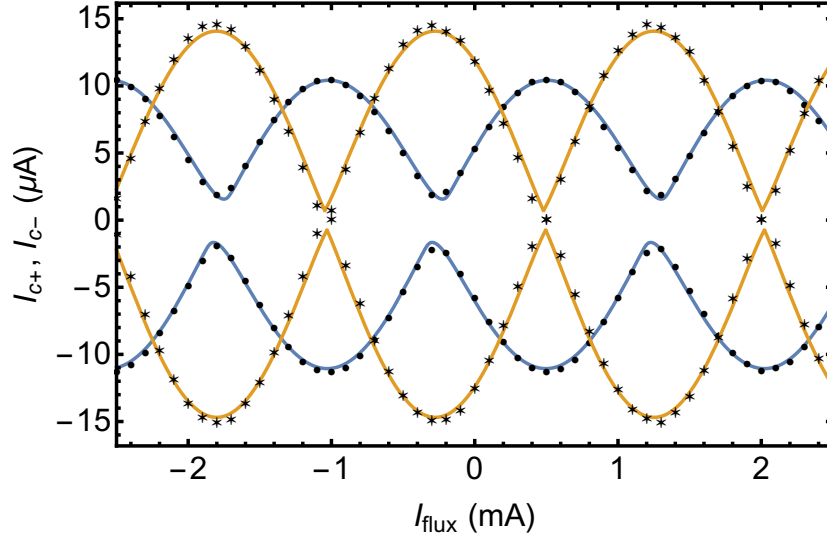


Figure 9.6: *Fitting the P and AP states from SQUID 2A-4.* At a given applied flux current I_{flux} , each data point represents the positive or negative critical current values extracted from a measured I - V curve that was fit to the Ivanchenko Zil'berman function Eq. (6.2) for the P (circles) and AP (stars) states. The resulting oscillation data has good agreement with the SQUID theory from Ch. 7, where the lines represent the nonlinear least-squares fits for the P (blue) and AP (yellow) states. The associated best-fit parameters and errors are listed in Table 9.1, which confirms the relative π -phase shift between the two states. The P and AP states shown were measured after applying set fields, $\mu_0 H_{\text{set}}$, of 0 mT and 2.8 mT, respectively, after the sample was initialized in a set field of -150 mT.

or Ch. 8, varying somewhat sample to sample.

Table 9.1: *Best-fit parameters for the P and AP states for SQUID 2A-4.* The value of α_L in the fit is fixed at zero and the total inductance L is fixed at the nominal value of 9 pH, thus determining β_L . The phase difference between the two states is $\approx \pi$ (ϕ_{shift} is listed in units of 2π).

State	β_L	α_I	I_{c+} (μA)	$ I_{c-} $ (μA)	ϕ_{shift}	$\phi_{\text{shift}}^P - \phi_{\text{shift}}^{AP}$
P	4.67×10^{-2}	$(1.50 \pm 0.06) \times 10^{-1}$	5.20 ± 0.02	5.52 ± 0.02	0.329 ± 0.001	0.509 ± 0.003
AP	6.27×10^{-2}	$(-1.60 \pm 1.75) \times 10^{-2}$	7.04 ± 0.06	7.34 ± 0.06	-0.180 ± 0.002	

The SQUID oscillations are then fit to SQUID theory described in Ch. 7, to confirm the 0 - π phase changes between the P and AP states and to extract quantitative information

about the critical currents in each of the junctions. Best-lines fits are shown in Fig. 9.6 with the corresponding fit parameters and their uncertainties listed in Table 9.1. Similar plots for each of the other six SQUIDs measured can be found in the Appendix.

As expected from the design geometry, the SQUID oscillations are symmetric due to balanced inductances in the two arms of the SQUID. We find that better quality fits are obtained if we fix the inductance asymmetry parameter (Eq. (7.19)) to $\alpha_L = 0$, reducing the number of free fitting parameters. Thus in all the fits that follow we set $\alpha_L = 0$. In both the P and AP states, the fits produce a very small screening parameter, for example $\beta_L \approx 0.047$ for the data shown in Fig. 9.6, allowing the depth of the modulation to be very deep. As the data indicates, often the value of I_c at the oscillation minima are very close to zero. Compared to the spin-singlet SQUID data from Ch. 7, the fits to the spin-triplet SQUIDs also have a much smaller critical current asymmetry parameter α_I . Due to the small values of β_L and α_I the I_{c+} and I_{c-} data are hardly shifted with respect to each other.

Most importantly, the relative phase shift between the P and AP state is almost exactly π within the margin of error, as shown in the last column of Table 9.1 where the phase difference is listed in units of 2π . Table 9.2 contains a summary of all seven samples measured, each of which shows a π phase difference between the P and the AP states. Table 9.2 also shows that when most of the samples transition from the P to the AP state, one of the two junctions critical current changes, while the critical current of the other junction stays essentially constant. However, for SQUIDs 2A-2 and 4A-4 the current in both of the junctions appears to change. We do not fully understand this issue, given the very good agreement between the measured data and the fits.

Table 9.2: *Summary of the the seven spin-triplet SQUID samples measured.* Fitting the data to the SQUID theory from Ch. 7, and fixing the total inductance to the nominal value of 9 pH, we find that the phase difference between the P and the AP states in each of the SQUID is $\approx \pi$ (ϕ_{shift} is listed in units of 2π). Moreover, from the fit parameters we can extract the values of the critical current in each of the two junctions. Typically, we find that between the two states only the critical current in the elliptical junction (I_{c1}) changes in magnitude, while the critical current in the other junction (I_{c2}) is approximately constant. The value $2n$ is the total number of [Pd/Co] bilayers in the F layer.

SQUID Name	$2n$	State	I_{c1} (μA)	I_{c2} (μA)	$\phi_{\text{shift}}^P - \phi_{\text{shift}}^{AP}$
2A-1	4	P	6.65 ± 0.08	4.20 ± 0.08	0.491 ± 0.005
		AP	6.90 ± 0.12	4.18 ± 0.12	
2A-2	4	P	5.66 ± 0.10	5.61 ± 0.10	-0.458 ± 0.004
		AP	4.09 ± 0.14	4.02 ± 0.14	
2A-3	4	P	4.53 ± 0.12	4.56 ± 0.12	0.480 ± 0.004
		AP	6.88 ± 0.07	4.67 ± 0.07	
2A-4	4	P	4.56 ± 0.04	6.16 ± 0.04	0.509 ± 0.003
		AP	7.30 ± 0.15	7.08 ± 0.15	
3A-3	6	P	0.80 ± 0.30	0.79 ± 0.30	-0.481 ± 0.010
		AP	1.99 ± 0.02	1.34 ± 0.02	
4A-1	6	P	0.60 ± 0.33	3.16 ± 0.33	0.618 ± 0.005
		AP	1.45 ± 0.03	3.87 ± 0.03	
4A-2	6	P	1.32 ± 0.04	2.41 ± 0.04	-0.507 ± 0.004
		AP	3.01 ± 0.01	1.61 ± 0.01	

9.4 Repeated Switching Experiment

To gather statistics on the reproducibility of the magnetic switching of these devices, and as a preliminary test of their robustness as a magnetic memory, we fixed the value of I_{flux} near where the SQUID oscillation is at a minimum in the P-state (or a maximum in the AP-

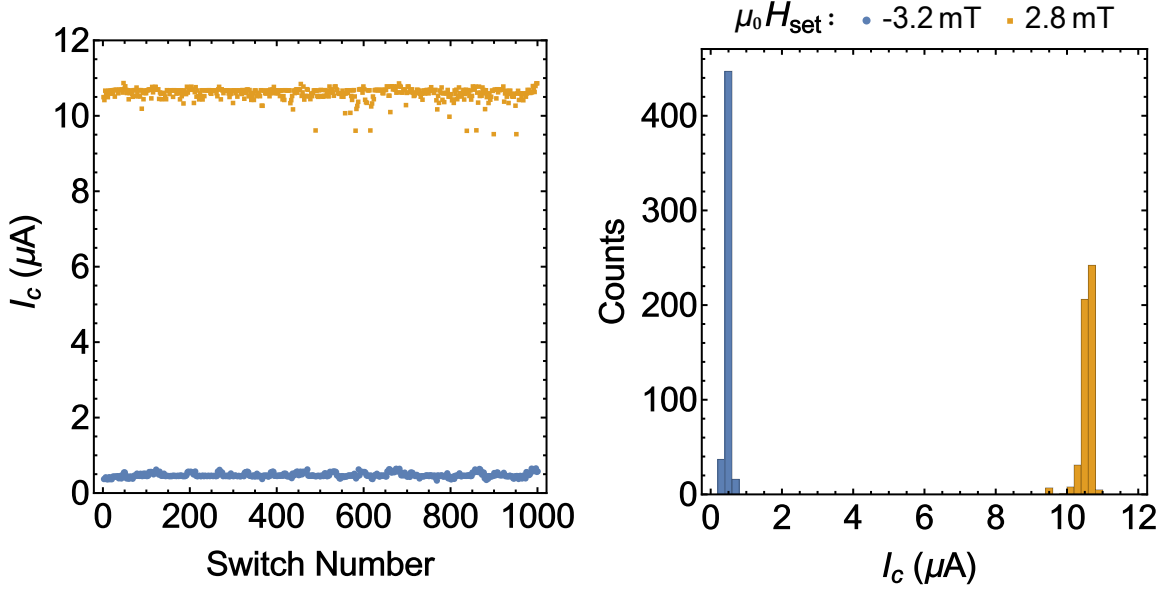


Figure 9.7: *Repeated switching between the P and the AP-states.* The SQUID was repeatedly cycled between the P and the AP states a thousand times. To achieve a large I_c contrast between the two states, the current in the flux line was fixed at -0.2 mA, where I_c is at a maximum in the P-state (and a minimum in the AP-state), as shown in Fig. 9.4. We plot $I_{c,\text{Avg}}$, obtained from fitting the measured I - V curves to the square root function (Eq. (6.1)), versus the number of times the junction has been switched (left). No major switching errors occur after a thousand cycles, with narrow spreads in I_c for each of the two states. We plot a histogram where the I_c values have been binned into units of 0.2 μA (right).

state), for example at -0.2 mA in Fig. 9.4. Then, we repeatedly alternated $\mu_0 H_{\text{set}}$ between two field values just beyond $\mu_0 H_{c,\text{PY1}}$ in the positive and negative directions, to switch the SQUID back and forth between the P and AP states. In Fig. 9.7(a), we plot the value of $I_{c,\text{Avg}}$ (fit using the square root function) versus the number of switches. Over the course of 1000 repeated switches the SQUID successfully alternated back-and-forth between the P and the AP states without any major errors. We arbitrarily define the “error” threshold to be when the value of a given I_c , in either the P or the AP states, at a given I_{flux} , deviates by more than 20 % of its average value in that given state.

To get an idea for the spread in distribution of I_c 's, in Fig. 9.7(b) we bin the I_c values with even and odd switch numbers into two histograms, where the size of each bin represents

0.2 μA . The distributions of I_c in each state are very tight, and the two do not overlap so the P and AP states can, in principle, serve as the logical 0 and 1 states of the memory.

9.5 SQUID Measurements Below 4.2 K in a Dilution Refrigerator

We independently measured the spin-triplet SQUID samples at temperatures below 4.2 K in an Oxford dilution refrigerator, due to several motivating factors. First, the I - V curves from the previous set of measurements all appeared to be thermally rounded near the critical current, particularly those with very small $I_c < 1 \mu\text{A}$, resulting in somewhat larger T_{eff} . Second, the maximum I_c values in the spin-triplet SQUIDs were slightly smaller than expected, based on the individual junction results from Ch. 8. We suspected that additional electromagnetic interference, either from the SQUID itself, the additional measurement equipment (such as the flux line current source), or external sources, might be limiting the I_c of the devices. The low noise rf-SQUID based electronics system previously described in Ch. 5, has superb RMS voltage noise (≈ 6 pV measuring over 10 power line cycles), but the measurement probe used in conjunction with it has no rf-filtering.

The Oxford dilution refrigerator unit in our lab has rf-filtered lines, comparatively better isolation, and can measure over a range of temperatures from 40 mK - 5 K. On the other hand, the dilution refrigerator system is not equipped with the sensitive rf-SQUID electronics. Instead, we used a lock-in amplifier to measure $\partial V/\partial I$ versus the measurement current, which can be integrated to obtain an I - V curve.

We wished to address three main questions: What is the temperature dependence of I_c ? Is I_c in the spin-triplet SQUIDs larger while measured in a system with better rf-filtering? And finally, would the I - V curves have less thermal rounding? To address these

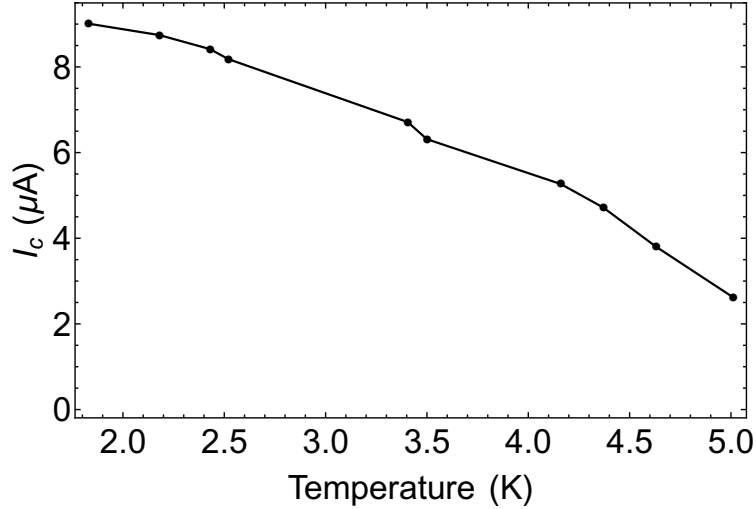


Figure 9.8: *Critical current versus temperature for SQUID 2A-2 in a dilution refrigerator.* The critical current decreases inversely with temperature, but is not substantially larger at 1-2 K compared to the previous measurements at 4.2 K. The lines connecting the data points are only to guide the eye.

questions we measured the temperature dependence of the critical current, in addition to several oscillations versus the applied flux for two different SQUID samples. Unfortunately, due to a small helium leak in the dilution refrigerator we were only able to measure the SQUIDs from about 5 K down to just above 1 K.

To answer the first question is that the value of the critical current only increases modestly with decreasing temperature. Figure 9.8 shows the temperature dependence of I_c at a fixed value of I_{flux} for a different SQUID sample than previously discussed (SQUID 2A-2, other plots from this sample can be found in the Appendix). We measured that the critical current increases with decreasing temperature, but is only about 30 % larger at 2 K than at 4.2 K. The answer to the second question seems to be no: for two different samples the critical current at 4.2 K measured while using the dilution refrigerator system is almost identical to the value measured using the rf-SQUID comparator measurement system. To address the third question, we fit some of the I - V curves for SQUID 2A-1, shown in Fig. 9.9, to the

Ivanchenko-Zil'berman function. Even at 2.0 K we find that the I - V curves display similar thermal rounding in the dilution refrigerator system as in the rf SQUID comparator system. The temperature dependence of I_c for that sample at zero flux current shown in Fig. 9.9 behaved similarly to that of SQUID 2A-2, shown in Fig. 9.8.

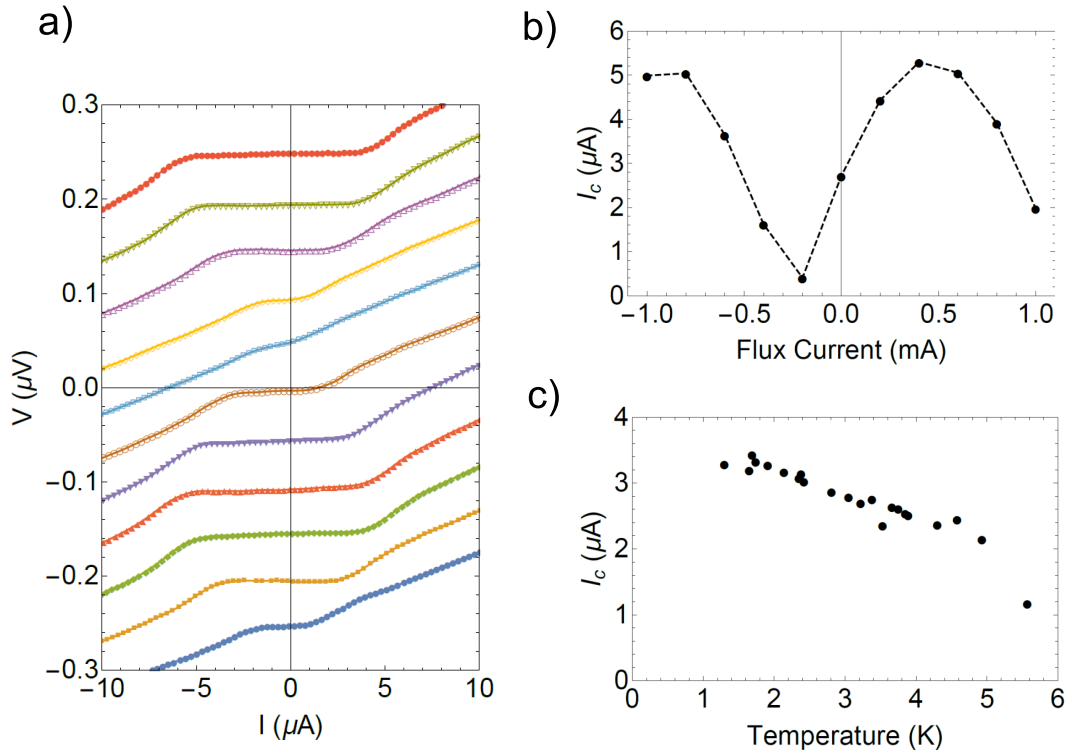


Figure 9.9: *Critical current versus flux-line current and temperature for SQUID 2A-1 in a dilution refrigerator.* The measured $\partial V/\partial I$ curves are converted into I - V curves by numerical integration. With the sample temperature near 2.0 K the I - V curves shown in (a) display similar thermal rounding compared to junctions measured in the low noise rf-SQUID system. In (a) each I - V curve corresponds to the different values of the applied flux current (ranging from ± 1 mA) and are successively offset by $0.25 \mu\text{V}$ for clarity. The lines represent fits to the Ivanchenko-Zil'berman function, Eq. (6.2). In (b) we plot the critical current at 2.0 K (fit using the square root function) versus the applied flux current, where the dashed line is only to guide the eye. In (c) we fix the flux current at 0 mA and show that the critical current increases with decreasing temperature, but is not substantially larger at 1-2 K compared to the previous measurements at 4.2 K.

9.6 Conclusion

In this chapter we have shown the first demonstrations of phase-controllable Josephson junctions that carry long range spin-triplet supercurrent. In seven different SQUID devices, we measured that the ground-state phase of the junction can be switched between the zero or π -phase states. Many of the junctions can be reliably switched between the two states on the order of 1000 times without error.

Such junctions could be useful for superconducting single-flux quantum circuits [116]; in particular, we envision a superconducting memory based on such a device [18, 23]. There are easier ways to make a phase-controllable memory device; as shown in Ch. 7, the simpler spin-valve Josephson junction containing only two magnetic layers of appropriate thicknesses can also exhibit controllable $0-\pi$ switching. In those devices, the physical mechanism of the $0-\pi$ phase shift is different; it relies on the accurate tuning of the thicknesses of the two magnetic layers so that the total phase shift acquired by an electron pair traversing the sample is closer to an even or odd multiple of π when the two magnetizations are parallel or antiparallel.

In the spin-triplet devices presented in this chapter, the $0-\pi$ switching is caused by spin rotations rather than phase accumulation, so the behavior is less sensitive to the exact thicknesses of the F' and F'' layers (as long as those layers are not close to the minima in their own $0-\pi$ transition curves). We believe that is one explanation for the high degree of consistency between the seven spin-triplet SQUID samples measured, compared to the spin-valve SQUIDs discussed in Ch. 7. In addition, the central SAF geometry used in the spin-triplet junctions may help improve the reliability of the device, canceling stray magnetic fields that would otherwise be detrimental to the other in-plane ferromagnetic layers.

We also demonstrated that making the shape of the fixed junction in the SQUID a large aspect ratio “hex” geometry instead of an ellipse could potentially be an important feature of future test SQUIDs. Note that in cryogenic memory applications such as JMRAM, only one controllable ferromagnetic junction is required, so the hex-shaped junction would not be used. Also, the hex junctions still require further experimental study; we can only indirectly guess that the hex shape played a role in the relative stability of these junctions. Detailed magnetometry studies using magnetic bit arrays of the type discussed in Ch. 5 should be performed on elliptical and hex junctions of different aspect ratios to substantiate the above claim.

One potential downside to these spin-triplet junctions compared to those containing spin-valves is that the critical currents are considerably smaller. There are several different means by which the spin-triplet supercurrent could possibly be enhanced using the scheme presented in this chapter. For example, it is not clear that we have completely maximized the conversion from spin-singlet to the long range spin-triplet correlations. If the Ni layers have multiple domains and are not completely aligned by the 150 mT initialization field, it could lead to a decreased critical current. Remeasuring these samples with larger initialization fields to better align the Ni layers would be one simple way of testing this hypothesis (we would not want to disturb the out-of-plane magnetization F layer, but the ± 150 mT used here may have been somewhat conservative). One could also try replacing the $F'' = \text{Ni}$ layer with another ferromagnet that is more likely to be single domain. Also, in the F layer we used Ru as the coupling layer in the center of the SAF, which we have found decreases the critical current in $S/N/F/N/S$ junctions by roughly a factor of two compared to Cu [144]. Using a different coupling layer in the center of the SAF may also be worth exploring. Finally, using a magnetically weaker ferromagnetic material for F' instead of Py could also help in

generating larger amplitude critical currents.

Chapter 10

Conclusion

In this final chapter we summarize the results presented in this thesis, revisit some open questions to be explored in future work, and discuss the outlook for energy efficient superconducting memory.

After reviewing the basic theoretical concepts behind superconductivity and ferromagnetism in Chs. 2 and 3, in Ch. 4 we discussed how the the interplay of superconductivity and ferromagnetism can be used in various types of ferromagnetic Josephson junctions. We described various schemes by which ferromagnetic Josephson junctions can be manipulated to carry spin-singlet or spin-triplet supercurrent, theoretical concepts that underpin all of the experiments presented in the later chapters. After discussing the experimental methods, procedures, and equipment in Ch. 5 that were used to fabricate and measure the Josephson junction and SQUID samples in our lab, in Ch. 6 we briefly outlined a scheme for using ferromagnetic Josephson junctions as a phase-sensitive superconducting memory.

In Ch. 6 we also presented four separate experimental materials characterization studies of Josephson junctions containing a central ferromagnetic layer of either $\text{Ni}_{65}\text{Fe}_{15}\text{Co}_{20}$, Py, $\text{Pd}_{97}\text{Fe}_3$, or Ni. Systematic studies of the material properties of such junctions, including the $0-\pi$ transition thickness, switching fields, and shifts in the Fraunhofer patterns versus F -layer thickness were examined.

Of the materials studied, we eventually settled upon Py and Ni as the respective free and fixed layers for both our spin-valve and spin-triplet junctions. In general, we value Py

primarily for its excellent magnetic properties and controllable switching at a low magnetic fields. Meanwhile, Ni, despite its unfavorable magnetic properties was chosen largely because of its ability to permit large critical currents to pass through Josephson junctions.

In Ch. 6 we showed that NiFeCo is another potential candidate alloy for a fixed layer. That work led to several follow-up studies by our group to examine its applicability in cryogenic memory devices.[†] Also, we examined the enticing possibility of using much weaker ferromagnetic layers for the free layer, such as dilute alloys of PdFe, which would allow us to make the free layer much thicker yet permit large critical currents. While the Josephson junctions containing Pd₉₇Fe₃ showed those layers had comparable switching fields to Py, and with relatively small magnetization, unfortunately the magnetic switching was not as sharp as desired. This has since led to other studies in our group (still in progress) in which we are increasing the Fe concentration of the alloy to improve its magnetic properties.

In Ch. 7, we discussed the first experimental demonstration that the phase state of a Josephson junction can be controllably switched between 0 and π , *i.e.* a phase-sensitive cryogenic one-bit memory device using spin-singlet supercurrent. The phase-sensitive detection was achieved by adding two ferromagnetic Josephson junctions with a “spin-valve” configuration into a SQUID loop. My main contribution to that effort was the development of a general asymmetric SQUID fitting program necessary for the unambiguous proof that the devices switched between the phase values of 0 and π . The Ni/Py spin-valve junctions similar to those discussed in Ch. 7 have since gone on to be a central part of an operational superconducting memory cell by our collaborators at Northrop Grumman Corporation [23].

In Ch. 8, we presented magnetic and transport measurements on a new configuration

[†]NiFeCo was later implemented into spin-valve SQUID samples by Bethany Niedzielski, replacing Ni as the hard layer, with mixed success. Those Py/NiFeCo-based spin-valve junctions suffered from some variability in the magnetic switching and overall had smaller critical current compared to the Py/Ni based spin-valves. Refer to Ref. [144] for more details.

of materials by which we are able to generate spin-triplet supercurrent through the fine control of three ferromagnetic layers with noncolinear magnetizations. The central layer is a synthetic antiferromagnet (SAF) composed of [Pd/Co] multilayers on either side of a Ru spacer with magnetization perpendicular to the plane. The other two ferromagnetic layers, either Py or Ni, have in-plane magnetization. Contrary to other approaches, we demonstrated the viability of our scheme in which the SAF has perpendicular magnetic anisotropy, which could be an important step for future devices. Our approach allows the junctions to be patterned into non-circular geometries to take advantage of shape anisotropy, meanwhile the SAF helps cancel the stray fields that were thought to cause problems with other out-of-plane spin-triplet control experiments [109]. We demonstrated that the electron pairs in the central layer of the junctions in Ch. 8 predominantly have long range spin-triplet correlations. This was demonstrated by observing the characteristic slow decay of the critical current in those junctions versus the layer thickness compared to other junctions without the in-plane layers that carry only spin-singlet supercurrent. Work is underway by Victor Aguilar to characterize the extent to which the spin-singlet supercurrent decays in these type of junctions.

The junctions in Ch. 8 were then implemented in Ch. 9 in SQUIDS carrying spin-triplet supercurrent. We verified experimentally one of the most salient predictions of the spin-triplet theory, namely that a Josephson junction containing three magnetic layers with noncolinear magnetizations should exhibit a ground-state phase shift of either zero or π depending on the relative orientations of those magnetizations. We showed in seven different spin-triplet SQUID devices that the phase can be reliably switched between the zero or π states. A number of the SQUIDS measured were able to switch between the two phase-states on the order of a thousand times without error, demonstrating that this type of phase-controllable

junction could also be used as a novel memory element in a superconducting computer.

The future for superconducting computing is bright. As highlighted in Ch. 1, recent advances in superconducting logic and the potential for energy-efficient solutions to growing energy problems, as well as the rise of quantum computing, have helped reinvigorate the field. Superconducting memory using ferromagnetic Josephson junctions, such as those presented in this thesis, still need major development before being implemented in large-scale superconducting computers. However, in the last six years significant proof-of-concept demonstrations by many groups including our own, such as those presented in Ch. 7 and Ch. 9 have been realized experimentally.

Simultaneously controlling superconductivity and ferromagnetism in Josephson junction based devices is difficult, given the inherent material science and fabrication challenges, as well the relative difficulty in theoretically examining junctions with complex magnetic multilayers. Hopefully the experiments presented in this thesis, beyond their interest to basic science, have highlighted some of the features that ferromagnetic Josephson junctions bring to the field of superconducting computing, in addition to exposing some of the challenges that need to be solved for progress to continue. Novel approaches to superconducting memory such as spin-triplet based devices are rich for exploration and it will be exciting to see the role they may play in the future development of the field.

APPENDIX

Spin-triplet SQUID data

In this appendix we provide the complete data series of measurements and analysis of SQUID samples carrying spin-triplet supercurrent from the experiments described in Ch. 9. The sample numbering convention (*e.g.* 2A-4) is to first list the chip name (2A, 3A, etc.) followed by the number of the SQUID (each chip contains four SQUIDs). The plots and analysis for SQUID 2A-4 can be found in Ch. 9.

SQUID 2A-1

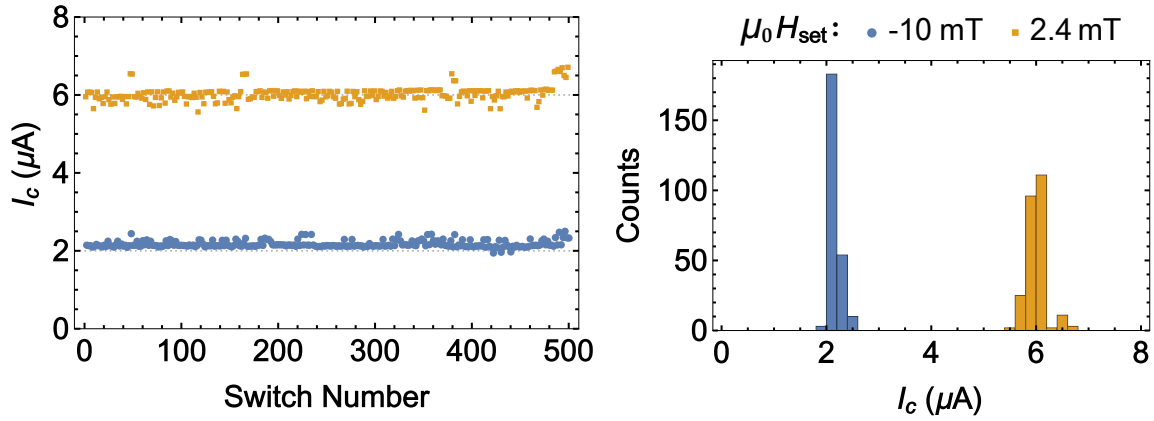


Figure 1: *Repeated switching between the P and the AP-states from SQUID 2A-1.* We plot $I_{c,\text{Avg}}$, obtained from fitting the measured I - V curves to the square root function (Eq. (6.1)), versus the number of times the junction has been switched (left). No major switching errors occur after a 500 switches, with narrow spreads in I_c for each of the two states. We plot a histogram where the I_c values have been binned into units of $0.2 \mu\text{A}$ (right).

Table 1: *Best-fit parameters for the P and AP states for SQUID 2A-1.* The value of α_L in the fit is fixed at zero. The phase difference between the two states is $\approx \pi$ (ϕ_{shift} is listed in units of 2π).

State	β_L	α_I	I_{c+} (μA)	$ I_{c-} $ (μA)	ϕ_{shift}	$\phi_{\text{shift}}^P - \phi_{\text{shift}}^{AP}$
<i>P</i>	4.47×10^{-2}	$(2.27 \pm 0.01) \times 10^{-1}$	5.25 ± 0.04	5.60 ± 0.04	0.156 ± 0.002	0.491 ± 0.005
<i>AP</i>	4.80×10^{-2}	$(2.45 \pm 0.15) \times 10^{-1}$	5.34 ± 0.06	5.74 ± 0.06	-0.335 ± 0.003	

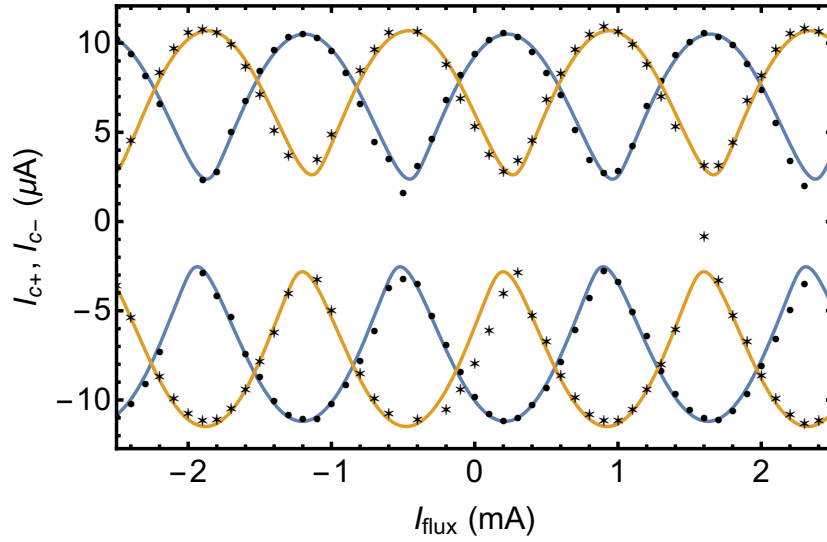


Figure 2: *Fitting the P and AP states from SQUID 2A-1.* At a given applied flux current I_{flux} , each data point represents the positive or negative critical current values extracted from a measured I - V curve that was fit to the Ivanchenko Zil'berman function Eq. (6.2) for the P (circles) and AP (stars) states. For a few I - V curves the Ivanchenko Zil'berman fits did not converge, thus there are some missing data points in the plot. The resulting oscillation data has good agreement with the asymmetric SQUID theory from Ch. 7, where the lines represent the nonlinear least-squares fits for the P (blue) and AP (yellow) states. The associated best-fit parameters and uncertainties are listed in Table 1, which confirms the relative π -phase shift between the two states. The P and AP states shown were measured after applying set fields, $\mu_0 H_{\text{set}}$, of 0 mT and 2.3 mT, respectively, after the junctions were initialized in a -150 mT set field.

SQUID 2A-2

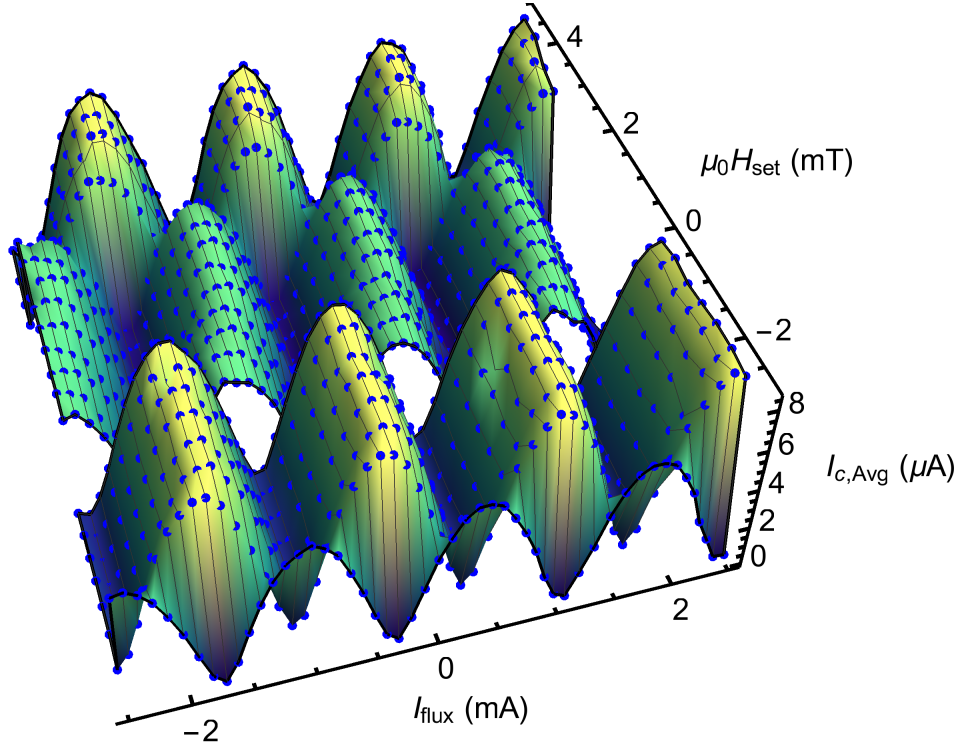


Figure 3: A 3D plot of a complete minor magnetization loop, for SQUID 2A-2. We show the oscillations in $I_{c,\text{Avg}}$ versus the flux line current, I_{flux} , measured after applying different values of the set field, $\mu_0 H_{\text{set}}$. All the SQUID oscillations are measured at zero field. Starting at zero field and increasing $\mu_0 H_{\text{set}}$ in the positive direction, the SQUID switches from the P to the AP state and will remain in that state even if $\mu_0 H_{\text{set}}$ is increased or decreased slightly in either direction. Next, returning to zero field, $\mu_0 H_{\text{set}}$ is applied in the negative field direction until the SQUID switches from the AP state back into the P state. The phase of the SQUID can thus be controllably set to either 0 or π on demand.

Table 2: Best-fit parameters for the P and AP states for SQUID 2A-2. The value of α_L in the fit is fixed at zero. The phase difference between the two states is $\approx \pi$ (ϕ_{shift} is listed in units of 2π).

State	β_L	α_I	I_{c+} (μA)	$ I_{c-} $ (μA)	ϕ_{shift}	$\phi_{\text{shift}}^P - \phi_{\text{shift}}^{AP}$
P	4.84×10^{-2}	$(-0.37 \pm 1.51) \times 10^{-2}$	5.56 ± 0.04	5.71 ± 0.03	-0.194 ± 0.001	-0.458 ± 0.004
AP	3.53×10^{-2}	$(-0.79 \pm 3.08) \times 10^{-2}$	4.01 ± 0.04	4.11 ± 0.04	0.265 ± 0.003	

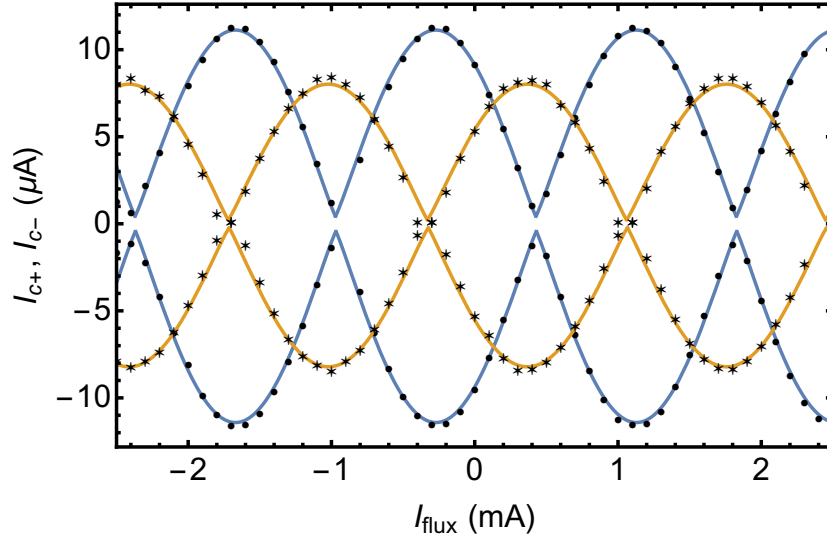


Figure 4: *Fitting the P and AP states from SQUID 2A-2.* At a given applied flux current I_{flux} , each data point represents the positive or negative critical current values extracted from a measured I - V curve that was fit to the Ivanchenko Zil'berman function Eq. (6.2) for the P (circles) and AP (stars) states. The resulting oscillation data has good agreement with the asymmetric SQUID theory from Ch. 7, where the lines represent the nonlinear least-squares fits for the P (blue) and AP (yellow) states. The associated best-fit parameters and uncertainties are listed in Table 2, which confirms the relative π -phase shift between the two states. The P and AP states shown were measured after applying set fields, $\mu_0 H_{\text{set}}$, of 0 mT and -2.8 mT, respectively, after the junctions were initialized in a -150 mT set field.

SQUID 2A-3

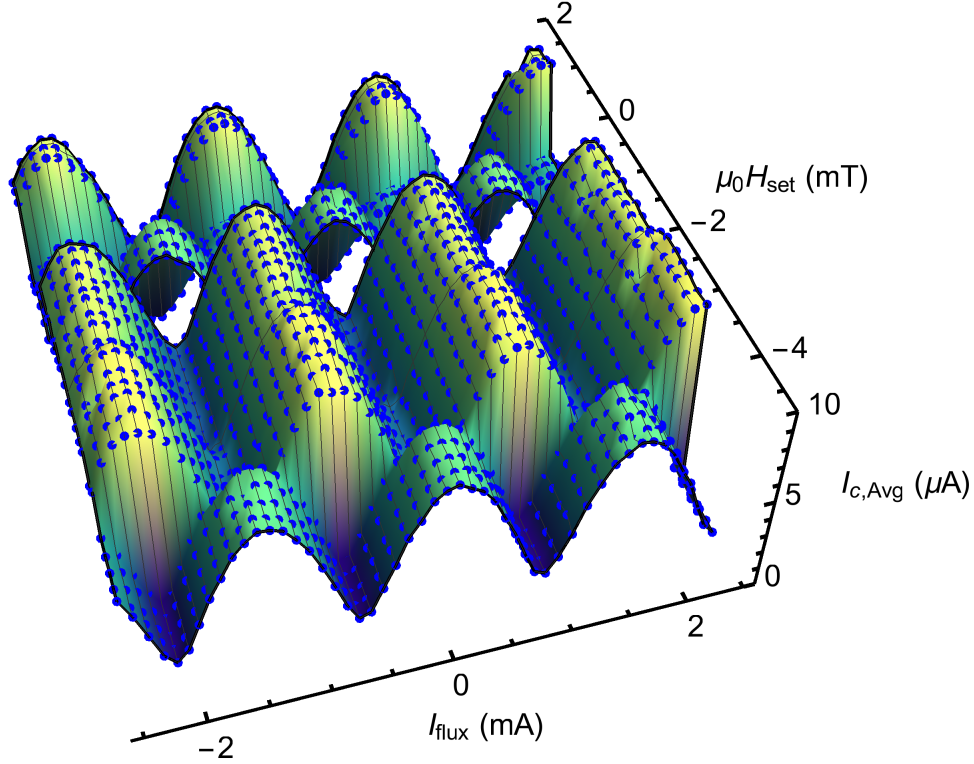


Figure 5: A 3D plot of a complete minor magnetization loop, for SQUID 2A-3. We show the oscillations in $I_{c,\text{Avg}}$ versus the flux line current, I_{flux} , measured after applying different values of the set field, $\mu_0 H_{\text{set}}$. All the SQUID oscillations are measured at zero field. Starting at zero field and increasing $\mu_0 H_{\text{set}}$ in the positive direction, the SQUID switches from the P to the AP state and will remain in that state even if $\mu_0 H_{\text{set}}$ is increased or decreased slightly in either direction. Next, returning to zero field, $\mu_0 H_{\text{set}}$ is applied in the negative field direction until the SQUID switches from the AP state back into the P state. The phase of the SQUID can thus be controllably set to either 0 or π on demand.

Table 3: Best-fit parameters for the P and AP states for SQUID 2A-3. The value of α_L in the fit is fixed at zero. The phase difference between the two states is $\approx \pi$ (ϕ_{shift} is listed in units of 2π).

State	β_L	α_I	I_{c+} (μA)	$ I_{c-} $ (μA)	ϕ_{shift}	$\phi_{\text{shift}}^P - \phi_{\text{shift}}^{AP}$
P	3.95×10^{-2}	$(-0.33 \pm 2.20) \times 10^{-2}$	4.50 ± 0.04	4.59 ± 0.04	0.069 ± 0.002	0.480 ± 0.004
AP	5.02×10^{-2}	$(1.91 \pm 0.09) \times 10^{-1}$	5.73 ± 0.04	5.82 ± 0.03	-0.411 ± 0.002	

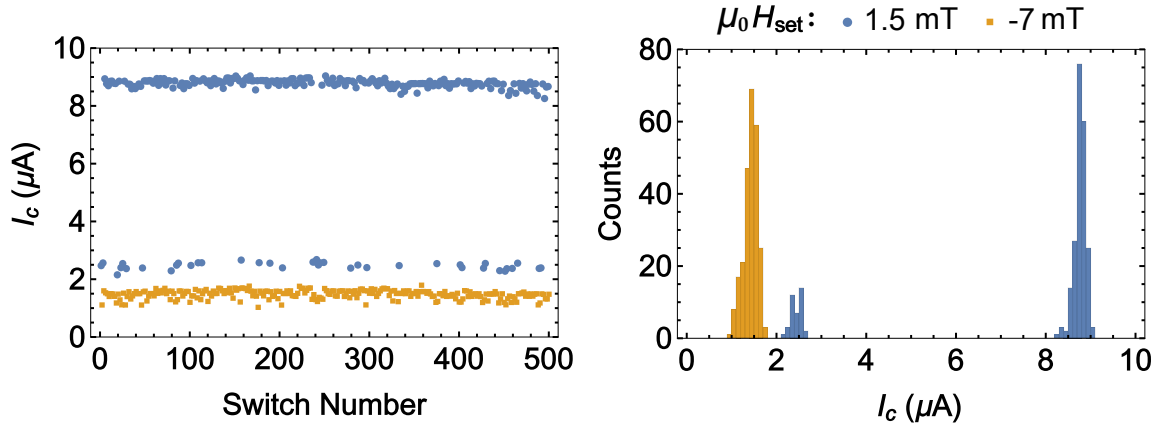


Figure 6: *Repeated switching between the P and the AP-states from SQUID 2A-3.* We plot $I_{c,\text{Avg}}$, obtained from fitting the measured I - V curves to the square root function (Eq. (6.1)), versus the number of times the junction has been switched (left). When the window of fields in which $(\mu_0 H_{c,\text{Py}_1} < \mu_0 H_{\text{set}} < \mu_0 H_{c,\text{Py}_2})$ is small, the error rates increase. In switching to the AP state the error rate was $\approx 16 \%$. We presume that the variability in the set field occasionally will cause the Py layer in both junctions to switch). However, the SQUID always switched back into the P-state. We plot a histogram where the I_c values have been binned into units of $0.2 \mu\text{A}$ (right).

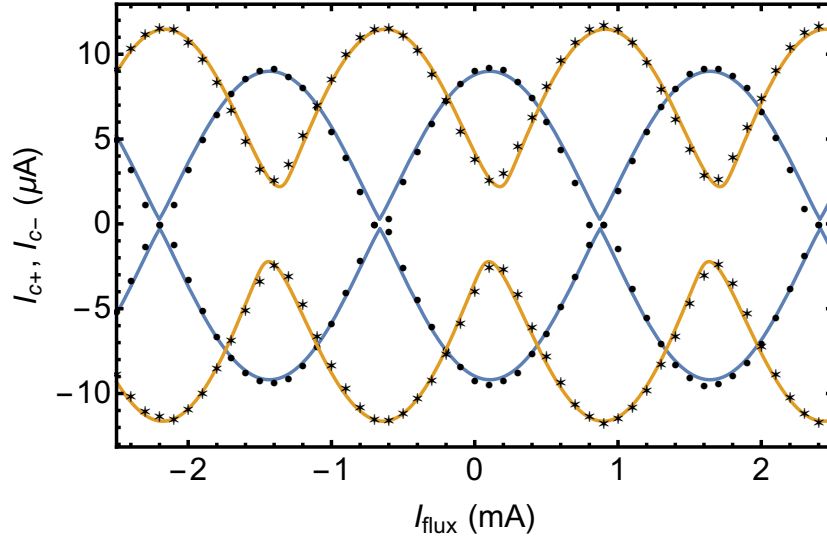


Figure 7: *Fitting the P and AP states from SQUID 2A-3.* At a given applied flux current I_{flux} , each data point represents the positive or negative critical current values extracted from a measured I - V curve that was fit to the Ivanchenko Zil'berman function Eq. (6.2) for the P (circles) and AP (stars) states. The resulting oscillation data has good agreement with the asymmetric SQUID theory from Ch. 7, where the lines represent the nonlinear least-squares fits for the P (blue) and AP (yellow) states. The associated best-fit parameters and errors are listed in Table 3, which confirms the relative π -phase shift between the two states. The P and AP states shown were measured after applying set fields, $\mu_0 H_{\text{set}}$, of 0 mT and 1.6 mT, respectively, after the junctions were initialized in a -150 mT set field.

SQUID 3A-3

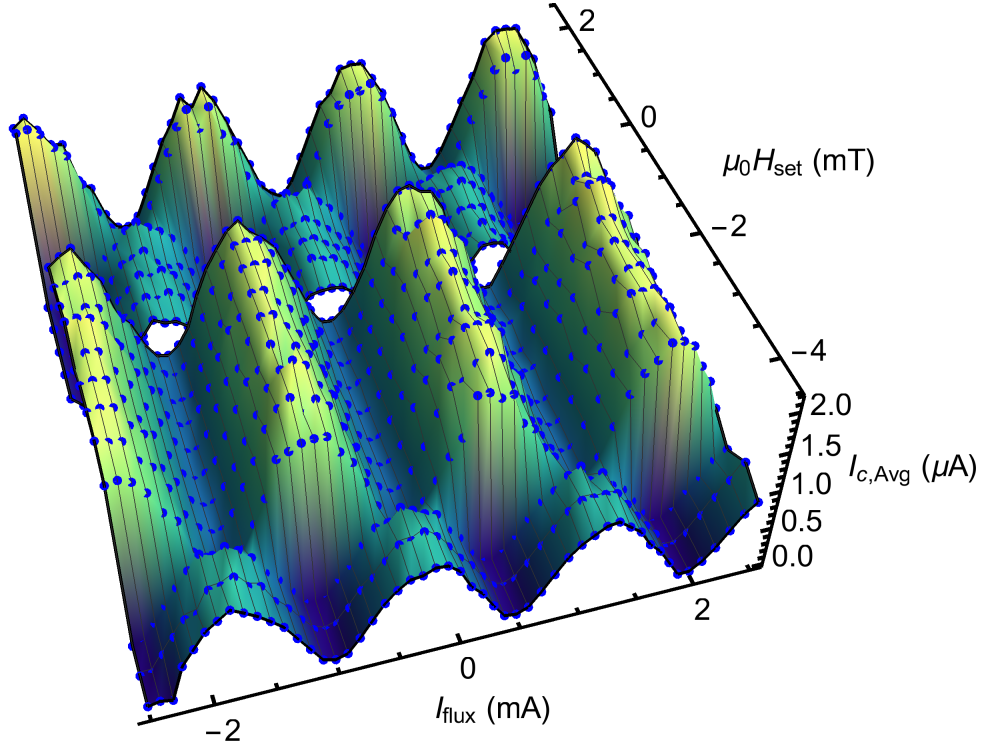


Figure 8: A 3D plot of a complete minor magnetization loop, for SQUID 3A-3. We show the oscillations in $I_{c,\text{Avg}}$ versus the flux line current, I_{flux} , measured after applying different values of the set field, $\mu_0 H_{\text{set}}$. All the SQUID oscillations are measured at zero field. Starting at zero field and increasing $\mu_0 H_{\text{set}}$ in the positive direction, the SQUID switches from the P to the AP state and will remain in that state even if $\mu_0 H_{\text{set}}$ is increased or decreased slightly in either direction. Next, returning to zero field, $\mu_0 H_{\text{set}}$ is applied in the negative field direction until the SQUID switches from the AP state back into the P state. The phase of the SQUID can thus be controllably set to either 0 or π on demand.

Table 4: Best-fit parameters for the P and AP states for SQUID 3A-3. The value of α_L in the fit is fixed at zero. The phase difference between the two states is $\approx \pi$ (ϕ_{shift} is listed in units of 2π).

State	β_L	α_I	I_{c+} (μA)	$ I_{c-} $ (μA)	ϕ_{shift}	$\phi_{\text{shift}}^P - \phi_{\text{shift}}^{AP}$
P	0.69×10^{-2}	$(0.16 \pm 3.77) \times 10^{-1}$	0.84 ± 0.03	0.75 ± 0.03	-0.072 ± 0.009	0.481 ± 0.010
AP	1.45×10^{-2}	$(1.97 \pm 0.09) \times 10^{-1}$	1.67 ± 0.01	1.66 ± 0.01	0.409 ± 0.002	

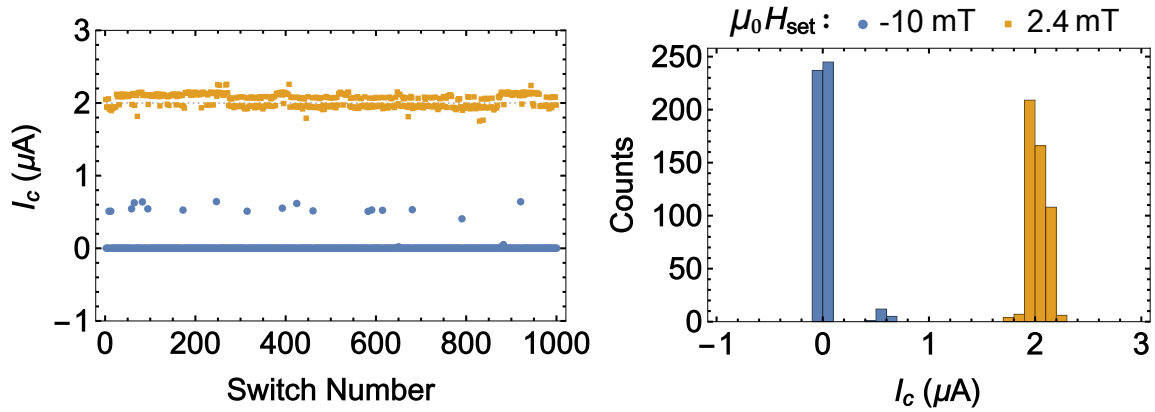


Figure 9: *Repeated switching between the P and the AP-states from SQUID 3A-3.* We plot $I_{c,\text{Avg}}$, obtained from fitting the measured I - V curves to the square root function (Eq. (6.1)), versus the number of times the junction has been switched (left). After 1000 cycles, in switching to the P state the error rate was $\approx 4\%$. We plot a histogram where the I_c values have been binned into units of $0.2 \mu\text{A}$ (right).

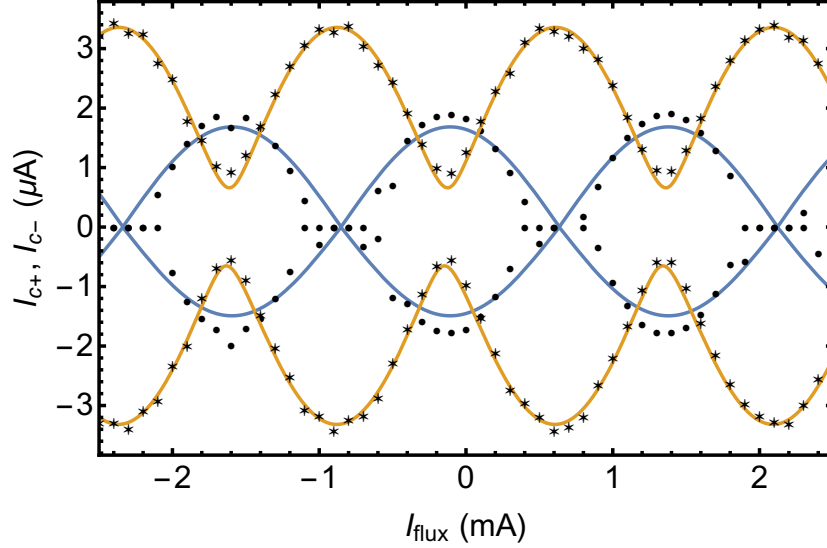


Figure 10: *Fitting the P and AP states from SQUID 3A-3.* At a given applied flux current I_{flux} , each data point represents the positive or negative critical current values extracted from a measured I - V curve that was fit to the Ivanchenko Zil'berman function Eq. (6.2) for the P (circles) and AP (stars) states. The Ivanchenko Zil'berman fits occasionally do not converge, typically at small values of the critical current, thus there are some missing data points in the plot. The resulting oscillation data has good agreement with the asymmetric SQUID theory from Ch. 7, where the lines represent the nonlinear least-squares fits for the P (blue) and AP (yellow) states. The associated best-fit parameters and errors are listed in Table 3, which confirms the relative π -phase shift between the two states. The P and AP states shown were measured after applying set fields, $\mu_0 H_{\text{set}}$, of 0.0 mT and 2.4 mT, respectively, after the junctions were initialized in a -150 mT set field.

SQUID 4A-1

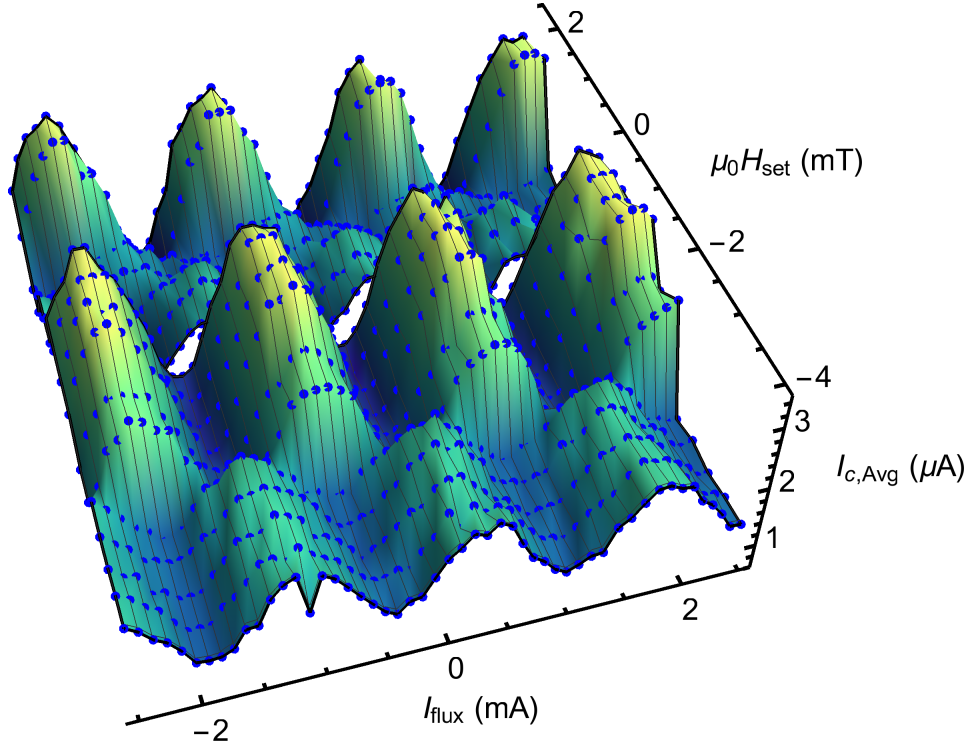


Figure 11: A 3D plot of a complete minor magnetization loop, for SQUID 4A-1. We show the oscillations in $I_{c,\text{Avg}}$ versus the flux line current, I_{flux} , measured after applying different values of the set field, $\mu_0 H_{\text{set}}$. All the SQUID oscillations are measured at zero field. Starting at zero field and increasing $\mu_0 H_{\text{set}}$ in the positive direction, the SQUID switches from the P to the AP state and will remain in that state even if $\mu_0 H_{\text{set}}$ is increased or decreased slightly in either direction. Next, returning to zero field, $\mu_0 H_{\text{set}}$ is applied in the negative field direction until the SQUID switches from the AP state back into the P state. The phase of the SQUID can thus be controllably set to either 0 or π on demand.

Table 5: Best-fit parameters for the P and AP states for SQUID 4A-1. The value of α_L in the fit is fixed at zero. The phase difference between the two states is $\approx \pi$ (ϕ_{shift} is listed in units of 2π).

State	β_L	α_I	I_{c+} (μA)	$ I_{c-} $ (μA)	ϕ_{shift}	$\phi_{\text{shift}}^P - \phi_{\text{shift}}^{AP}$
P	1.72×10^{-2}	$(6.81 \pm 0.45) \times 10^{-1}$	1.82 ± 0.02	1.95 ± 0.02	0.220 ± 0.025	0.618 ± 0.005
AP	2.31×10^{-2}	$(4.55 \pm 0.06) \times 10^{-1}$	2.57 ± 0.02	2.74 ± 0.01	0.455 ± 0.005	

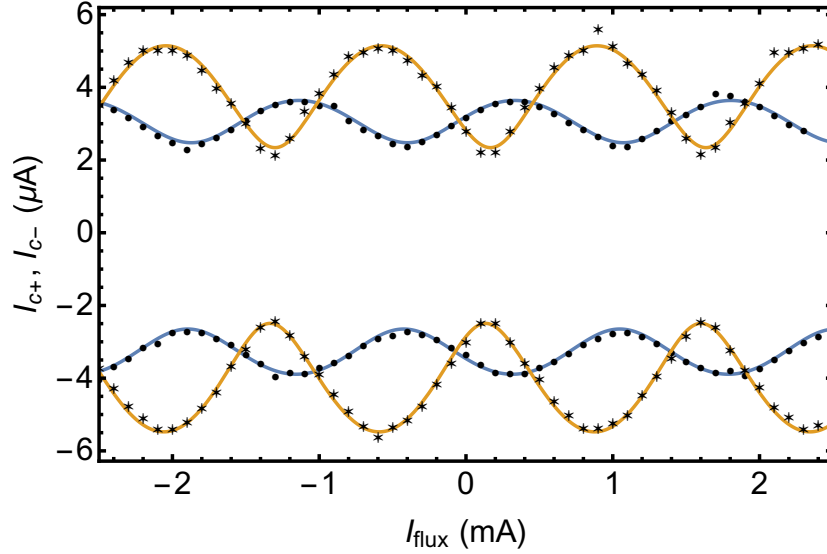


Figure 12: *Fitting the P and AP states from SQUID 4A-1.* At a given applied flux current I_{flux} , each data point represents the positive or negative critical current values extracted from a measured I - V curve that was fit to the Ivanchenko Zil'berman function Eq. (6.2) for the P (circles) and AP (stars) states. The Ivanchenko Zil'berman fits occasionally do not converge, typically at small values of the critical current, thus there are some missing data points in the plot. The resulting oscillation data has good agreement with the asymmetric SQUID theory from Ch. 7, where the lines represent the nonlinear least-squares fits for the P (blue) and AP (yellow) states. The associated best-fit parameters and errors are listed in Table 3, which confirms the relative π -phase shift between the two states. The P and AP states shown were measured after applying set fields, $\mu_0 H_{\text{set}}$, of 0.8 mT and 2.0 mT, respectively, after the junctions were initialized in a -150 mT set field.

SQUID 4A-2

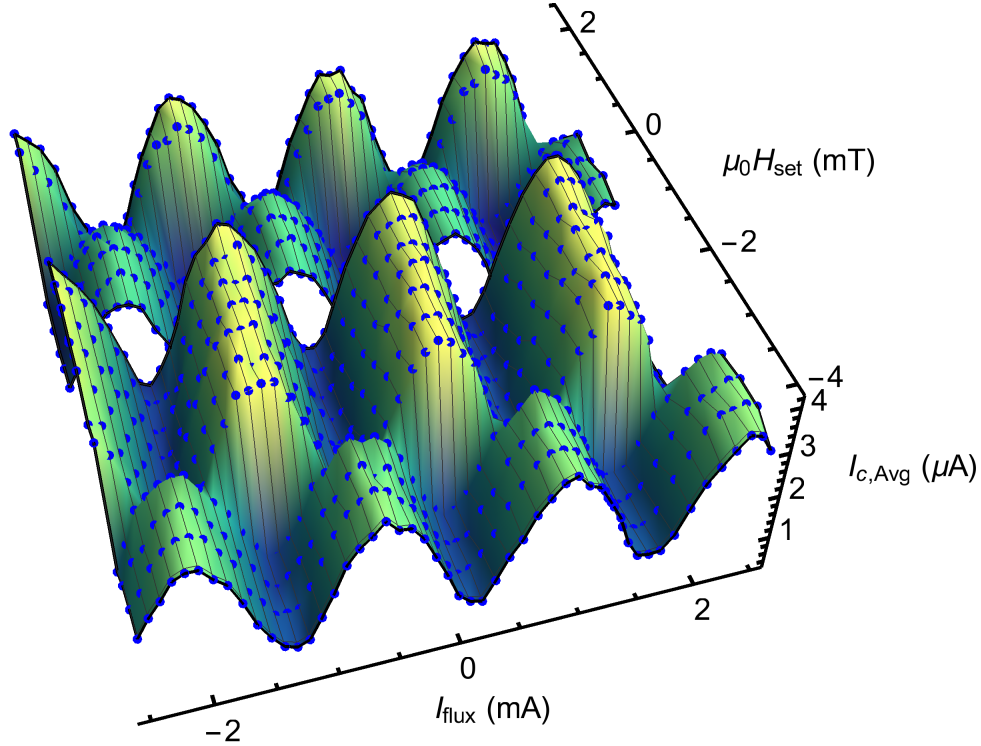


Figure 13: A 3D plot of a complete minor magnetization loop, for SQUID 4A-2. We show the oscillations in $I_{c,\text{Avg}}$ versus the flux line current, I_{flux} , measured after applying different values of the set field, $\mu_0 H_{\text{set}}$. All the SQUID oscillations are measured at zero field. Starting at zero field and increasing $\mu_0 H_{\text{set}}$ in the positive direction, the SQUID switches from the P to the AP state and will remain in that state even if $\mu_0 H_{\text{set}}$ is increased or decreased slightly in either direction. Next, returning to zero field, $\mu_0 H_{\text{set}}$ is applied in the negative field direction until the SQUID switches from the AP state back into the P state. The phase of the SQUID can thus be controllably set to either 0 or π on demand.

Table 6: Best-fit parameters for the P and AP states for SQUID 4A-2. The value of α_L in the fit is fixed at zero. The phase difference between the two states is $\approx \pi$ (ϕ_{shift} is listed in units of 2π).

State	β_L	α_I	I_{c+} (μA)	$ I_{c-} $ (μA)	ϕ_{shift}	$\phi_{\text{shift}}^P - \phi_{\text{shift}}^{AP}$
P	0.16×10^{-1}	$(2.93 \pm 0.13) \times 10^{-1}$	1.84 ± 0.02	1.90 ± 0.02	-0.116 ± 0.003	-0.508 ± 0.004
AP	0.20×10^{-1}	$(-3.05 \pm 0.04) \times 10^{-1}$	2.28 ± 0.01	2.34 ± 0.01	0.391 ± 0.001	

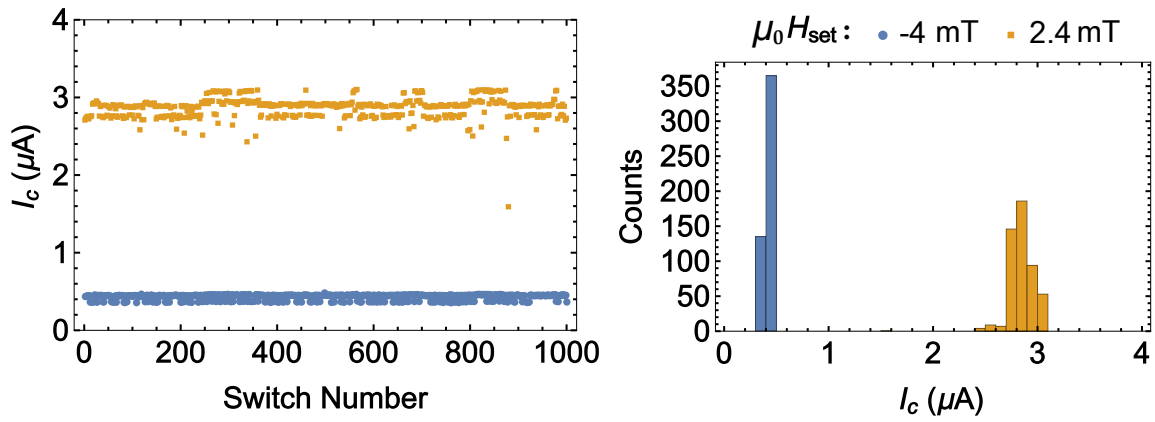


Figure 14: *Repeated switching between the P and the AP-states from SQUID 4A-2.* We plot $I_{c,\text{Avg}}$, obtained from fitting the measured I - V curves to the square root function (Eq. (6.1)), versus the number of times the junction has been switched (left). After 1000 cycles, switching between the P and AP states there was only one major error, though there is some spread in the critical current value in the AP state. We plot a histogram where the I_c values have been binned into units of $0.2 \mu\text{A}$ (right).

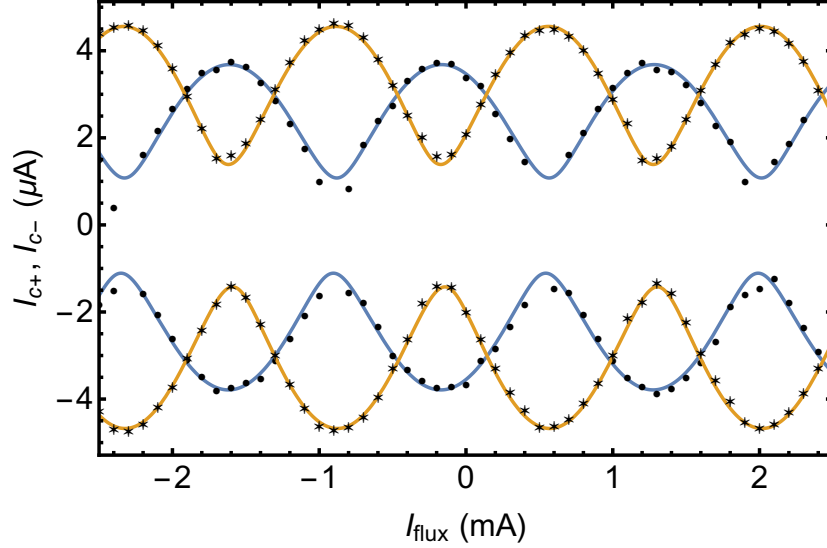


Figure 15: *Fitting the P and AP states from SQUID 4A-2.* At a given applied flux current I_{flux} , each data point represents the positive or negative critical current values extracted from a measured I - V curve that was fit to the Ivanchenko Zil'berman function Eq. (6.2) for the P (circles) and AP (stars) states. The Ivanchenko Zil'berman fits occasionally do not converge, typically at small values of the critical current, thus there are some missing data points in the plot. The resulting oscillation data has good agreement with the asymmetric SQUID theory from Ch. 7, where the lines represent the nonlinear least-squares fits for the P (blue) and AP (yellow) states. The associated best-fit parameters and errors are listed in Table 3, which confirms the relative π -phase shift between the two states. The P and AP states shown were measured after applying set fields, $\mu_0 H_{\text{set}}$, of 0 mT and 2.0 mT, respectively, after the junctions were initialized in a -150 mT set field.

REFERENCES

REFERENCES

- [1] D. S. Holmes, A. L. Ripple, and M. A. Manheimer. Energy-efficient superconducting computing—power budgets and requirements. *IEEE Trans. Appl. Supercond.*, 23(3):1701610, 2013.
- [2] M. A. Manheimer. Cryogenic computing complexity program: Phase 1 introduction. *IEEE Trans. Appl. Supercond.*, 25(3):1–4, 2015.
- [3] D. S. Holmes, A. M. Kadin, and M. W. Johnson. Superconducting computing in large-scale hybrid systems. *Computer*, 48(12):34–42, 2015.
- [4] D. A. Buck. The cryotron—a superconductive computer component. *Proc. IRE*, 44(4):482–493, 1956.
- [5] K. K. Likharev, O. A. Mukhanov, and V. K. Semenov. Resistive single flux quantum logic for the Josephson-junction digital technology. In *SQUID’85*, pages 1103–1108. Walter de Gruyter, Berlin, 1985.
- [6] K. K. Likharev and V. K. Semenov. RSFQ logic/memory family: A new Josephson-junction technology for sub-terahertz-clock-frequency digital systems. *IEEE Trans. Appl. Supercond.*, 50(1), 1991.
- [7] W. Chen, A. V. Rylyakov, V. Patel, J. E. Lukens, and K. K. Likharev. Rapid single flux quantum T-flip flop operating up to 770 GHz. *IEEE Trans. Appl. Supercond.*, 9(2):3212–3215, 1999.
- [8] Q. P. Herr, A. Y. Herr, O. T. Oberg, and A. G. Ioannidis. Ultra-low-power superconductor logic. *J. App. Phys.*, 109(10):103903, 2011.
- [9] O. A. Mukhanov. Energy-efficient single flux quantum technology. *IEEE Trans. Appl. Supercond.*, 21(3):760–769, 2011.
- [10] D. E. Kirichenko, S. Sarwana, and A. F. Kirichenko. Zero static power dissipation biasing of RSFQ circuits. *IEEE Trans. Appl. Supercond.*, 21(3):776–779, 2011.
- [11] F. Bedard, N. Welker, G. R. Cotter, M. A. Escavage, and J. T. Pinkston. Superconducting technology assessment. *National Security Agency, Office of Corporate Assessments*, 2005.

- [12] C. Bell, G. Burnell, C. W. Leung, E. J. Tarte, D.-J. Kang, and M. G. Blamire. Controllable Josephson current through a pseudospin-valve structure. *Appl. Phys. Lett.*, 84(7):1153–1155, 2004.
- [13] V. V. Ryazanov, V. V. Bol’ginov, D. S. Sobanin, I. V. Vernik, S. K. Tolpygo, A. M. Kadin, and O. A. Mukhanov. Magnetic Josephson junction technology for digital and memory applications. *Physics Procedia*, 36:35–41, 2012.
- [14] T. I. Larkin, V. V. Bol’ginov, V. S. Stolyarov, V. V. Ryazanov, I. V. Vernik, S. K. Tolpygo, and O. A. Mukhanov. Ferromagnetic Josephson switching device with high characteristic voltage. *Appl. Phys. Lett.*, 100(22):222601, 2012.
- [15] I. V. Vernik, V. V. Bol’ginov, S. V. Bakurskiy, A. A. Golubov, M. Y. Kupriyanov, V. V. Ryazanov, and O. A. Mukhanov. Magnetic Josephson Junctions With Superconducting Interlayer for Cryogenic Memory. *IEEE Trans. Appl. Supercond.*, 23(3):1701208, 2013.
- [16] M. Abd El Qader, R. K. Singh, S. N. Galvin, L. Yu, J. M. Rowell, and N. Newman. Switching at small magnetic fields in Josephson junctions fabricated with ferromagnetic barrier layers. *Appl. Phys. Lett.*, 104(2):022602, 2014.
- [17] B. Baek, W. H. Rippard, S. P. Benz, S. E. Russek, and P. D. Dresselhaus. Hybrid superconducting-magnetic memory device using competing order parameters. *Nat. Commun.*, 5:3888, 2014.
- [18] E. C. Gingrich, B. M. Niedzielski, J. A. Glick, Y. Wang, D. L. Miller, R. Loloee, W. P. Pratt Jr., and N. O. Birge. Controllable $0 - \pi$ Josephson junctions containing a ferromagnetic spin valve. *Nat. Phys.*, 12(6):564–567, 2016.
- [19] J. A. Glick, M. A. Khasawneh, B. M. Niedzielski, R. Loloee, W. P. Pratt Jr., N. O. Birge, E. C. Gingrich, P. G. Kotula, and N. Missert. Critical current oscillations of elliptical Josephson junctions with single-domain ferromagnetic layers. *J. App. Phys.*, 122(13):133906, 2017.
- [20] J. A. Glick, R. Loloee, W. P. Pratt, and N. O. Birge. Critical current oscillations of Josephson junctions containing PdFe nanomagnets. *IEEE Trans. App. Supercond.*, 27(4):1–5, 2017.
- [21] J. A. Glick, S. Edwards, D. Korucu, V. Aguilar, B. M. Niedzielski, R. Loloee, W. P. Pratt Jr., N. O. Birge, P. G. Kotula, and N. Missert. Spin-triplet supercurrent in Josephson junctions containing a synthetic antiferromagnet with perpendicular magnetic anisotropy. *arXiv:1710.07247*, 2017.
- [22] A. Y. Herr, Q. P. Herr, and O. Naaman. Phase hysteretic magnetic Josephson junction memory cell, Dec. 8, 2015. US Patent 9,208,861 B2.

- [23] I. M. Dayton, T. Sage, E. C. Gingrich, M. G. Loving, T. F. Ambrose, N. P. Siwak, S. Keebaugh, C. Kirby, D. L. Miller, A. Y. Herr, and Naaman O. Experimental demonstration of a Josephson magnetic memory cell with a programmable π -junction. *arXiv:1711.01681*, 2017.
- [24] H. K. Onnes and K. Hof. *Commun. Phys. Lab. Univ. Leiden.*, 120b, 122b, 124c, 1911.
- [25] W. Meissner and R. Ochsenfeld. Ein neuer effekt bei eintritt der supraleitfähigkeit. *Naturwissenschaften*, 21(44):787–788, 1933.
- [26] F. London and H. London. The electromagnetic equations of the supraconductor. *Proc. Royal Soc. A*, 149(866):71–88, 1935.
- [27] F. London. Macroscopical interpretation of supraconductivity. *Proc. Royal Soc. A*, 152:24–34, 1935.
- [28] C. J. Gorter and H. B. G. Casimir. The thermodynamics of the superconducting state. *Phys. Z.*, 35:963–966, 1934.
- [29] V. L. Ginzburg and L. D. Landau. On the theory of superconductivity. *Zh. Eksp. Teor. Fiz.*, 20:1064–1082, 1950.
- [30] L. P. Gor'kov. Microscopic derivation of the Ginzburg-Landau equations in the theory of superconductivity. *Sov. Phys. JETP*, 9(6):1364–1367, 1959.
- [31] L. P. Gor'kov. Theory of superconducting alloys in a strong magnetic field near the critical temperature. *Sov. Phys. JETP*, 10:998, 1960.
- [32] J. Bardeen, L. N. Cooper, and J. R. Schrieffer. Microscopic theory of superconductivity. *Phys. Rev.*, 106(1):162, 1957.
- [33] J. Bardeen, L. N. Cooper, and J. R. Schrieffer. Theory of superconductivity. *Phys. Rev.*, 108(5):1175, 1957.
- [34] C. A. Reynolds, B. Serin, W. H. Wright, and L. B. Nesbitt. Superconductivity of isotopes of mercury. *Phys. Rev.*, 78(4):487, 1950.
- [35] E. Maxwell. Isotope effect in the superconductivity of mercury. *Phys. Rev.*, 78(4):477, 1950.
- [36] L. N. Cooper. Bound electron pairs in a degenerate Fermi gas. *Phys. Rev.*, 104(4):1189, 1956.
- [37] H. Fröhlich. Interaction of electrons with lattice vibrations. *Proc. Roy. Soc. A*, 215(1122):291–298, 1952.

- [38] J. Bardeen and D. Pines. Electron-phonon interaction in metals. *Phys. Rev.*, 99(4):1140, 1955.
- [39] M. Tinkham. *Introduction to Superconductivity*. McGraw-Hill, 2nd edition, 1996.
- [40] I. Giaever. Energy Gap in Superconductors Measured by Electron Tunneling. *Phys. Rev. Lett.*, 5:147–148, 1960.
- [41] T. A. Fulton and L. N. Dunkleberger. Lifetime of the zero-voltage state in Josephson tunnel junctions. *Phys. Rev. B*, 9:4760–4768, 1974.
- [42] W. C. Stewart. Current-voltage characteristics of Josephson junctions. *App. Phys. Lett.*, 12(8):277–280, 1968.
- [43] D. E. McCumber. Effect of ac impedance on dc voltage-current characteristics of superconductor weak-link junctions. *J. App. Phys.*, 39(7):3113–3118, 1968.
- [44] B. S. Deaver and W. M. Fairbank. Experimental Evidence for Quantized Flux in Superconducting Cylinders. *Phys. Rev. Lett.*, 7:43–46, 1961.
- [45] R. Doll and M. Näbauer. Experimental Proof of Magnetic Flux Quantization in a Superconducting Ring. *Phys. Rev. Lett.*, 7:51–52, 1961.
- [46] W. A. Little and R. D. Parks. Observation of Quantum Periodicity in the Transition Temperature of a Superconducting Cylinder. *Phys. Rev. Lett.*, 9:9–12, 1962.
- [47] P. Weiss. La variation du ferromagnétisme avec la température. *Compt. Rend.*, 143:1136–1139, 1906.
- [48] W. Heisenberg. Mehrkörperproblem und resonanz in der quantenmechanik. *Zeitschrift für Physik*, 38(6):411–426, 1926.
- [49] P. A. M. Dirac. On the theory of quantum mechanics. *Proc. R. Soc. London A*, 112(762):661–677, 1926.
- [50] L. Landau and E. Lifshitz. On the theory of the dispersion of magnetic permeability in ferromagnetic bodies. *Phys. Zeitsch. der Sow*, 8(153):153–169, 1935.
- [51] E. C. Stoner and E. P. Wohlfarth. A mechanism of magnetic hysteresis in heterogeneous alloys. *Phil. Trans. R. Soc. Lond. A*, 240(826):599–642, 1948.
- [52] A. Thiaville. Extensions of the geometric solution of the two dimensional coherent magnetization rotation model. *J. Magn. Magn. Mater.*, 182(1):5–18, 1998.
- [53] R. Holm and W. Meissner. Messungen mit hilfe von flüssigem helium. xiii. *Zeitschrift für Physik*, 74(11):715–735, 1932.

- [54] G. Deutscher and P. G. De Gennes. *Superconductivity*, volume 2. Marcel Dekker, New York, 1969.
- [55] A. F. Andreev. The thermal conductivity of the intermediate state in superconductors. *Sov. Phys. JETP.*, 46(5):1823–1828, 1964.
- [56] B. Pannetier and H. Courtois. Andreev reflection and proximity effect. *J. Low Temp. Phys.*, 118(5-6):599–615, 2000.
- [57] A. I. Buzdin. Proximity effects in superconductor-ferromagnet heterostructures. *Rev. Mod. Phys.*, 77:935–976, 2005.
- [58] E. A. Demler, G. B. Arnold, and M. R. Beasley. Superconducting proximity effects in magnetic metals. *Phys. Rev. B*, 55:15174–15182, 1997.
- [59] P. Fulde and R. A. Ferrell. Superconductivity in a strong spin-exchange field. *Phys. Rev.*, 135:A550–A563, 1964.
- [60] A. I. Larkin and Yu. N. Ovchinnikov. Inhomogeneous State of Superconductors. *Zh. Eksp. Teor. Fiz.*, 47:1136, 1964. [*Soviet Physics J. Exp. Theor. Phys.*, **20**, 762, (1965)].
- [61] A. I. Buzdin, L. N. Bulaevskii, and S. V. Panyukov. Critical-current oscillations as a function of the exchange field and thickness of the ferromagnetic metal (F) in an S-F-S Josephson junction. *Pis'ma Zh. Eksp. Teor. Fiz.*, 35(4):147–148, 1982. [*J. Exp. Theor. Phys. Lett.*, **35**, 4, 20 (1982)].
- [62] C. Kittel. *Introduction to solid state physics*. Wiley, 2005.
- [63] T. Mühge, N. N. Garif'yanov, Yu. V. Goryunov, G. G. Khaliullin, L. R. Tagirov, K. Westerholt, I. A. Garifullin, and H. Zabel. Possible origin for oscillatory superconducting transition temperature in superconductor/ferromagnet multilayers. *Phys. Rev. Lett.*, 77(9):1857, 1996.
- [64] C. Strunk, C. Sürgers, U. Paschen, and H. v. Löhneysen. Superconductivity in layered Nb/Gd films. *Phys. Rev. B*, 49(6):4053, 1994.
- [65] T. Kontos, M. Aprili, J. Lesueur, F. Genêt, B. Stephanidis, and R. Boursier. Josephson Junction through a Thin Ferromagnetic Layer: Negative Coupling. *Phys. Rev. Lett.*, 89:137007, 2002.
- [66] K. M. Boden, W. P. Pratt Jr., and N. O. Birge. Proximity-induced density-of-states oscillations in a superconductor/strong-ferromagnet system. *Phys. Rev. B*, 84(2):020510, 2011.
- [67] L. N. Bulaevskii, V. V. Kuzii, and A. A. Sobyanin. Superconducting system with weak coupling to the current in the ground state. *Sov. JETP Lett.*, 25(7):290–294, 1977.

- [68] V. V. Ryazanov, V. A. Oboznov, A. Yu. Rusanov, A. V. Veretennikov, A. A. Golubov, and J. Aarts. Coupling of Two Superconductors through a Ferromagnet: Evidence for a π Junction. *Phys. Rev. Lett.*, 86:2427–2430, 2001.
- [69] Y. Blum, A. Tsukernik, M. Karpovski, and A. Palevski. Oscillations of the superconducting critical current in Nb-Cu-Ni-Cu-Nb junctions. *Phys. Rev. Lett.*, 89:187004, 2002.
- [70] H. Sellier, C. Baraduc, F. Lefloch, and R. Calemczuk. Temperature-induced crossover between 0 and π states in S/F/S junctions. *Phys. Rev. B*, 68:054531, 2003.
- [71] V. Shelukhin, A. Tsukernik, M. Karpovski, Y. Blum, K. B. Efetov, A. F. Volkov, T. Champel, M. Eschrig, T. Löfwander, G. Schön, and A. Palevski. Observation of periodic π -phase shifts in ferromagnet-superconductor multilayers. *Phys. Rev. B*, 73:174506, 2006.
- [72] M. Weides, M. Kemmler, E. Goldobin, D. Koelle, R. Kleiner, H. Kohlstedt, and A. Buzdin. High quality ferromagnetic 0 and π Josephson tunnel junctions. *Appl. Phys. Lett.*, 89:122511, 2006.
- [73] J. W. A. Robinson, S. Piano, G. Burnell, C. Bell, and M. G. Blamire. Critical current oscillations in strong ferromagnetic π junctions. *Phys. Rev. Lett.*, 97:177003, 2006.
- [74] J. W. A. Robinson, S. Piano, G. Burnell, C. Bell, and M. G. Blamire. Zero to π transition in superconductor-ferromagnet-superconductor junctions. *Phys. Rev. B*, 76:094522, 2007.
- [75] A. A. Bannykh, J. Pfeiffer, V. S. Stolyarov, I. E. Batov, V. V. Ryazanov, and M. Weides. Josephson tunnel junctions with a strong ferromagnetic interlayer. *Phys. Rev. B*, 79:054501, 2009.
- [76] T. S. Khaire, W. P. Pratt Jr., and N. O. Birge. Critical current behavior in Josephson junctions with the weak ferromagnet PdNi. *Phys. Rev. B*, 79:094523, 2009.
- [77] B. M. Niedzielski, E. C. Gingrich, R. Loloee, W. P. Pratt Jr., and N. O. Birge. S/F/S Josephson junctions with single-domain ferromagnets for memory applications. *Supercond. Sci. Technol.*, 28(8):085012, 2015.
- [78] F. S. Bergeret, A. F. Volkov, and K. B. Efetov. Josephson current in superconductor-ferromagnet structures with a nonhomogeneous magnetization. *Phys. Rev. B*, 64:134506, 2001.
- [79] A. Kadigrobov, R. I. Shekhter, and M. Jonson. Quantum spin fluctuations as a source of long-range proximity effects in diffusive ferromagnet-superconductor structures. *EPL (Europhysics Letters)*, 54(3):394, 2001.

- [80] M. Eschrig, J. Kopu, J. C. Cuevas, and G. Schön. Theory of half-metal/superconductor heterostructures. *Phys. Rev. Lett.*, 90:137003, 2003.
- [81] A. F. Volkov, F. S. Bergeret, and K. B. Efetov. Odd triplet superconductivity in superconductor-ferromagnet multilayered structures. *Phys. Rev. Lett.*, 90:117006, 2003.
- [82] F. S. Bergeret, A. F. Volkov, and K. B. Efetov. Odd triplet superconductivity and related phenomena in superconductor-ferromagnet structures. *Rev. Mod. Phys.*, 77:1321–1373, 2005.
- [83] R. S. Keizer, S. T. B. Goennenwein, T. M. Klapwijk, G. Miao, G. Xiao, and A. Gupta. A spin triplet supercurrent through the half-metallic ferromagnet CrO₂. *Nature*, 439(7078):825–827, 2006.
- [84] I. Sosnin, H. Cho, V. T. Petrashov, and A. F. Volkov. Superconducting phase coherent electron transport in proximity conical ferromagnets. *Phys. Rev. Lett.*, 96:157002, 2006.
- [85] T. S. Khaire, M. A. Khasawneh, W. P. Pratt Jr., and N. O. Birge. Observation of Spin-Triplet Superconductivity in Co-Based Josephson Junctions. *Phys. Rev. Lett.*, 104:137002, 2010.
- [86] J. W. A. Robinson, J. D. S. Witt, and M. G. Blamire. Controlled Injection of Spin-Triplet Supercurrents into a Strong Ferromagnet. *Science*, 329(5987):59–61, 2010.
- [87] D. Sprungmann, K. Westerholt, H. Zabel, M. Weides, and H. Kohlstedt. Evidence for triplet superconductivity in Josephson junctions with barriers of the ferromagnetic Heusler alloy Cu₂MnAl. *Phys. Rev. B*, 82:060505, 2010.
- [88] M. S. Anwar, F. Czeschka, M. Hesselberth, M. Porcu, and J. Aarts. Long-range supercurrents through half-metallic ferromagnetic CrO₂. *Phys. Rev. B*, 82:100501, 2010.
- [89] J. Wang, M. Singh, M. Tian, N. Kumar, B. Liu, C. Shi, J. K. Jain, N. Samarth, T. E. Mallouk, and M. H. W. Chan. Interplay between superconductivity and ferromagnetism in crystalline nanowires. *Nat. Phys.*, 6(5):389–394, 2010.
- [90] C. Klose, T. S. Khaire, Y. Wang, W. P. Pratt, N. O. Birge, B. J. McMorran, T. P. Ginley, J. A. Borchers, B. J. Kirby, B. B. Maranville, and J. Unguris. Optimization of spin-triplet supercurrent in ferromagnetic Josephson junctions. *Phys. Rev. Lett.*, 108:127002, 2012.
- [91] P. V. Leksin, N. N. Garif’yanov, I. A. Garifullin, Ya. V. Fominov, J. Schumann, Y. Krupskaya, V. Kataev, O. G. Schmidt, and B. Büchner. Evidence for triplet superconductivity in a superconductor-ferromagnet spin valve. *Phys. Rev. Lett.*, 109:057005, 2012.

- [92] V. I. Zdravkov, J. Kehrle, G. Obermeier, D. Lenk, H.-A. Krug von Nidda, C. Müller, M. Yu. Kupriyanov, A. S. Sidorenko, S. Horn, R. Tidecks, and L. R. Tagirov. Experimental observation of the triplet spin-valve effect in a superconductor-ferromagnet heterostructure. *Phys. Rev. B*, 87:144507, 2013.
- [93] N. Banerjee, C. B. Smiet, R. G. J. Smits, A. Ozaeta, F. S. Bergeret, M. G. Blamire, and J. W. A. Robinson. Evidence for spin selectivity of triplet pairs in superconducting spin valves. *Nat. Commun.*, 5:3048, 2014.
- [94] N. Banerjee, J. W. A. Robinson, and M. G. Blamire. Reversible control of spin-polarized supercurrents in ferromagnetic Josephson junctions. *Nat. Commun.*, 5:4771 EP, 2014.
- [95] A. Iovan, T. Golod, and V. M. Krasnov. Controllable generation of a spin-triplet supercurrent in a Josephson spin valve. *Phys. Rev. B*, 90:134514, 2014.
- [96] X. L. Wang, A. Di Bernardo, N. Banerjee, A. Wells, F. S. Bergeret, M. G. Blamire, and J. W. A. Robinson. Giant triplet proximity effect in superconducting pseudo spin valves with engineered anisotropy. *Phys. Rev. B*, 89:140508, 2014.
- [97] A. A. Jara, C. Safranski, I. N. Krivorotov, C. Wu, A. N. Malmi-Kakkada, O. T. Valls, and K. Halterman. Angular dependence of superconductivity in superconductor/spin-valve heterostructures. *Phys. Rev. B*, 89:184502, 2014.
- [98] M. G. Flokstra, T. C. Cunningham, J. Kim, N. Satchell, G. Burnell, P. J. Curran, S. J. Bending, C. J. Kinane, J. F. K. Cooper, S. Langridge, A. Isidori, N. Pugach, M. Eschrig, and S. L. Lee. Controlled suppression of superconductivity by the generation of polarized Cooper pairs in spin-valve structures. *Phys. Rev. B*, 91:060501, 2015.
- [99] A. Singh, S. Voltan, K. Lahabi, and J. Aarts. Colossal Proximity Effect in a Superconducting Triplet Spin Valve Based on the Half-Metallic Ferromagnet CrO_2 . *Phys. Rev. X*, 5:021019, 2015.
- [100] J. Linder and J. W. A. Robinson. Superconducting spintronics. *Nat. Phys.*, 11(4):307–315, 2015.
- [101] M. Eschrig. Spin-polarized supercurrents for spintronics: a review of current progress. *Rep. Prog. Phys.*, 78(10):104501, 2015.
- [102] A. Di Bernardo, S. Diesch, Y. Gu, J. Linder, G. Divitini, C. Ducati, E. Scheer, M. G. Blamire, and J. W. A. Robinson. Signature of magnetic-dependent gapless odd frequency states at superconductor/ferromagnet interfaces. *Nat. Commun.*, 6:8053, 2015.
- [103] Z. Feng, J. W. A. Robinson, and M. G. Blamire. Out of plane superconducting Nb/Cu/Ni/Cu/Co triplet spin-valves. *Appl. Phys. Lett.*, 111(4):042602, 2017.

- [104] C. Cirillo, S. Voltan, E. A. Ilyina, J. M. Hernandez, A. Garcia-Santiago, J. Aarts, and C. Attanasio. Long-range proximity effect in Nb-based heterostructures induced by a magnetically inhomogeneous permalloy layer. *New J. Phys.*, 19(2):023037, 2017.
- [105] M. Houzet and A. I. Buzdin. Long range triplet Josephson effect through a ferromagnetic trilayer. *Phys. Rev. B*, 76:060504, 2007.
- [106] E. C. Gingrich, P. Quarterman, Y. Wang, R. Loloee, W. P. Pratt Jr., and N. O. Birge. Spin-triplet supercurrent in Co/Ni multilayer Josephson junctions with perpendicular anisotropy. *Phys. Rev. B*, 86:224506, 2012.
- [107] W. M. Martinez, W. P. Pratt Jr., and N. O. Birge. Amplitude Control of the Spin-Triplet Supercurrent in $S/F/S$ Josephson Junctions. *Phys. Rev. Lett.*, 116:077001, 2016.
- [108] M. Eschrig. Spin-polarized supercurrents for spintronics. *Phys. Today*, 64:43, 2011.
- [109] E. C. Gingrich. *Phase control of the spin-triplet state in $S/F/S$ Josephson junctions*. PhD thesis, Michigan State University, 2014.
- [110] E. Terzioglu and M. R. Beasley. Complementary Josephson junction devices and circuits: a possible new approach to superconducting electronics. *IEEE Trans. Appl. Supercond.*, 8:48–53, 1998.
- [111] L. B. Ioffe, V. B. Geshkenbein, M. V. Feigel'man, A. L. Fauchere, and G. Blatter. Environmentally decoupled sds-wave Josephson junctions for quantum computing. *Nature*, 398:679–681, 1999.
- [112] G. Blatter, V. B. Geshkenbein, and L. B. Ioffe. Design aspects of superconducting-phase quantum bits. *Phys. Rev. B*, 63:174511, 2001.
- [113] A. V. Ustinov and V. K. Kaplunenko. Rapid single-flux quantum logic using π -shifters. *J. App. Phys.*, 94(8):5405–5407, 2003.
- [114] T. Yamashita, K. Tanikawa, S. Takahashi, and S. Maekawa. Superconducting π qubit with a ferromagnetic Josephson junction. *Phys. Rev. Lett.*, 95:097001, 2005.
- [115] M. I. Khabipov. A single flux quantum circuit with a ferromagnet-based Josephson π -junction. *Supercond. Sci. Technol.*, 23:045032, 2010.
- [116] A. K. Feofanov, V. A. Oboznov, V. V. Bol'ginov, J. Lisenfeld, S. Poletto, V. V. Ryazanov, A. N. Rossolenko, M. Khabipov, D. Balashov, A. B. Zorin, P. N. Dmitriev, V. P. Koshelets, and A. V. Ustinov. Implementation of superconductor/ferromagnet/superconductor π -shifters in superconducting digital and quantum circuits. *Nat. Phys.*, 6(8):593–597, 2010.

- [117] A. Y. Herr and Q. P. Herr. Josephson magnetic random access memory system and method, Sept. 18, 2012. US Patent 8,270,209.
- [118] E. Goldobin, H. Sickinger, M. Weides, N. Ruppelt, H. Kohlstedt, R. Kleiner, and D. Koelle. Memory cell based on a ϕ Josephson junction. *App. Phys. Lett.*, 102(24), 2013.
- [119] S. V. Bakurskiy, N. V. Klenov, I. I. Soloviev, V. V. Bol’ginov, V. V. Ryazanov, I. V. Vernik, O. A. Mukhanov, M. Yu. Kupriyanov, and A. A. Golubov. Theoretical model of superconducting spintronic SIsFS devices. *App. Phys. Lett.*, 102(19), 2013.
- [120] N. Ruppelt, H. Sickinger, R. Menditto, E. Goldobin, D. Koelle, R. Kleiner, O. Vavra, and H. Kohlstedt. Observation of $0 - \pi$ transition in SIsFS Josephson junctions. *Appl. Phys. Lett.*, 106(2):022602, 2015.
- [121] S. V. Bakurskiy, V. I. Filippov, V. I. Ruzhickiy, N. V. Klenov, I. I. Soloviev, M. Yu. Kupriyanov, and A. A. Golubov. Current-phase relations in SIsFS junctions in the vicinity of $0 - \pi$ transition. *Phys. Rev. B*, 95:094522, 2017.
- [122] Y. Wang, W. P. Pratt Jr., and N. O. Birge. Area-dependence of spin-triplet supercurrent in ferromagnetic Josephson junctions. *Phys. Rev. B*, 85:214522, 2012.
- [123] C. D. Thomas, M. P. Ulmer, and J. B. Ketterson. Superconducting tunnel junction base electrode planarization. *J. App. Phys.*, 84(1):364–367, 1998.
- [124] H. Kohlstedt, F. König, P. Henne, N. Thyssen, and P. Caputo. The role of surface roughness in the fabrication of stacked Nb/Al–AlO_x/Nb tunnel junctions. *J. App. Phys.*, 80(9):5512–5514, 1996.
- [125] Paul G. Kotula, Michael R. Keenan, and Joseph R. Michael. Tomographic Spectral Imaging with Multivariate Statistical Analysis: Comprehensive 3D Microanalysis. *Micross. and Microanal.*, 12:36–48, 2 2006.
- [126] D. L. Edmunds, W. P. Pratt Jr., and J. A. Rowlands. 0.1 ppm four-terminal resistance bridge for use with a dilution refrigerator. *Rev. Sci. Instrum.*, 51(11):1516–1522, 1980.
- [127] A. Barone and G. Paternò. *Physics and applications of the Josephson effect*. Wiley, 1982.
- [128] L. Vila, W. Park, J. A. Caballero, D. Bozec, R. Loloee, W. P. Pratt Jr., and J. Bass. Current perpendicular magnetoresistances of NiFeCo and NiFe “Permalloys”. *J. App. Phys.*, 87(12):8610–8614, 2000.

- [129] Y. M. Ivanchenko and L. A. Zil'berman. The Josephson Effect in Small Tunnel Contacts. *Zh. Eksp. Teor. Fiz.*, 55:2395–2402, 1968. [*Soviet Physics J. Exp. Theor. Phys.*, **28**, 6, (1969)].
- [130] V. Ambegaokar and B. I. Halperin. Voltage Due to Thermal Noise in the dc Josephson Effect. *Phys. Rev. Lett.*, 22:1364–1366, 1969.
- [131] A. I. Buzdin and M. Yu. Kupriyanov. Josephson junction with a ferromagnetic layer. *Pis'ma Zh. Eksp. Teor. Fiz.*, 53(6):308–312, 1991. [*J. Exp. Theor. Phys. Lett.*, **53**, 6, 321 (1991)].
- [132] N. G. Pugach, M. Yu. Kupriyanov, E. Goldobin, R. Kleiner, and D. Koelle. Superconductor-insulator-ferromagnet-superconductor Josephson junction: From the dirty to the clean limit. *Phys. Rev. B*, 84:144513, 2011.
- [133] Z. Radović, N. Lazarides, and N. Flytzanis. Josephson effect in double-barrier superconductor-ferromagnet junctions. *Phys. Rev. B*, 68:014501, 2003.
- [134] P. H. Barsic, O. T. Valls, and K. Halterman. Thermodynamics and phase diagrams of layered superconductor/ferromagnet nanostructures. *Phys. Rev. B*, 75:104502, 2007.
- [135] J. Bass. CPP magnetoresistance of magnetic multilayers: A critical review. *J. Magn. Mater.*, 408:244 – 320, 2016.
- [136] M. Fauré, A. I. Buzdin, A. A. Golubov, and M. Yu. Kupriyanov. Properties of superconductor/ferromagnet structures with spin-dependent scattering. *Phys. Rev. B*, 73:064505, 2006.
- [137] S. V. Bakurskiy, A. A. Golubov, N. V. Klenov, M. Yu. Kupriyanov, and I. I. Soloviev. Josephson effect in SIFS tunnel junctions with domain walls in the weak link region. *Pis'ma Zh. Eksp. Teor. Fiz.*, 101(11):863–868, 2015. [*J. Exp. Theor. Phys. Lett.*, **101**, 11, 765–771 (2015)].
- [138] D. M. Heim, N. G. Pugach, M. Yu. Kupriyanov, E. Goldobin, D. Koelle, R. Kleiner, N. Ruppelt, M. Weides, and H. Kohlstedt. The effect of normal and insulating layers on $0 - \pi$ transitions in Josephson junctions with a ferromagnetic barrier. *New J. Phys.*, 17(11):113022, 2015.
- [139] S. Senoussi, I. A. Campbell, and A. Fert. Evidence for local orbital moments on Ni and Co impurities in Pd. *Solid State Commun.*, 21(3):269 – 271, 1977.
- [140] H. Z. Arham, T. S. Khaire, R. Loloee, W. P. Pratt Jr., and N. O. Birge. Measurement of spin memory lengths in PdNi and PdFe ferromagnetic alloys. *Phys. Rev. B*, 80:174515, 2009.

- [141] L. S. Uspenskaya, A. L. Rakhmanov, L. A. Dorosinskii, A. A. Chugunov, V. S. Stolyarov, O. V. Skryabina, and S. V. Egorov. Magnetic patterns and flux pinning in Pd_{0.99}Fe_{0.01}-Nb hybrid structures. *Pis'ma Zh. Eksp. Teor. Fiz.*, 97(3):176–179, 2013. [*J. Exp. Theor. Phys. Lett.*, **97**, 3, 155–158 (2013)].
- [142] B. Baek. Private communication. One may need 400 mT to initialize the magnetization direction of a thin Ni nanomagnet, whereas we used only 260 mT.
- [143] B. Baek, M. L. Schneider, M. R. Pufall, and W. H. Rippard. Phase Offsets in the Critical-Current Oscillations of Josephson Junctions Based on Ni and Ni-(Ni₈₁Fe₁₉)_xNb_y Barriers. *Phys. Rev. Appl.*, 7:064013, 2017.
- [144] B. M. Niedzielski. *Phase Sensitive Measurements of Ferromagnetic Josephson Junctions for Cryogenic Memory Applications*. PhD thesis, Michigan State University, 2017.
- [145] B. Baek. Spin-transfer torque switching in nanopillar superconducting-magnetic hybrid Joseph junctions. *Phys. Rev. Appl.*, 3:011001, 2015.
- [146] W.-T. Tsang and T. Van Duzer. DC analysis of parallel arrays of two and three Josephson junctions. *J. App. Phys.*, 46(10):4573–4580, 1975.
- [147] A. F. Volkov and K. B. Efetov. Odd spin-triplet superconductivity in a multilayered superconductor-ferromagnet Josephson junction. *Phys. Rev. B*, 81:144522, 2010.
- [148] L. Trifunovic and Z. Radović. Long-range spin-triplet proximity effect in Josephson junctions with multilayered ferromagnets. *Phys. Rev. B*, 82:020505, 2010.
- [149] M. Schneider, October 2015. Private communication.
- [150] Y.-J. Chang, A. Canizo-Cabrera, V. Garcia-Vazquez, Y.-H. Chang, and T.-H. Wu. Perpendicular magnetic tunnel junctions with synthetic antiferromagnetic pinned layers based on [Co/Pd] multilayers. *J. App. Phys.*, 113(17):17B909, 2013.
- [151] J.-B. Lee, G.-G. An, S.-M. Yang, H.-S. Park, W.-S. Chung, and J.-P. Hong. Thermally robust perpendicular Co/Pd-based synthetic antiferromagnetic coupling enabled by a W capping or buffer layer. *Sci. Rep.*, 6:21324, 2016.
- [152] D. Smith, V. Parekh, E. Chunsheng, S. Zhang, W. Donner, T. R. Lee, S. Khizroev, and D. Litvinov. Magnetization reversal and magnetic anisotropy in patterned Co/Pd multilayer thin films. *J. App. Phys.*, 103(2):023920, 2008.
- [153] B. M. Niedzielski, T. J. Bertus, J. A. Glick, R. Loloee, W. P. Pratt Jr., and N. O. Birge. Spin-valve Josephson junctions for cryogenic memory. *arXiv:1709.04815*, 2017.

- [154] P. G. Kotula and M. R. Keenan. Application of multivariate statistical analysis to STEM X-ray spectral images: Interfacial analysis in microelectronics. *Microsc. and Microanal.*, 12(6):538–544, 2006.
- [155] V. V. Ryazanov. Josephson superconductor-ferromagnet-superconductor π -contact as an element of a quantum bit (experiment). *Phys. Usp.*, 42(8):825, 1999.
- [156] D. Korucu. unpublished, 2016.
- [157] H. Y. T. Nguyen, R. Acharyya, E. Huey, B. Richard, R. Loloee, W. P. Pratt Jr., J. Bass, S. Wang, and K. Xia. Conduction electron scattering and spin flipping at sputtered Co/Ni interfaces. *Phys. Rev. B*, 82:220401, 2010.
- [158] S. D. Pollard, J. A. Garlow, J. Yu, Z. Wang, Y. Zhu, and H. Yang. Observation of stable Néel skyrmions in cobalt/palladium multilayers with Lorentz transmission electron microscopy. *Nat. Commun.*, 8:14761, 2017.